



<https://www.gurugramuniversity.ac.in>

ISSN: 3107-4715 (Online)

INTERNATIONAL JOURNAL OF SCIENCE & TECHNOLOGY (PRAGYANAM)

An Annual Peer-Reviewed Journal

GURUGRAM UNIVERSITY, GURUGRAM

(A State Govt. University Established Under Haryana Act 17 of 2017)

VOLUME 1

ISSUE 1

JANUARY–DECEMBER 2025

Published by

**Department of Engineering & Technology
Gurugram University, Gurugram, Delhi-NCR, India**

PEN TO PRINT PUBLISHING



INTERNATIONAL JOURNAL OF SCIENCE & TECHNOLOGY (PRAGYANAM) GURUGRAM UNIVERSITY, GURUGRAM

(A State Govt. University Established Under Haryana Act 17 of 2017)

Volume 1, Issue 1

ISSN: 3107-4715 (Online)

January–December 2025

International Advisory Board Members

CHIEF PATRON

PROF. SANJAY KAUSHIK

*Hon'ble Vice Chancellor, Gurugram University, Gurugram,
Haryana, India*

PROF. HARI M. UPADHYAYA

*Professor, School of Engineering,
London South Bank University, London, UK*

PROF. PRAVEEN KUMAR

*Director & Professor, Department of Computer Engineering,
Astana IT University, Kazakhstan*

PROF. DIANA BOGDANOVA

University of Science and Technology, UFA, Russia

PROF. NISHITH PRAKASH

Northeastern University, Boston, Massachusetts, USA

PROF. VALLIAPPAN RAJU

Brno University, Czech Republic

PROF. MICHAEL ONYEMA EDEH

*Deputy Dean, Faculty of Allied Health and Applied
Sciences, Coal City University, Nigeria*

PROF. VALDEMAR VICENTE

*Head of GOiás Information Systems and Software
Engineering Research Team (GoIn-Sight), Graciano Neto,
Federal University of GOiás GOiânia, Brazil*

PROF. NARESH KUMAR

*Computer Science, DMPS, University of Nizwa Sultanate of
Oman*

PROF. FILIPPO S. BOI

College of Physics, Sichuan University, China

PROF. HAIDER RAZA

University of Essex, UK

PROF. HEIM LEVOKOVITZ

University of Massachusetts, UMass, Lowell USA

PROF. EDEH MICHAEL ONYEMA

Coal City University, Nigeria

PROF. SALIL KANHERE

CSE Deptt., UNSW, Sydney, Australia

PROF. AHMAD RIFQI MD ZAIN

*Institute of Microengineering and Nanoelectronics (IMEN),
Universiti Kebangsaan Malaysia (UKM)*

DR. KUSUM YADAV

University of Ha'il, Kingdom of Saudi Arabia

DR. ARCHANA KUMARI

*Department of Medicine University of Saskatchewan
Saskatoon, Canada*

DR. PRASUN KUMAR

Chungbuk National University, South Korea

DR. MANOJ KUMAR

University of Wollongong Dubai, UAE

DR. ABD KHAMIM ISMAIL

*Associate Professor, Department of Physics, Faculty of
Science, Universiti Teknologi Malaysia (UTM)*

DR. ABD RASHID BIN MOHD YUSOFF

*Associate Professor, Department of Physics, Faculty of
Science, Universiti Teknologi Malaysia (UTM)*

DR. MOHD MURTADHA MOHAMAD

*Associate Professor, Faculty of Computing, Universiti
Teknologi Malaysia (UTM)*

DR. AHMED HAMAD

*Food Hygiene and Control Department, Benha University,
Egypt*

DR. SUMIT CHAKRAVARTY

Kennesaw State University, USA

DR. RIAZ KHAN

*Associate Professor (Research), Yangtze River Delta
Research Institute, China*

DR. LOCHANDKA RANTHUNGA

Faculty of Engineering, University of Moratuwa, Sri Lanka

PRASHANT SHEKHAR

Client Partner, Infosys, USA

REETA JHA

Senior Director, Data & Analytics Leader at Travelers, USA

National Advisory Board Members

CHIEF PATRON

PROF. SANJAY KAUSHIK

Hon'ble Vice Chancellor, Gurugram University, Gurugram, Haryana, India

PROF. DINESH KUMAR

Hon'ble Vice Chancellor, Vishwakarma Skill University, Palwal, Haryana, India

PROF. R. K. MITTAL

Hon'ble Vice Chancellor, Chaudhary Bansi Lal University, Haryana, India

PROF. RANJANA JHA

Hon'ble Vice Chancellor, IGDTUW, New Delhi, India

PROF. DHARMINDER KUMAR

Former Director, CSE Department, GJUST, Hisar, Haryana, India

PROF. DURGA TOSHWAL

IIT, Roorkee, Uttarakhand, India

PROF. ANIL K. SAINI

Dean of Faculty, GGSIPU, New Delhi, India

PROF. VIKRAM SINGH

JCBOSEUST, YMCA Faridabad, India

PROF. M. N. HODA

Director (BVICAM), GGSIPU, New Delhi, India

PROF. VASUDHA BHATNAGAR

HOD (CSE), Delhi University, New Delhi, India

PROF. RAKESH KUMAR

Chairman (CS & Applications), Kurukshetra University, Kurukshetra, India

PROF. SUCHITA UPADHYAY

CS & Applications, Kurukshetra University, Kurukshetra, India

PROF. SHAMPA CHAKRAVERTY

NSUT, New Delhi, India

PROF. ANURAG JAIN

GGSIU, New Delhi, India

PROF. NAVEEN KUMAR

Gurugram University, Delhi-NCR, India

PROF. ANJU VERMA

GJUST, Hisar, Haryana, India

PROF. HEMA BANATI

Delhi University, New Delhi, India

PROF. PARDEEP AHLAWAT

MDU, Rohtak, Haryana, India

PROF. SURJEET DAYAL

CSE, Amity University, Noida (UP), India

PROF. V. V. SUBRAHMANYAM

IGNOU, New Delhi, India

PROF. SATYAM BARODA

MDU, Rohtak, Haryana, India

PROF. BIKRAMJIT CHAKRABORTY

Department of Architecture, RVCA, Bangalore, India

PROF. KULBHUSHAN JAIN

CEPT University, Ahmedabad, Gujarat, India

DR. MUKESH PRATAP SINGH

Jamia Millia Islamia, New Delhi, India

DR. RAHUL JOHARI

GGSIU, New Delhi, India

DR. RAVINDER KUMAR

CSE Department, Thapar University, Patiala, Punjab (India)

Editorial Board Members

CHIEF PATRON

Prof. Sanjay Kaushik

Vice Chancellor, Gurugram University, Gurugram, Haryana, India

PATRON(S)

Dr. Sanjay Arora

Registrar, Gurugram University, Gurugram, Haryana, India

EDITOR-IN-CHIEF

Prof. Shyam Sunder Tyagi

Dean, Faculty of Science and Technology, Gurugram University, Gurugram, Haryana, India

EDITOR

Prof. Rashmi Jha

Professor-Adjunct, Department of Engg. & Tech., Gurugram University, Gurugram, Haryana, India

ASSOCIATE EDITORS

Dr. Charu Gandhi

Associate Professor, Department of Engg. & Tech.,
Gurugram University, Gurugram, Haryana, India

Dr. Rakesh Garg

Associate Professor, Department of Engg. & Tech.,
Gurugram University, Gurugram, Haryana, India

Dr. Archana Dixit

Associate Professor, Maths Department,
Gurugram University, Gurugram, Haryana, India

Dr. Ranjeet

Associate Professor, Physics Department, Gurugram
University, Gurugram, Haryana, India

INTERNATIONAL EDITORIAL BOARD MEMBERS

Prof. Hari M. Upadhyaya

Professor, School of Engineering,
London South Bank University, London, UK

Prof. Praveen Kumar

Director & Professor, Department of Computer
Engineering, Astana IT University, Kazakhstan

Dr. Kusum Yadav

Associate Professor, College of Computer Science and Engineering. University of Ha'il, Kingdom of Saudi Arabia

International Journal of Science and Technology (PRAGYANAM) is published annually by joint collaboration of Editorial team of Engineering & Technology and Applied Sciences Departments under the aegis of Gurugram University, Gurugram, Delhi-NCR (India). The views expressed in this journal are those of the authors. No part of this publication may be produced in any form without the written permission of the publisher.

Printed by Pen to Print Publishing LLP, WZ-911/2, Street Shanker Lal, Ring Road, Naraina, New Delhi 110028
E-mail: pen2print.publishing@gmail.com | Mob. 9868029307, 7011949570



Contents

<i>International Advisory Board Members</i>	i
<i>National Advisory Board Members</i>	ii
<i>Editorial Board Members</i>	iii
<i>Message from the Vice Chancellor</i>	vii
<i>Foreword</i>	ix
<i>Editorial Note</i>	xi
1. Nickel-Based Nanocomposites with Tunable Optical Properties for Sustainable Solar Energy Solutions	1
<i>Soumya Rai, Himani Chaudhary, Peeyush Phogat, Shreya, Ranjana Jha & Sukhvir Singh</i>	
2. Absorption Enhancement in Silicon Solar Cell by Incorporation of Metal Nanoparticles	14
<i>Mohd Amir, Mukesh Pratap Singh & Iram Masood</i>	
3. Morphological and Optical Analysis of Tungsten Oxide Nanosheets for Gas Sensing Application	22
<i>Tamanna Jindal, Peeyush Phogat, Shreya, Ranjana Jha & Sukhvir Singh</i>	
4. Organic Solar Cell Based with Inorganic Transport Layers: Performance Analysis and Optimization	33
<i>Iram Masood, Mukesh Pratap Singh & Mohd Amir</i>	
5. A Learning based Model for Wheat Disease Detection and Classification	41
<i>Rakesh Garg, Neetu Singla, Charu, Sachin Lalar & Shubham Goel</i>	
6. Energy Consumption Trends in India and Its Impact on Indian Economy	54
<i>Meraj Alam, Rajesh Kumar Saluja, Priyanka Vashisht, Nishi Gupta & Rashmi Jha</i>	
7. Trajectory Tracking Control of a Two-Link Manipulator Including Actuator Dynamics Based on Sliding Mode Controller	61
<i>Manju Rani & Naveen Kumar</i>	
8. Study of Wave Propagation in Piezo-visco-thermo-elastic Material	68
<i>Vipin Gupta & Daksh Sen</i>	
9. Fixed Point for Chatterjea Contraction and Its Application to Cauchy Problem	76
<i>Anshuka Kadyan, Savita Rathee & Anil Kumar</i>	
10. Techniques of Improving Electric Characteristics of Si Strip Sensors Equipped using Various Isolation Methods	87
<i>Ranjeet Dalal</i>	
11. Visual Narratives: Enhancing Image Captioning with CNN-RNN-LSTM Fusion	91
<i>Kapil Kumar Choudhary, Naveen Kumar & Dishant Kumar</i>	
Book Review	99
Call for Papers	103
Certificate of Originality	104
Editorial Board Member's Profiles	105



Message from the Vice Chancellor



It gives me immense pride and joy to announce the launch of our new journal, International Journal of Science & Technology (PRAGYANAM), spearheaded by the Department of Engineering and Technology, Gurugram University, Gurugram, Haryana (India). This initiative marks a significant milestone in our academic journey, reflecting our unwavering commitment to fostering innovation, research excellence and interdisciplinary collaboration.

PRAGYANAM is not merely a journal; it is a visionary platform created to nurture the spirit of inquiry, encourage scholarly exchange, and promote global research dialogue. By bridging the gap between fundamental research and real-world application, this journal is poised to become a catalyst for scientific advancement and societal transformation.

IJST (PRAGYANAM) will cover a broad spectrum of topics in science and technology—from advancements in artificial intelligence to applied sciences, renewable energy systems, cutting-edge material science, robotics, communication networks, and sustainable engineering practices. By embracing these diverse areas, the journal aims to become a trusted source of knowledge for both academia and industry.

This scholarly initiative also reflects our university's strategic goal to elevate its academic standing through impactful research, international collaborations and fostering a culture of publication and innovation. It stands as a testament to our belief that knowledge must continuously evolve and be disseminated to serve humanity at large.

This endeavour would not have been possible without the relentless dedication and meticulous efforts of the editorial team. Their vision, hard work and attention to detail have ensured that this journal upholds the highest standards of quality and relevance. I commend their commitment and enthusiasm in bringing this dream to fruition.

I extend my heartfelt congratulations to the editorial team and all contributors who have worked tirelessly to bring this vision to life. I am confident that the journal will pave the way for many young researchers and academicians to contribute meaningfully to the world of science and technology.

May IJST (PRAGYANAM) inspire and ignite the minds of many in the years to come.

Extending heartfelt wishes for the grand success of this prestigious academic endeavour of international acclaim!

Prof. Sanjay Kaushik

Chief Patron – IJST (PRAGYANAM) &
Vice Chancellor
Gurugram University, Gurugram (India)



Foreword

Dear Readers,

As the Editor-in-Chief of the Gurugram University Journal – “*International Journal of Science & Technology (PRAGYANAM)*”, I am thrilled to present its latest edition showcasing cutting-edge research and innovative findings across various interdisciplinary fields. Welcome to the “First Edition (Jan-Dec 2025 issue)” of our Journal where we bring together insights and innovations from the diverse fields of Engineering & Technology, Computer Science and Applied Sciences disciplines. As we navigate the complex landscape of modern research, our journal serves as a platform for interdisciplinary dialogue and collaboration, fostering a deeper understanding of the interconnection between these domains.

In this issue, we are proud to present a wide array of articles that delve into cutting-edge research and thought-provoking analysis. From advancements in engineering that push the boundaries of technological innovation to strategic insights in management that shape the future of organizations, each contribution represents a unique perspective on the challenges and opportunities facing our world today.

In the realm of Applied Sciences, our contributors explore groundbreaking discoveries that have the potential to revolutionize industries and improve quality of life. From breakthroughs in technology to its innovative applications in day-to-day modern life, the interdisciplinary nature of our journal allows for the cross-pollination of ideas and the emergence of novel solutions to complex problems.

As editors, we are continually inspired by the dedication and passion of our contributors, whose innovative research work reflects the diversity and richness of the interdisciplinary landscape. We are genuinely grateful for their commitment to advancing knowledge and driving positive change in their respective fields.

In this endeavour, I wish to express my heartfelt gratitude to our Hon’ble Vice Chancellor, Prof. Sanjay Kaushik of Gurugram University, for his visionary leadership in fostering a strong research culture across the university and its affiliated colleges. I am deeply thankful to our esteemed Patron, Dr. Sanjay Arora (Registrar), for his unwavering faith in the capabilities of the editorial team. I would also like to acknowledge the continuous support and insights of the National and International Advisory Board Members of the journal.

I wish to extend my deep appreciation to the committed efforts of our editorial team in creating the first edition of our yearly international journal. Being associated with IJST (PRAGYANAM) is both an honour and a humbling privilege, given its dedication to maintaining the utmost standards of research excellence. I encourage the team to persist in their diligent efforts to ensure the journal’s inclusion and indexing in reputable citation databases.

We invite our readers to engage with the content presented in this issue, to explore new ideas and to join us in the pursuit of interdisciplinary excellence. Together, let us continue to push the boundaries of knowledge and create a better, more sustainable future for all.

Thank you for your continued support!

Prof. S. S. Tyagi
Editor-in-Chief



Editorial Note

It is with great pride and enthusiasm that I present the inaugural edition of the “*International Journal of Science & Technology (PRAGYANAM)*”, the journal of the Department of Engineering and Technology, Gurugram University, Gurugram. This journal is built on the conviction that science and technology are the driving forces behind progress, offering innovative solutions to global challenges and paving the way for new discoveries.

As we launch this first edition, I am pleased to introduce a diverse collection of articles that highlight groundbreaking research across a wide array of disciplines. From Artificial Intelligence and Machine Learning to sustainable energy solutions, biotechnology, semiconductors, optical and nano-physics, this edition encapsulates the dynamic nature of contemporary scientific research and technological advancements. Each research contribution is a reflection of the efforts of researchers, practitioners, and scholars dedicated to expanding the horizons of human understanding in science and technology.

The research presented here showcases the potential of cutting-edge technologies to address present-day global challenges and create a more sustainable, connected future. This edition consists of two sections—the first presents 11 research papers, followed by a book review.

The first paper titled, “Nickel-Based Nanocomposites with Tunable Optical Properties for Sustainable Solar Energy Solutions” by Soumya Rai, Himani Chaudhary, Peeyush Phogat, Shreya, Ranjana Jha & Sukhvir Singh explores the development of nickel-based nanocomposites with tunable optical properties to enhance solar energy efficiency. By manipulating these optical characteristics, the authors offer a promising solution to improve solar energy conversion and advance sustainable energy strategies.

Mohd. Amir, Mukesh Pratap Singh & Iram Masood contribute the paper titled, “Absorption Enhancement in Silicon Solar Cells by Incorporation of Metal Nanoparticles”, which investigates how metal nanoparticles can enhance light absorption in silicon solar cells. Their findings demonstrate a significant improvement in solar cell efficiency, pointing to more effective energy harvesting solutions.

The paper titled “Morphological and Optical Analysis of Tungsten Oxide Nanosheets for Gas Sensing Applications” by Tamanna Jindal, Peeyush Phogat, Shreya, Ranjana Jha & Sukhvir Singh presents a comprehensive study on tungsten oxide nanosheets, emphasizing their gas-sensing potential by analyzing their morphological and optical characteristics for industrial and environmental applications.

The next contribution, titled “Organic Solar Cell Based with Inorganic Transport Layers: Performance Analysis and Optimization” by Iram Masood, Mukesh Pratap Singh & Mohd. Amir, investigates the optimization of organic solar cells using inorganic transport layers. The study suggests enhanced charge transport and improved device stability—crucial for the future of efficient solar energy devices.

“A Learning-Based Model for Wheat Disease Detection and Classification” by Rakesh Garg, Neetu Singla, Charu, Sachin Lalar & Shubham Goel introduces a machine learning model utilizing image processing for early detection and classification of wheat diseases, supporting timely interventions and reducing crop losses.

The paper “Energy Consumption Trends in India and Its Impact on the Indian Economy” by Meraj Alam, Rajesh Kumar Saluja, Priyanka Vashisht, Nishi Gupta & Rashmi Jha studies India’s energy consumption patterns and their broader economic impact. It highlights key challenges and opportunities, offering insights into sustainable economic growth aligned with energy efficiency.

A notable research titled “Trajectory Tracking Control of a Two-Link Manipulator Including Actuator Dynamics Based on Sliding Mode Controller” by Manju Rani & Naveen Kumar focuses on improving robotic trajectory tracking using sliding mode control, significantly enhancing the accuracy and reliability of industrial automation systems.

“Study of Wave Propagation in Piezo-Visco-Thermo-Elastic Material” by Vipin Gupta & Daksh Sen offers a theoretical framework for understanding wave behavior in complex elastic materials, with implications in sensor technology and energy harvesting.

The paper “Fixed Point for Chatterjea Contraction and Its Application to Cauchy Problem” by Anshuka Kadyan, Savita Rathee & Anil Kumar explores fixed point theory and its application to the Cauchy problem, offering new mathematical approaches for solving differential equations.

“Techniques of Improving Electric Characteristics of Si Strip Sensors Equipped Using Various Isolation Methods” by Ranjeet Dalal investigates isolation techniques to enhance the performance of silicon strip sensors, which are critical in high-energy physics and medical imaging applications.

The final research paper, “Visual Narratives: Enhancing Image Captioning with CNN-RNN-LSTM Fusion” by Kapil Kumar Choudhary, Naveen Kumar & Dishant Kumar, introduces a fusion model using CNN, RNN, and LSTM to enhance image captioning. This method improves contextual relevance in visual recognition and language processing, advancing AI technologies.

The Book Review section includes a review of “Machine Learning Using Python” by Manaranjan Pradhan and U. Dinesh Kumar. The reviewer, Rashmi Jha, finds the book to be a well-structured and practical guide for beginners in machine learning. It comprehensively covers essential concepts in a lucid manner, serving as a useful reference for both students and professionals.

Each of these studies contributes valuable insights—from sustainable technologies to advancements in artificial intelligence and robotics. The PRAGYANAM journal aspires to be a global platform for high-quality research that expands the boundaries of knowledge while delivering practical solutions to improve lives and shape the future. With a steadfast commitment to academic integrity, the journal upholds rigorous peer-review standards to ensure scholarly excellence in every publication.

I express my heartfelt gratitude to all contributors, reviewers, editors and supporters who made this milestone possible. I would like to extend my immense gratitude to Prof. Sanjay Kaushik, Hon’ble Vice Chancellor and the Chief Patron of Gurugram University, for his constant support and motivation throughout the journal publication process. I am also thankful to our esteemed Patron, Dr. Sanjay Arora (Registrar), for his help in making the journal publication a success. Your insights and direction were instrumental in every step. I sincerely acknowledge the visionary leadership and academic mentorship of Prof. S.S. Tyagi – Editor-in-Chief, whose support has been instrumental throughout this journey. I also thank the Associate Editors – Dr. Charu Gandhi, Dr. Rakesh Garg, Dr. Archana Dixit and Dr. Ranjeet for their editorial skills, valuable contributions and timely support. My deep appreciation also goes to the International Editorial Board Members, Prof. Hari M. Upadhyaya, Prof. Praveen Kumar and Dr. Kusum Yadav for their scholarly insights and global perspective that added immense value to this edition.

PRAGYANAM aims to be a valuable resource for students, educators, researchers and professionals worldwide, fostering a dynamic community dedicated to advancing science, technology and societal progress.

Prof. Rashmi Jha
(Editor)



Nickel-Based Nanocomposites with Tunable Optical Properties for Sustainable Solar Energy Solutions

Soumya Rai¹, Himani Chaudhary², Peeyush Phogat³, Shreya⁴, Ranjana Jha⁵ & Sukhvir Singh⁶

ABSTRACT

The increasing global demand for efficient solar energy harvesting materials has fueled the development of innovative nanocomposites. Among these, Nickel hydroxide/nickel sulphide (Ni(OH)₂/NiS) and nickel oxide/nickel sulphide (NiO/NiS) nanocomposites hold great promise owing to their distinct structural and optical properties. These nanocomposites were synthesized using the hydrothermal method, a process that ensures uniformity and high-quality material production. Structural analysis via X-ray diffraction (XRD) revealed hexagonal crystalline structures for Ni(OH)₂ and NiS, while NiO exhibited a cubic structure. Morphological studies using Field Emission Scanning Electron Microscopy (FESEM) highlighted distinct features: 2D nanosheets were observed for Ni(OH)₂, NiO, and NiO/NiS, whereas Ni(OH)₂/NiS exhibited intriguing broccoli-like structures. Optical characterization through UV-Visible spectroscopy demonstrated a significant reduction in band gaps, from 4.4 eV for Ni(OH)₂ and 3.1 eV for NiO to 1.08 eV and 1.3 eV in their respective nanocomposites. This band gap narrowing enhances light absorption, making these materials highly suitable for solar energy applications. FT-IR analysis highlighted distinctive peaks especially in the fingerprint regions, such as the Ni-O vibrations and the C=S stretching, confirming the successful incorporation of NiS into the nanocomposites. These findings underline the potential of Ni(OH)₂/NiS and NiO/NiS nanocomposites as cost-effective and high-performance alternatives for solar cells, advancing sustainable energy technologies and opening the door to more effective photovoltaic systems.

Keywords: Nickel Hydroxide, Nickel Oxide, Nickel Sulphide, Optical Properties, Solar Cells

INTRODUCTION

The increasing requirement for renewable energy alternatives has driven significant research into advanced materials for solar cells, focusing on enhancing efficiency, stability, and cost-effectiveness. Scientists aim to develop innovative materials that not only improve energy conversion rates but also offer long-term durability and affordability. This endeavour is essential to reducing dependency on

fossil fuels and supplying the world's energy demands in a sustainable manner and advancing the adoption of clean, renewable energy technologies [1]-[7]. Solar cells harness sunlight to generate electricity via the photovoltaic effect, a process that relies heavily on the properties of semiconducting materials. These materials are engineered to optimize light absorption, efficiently capturing solar energy, and to enhance charge carrier dynamics, ensuring effective separation

¹ Research Lab for Energy System, Department of Physics, Netaji Subhas University of Technology, New Delhi, India.
E-mail: soumyarai.sr16@gmail.com

² Research Lab for Energy System, Department of Physics, Netaji Subhas University of Technology, New Delhi, India.
E-mail: chnehasingh1998@gmail.com

³ Research Lab for Energy System, Department of Physics, Netaji Subhas University of Technology, New Delhi, India.
E-mail: peeyush.phogat@gmail.com

⁴ Research Lab for Energy System, Department of Physics, Netaji Subhas University of Technology, New Delhi, India.
E-mail: shreyasharma.aug15@gmail.com

⁵ Research Lab for Energy System, Department of Physics, Netaji Subhas University of Technology, New Delhi, India.
E-mail: drranjanajha@gmail.com

⁶ Research Lab for Energy System, Department of Physics, Netaji Subhas University of Technology, New Delhi, India.
E-mail: sukhvirster@gmail.com

and transport of holes and electrons. The performance of solar cells depends on the careful design and selection of these semiconductors to achieve high efficiency and sustainability [8]-[12]. Nickel-based compounds, particularly nickel hydroxide (Ni(OH)_2) and nickel oxide (NiO), have attracted a lot of interest because of their potential in energy applications and because of their distinct optical, electrochemical, and electronic characteristics. These compounds exhibit excellent catalytic activity, high stability, and efficient charge storage capabilities, rendering them appropriate for a range of uses, including energy storage devices, supercapacitors, batteries, and electrocatalysis. Their ability to facilitate efficient electron transfer and energy conversion processes positions them as promising materials for advancing sustainable energy technologies [13]-[16].

Nickel hydroxide (Ni(OH)_2), composed of nickel (Ni^{2+}) and hydroxide (OH^-) ions, is a versatile and widely utilized material in energy storage systems. It plays a crucial role in nickel-metal hydride (NiMH) batteries, where it serves as the active electrode material. Its high energy density, stability, and efficient charge-discharge characteristics make it essential for rechargeable battery technologies [17]. Its layered structure facilitates ion transport, making it a promising candidate for energy applications [18]-[22]. However, Ni(OH)_2 alone faces significant challenges when used in solar cell applications, such as low electrical conductivity, limited visible light absorption, and potential instability under operational conditions. These limitations make Ni(OH)_2 less effective as a photoactive material for efficient energy conversion in solar cells. The low conductivity hampers the efficient transport of charge carriers, while the restricted absorption of visible light reduces its overall performance in harnessing solar energy. Additionally, Ni(OH)_2 's susceptibility to degradation under varying environmental conditions can affect the longevity and stability of solar devices.

To address these drawbacks, Ni(OH)_2 can be thermally treated or calcined to form nickel oxide (NiO), a more robust and thermally stable material. NiO possesses a wide band gap and p-type semiconducting properties, which enhance its suitability for solar cell applications. These improvements in electrical and optical properties make NiO a more effective material for increasing the efficiency and stability of solar cells [23]-[27]. The

transformation of nickel hydroxide (Ni(OH)_2) into nickel oxide (NiO) involves heating the material to remove water, resulting in a crystalline NiO structure with improved chemical stability and thermal resistance. NiO 's wide band gap makes it a suitable material for charge transport layers in solar cells, enhancing efficiency in energy conversion. However, its limited absorption in the visible spectrum restricts its ability to function effectively as a standalone photoactive material. To address this challenge, researchers have focused on combining NiO with narrow-bandgap semiconductors to create hybrid nanocomposites. These hybrid structures aim to leverage the strengths of both materials, optimizing performance.

Nickel sulfide (NiS), known for its excellent visible light absorption and catalytic properties, has emerged as a promising candidate for these hybrid systems. By integrating NiS with NiO , these nanocomposites can potentially overcome the optical limitations of NiO , improving the efficiency of applications such as solar energy conversion [28]-[31]. The integration of NiS into Ni(OH)_2 or NiO matrices results in nanocomposites with synergistic properties, including enhanced light absorption in both UV and visible region and reduced energy bandgap. These enhancements are critical for achieving higher solar energy conversion efficiencies.

Recent studies have explored a wide range of materials to enhance the efficiency and cost-effectiveness of solar cells, focusing on perovskites [32]-[34], quantum dots [35]-[37], and metal oxides [38]-[40]. Perovskites have shown exceptional performance in solar cell applications due to their high-power conversion efficiencies, but their stability issues and potential toxicity present significant challenges for long-term use and commercial scalability [41]. Quantum dots, on the other hand, offer the advantage of tunable band gaps, allowing for precise control over the light absorption spectrum. However, their complex fabrication processes and potential issues with stability and scalability hinder their widespread application. Metal oxides including titanium dioxide (TiO_2) and zinc oxide (ZnO) are widely utilized as electron transport materials in solar cells. Although they offer good electron mobility and stability, they often lack sufficient light absorption properties in the visible range, limiting their overall efficiency in solar energy conversion [42]. These challenges continue to drive research into new,

more effective materials. Nickel-based materials are highly regarded for their environmental compatibility, cost-effectiveness, and ease of synthesis, making them excellent candidates for sustainable solar energy applications. Their abundant availability, low cost, and efficient performance in energy conversion processes ensure they are an attractive alternative to more expensive or environmentally harmful materials in solar technologies.

This study investigates the hydrothermal synthesis of nickel hydroxide ($\text{Ni}(\text{OH})_2$) and its subsequent calcination to nickel oxide (NiO), followed by the integration of nickel sulfide (NiS) to form $\text{Ni}(\text{OH})_2/\text{NiS}$ and NiO/NiS nanocomposites. These nanocomposites are further investigated on the basis of their structural, optical, morphological and chemical properties. The combination of $\text{Ni}(\text{OH})_2$ and NiO , both of which are known for their wide-bandgap stability, with NiS , a material renowned for its excellent visible light absorption and catalytic efficiency, results in the creation of advanced nanocomposites. These nanocomposites effectively address the limitations of each individual component, enhancing the overall performance of solar energy devices. The $\text{Ni}(\text{OH})_2/\text{NiS}$ and NiO/NiS nanocomposites exhibit enhanced optical absorption properties, particularly in the visible light spectrum, making them highly suitable for solar energy harvesting. Additionally, the materials show improved stability, crucial for long-term efficiency in photovoltaic applications. The synergistic effect between the components contributes to better charge separation and transport, leading to higher photocatalytic and photovoltaic performance compared to individual $\text{Ni}(\text{OH})_2$, NiO , or NiS materials.

The study highlights that these nickel-based nanocomposites hold significant promise as cost-effective and sustainable solutions for next-generation solar cells. Their synthesis through a relatively simple hydrothermal method, followed by calcination, offers a scalable approach for large-scale production. The integration of NiS enhances the overall material properties, enabling the development of efficient photovoltaic materials that can contribute to the global transition towards cleaner, renewable energy sources. This work represents a significant step toward advancing solar technologies, positioning nickel-based

nanocomposites as key materials for future energy harvesting systems.

EXPERIMENTAL SECTION

Chemicals Used

The chemicals and reagents used in the synthesis process are listed in Table 1, detailing their manufacturer names and purity percentages. Absolute ethanol and de-ionized (DI) water with a resistivity greater than 5M were utilized for synthesis and cleaning steps, ensuring high-quality and contamination-free results. These high-purity solvents played a crucial role in the preparation of the nanocomposites, maintaining the integrity of the experimental procedure and contributing to reliable and reproducible outcomes.

Table 1. Chemicals used in the synthesis process

<i>Chemical Name</i>	<i>Chemical Formula</i>	<i>Manufacturer Company</i>	<i>Purity</i>
Nickel Nitrate Hexahydrate	$\text{Ni}(\text{NO}_3)_2 \cdot 6\text{H}_2\text{O}$	M/s Thomas Baker	99%
Sodium Hydroxide	NaOH	M/s Thomas Baker	99%
Sodium Sulphide	Na_2S	M/s Thomas Baker	98%

Synthesis Process

A simple and efficient single-step hydrothermal synthesis method was employed to fabricate the materials. Nickel hydroxide ($\text{Ni}(\text{OH})_2$) was synthesized by dissolving 0.27 M nickel nitrate hexahydrate in 40 mL of de-ionized (DI) water under continuous magnetic stirring for 30 minutes at room temperature, ensuring complete dissolution and uniformity of the solution. In a separate step, a 2.0 M sodium hydroxide (NaOH) solution was made starting with dissolving 2 grams NaOH in 25 mL DI water and stirring the solution for 30 minutes to achieve a homogeneous mixture. The NaOH solution was then introduced dropwise to the nickel nitrate solution under continuous stirring to facilitate controlled precipitation. This was followed by 3 hours of additional stirring to promote the formation of uniform nanoparticles. After that, the mixture was moved to a Teflon-lined stainless-steel autoclave and heated hydrothermally at 220°C for 24 hours. After the reaction, the resulting particles were collected by centrifugation, which were then repeatedly cleaned with ethanol and DI water to get

rid of contaminants, dried in a vacuum oven at 60°C to ensure even dehydration, and then crushed into a fine powder. This sample, designated as NB (color-coded blue), represented pure $\text{Ni}(\text{OH})_2$.

To convert nickel hydroxide into nickel oxide (NiO), sample NB was calcined at 350°C for 1 hour. This thermal treatment resulted in sample NA, which was color-coded pink. For the synthesis of $\text{Ni}(\text{OH})_2/\text{NiS}$ nanocomposites, 0.17 M of sample NB was dispersed in 15 mL DI and mixed for 30 minutes to ensure uniform dispersion. Simultaneously, a 0.17 M sodium sulfide (Na_2S) solution was prepared and added dropwise to the $\text{Ni}(\text{OH})_2$ suspension under continuous stirring for 3 hours to facilitate the interaction and formation of the nanocomposite. After that, the mixture was placed in an autoclave and hydrothermally treated for 24 hours at 220°C. The final product was washed, dried, and ground into a uniform powder, resulting in the sample NB/NS, color-coded red. Using a similar procedure, sample NA was used instead of NB to prepare NiO/NiS nanocomposites, designated as NA/NS and color-coded green. This approach ensured precise control over material properties, enabling their application in advanced energy and catalytic technologies.

RESULTS AND DISCUSSION

X-Ray Diffraction

An advanced analytical model, Expert PRO X-Ray Diffractometer, equipped with copper $\text{K}\alpha$ radiation (wavelength 1.54 Å), was employed to investigate the structural properties of the synthesized samples. The XRD patterns recorded across a wide 2θ range of 10° to 90°, captured detailed crystallographic information, as illustrated in fig. 1, which also includes the corresponding matched JCPDS file numbers. Sample NB exhibited a well-defined hexagonal crystal structure characteristic of $\text{Ni}(\text{OH})_2$. However, upon calcination at 350°C, the crystal structure underwent a transformation to a cubic phase, as observed in sample NA. This structural transition can be attributed to the thermal energy provided during calcination, which rearranged the nickel and oxygen ions. The process caused a transition from a layered hydroxide structure to a more compact and thermodynamically stable cubic NiO phase. At elevated temperatures, the cubic

structure of NiO is inherently more stable, driving this transformation.

The incorporation of nickel sulfide (NiS) into the matrices of $\text{Ni}(\text{OH})_2$ and NiO further modified the structural properties, as observed in the XRD patterns of samples NB/NS and NA/NS. The inclusion of NiS introduced additional diffraction peaks, indicative of the formation of new crystallographic phases within the composites. This likely reflects enhanced crystallinity, improved atomic ordering, and a reduction in structural defects. The crystallographic interactions between NiS and the host matrices appeared to strengthen the material's structural integrity, with better atomic alignment and reduced disorder. These modifications, as evident from the additional peaks in the XRD patterns, indicate improved charge transport and enhanced light absorption properties. These characteristics make the NiS -based nanocomposites highly promising candidates for advanced solar cell applications, showcasing their potential for efficient energy conversion in sustainable energy solutions.

The Debye-Scherrer equation is important for determining the crystallite size of materials from X-ray diffraction (XRD) patterns. It provides insights into the structural characteristics of nanoparticles, helping to quantify their size and assess the material's quality. This information is crucial for understanding the material's properties, such as its optical, electrical, and mechanical behavior. The Debye-Scherrer equation was utilised to assess the size of the crystallites of the as-synthesized samples [43]-[46] as given by equation-1,

$$d = K \frac{\lambda}{\beta \cos \theta} \quad \dots(1)$$

Here, d denotes the average size of crystallite, value of shape constant K is 0.9, λ depicts the wavelength of x-ray (1.54 Å), β specifies the full width at half maxima (FWHM), θ refers to the Bragg's angle of corresponding peaks [50], [51]. The average crystallite sizes for samples NB, NA, NB/NS, and NA/NS were computed using the formula and the values are depicted in Table 2. The reduction in crystallite size observed from NB to NA upon calcination is primarily attributed to the decomposition of hydroxide layers in $\text{Ni}(\text{OH})_2$ and the subsequent reorganization of atoms during the thermal process. This transformation leads

to the separation of atoms and restricts extensive grain growth, resulting in a smaller crystallite size in the calcined sample (NA).

The calcination process causes the transition from a layered hydroxide structure to a more compact, thermodynamically stable cubic NiO phase, which further limits the growth of crystallites. In contrast, the incorporation of nickel sulfide (NiS) into both NB and NA matrices results in an increase in crystallite size, as observed in the NB/NS and NA/NS nanocomposites. This increase in size is likely due to the interaction between NiS and the host matrix, which facilitates the coalescence of grains. The presence of NiS encourages the formation of larger crystalline domains, enhancing the overall crystallinity of the nanocomposites. The variation in crystallite size highlights the significant impact of thermal treatment and composite formation on the structural evolution of the materials, affecting their properties and potential applications. The performance of the nanocomposites is improved by this structural modification, which also makes them more appropriate for cutting-edge energy applications like solar cells.

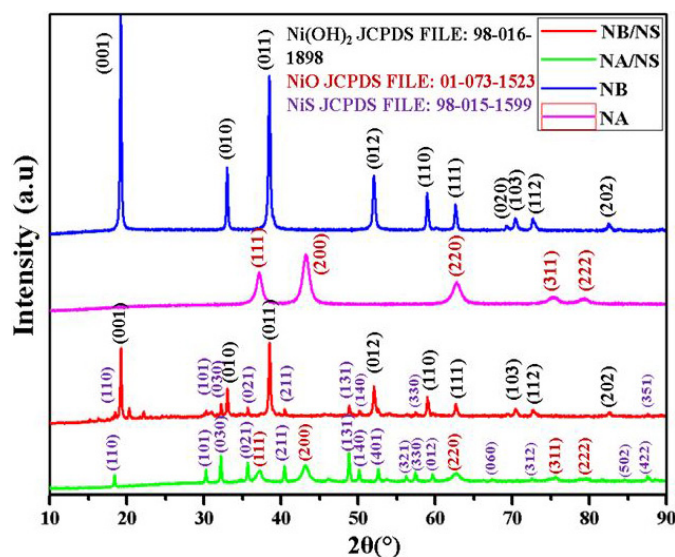


Fig. 1. XRD patterns of the as-synthesized samples

Table 2. Average value of crystallite sizes of the samples

Sample	Crystallite size (nm)
NB	44
NA	29
NB/NS	62
NA/NS	47

UV-Visible Spectroscopy

The optical properties of the samples were investigated using a SHIMADZU UV-2600i UV-Visible spectrometer, and the diffuse reflectance spectroscopy technique was employed to evaluate the samples' optical behavior across a wavelength range of 190-850 nm [Fig. 2(a-d)]. As seen in Fig. 2(a & b), the absorption characteristics of the as-synthesized samples, NB and NA, were predominantly observed in the ultraviolet (UV) region, indicating that both materials possess a high energy bandgap. This is typical for Ni(OH)₂ and NiO, which have wide bandgaps that absorb primarily in the UV spectrum. However, when nickel sulfide (NiS) was incorporated into the matrices of Ni(OH)₂ and NiO to form the nanocomposites NB/NS and NA/NS, a significant change in the optical absorption behavior was noted. These nanocomposites exhibited absorption extending from the UV region into the visible range, a notable broadening in comparison to the pure materials as seen in Fig. 2(c & d).

There are several reasons for this shift in the absorption spectra, such as the incorporation of sulphur, the existence of structural flaws, electronic modifications, or the formation of new compounds that exhibit altered electronic properties. The extended visible absorption in the nanocomposites suggests that the incorporation of NiS enhanced the ability of these materials to capture photons from a broader portion of the solar spectrum. This improvement in photon absorption is crucial for efficient solar energy harvesting, as it enables the material to make better use of available sunlight. Additionally, the enhanced visible absorption facilitates the generation of more electron-hole pairs, improving the overall photocatalytic and photoelectronic performance of the nanocomposites. Therefore, these NB/NS and NA/NS nanocomposites are particularly promising for solar energy applications, as they can effectively harness a wider range of the solar spectrum, enhancing their efficiency in energy conversion.

Tauc plot analysis is crucial for determining the optical bandgap of materials, particularly semiconductors and nanocomposites. By plotting $(\alpha h\nu)^2$ against $h\nu$, it allows for the estimation of the material's bandgap energy from the linear portion of the curve. This method helps in understanding the material's electronic structure, its potential for optoelectronic applications,

and its suitability for solar energy conversion or photocatalysis based on its ability to absorb light. The Tauc plot equation [47]-[50] is given as follows,

$$\alpha h\nu = A[h\nu - E_g]^{1/n} \quad \dots(2)$$

Here, α refers to the absorption coefficient, A denotes the proportionality constant, E_g depicts the bandgap and the nature of transition is shown by exponent n . The Tauc plot analysis yielded useful insights about the optical bandgaps of the synthesised materials, revealing values of 4.4 eV, 3.1 eV, 1.08 eV, and 1.3 eV for NB, NA, NB/NS, and NA/NS, respectively. The significant reduction in bandgap observed in the nanocomposites compared to the pure samples can be attributed to the incorporation of sulphur (S). Sulphur introduces defect states within the crystal structure, which alters the electronic configuration and narrows the energy gap between the conduction and valence bands. This reduction in the bandgap facilitates the absorption of photons in the visible light spectrum, which is typically not possible for materials with wider bandgaps like $\text{Ni}(\text{OH})_2$ and NiO . As a result, the nanocomposites (NB/NS and NA/NS) exhibit enhanced light absorption properties, making them more efficient for solar energy applications. The ability to absorb a broader range of light wavelengths improves their potential for energy conversion, particularly for solar cells and other optoelectronic devices.

The refractive index measures how much light is twisted, or refracted, when it travels through a substance. It is crucial for solar cell applications as it affects light absorption, transmission, and reflection at the material interfaces. A higher refractive index can enhance light trapping within the solar cell, increasing the likelihood of photon absorption. Optimizing the refractive index helps improve the efficiency of solar cells by maximizing light capture and minimizing energy losses due to reflection. The refractive indices of the samples were determined using a standard equation [51]-[53] as given by,

$$\frac{n^2 - 1}{n^2 + 2} = 1 - \sqrt{\frac{E_g}{20}} \quad \dots(3)$$

Here, n depicts the refractive index, while E_g denotes the corresponding band gap. The refractive index values obtained from the analysis were 2.09, 2.36, 3.30, and 3.12 for samples NB, NA, NB/NS, and NA/NS,

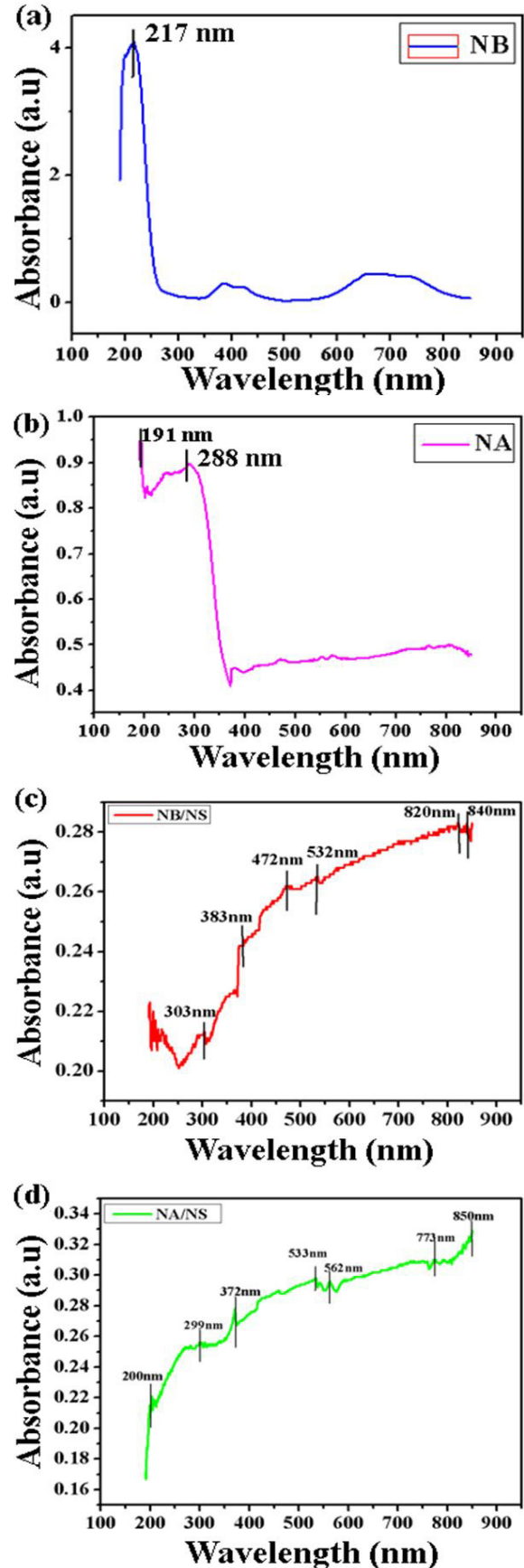


Fig. 2: (a-d) Absorption Spectra of the samples

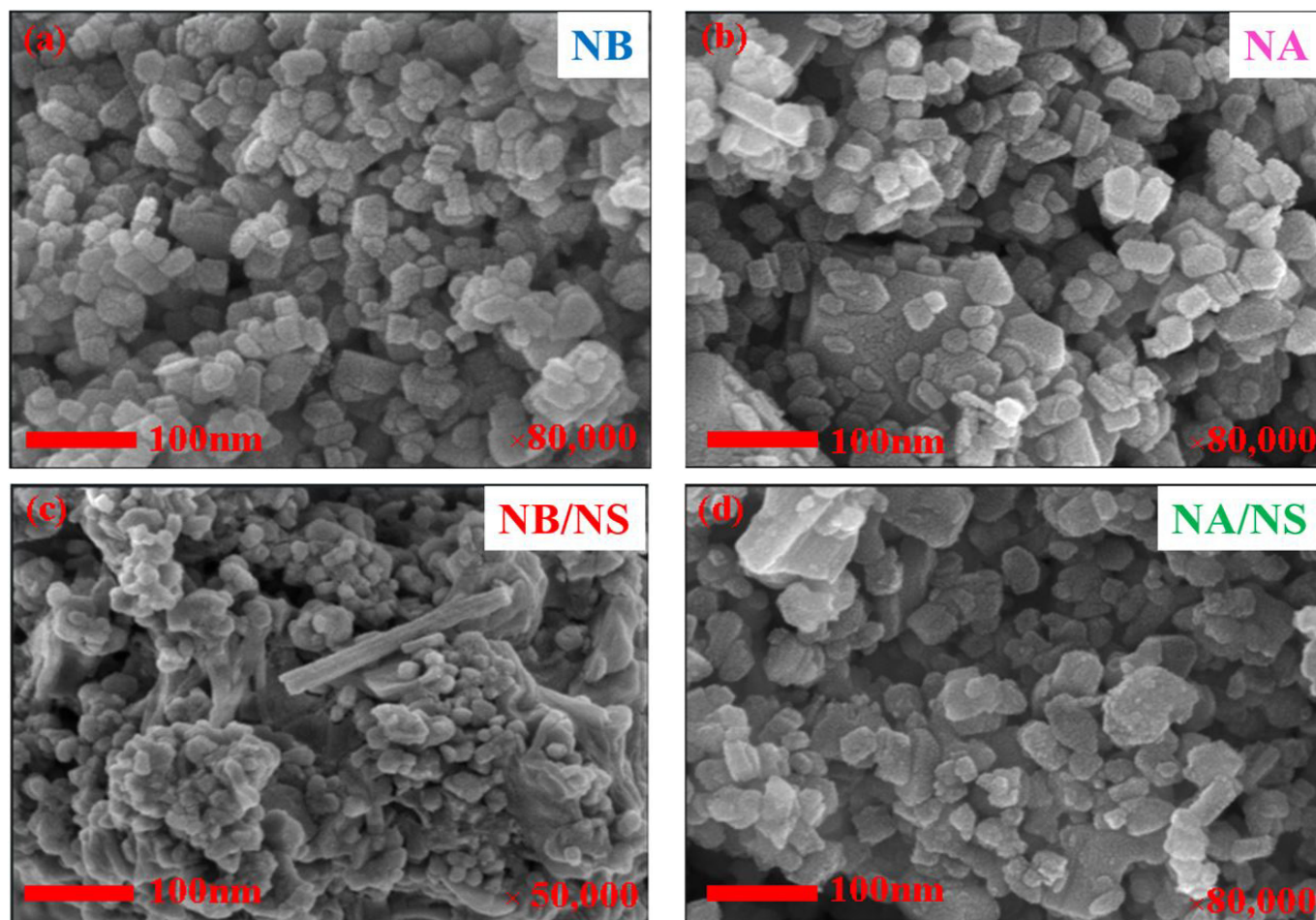
respectively. The higher refractive indices observed for the nanocomposites compared to the pristine samples suggest an increase in optical density, indicating that these materials are more capable of bending light. This enhanced light-trapping capability is particularly beneficial for solar cell applications, as it leads to better photon absorption. A higher refractive index improves the interaction between light and the material, allowing more light to be absorbed rather than reflected. This is essential for maximizing the photon-to-electron conversion efficiency in solar cells.

By reducing reflection losses and increasing the amount of light that enters the material, these nanocomposites offer significant advantages in terms of energy harvesting, making them highly promising candidates for improving the reliability and efficacy of solar energy equipments.

Morphological Analysis

FESEM characterization provides an essential tool for studying the surface morphology of materials at the

nanoscale level, offering insights into their structural properties. In this study, FESEM analysis was conducted using a JEOL FESEM 7610FPlus model, coupled with EDX spectroscopy to explore the element composition and morphology of the synthesized samples. The results, depicted in Fig. 3(a-d), reveal distinct structural features for each sample. Sample NB, which consists of pure $\text{Ni}(\text{OH})_2$, displayed a 2D nanosheet morphology (Fig. 3a). These nanosheets were thin, flat, and interconnected, characteristic of layered materials. This structure is beneficial for improving charge transport and providing a large surface area for interactions with light. Upon calcination to form NiO in sample NA, the nanosheet morphology persisted (Fig. 3b). This stability can be attributed to controlled calcination conditions (temperature and time), which prevented excessive structural rearrangement. Additionally, the inherent stability of $\text{Ni}(\text{OH})_2$ nanosheets may have played a role in preserving this morphology during the transformation to NiO. When NiS was incorporated into the matrices to form the nanocomposites, the morphology of the samples changed significantly.



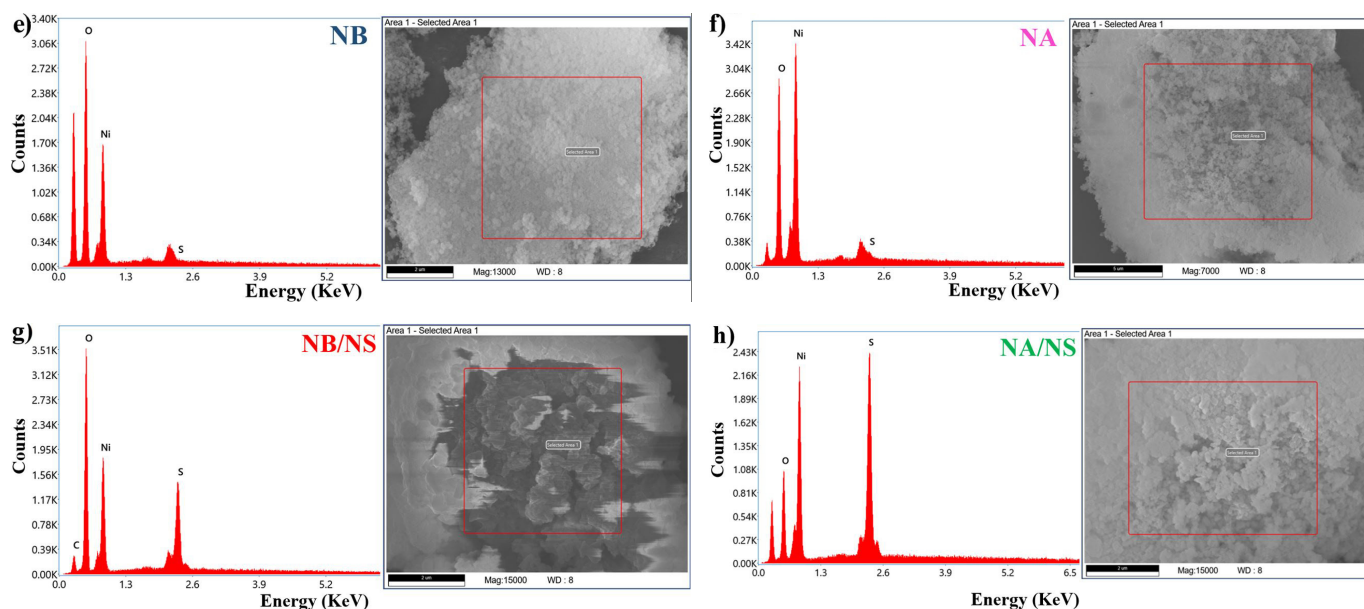


Fig. 3. (a-d) FESEM images, (e-h) EDX patterns of the samples

For the NB/NS sample, a broccoli-like structure with intricate branching was observed (Fig. 3c). The development of this unique structure is likely due to the influence of sulphur on the surface energy and crystal growth, which induces the formation of a more complex network. This branching morphology increases the material's surface area and facilitates better charge transport and light absorption, both of which are crucial for enhancing the efficacy of solar cells.

In the NA/NS scenario, the incorporation of NiS led to a shift in morphology to clustered 2D nanosheets (Fig. 3d). The presence of sulphur likely played a significant role in altering the growth processes, leading to this new structure. The clustered morphology enhances surface interaction, which is critical for efficient charge separation in solar cell applications. These changes in morphology, induced by the incorporation of NiS, are expected to improve the overall performance of the nanocomposites, making them more suitable for use in high-performance solar cells.

EDX analysis, shown in fig. 3(e-h), was used to verify the elemental composition of the samples. For samples NB and NA, the EDX spectra revealed distinct peaks for nickel (Ni) and oxygen (O), indicating the presence of $\text{Ni}(\text{OH})_2$ and NiO in these respective samples. This was consistent with the expected composition of these materials. In contrast, for the nanocomposites NB/NS and NA/NS, the EDX spectra showed additional

peaks for sulphur (S), confirming the successful incorporation of NiS into the matrices of $\text{Ni}(\text{OH})_2$ and NiO. The presence of sulphur in the nanocomposites further supports the formation of the $\text{Ni}(\text{OH})_2/\text{NiS}$ and NiO/NiS composite structures. Carbon peaks were also observed in all the samples, which originated from the carbon tape used during the EDX analysis. These findings validated the effective synthesis of the intended nanocomposites and offered insightful information on the elemental composition.

Chemical Analysis

The Fourier Transform Infrared Spectroscopy (FTIR) analysis was utilised to study the bond formations and functional groups existing in the synthesized samples. The FTIR spectra were recorded using the FT-IR Spectrum 2 spectrometer from Perkin Elmer, spanning a wavenumber range of $4000\text{--}500\text{ cm}^{-1}$. The resulting spectra are shown in fig. 4. For the pure nickel-based samples, broad peaks at 3404 cm^{-1} , 3424 cm^{-1} , and 3439 cm^{-1} were observed in samples NB, NA, and NA/NS, respectively. These peaks are characteristic of O-H stretching vibrations, which are likely attributed to absorbed water molecules on the surfaces of the samples [54],[55]. The presence of these O-H stretching bands is a common feature in metal hydroxides, where water molecules interact with the surface [56]. In the NB/NS sample, this O-H stretching band was found to shift slightly to 3627 cm^{-1} , suggesting a stronger hydrogen

bonding interaction or a change in the local chemical environment caused by the incorporation of NiS into the matrix.

Additionally, all samples exhibited weak bands in the range of 3000–2800 cm^{-1} , indicating the presence of C-H stretching vibrations [57], which are likely from organic residues or impurities in the samples. The presence of carbon-containing groups was further supported by the moderate peaks observed around 1739 cm^{-1} for NB/NS and 1706 cm^{-1} for NA/NS, which are indicative of C=O stretching vibrations [58]. This may be attributed to the carbonyl groups in surface residues or adsorbed organic molecules.

A noticeable shift in the peaks corresponding to C=C stretching vibrations [59] was observed in samples NA, NB, and NA/NS, with bands ranging from 1627 cm^{-1} to 1635 cm^{-1} . These shifts could be associated with changes in the electronic environment around the carbon-carbon bonds, possibly due to the presence of structural defects or interactions with other components in the samples. The peaks between 1375 cm^{-1} and 1150 cm^{-1} are attributed to C-O stretching vibrations, further affirming the existence of carbon-oxygen bonds, likely from organic contaminants or adsorbed species.

One of the most distinctive features in the FTIR spectra of the nanocomposites is the peak observed at 675 cm^{-1} in the NB/NS sample, which corresponds to C=S stretching vibrations. This peak is a clear indication of the incorporation of sulphur into the nanocomposite, confirming the successful synthesis of the $\text{Ni}(\text{OH})_2/\text{NiS}$ and NiO/NiS nanocomposite structures. The presence of C=S stretching vibrations further supports the formation of nickel-sulphide interactions within the nanocomposite.

In the fingerprint region of the FTIR spectra, a sharp and prominent peak was observed at 522 cm^{-1} in the NB/NS sample, which corresponds to Ni-O vibrations [60], confirming the presence of nickel-oxide bonds in the material. A broad peak at 539 cm^{-1} was also noticed in sample NB, which can be attributed to Ni-OH stretching vibrations [61], demonstrating the existence of hydroxyl groups in the $\text{Ni}(\text{OH})_2$ phase. Lastly, for all samples, peaks between 435 cm^{-1} and 419 cm^{-1} were observed, corresponding to Ni-O vibrations [62], which is a signature feature of nickel oxide bonds, confirming the formation of nickel oxide in the synthesized

materials. These FTIR results provide detailed insights into the chemical bonding and functional groups existing in the materials, supporting the successful synthesis of the nickel-based nanocomposites with NiO and NiS incorporation.

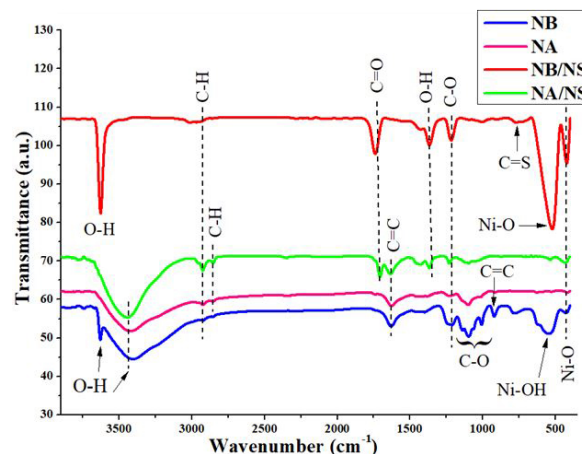


Fig. 4. FTIR spectra of the samples

CONCLUSION

The present study successfully demonstrated the hydrothermal synthesis and characterization of $\text{Ni}(\text{OH})_2$, NiO, and their respective nanocomposites with nickel sulfide (NiS), targeting advanced solar energy applications. XRD analysis affirmed the effective formation of hexagonal $\text{Ni}(\text{OH})_2$, NiS, and cubic NiO phases, showcasing well-defined crystalline structures of the samples. FESEM highlighted distinct morphologies, with $\text{Ni}(\text{OH})_2$ and NiO maintaining nanosheet-like structures, while the nanocomposites exhibited a unique broccoli-like morphology, enhancing surface area and providing more active sites for interactions. Optical analysis via UV-Visible spectroscopy indicated a significant reduction in the band gap values from 4.4 eV and 3.1 eV for pure $\text{Ni}(\text{OH})_2$ and NiO, respectively, to 1.08 eV and 1.3 eV in the $\text{Ni}(\text{OH})_2/\text{NiS}$ and NiO/NiS nanocomposites. This bandgap reduction is essential because it allows the materials to absorb a wider range of light, especially visible light, which is essential for improving the efficiency of solar energy harvesting.

The integration of NiS with $\text{Ni}(\text{OH})_2$ and NiO results in a synergistic effect that improves the optical and electronic properties of the materials, addressing the limitations often observed in their standalone counterparts. This combination not only improves visible light absorption but also promotes better charge

carrier mobility, an essential factor in enhancing the overall efficiency of solar energy conversion. Additionally, the nanocomposites exhibited an excellent balance of stability and enhanced electronic characteristics, making them promising candidates for use in solar cells. These findings emphasize the potential of nickel-based nanocomposites as cost-effective, environmentally friendly alternatives to conventional materials in solar energy applications.

This research highlights the importance of material engineering strategies to tailor properties for sustainable energy solutions. The ability to fine-tune these properties opens avenues for further optimization in solar cell design. Future studies could explore the integration of these nanocomposites into working solar cell prototypes to assess their practical performance, long-term stability, and scalability, thus supporting the development of sustainable, effective energy technologies. Additionally, further characterization techniques like cyclic voltammetry (CV), electrochemical impedance spectroscopy (EIS), and electrochemical charge-discharge tests could be employed to assess the charge storage capacity, electrochemical stability, and efficiency of these nanocomposites in energy storage and conversion systems. These methods will provide a deeper understanding of the materials' behavior under different electrochemical conditions, ensuring their reliability and performance in practical applications. Thin-film deposition techniques, such as spin coating or sputtering, can also be explored to fabricate thin-film solar cells, providing insights into their scalability and efficiency for large-scale applications. This would enable better integration into photovoltaic devices, enhancing their commercial viability.

ACKNOWLEDGMENTS

The authors gratefully acknowledge essential resources provided by Prof. Anand Srivastava, Hon. Vice Chancellor of Netaji Subhas University of Technology (former Netaji Subhas Institute of Technology, University of Delhi).

DECLARATION OF COMPETING INTEREST

The authors confirm that no financial conflicts or personal relationships exist that could have impacted the research presented in this paper.

ETHICAL APPROVAL

All the authors have worked in accordance with the ethical standards and approved by Netaji Subhas University of Technology.

REFERENCES

- [1] L. M. Shaker, A. A. Al-Amiery, M. M. Hanoon, W. K. Al-Azzawi, and A. A. H. Kadhum, "Examining the influence of thermal effects on solar cells: a comprehensive review," *Sustainable Energy Research* 2024 11:1, vol. 11, no. 1, pp. 1–30, Feb. 2024, doi: 10.1186/S40807-024-00100-8.
- [2] P. Phogat, S. Shreya, R. Jha, and S. Singh, "Impedance Study of Zinc Sulphide Quantum Dots via One Step Green Synthesis," *Materials Science Forum*, vol. 1099, pp. 119–125, Oct. 2023, doi: 10.4028/P-G1CCXQ.
- [3] Dipti, P. Phogat, Shreya, D. Kumari, and S. Singh, "Fabrication of tunable band gap carbon based zinc nanocomposites for enhanced capacitive behaviour," *Phys Scr*, vol. 98, no. 9, Sep. 2023, doi: 10.1088/1402-4896/ACF07B.
- [4] P. Phogat, Shreya, R. Jha, and S. Singh, "Optical and Microstructural Study of Wide Band Gap ZnO@ZnS Core-Shell Nanorods to be Used as Solar Cell Applications," pp. 419–429, 2023, doi: 10.1007/978-981-99-2349-6_38.
- [5] Shreya, P. Phogat, R. Jha, and S. Singh, "Elevated Refractive Index of MoS₂ Amorphous Nanoparticles with a Reduced Band Gap Applicable for Optoelectronics," pp. 431–439, 2023, doi: 10.1007/978-981-99-2349-6_39.
- [6] T. Kumar, Shreya, P. Phogat, V. Sahgal, and R. Jha, "Surfactant-mediated modulation of morphology and charge transfer dynamics in tungsten oxide nanoparticles," *Phys Scr*, vol. 98, no. 8, Aug. 2023, doi: 10.1088/1402-4896/ACE566.
- [7] S. Rai, Shreya, P. Phogat, R. Jha, and S. Singh, "Hydrothermal synthesis and characterization of selenium-doped MoS₂ for enhanced optoelectronic properties," *MATEC Web of Conferences*, vol. 393, p. 01008, Mar. 2024, doi: 10.1051/MATECONF/202439301008.
- [8] S. Sharma, P. Phogat, R. Jha, and S. Singh, "Electrochemical and Optical Properties of Microwave Assisted MoS₂ Nanospheres for Solar Cell Application," *International Journal of Smart Grid and Clean Energy*, pp. 66–72, 2023, doi: 10.12720/SGCE.12.3.66-72.
- [9] Shreya, P. Phogat, R. Jha, and S. Singh, "Microwave-synthesized γ -WO₃ nanorods exhibiting high current density and diffusion characteristics," *Transition Metal Chemistry*, vol. 48, no. 3, pp. 167–183, Jun. 2023, doi: 10.1007/S11243-023-00533-Y.

- [10] P. Phogat, Shreya, R. Jha, and S. Singh, "Diffusion Controlled Features of Microwave Assisted ZnS/ZnO Nanocomposite with Reduced Band Gap," *ECS Journal of Solid State Science and Technology*, vol. 12, no. 3, p. 034004, Mar. 2023, doi: 10.1149/2162-8777/ACC426.
- [11] P. PHOGAT, . S., R. JHA, and S. Singh, "Electrochemical Analysis of Thermally Treated Two Dimensional Zinc Sulphide Hexagonal Nano-Sheets with Reduced Band Gap," *Phys Scr*, Dec. 2023, doi: 10.1088/1402-4896/AD0D93.
- [12] D. Kumari, Shreya, P. Phogat, Dipti, S. Singh, and R. Jha, "Enhanced electrochemical behavior of C@CdS Core-Shell heterostructures," *Materials Science and Engineering: B*, vol. 301, p. 117212, Mar. 2024, doi: 10.1016/J.MSEB.2024.117212.
- [13] P. Phogat, Shreya, R. Jha, and S. Singh, "Phase Transition of Thermally Treated Polyhedral Nano Nickel Oxide with Reduced Band Gap," *MATEC Web of Conferences*, vol. 393, p. 01001, Mar. 2024, doi: 10.1051/MATECCONF/202439301001.
- [14] E. R. Beach, K. Shqau, S. E. Brown, S. J. Rozeveld, and P. A. Morris, "Solvothermal synthesis of crystalline nickel oxide nanoparticles," *Mater. Chem. Phys.*, vol. 115, no. 1, p. 371, May 2009, doi: 10.1016/j.matchemphys.2008.12.018.
- [15] Q. Yang, J. Sha, X. Ma, and D. Yang, "Synthesis of NiO nanowires by a sol-gel process," *Mater. Lett.*, vol. 59, no. 14–15, p. 1967, Jun. 2005, doi: 10.1016/j.matlet.2005.02.037.
- [16] P. Palanisamy and A. M. Raichur, "Synthesis of spherical NiO nanoparticles through a novel biosurfactant mediated emulsion technique," *Mater. Sci. Eng. C*, vol. 29, no. 1, p. 199, Jan. 2009, doi: 10.1016/j.msec.2008.06.008.
- [17] E. Shangguan, Z. Chang, H. Tang, X. Z. Yuan, and H. Wang, "Synthesis and characterization of high-density non-spherical Ni(OH)₂ cathode material for Ni–MH batteries," *Int J Hydrogen Energy*, vol. 35, no. 18, pp. 9716–9724, Sep. 2010, doi: 10.1016/J.IJHYDENE.2010.06.096.
- [18] D. S. Hall, D.J. Lockwood, C. Bock, and B.R. MacDougall, "Nickel hydroxides and related materials: a review of their structures, synthesis and properties," *Proceedings of the Royal Society A: Mathematical, Physical and Engineering Sciences*, vol. 471, no. 2174, Feb. 2015, doi: 10.1098/RSPA.2014.0792.
- [19] L. Zhang et al., "Ni(OH)₂ nanoparticles encapsulated in conductive nanowire array for high-performance alkaline seawater oxidation," *Nano Res*, vol. 15, no. 7, pp. 6084–6090, Jul. 2022, doi: 10.1007/S12274-022-4391-6/METRICS.
- [20] J. Ji et al., "Nanoporous Ni(OH)₂ thin film on 3D ultrathin-graphite foam for asymmetric supercapacitor," *ACS Nano*, vol. 7, no. 7, pp. 6237–6243, Jul. 2013, doi: 10.1021/nn4021955.
- [21] H. B. Li et al., "Amorphous nickel hydroxide nanospheres with ultrahigh capacitance and energy density as electrochemical pseudocapacitor materials," *Nat. Commun.*, vol. 4, p. 1894, 2012, doi: 10.1038/ncomms2932.
- [22] R. Wang, J. Lang, Y. Liu, Z. Lin, and X. Yan, "Ultra-small, size-controlled Ni(OH)₂ nanoparticles: elucidating the relationship between particle size and electrochemical performance for advanced energy storage devices," *NPG Asia Materials* 2015, vol. 7, no. 6, pp. e183–e183, Jun. 2015, doi: 10.1038/am.2015.42.
- [23] R. Goel, R. Jha, and C. Ravikant, "Investigating the structural, electrochemical, and optical properties of p-type spherical nickel oxide (NiO) nanoparticles," *Journal of Physics and Chemistry of Solids*, vol. 144, p. 109488, Sep. 2020, doi: 10.1016/J.JPCS.2020.109488.
- [24] Y. Xia et al., "One-dimensional nanostructures: Synthesis, characterization, and applications," *Adv. Mater.*, vol. 15, no. 5, p. 353, Mar. 2003, doi: 10.1002/adma.200390087.
- [25] G. J. Li, X. X. Huang, Y. Shi, and J. K. Guo, "Preparation and characteristics of nanocrystalline NiO by organic solvent method," *Mater. Lett.*, vol. 51, no. 4, p. 325, Nov. 2001, doi: 10.1016/S0167-577X(01)00312-3.
- [26] M. Alagiri, S. Ponnusamy, and C. Muthamizhchelvan, "Synthesis and characterization of NiO nanoparticles by sol-gel method," *Journal of Materials Science: Materials in Electronics*, vol. 23, no. 3, pp. 728–732, Mar. 2012, doi: 10.1007/S10854-011-0479-6/FIGURES/8.
- [27] F. J. Morin, "Electrical Properties of NiO," *Physical Review*, vol. 93, no. 6, pp. 1199–1204, 1954, doi: 10.1103/PhysRev.93.1199.
- [28] A. Sharma, P.R. Makgwane, E. Lichtfouse, N. Kumar, A. H. Bandegharaei, and M. Tahir, "Recent advances in synthesis, structural properties, and regulation of nickel sulfide-based heterostructures for environmental water remediation: An insight review," *Environmental Science and Pollution Research* 2023, vol. 30, no. 24, pp. 64932–64948, Apr. 2023, doi: 10.1007/S11356-023-27093-Z.
- [29] Y. Chen, Y. Cheng, T. Zhang, H. Zhang, and S. Zhong, "Photodeposition of NiS thin film enhanced the visible light hydrogen evolution performance of CdS nanoflowers," *Int J Hydrogen Energy*, vol. 77, pp. 184–192, Aug. 2024, doi: 10.1016/J.IJHYDENE.2024.06.130.
- [30] R. Boughalmi, R. Rahmani, A. Boukhachem, B. Amrani, K. Driss-Khodja, and M. Amlouk, "Metallic behavior of NiS thin film under the structural, optical, electrical and ab initio investigation frameworks," *Mater Chem*

- Phys*, vol. 163, pp. 99–106, Aug. 2015, doi: 10.1016/J.MATCHEMPHYS.2015.07.019.
- [31] M. Mollavali, C. Falamaki, and S. Rohani, “Efficient light harvesting by NiS/CdS/ZnS NPs incorporated in C, N-co-doped-TiO₂ nanotube arrays as visible-light sensitive multilayer photoanode for solar applications,” *Int J Hydrogen Energy*, vol. 43, no. 19, pp. 9259–9278, May 2018, doi: 10.1016/J.IJHYDENE.2018.03.102.
- [32] D. Wang, M. Wright, N. K. Elumalai, and A. Uddin, “Stability of perovskite solar cells,” *Solar Energy Materials and Solar Cells*, vol. 147, pp. 255–275, Apr. 2016, doi: 10.1016/J.SOLMAT.2015.12.025.
- [33] H. S. Jung and N. G. Park, “Perovskite Solar Cells: From Materials to Devices,” *Small*, vol. 11, no. 1, pp. 10–25, Jan. 2015, doi: 10.1002/SMLL.201402767.
- [34] M. A. Green, A. Ho-Baillie, and H. J. Snaith, “The emergence of perovskite solar cells,” *Nature Photonics* 2014, vol. 8, no. 7, pp. 506–514, Jun. 2014, doi: 10.1038/nphoton.2014.134.
- [35] S. Emin, S. P. Singh, L. Han, N. Satoh, and A. Islam, “Colloidal quantum dot solar cells,” *Solar Energy*, vol. 85, no. 6, pp. 1264–1282, Jun. 2011, doi: 10.1016/J.SOLENER.2011.02.005.
- [36] A. J. Nozik, “Quantum dot solar cells,” *Physica E Low Dimens Syst Nanostruct*, vol. 14, no. 1–2, pp. 115–120, Apr. 2002, doi: 10.1016/S1386-9477(02)00374-0.
- [37] Z. Yang et al., “Mixed-quantum-dot solar cells,” *Nature Communications* 2017, vol. 8, no. 1, pp. 1–9, Nov. 2017, doi: 10.1038/s41467-017-01362-1.
- [38] L. Hrostea, M. Boclinca, M. Socol, L. Leontie, A. Stanculescu, and M. Girtan, “Oxide/metal/oxide electrodes for solar cell applications,” *Solar Energy*, vol. 146, pp. 464–469, Apr. 2017, doi: 10.1016/J.SOLENER.2017.03.017.
- [39] R. Jose, V. Thavasi, and S. Ramakrishna, “Metal Oxides for Dye-Sensitized Solar Cells,” *Journal of the American Ceramic Society*, vol. 92, no. 2, pp. 289–301, Feb. 2009, doi: 10.1111/J.1551-2916.2008.02870.X.
- [40] Q. Zhang, C. S. Dandeneau, X. Zhou, and C. Cao, “ZnO Nanostructures for Dye-Sensitized Solar Cells,” *Advanced Materials*, vol. 21, no. 41, pp. 4087–4108, Nov. 2009, doi: 10.1002/ADMA.200803827.
- [41] Z. Yue, H. Guo, and Y. Cheng, “Toxicity of Perovskite Solar Cells,” *Energies* 2023, Vol. 16, Page 4007, vol. 16, no. 10, p. 4007, May 2023, doi: 10.3390/EN16104007.
- [42] S. S. Kanmani and K. Ramachandran, “Synthesis and characterization of TiO₂/ZnO core/shell nanomaterials for solar cell applications,” *Renew Energy*, vol. 43, pp. 149–156, Jul. 2012, doi: 10.1016/J.RENENE.2011.12.014.
- [43] Shreya, S. Rai, P. Phogat, R. Jha, and S. Singh, “Synergistic effects of Carbon@MoS₂ core-shell nanostructures on charge dynamics for future optoelectronic applications,” *Mater Chem Phys*, vol. 329, p. 130147, Jan. 2025, doi: 10.1016/J.MATCHEMPHYS.2024.130147.
- [44] P. Phogat, S. Rai, Shreya, R. Jha, and S. Singh, “High-performance self-powered electrochemical photodetectors based on co-precipitation and hydrothermally synthesized HgS nanoparticles,” *Journal of Materials Science: Materials in Electronics*, vol. 35, no. 22, pp. 1–15, Aug. 2024, doi: 10.1007/S10854-024-13299-5/METRICS.
- [45] Shreya, P. Phogat, R. Jha, and S. Singh, “Carbon nanospheres-induced enhanced capacitive dynamics in C/WS₂/WO₃ nanocomposites for high-performance electrochemical capacitors,” *Materials Science and Engineering: B*, vol. 304, Jun. 2024, doi: 10.1016/J.MSEB.2024.117390.
- [46] N. Shreya, P. Phogat, R. Jha, and S. Singh, “Enhanced Electrochemical Performance and Charge-Transfer Dynamics of 2D MoS₂/WO₃ Nanocomposites for Futuristic Energy Applications,” *ACS Appl Nano Mater*, vol. 7, no. 8, pp. 8593–8611, Apr. 2024, doi: 10.1021/ACSANM.3C06017/SUPPL_FILE/AN3C06017_SI_001.PDF.
- [47] S. Rai, Shreya, P. Phogat, R. Jha, and S. Singh, “Wide absorption spectrum and rapid response time of PEC photodetectors based on MoS₂–Se nanocomposites,” *Chem Eng Commun*, pp. 1–16, Jun. 2024, doi: 10.1080/00986445.2024.2362799.
- [48] Shreya, P. Phogat, R. Jha, and S. Singh, “Electrochemical study of cerium and iron doped MoO₃ nanoparticles showing potential for supercapacitor application,” *Next Materials*, vol. 5, p. 100260, Oct. 2024, doi: 10.1016/J.NXMATE.2024.100260.
- [49] P. Phogat, Shreya, R. Jha, and S. Singh, “Synthesis and characterization of C@CdS core-shell structures for high-performance capacitors,” *Next Materials*, vol. 5, p. 100246, Oct. 2024, doi: 10.1016/J.NXMATE.2024.100246.
- [50] T. Jindal, P. Phogat, Shreya, S. Singh, and R. Jha, “Electrochemical and optical comparison of Cr³⁺, Co²⁺, Ag¹⁺, Hg¹⁺ and Pb⁴⁺ doped WO₃ as a thin layer working electrode for electrochemical sensing,” *Appl Phys A Mater Sci Process*, vol. 130, no. 7, Jul. 2024, doi: 10.1007/S00339-024-07666-6.
- [51] P. Phogat, Shreya, R. Jha, and S. Singh, “Supercapacitive studies of hybrid materials based on cadmium deuterioxide chloride (CdDOCl) with activated carbon,” *J Mater Sci*, vol. 59, no. 26, pp. 11757–11780, Jul. 2024, doi: 10.1007/S10853-024-09874-0/FIGURES/10.
- [52] V. Sahgal, P. Phogat, Shreya, T. Kumar, R. Jha, and S. Singh, “Design strategies for morphologically ramified ZnO–ZnS core shell nano flowers for magnified electrochemical studies,” *Indian Journal of Physics*, pp.

- 1–22, May 2024, doi: 10.1007/S12648-024-03196-2/METRICS.
- [53] P. Phogat, Shreya, R. Jha, and S. Singh, “Photocatalytic Performance of ZnO@ZnS Core–Shell Heterostructures for Malachite Green and Rhodamine B Dye Degradation,” *Physica status solidi (a)*, p. 2400404, 2024, doi: 10.1002/PSSA.202400404.
- [54] Shreya, P. Phogat, R. Jha, and S. Singh, “Electrochemical analysis of hydrothermally synthesized 2D/1D WS₂/WO₃ nanocomposites for solar cell application,” *Journal of Physics and Chemistry of Solids*, vol. 192, p. 112110, Sep. 2024, doi: 10.1016/J.JPCS.2024.112110.
- [55] P. Phogat, Shreya, R. Jha, and S. Singh, “Synthesis of novel ZnO nanoparticles with optimized band gap of 1.4 eV for high-sensitivity photo electrochemical detection,” *Materials Today Sustainability*, vol. 27, p. 100823, Sep. 2024, doi: 10.1016/J.MTSUST.2024.100823.
- [56] P. Phogat, Shreya, R. Jha, and S. Singh, “Supercapacitive studies of hybrid materials based on cadmium deuterioxide chloride (CdDOCl) with activated carbon,” *J Mater Sci*, Jul. 2024, doi: 10.1007/S10853-024-09874-0.
- [57] Shreya, P. Phogat, S. Singh, and R. Jha, “Reduction mechanism of hydrothermally synthesized wide band gap ZnWO₄ nanorods for HER application,” *MATEC Web of Conferences*, vol. 393, p. 01004, Mar. 2024, doi: 10.1051/MATECCONF/202439301004.
- [58] P. Phogat, Shreya, R. Jha, and S. Singh, “Design and performance evaluation of 2D nickel oxide nanosheet thin film electrodes in energy storage devices,” *Indian Journal of Physics*, 2024, doi: 10.1007/S12648-024-03415-W.
- [59] S. Shreya, P. Phogat, R. Jha, and S. Singh, “Effect of Heterojunction Dynamics on Charge Transfer Mechanism in Type-II ZnS/MoS₂ Nanocomposite,” *ECS Meeting Abstracts*, vol. MA2024-01, no. 54, pp. 2894–2894, Aug. 2024, doi: 10.1149/MA2024-01542894MTGABS.
- [60] A. Rahdar, M. Aliahmad, and Y. Azizi, “NiO Nanoparticles: Synthesis and Characterization,” *Journal of Nanostructures*, vol. 5, no. 2, pp. 145–151, Apr. 2015, doi: 10.7508/JNS.2015.02.009.
- [61] D. P. Dubal, V.J. Fulari, and C.D. Lokhande, “Effect of morphology on supercapacitive properties of chemically grown β -Ni(OH)₂ thin films,” *Microporous and Mesoporous Materials*, vol. 151, pp. 511–516, Mar. 2012, doi: 10.1016/J.MICROMESO.2011.08.034.
- [62] O. O. Balayeva et al., “ β -NiS and Ni₃S₄ nanostructures: Fabrication and characterization,” *Mater Res Bull*, vol. 75, pp. 155–161, Mar. 2016, doi: 10.1016/J.MATERRESBULL.2015.11.037.



Absorption Enhancement in Silicon Solar Cell by Incorporation of Metal Nanoparticles

Mohd Amir¹, Mukesh Pratap Singh² & Iram Masood³

ABSTRACT

This study investigates the impact of strategically positioned metal nanoparticles (NPs) like Gold (Au), aluminum (Al), silver (Ag), and copper (Cu) on thin-film silicon (Si) to enhance optical absorption. The integration of NPs diminishes surface reflectance through forward scattering and near-field effects, thereby enhancing light coupling into the Si through the plasmonic properties of NPs. This dual enhancement in optical performance is achieved by optimising the radius and period of NPs. Subsequently, a comparative analysis is conducted among devices incorporating these NPs individually, revealing that Cu NPs yield the most significant absorption enhancement. A notable relative increase of 139.72% is observed in the current density (J_{sc}) with the utilisation of Cu NPs compared to the reference device, which lacks NPs. All simulations are executed using Lumerical finite-difference time-domain (FDTD) software.

Keywords: Thin Si Solar Cell, Metal Nanoparticles, Plasmonic, Light Trapping, FDTD

INTRODUCTION

Plasmons represent collective oscillations of free electrons within a material. These quasi-particles are similar to photons and phonons, arising from the quantization of plasma excitations [1], [2]. In recent years, plasmonic has emerged as a rapidly advancing field of research. This growth can be attributed to the continuous advancement in the fabrication and characterization methods of materials at nanoscale [3]–[5]. Additionally, various electromagnetic simulation techniques have been developed for understanding and harnessing plasmonic phenomena [6]–[8]. By adjusting the plasmonic properties, such as size and shape, of material at nanoscale, they find applications in various modern technologies, including photovoltaics (PV), plasmonic integrated circuits, plasmonic lasers, surface plasmon-enhanced LEDs, and bio-sensing [9], [10]. Plasmonic structures can be categorized into subgroups such as nanowires, nanorings, and nanoparticles, all of which exhibit unique optical characteristics due to their nanoscale dimensions. Consequently, the optical properties of materials at the interface of dielectric and metal nanostructures undergo significant

changes, leading to modifications in the local dielectric environment [3]–[5], [11]–[13]. When exposed to sunlight, surface plasmon resonance (SPR) occurs near the metal-dielectric interface, resulting in a strong enhancement of the electromagnetic (EM) field at the interface. The plasmons are those SPR that are resulted due to the interaction of nanostructures with the light, where collective oscillation of free electrons take place under the influence of oscillating electric field. The plasmons are broadly classified into three major categories namely localised surface plasmon (LSP), bulk plasmon (BP), and surface plasmon polaritons (SSP) [1], [2], [14].

One of the major drawbacks of PV technology is its high price of power per unit watt, compared to the available traditional power generation technologies. The cost of the power generated by Si-based PV may be reduced significantly by lowering the amount of material (Si) consumption in the manufacturing of these cells i.e., by optimising their thickness, while keeping the light absorption within the adequate limits. The use of metal nanoparticles (NPs) in the thin Si-based PV have a high potential to boost up

¹ Department of Applied Sciences & Humanities, Jamia Millia Islamia, New Delhi, India. E-mail: mohd169066@st.jmi.ac.in

² Department of Applied Sciences & Humanities, Jamia Millia Islamia, New Delhi, India. E-mail: mpsingh@jmi.ac.in

³ Department of Applied Sciences & Humanities, Jamia Millia Islamia, New Delhi, India. E-mail: iram188891@st.jmi.ac.in

their absorption ability by the means of plasmonic properties of NPs [5], [15]. The incorporation of the NPs scatters the light to large angles into the absorbing material (Si in this case) which increases the path length of the light and hence the reflection losses are minimised. Subsequently, the plasmonic effect like LSP may further enhance the absorption within the Si leading to high generation rate within the active material (Si) [2], [5], [8], [15], [16]. The incorporation of NPs in Si PV provides a cost-effective solution of enhancing its performance and reducing the cost of power per unit watt. The metal nanoparticles such as Al, Ag, Au, and Cu are some most commonly used materials in the Si-based PV due to their exceptional optoelectrical properties [15], [17]. These NPs shows excellent scattering and/or light absorbing properties. It is mandatory to maximise the scattering effect while minimising absorption within the nanoparticles themselves, across the range of wavelengths of interest. This delicate balance is required for optimising the photon-to-electron conversion efficiency within the device. The effective light trapping using the NPs in the thin films have been demonstrated by the Atwater et al. [18]. Spinelli et al. has optimised NPs arrays through impedance matching with the Si substrate, resulting in a substantial enhancement of absorption across a broad range of frequencies of the incident light [19]. It has also been reported in the literature that the side-coated mental NPs shows an ability to maximise the light coupling into the Si nanowires that significantly enhance the absorption [20]. The absorption enhancement within the Si nanowires has also been resulted via incorporation of metal NPs specifically in the long-wavelength region of the light spectrum [21], [22]. A study on the effect of Au NPs deposited on the Si nanopillars and nanoholes has been conducted by the Pudasaini et al. [23]. Whereas Huang et al. has shown an efficient light trapping within the Si nanopillars, using Ag nanospheres on the top of Si nanopillars [24]. The literature also reveals that the path length reduces, on increasing the gap between the NPs and the absorbing medium, resulting in substantial reduction in the scattering effect of the NPs. Therefore, it is crucial to maintain an appropriate gap between these two components [25].

The further advancement of the technology requires an analysis of light harvesting properties of the combined structure, consisting different metal NPs such as Al, Ag,

Au, and Cu. This critical examination of the different metal NPs may help the researchers and the industrialist to identify the most suitable metal NPs for the Si PV cells. In this work, we have performed a comparative numerical study to investigate the effect of various metal NPs (Al, Ag, Au, and Cu) on the absorption of Si PV cells. For the purpose we have designed four distinct devices (Device – A, B, C, D), comprising Al, Ag, Au, and Cu metal NPs, respectively, directly positioned on top of the Si substrate. To enhance the scattering and plasmonic effects leading to high absorption within the device, we have optimised the radius and the period of the metal NPs. A performance comparison is also made among all the devices at their respective optimised values of radius and the period.

SIMULATION DETAILS

This work utilises the Finite-Difference Time-Domain (FDTD) methods for executing all the simulation within the Lumerical program software. The program solves the Maxwell's electromagnetic (EM) wave equations described by the equations (1) to (4) in differential form.

$$\nabla \cdot E = \rho / \epsilon \quad \dots(1)$$

$$\nabla \cdot B = 0 \quad \dots(2)$$

$$\nabla \times E = -\partial B / \partial t \quad \dots(3)$$

$$\nabla \times H = J + \partial D / \partial t \quad \dots(4)$$

where, electric field is represented by E , magnetic flux is denoted by B , D is used for the displacement vector of electric field, and H shows the magnetic field. While the ρ and J are the volume charge density and current density, respectively. In the context of a Cartesian coordinate system, the expansion of the curl equations described above results in a set of six scalar equations as given below:

$$\frac{\partial E_x}{\partial t} = \frac{1}{\epsilon} \left(\frac{\partial H_z}{\partial y} - \frac{\partial H_y}{\partial z} - \sigma E_x \right) \quad \dots(5)$$

$$\frac{\partial E_y}{\partial t} = \frac{1}{\epsilon} \left(\frac{\partial H_x}{\partial z} - \frac{\partial H_z}{\partial x} - \sigma E_y \right) \quad \dots(6)$$

$$\frac{\partial E_z}{\partial t} = \frac{1}{\epsilon} \left(\frac{\partial H_y}{\partial x} - \frac{\partial H_x}{\partial y} - \sigma E_z \right) \quad \dots(7)$$

$$\frac{\partial H_x}{\partial t} = -\frac{1}{\mu} \left(\frac{\partial E_z}{\partial y} - \frac{\partial E_y}{\partial z} \right) \quad \dots(8)$$

$$\frac{\partial H_y}{\partial t} = -\frac{1}{\mu} \left(\frac{\partial E_x}{\partial z} - \frac{\partial E_z}{\partial x} \right) \quad \dots(9)$$

$$\frac{\partial H_z}{\partial t} = -\frac{1}{\mu} \left(\frac{\partial E_y}{\partial x} - \frac{\partial E_x}{\partial y} \right) \quad \dots(10)$$

Where σ is the conductivity and μ is the magnetic permeability. The equations (5) to (7) defines the temporal derivatives of electric field with respect to the spatial derivatives of the magnetic fields. In contrast, the subsequent three equations (8) to (10) describes the temporal derivatives of magnetic field with respect to the spatial derivatives of the magnetic fields. These scalar equations serve as the foundation for the FDTD method, which is used to simulate the interactions of EM waves with the materials in three-dimensional space. The Maxwell's curl equations are solved using Yee's algorithm by the program, which employs central difference numerical techniques for both spatial and temporal derivatives [26], [27]. The algorithm discretises the entire three-dimensional space into infinitely small cubic cells, known as Yee cells. This differs from the conventional method of separately calculating electric and magnetic fields by solving the wave equation. Within a single Yee cell, the normal to the faces of the cell represent the magnetic field vectors, while the edges of the cell define the electric field vectors [26], [27].

is defined as the centre-to-centre distance between the two consecutive NSs. In FDTD the periodic boundary conditions (PBC) are applied along x and y-axis, while perfectly matched layers (PMLs) are placed in the z-direction. A plane wave source propagating in the z-direction with a wavelength range span from 400 to 1100 nm is placed on the top of the structure as can be seen in the Fig. 1. To measure the exact transmittance a transmittance monitor is positioned at the interface of Si substrate and the NSs, while a reflectance monitor is positioned behind the source to measure the reflectance from the device structure. To record the electric field profile, scattering cross-section, absorption, photogeneration, and photocurrent, four distinct monitors are used, as illustrated in Fig. 1. To reduce computational load and save time, the lower limit for all these monitors is set at 500 nm into the Si substrate. Therefore, the Si thickness considered here is only 500 nm. To enhance the numerical accuracy of the program a finer mesh of size 2 nm is used for the NSs and for the rest of the FDTD region a non-uniform meshing is applied. The refractive index of the Si, Al, Ag, Au, and Cu are sourced from the internal data base of the Lumerical. The device structure for all four designed devices (Device-A, B, C, D) will remain consistent throughout the study, with the only variation being the material used for the nanospheres (NSs: Al, Ag, Au, and Cu for Device-A, B, C, and D, respectively).

RESULT AND DISCUSSION

Initially, we have set the period (p) at 400 nm and varied the radius (r) within the range of 10 to 150 nm for all the considered devices. To assess the performance of these devices, we compare them with a planar structure, i.e., a Si PV cell without NSs. The optimised value of r is determined for each device through an examination of various factors, including the reflectance, transmittance, NSs absorbance, device absorption, and solar generation rate. Subsequently, using the obtained optimised value of r , the value of p is varied from 250 to 650 nm. The same procedure is followed to obtain the optimised value of p as the one we have followed for the optimisation of the radius. Finally, a comparison is made between the performances of all the devices at their respective optimised values of r and p . The detailed discussion on the results is provided in the subsequent sections.

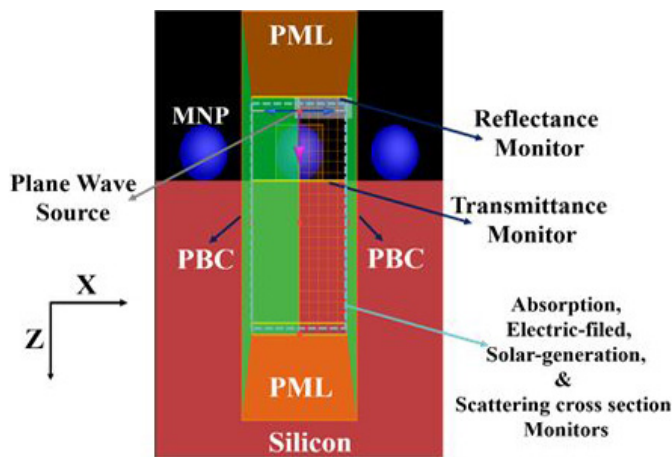


Fig. 1. A snapshot of FDTD simulation of the designed device

Fig. 1 provides a snapshot of the designed device, which includes spherical nanospheres (NSs) directly positioned on top of the Si substrate (1000 nm thick), with a specified radius (r) and period (p). The period

Effect of Radius Variation

When varying the radius of the NSs, we examined the average reflectance and transmittance for device-A as shown in Fig. 2(a) and (b). Notably, a significant lower average reflectance, particularly within the range of r_{Al} (radius of Al NS) from 60 to 140 nm, is observed. Therefore, to examine the spectral reflectance response over a range of wavelengths from 400 to 1100 nm, we have plotted it only within these ranges of r_{Al} . The reflectance spectrum, depicted in Fig. 2(c), exhibits a broad reduction in reflectance, primarily occurring within the 600 to 900 nm range when r_{Al} is set to 100 nm. This reduction in reflectance primarily occurs within the 600 to 900 nm range when r_{Al} is set to 100 nm. The decrease in reflectance can be attributed to the scattering effect of the Al NSs, which scatters the incident light to a wider range of angles, resulting in a longer path length for the light within the material and thus a higher probability of absorption. Fig. 2(d) illustrates that the best transmission of incident light into the Si substrate is also achieved at the same value of r_{Al} which is 100 nm. This reduced reflectance and increased transmittance couples the maximum incident light power to the Si substrate, where it is absorbed to generate photocarriers. The absorption within the device is also examined and presented in Fig. 3(a). It has been observed that as the radius varies from 60 nm onwards, the absorbed power (P_{abs}) increases for the wavelength range from 650 to 1100 nm. The power loss, which is the power absorbed by the nanospheres

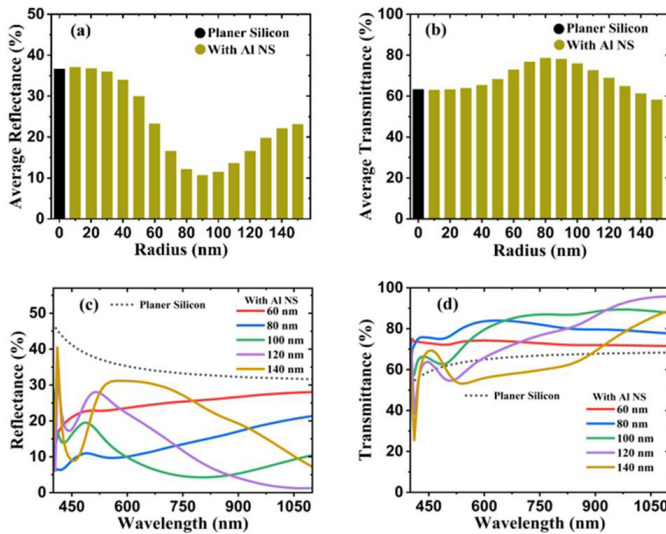


Fig. 2. The effect of the Al NS radius variation on (a) average reflectance, (b) average transmittance, (c) reflection spectrum, and (d) transmittance spectrum

(NSs), also increases as the radius increases beyond 100 nm. P_{abs} reduces significantly in the shorter wavelength region, as seen in Fig. 3(a) beyond 100 nm. The optimal value of r_{Al} is thus determined to be 100 nm, enhancing power absorption within the Si due to forward scattering and the plasmonic effect of the Al NSs, consequently leading to a higher generation rate and current density.

Similarly, the average reflectance and transmittance for device-B are influenced by varying the radius (r_{Ag}) of Ag NSs. At a radius of 80 nm, the average reflectance reaches its minimum, while the average transmittance achieves its maximum. However, the maximum generation rate is observed at 60 nm of r_{Ag} due to enhanced light coupling into the semiconductor from the plasmonic resonance of Ag NS. The P_{abs} is particularly pronounced in the shorter wavelength range of 400 to 450 nm at r_{Ag} of 60 nm as can be seen in Fig. 3(b). Therefore, the optimised value for r_{Ag} is determined to be 60 nm.

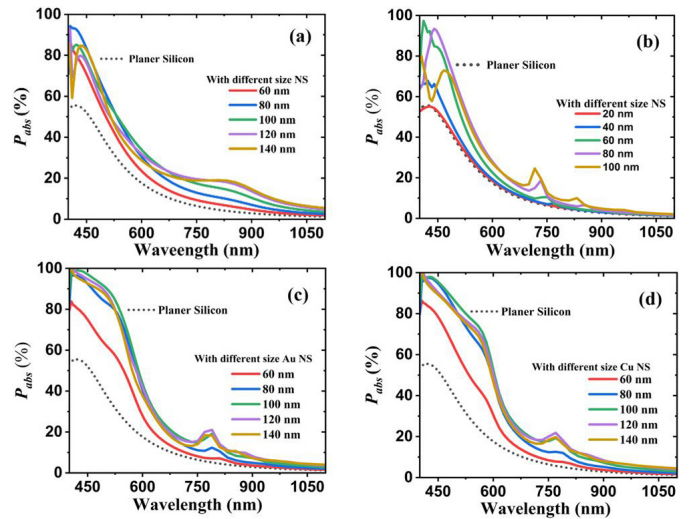


Fig. 3. Power absorption (P_{abs}) within the Si substrate at different radius of (a) Al nanosphere, (b) Ag nanosphere, (c) Au nanosphere, and (d) Cu nanosphere

For device-C with Au nanospheres, the minimum average reflectance occurs at r_{Au} (radius of Au NSs) of 100 nm, while the average transmittance remains nearly constant up to 80 nm for r_{Au} and decreases with further increases in r_{Au} . The decrease in average transmittance occurs due to spectral decrease in transmittance in shorter wavelengths, becoming more pronounced for r_{Au} beyond 80 nm. The absorbed power is maximised throughout the entire spectral range at r_{Au} of 100 nm, as shown in Fig. 3(c), leading to optimisation of r_{Au}

at 100 nm. On the other hand, for device-D with Cu NSs, the minimum average reflectance is achieved at r_{Cu} (radius of Cu NSs) of 100 nm, and the spectral reflectance response is particularly favorable at this radius compared to other spectral responses obtained with different r_{Cu} values. However, transmittance exhibits a decrease at shorter wavelengths as r_{Cu} increases, becoming more pronounced beyond 100 nm. The P_{abs} maximised throughout the entire spectral range at r_{Cu} of 100 nm, as depicted in Fig. 3(d), leading to optimised of r_{Cu} at 100 nm.

Effect of Periodicity

The period is systematically varied within the range of 250 to 650 nm for all devices, while keeping the radius of the NSs fixed at their respective optimised values.

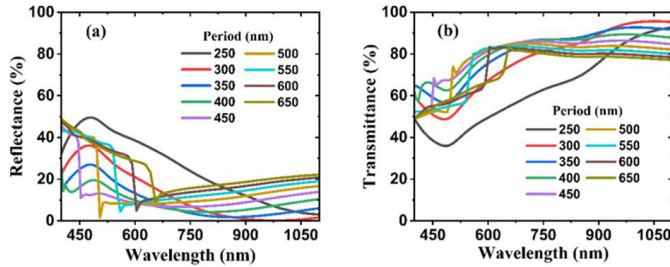


Fig. 4. Effect of Al NS period variation on (a) reflectance spectrum, and (b) transmittance spectrum

The reflectance and transmittance spectra of Device-A with Al NS are examined as shown in Fig. 4(a) and (b), respectively. The results reveal that the reflectance is at its minimum across the entire spectral range at a period (p_{AL}) of 400 nm, while the transmittance is maximised for this particular period value. The power loss, absorbed by the Al NS, at a period of 400 nm is relatively high for shorter wavelength ranges, specifically within the 400 to 450 nm range. However, beyond this range, this power loss significantly diminishes. While it is possible to further reduce this power loss by increasing the period beyond 400 nm, P_{abs} within the Si also decreases with an increase in period beyond 400 nm, as shown in Fig. 5(a). The most favorable spectral response for P_{abs} is achieved at 400 nm. Consequently, the value of p_{AL} is optimised at 400 nm, allowing for the simultaneous attainment of minimum reflectance, maximum transmittance, and maximum P_{abs} . Likewise, for Device-B with Ag NS, the period (p_{Ag}) is systematically varied. It is observed that as p_{Ag} increases from 250 nm and onwards, the spectral reflectance of the device also increases, while

the transmittance reduces. However, the power loss in the NSs and P_{abs} within the silicon decrease when p_{Ag} is increased. It can be observed from Fig. 5(b) that at a p_{Ag} value of 300 nm, the P_{abs} is maximised only for very short wavelengths and remains nearly the same as that for the P_{abs} value of 250 nm across the rest of the spectral range. Therefore, 300 nm is considered as the optimised value for P_{abs} in this case.

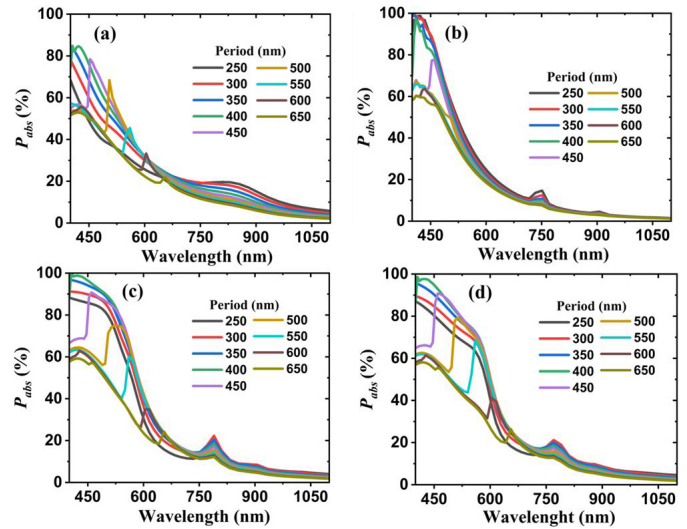


Fig. 5. Power absorption (P_{abs}) within the Si substrate at different period of (a) Al nanosphere, (b) Ag nanosphere, (c) Au nanosphere, and (d) Cu nanosphere

For device-C, the most favorable spectral responses for reflectance, transmittance, and P_{abs} within the Si are all achieved at a period (p_{Au}) of 400 nm, as evident from Fig. 5(c). A similar behavior of power loss (power absorption within the Au NS) is noticed, as in the previous case. It can be minimised by increasing the value of p_{Au} beyond 400 nm, but this comes at the cost of reduced P_{abs} , see Fig. 5(c). Therefore, the optimised choice for p_{Au} is determined to be 400 nm for Device-C. Finally, for device-D, the optimal spectral response in terms of reflectance, transmittance, and P_{abs} is achieved at a period (p_{Cu}) of 400 nm, as illustrated in Fig. 5(d). Consequently, the optimised choice for p_{Cu} is considered at 400 nm.

Performance Comparison of All the Devices

A comparison is made between the performances of all the devices at their respective optimised values of r and p . The transmittance and the power absorbed within the silicon (P_{abs}) for the all the devices are compared at their respective optimised values of radius and period, and these comparisons are presented in Fig. 6.

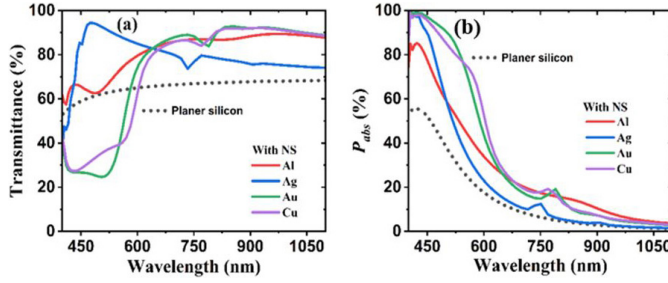


Fig. 6. Comparison of (a) transmittance spectrum, and (b) absorbance of the device at the respective optimised values of radius and period

The results reveals that in the shorter wavelength region below 650 nm, the transmittance is relatively higher for the devices-A and B, with the maximum transmittance observed in the device consisting Ag NS. However, in the wavelength range from 650 to 1100 nm, the devices-A, C and D exhibit higher transmittance, with maximum values that are nearly the same for the devices-C and D, i.e. the devices with Au and Cu NSs. Consequently, the best spectral distribution of the absorbed power (P_{abs}) is also obtained for the devices with Au and Cu NSs, as illustrated in Fig. 6(b). This relatively higher P_{abs} for the devices with Au and Cu NSs can be primarily attributed to the comparatively enhanced plasmonic effect of these metal nanoparticles. This enhancement is evident from the electric field distribution at a wavelength of 500 nm for all the devices, as shown in Fig. 7.

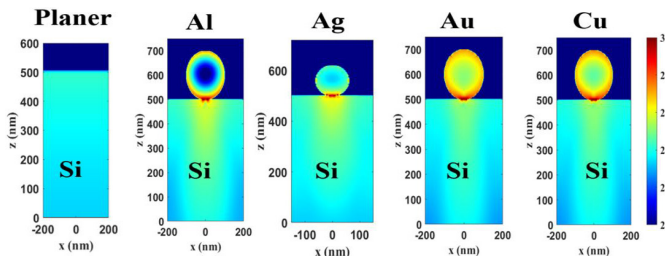


Fig. 7. Electric field distribution for the planner and the devices with NSs at the wavelength of 500 nm

Finally, the short-circuit current density (J_{sc}) is computed for all these devices and compared with the J_{sc} of the planar device. The comparison is presented in Table 1. It has been observed that the device-D i.e., the device consisting Cu NSs with obtained optimum radius (r_{Cu}) of 100 nm and a period (p_{Cu}) of 400 nm yields the highest enhancement in the J_{sc} value. The result of the best device, i.e. the device-D is also been compared with the previously reported values of J_{sc} in the literature and are presented in Table 2.

Table 1. Comparison table of current densities

S. No.	Device	J_{sc} (mA/cm ²)	Relative Increase in J_{sc} (%)
1	Planar	5.79	-
2	Device-A	10.95	89.12
3	Device-B	9.08	56.82
4	Device-C	13.46	132.46
5	Device-D	13.88	139.72

Table 2. Comparison of the results with reported literature

S. No.	J_{sc} (mA/cm ²)	Reference
1	21.00	[28]
2	27.73	[17]
3	31.40	[29]
5	139.72	Our results

CONCLUSION

The study demonstrates that substantial enhancement of optical absorption in thin-film silicon is achievable by strategically arranging metal nanoparticles (NPs) directly on its top. Notably, the investigation identifies gold (Au) and copper (Cu) NPs as the most effective at inducing a strong plasmonic effect, with Cu exhibiting the maximum enhancement in silicon. Furthermore, the incorporation of NPs on the silicon surface significantly reduces surface reflectance due to the forward scattering of NPs. This dual impact of plasmonic enhancement and reduced reflectance leads to a remarkable improvement in current density, increasing it from 5.79 mA/cm² to 10.95 mA/cm², 9.08 mA/cm², mA/cm², and 13.88 mA/cm² for devices featuring Al, Ag, Au, and Cu NPs, respectively.

ACKNOWLEDGMENT

Mr. Mohd Amir hereby expresses his gratitude to Maulana Azad National Fellowship (MANF), SRF for the financial assistance. We are especially thankful to Ansys for providing a trial version of Lumerical FDTD.

REFERENCES

- [1] C. D. Geddes, "Plasmonics - A vision for the future," *Plasmonics*, vol. 1, no. 1, pp. 1–2, Mar. 2006, doi: 10.1007/S11468-006-9010-Y/METRICS.
- [2] S.A. Maier, "Plasmonics: Fundamentals and applications," *Plasmon. Fundam. Appl.*, pp. 1–223, 2007, doi: 10.1007/0-387-37825-1/COVER.
- [3] X. Ren et al., "High Efficiency Organic Solar Cells Achieved by the Simultaneous Plasmon-Optical and

- Plasmon-Electrical Effects from Plasmonic Asymmetric Modes of Gold Nanostars,” *Small*, vol. 12, no. 37, pp. 5200–5207, Oct. 2016, doi: 10.1002/SMLL.201601949.
- [4] R. Bhatia and L. Kumar, “Functionalized carbon nanotube doping of P3HT:PCBM photovoltaic devices for enhancing short circuit current and efficiency,” *J. Saudi Chem. Soc.*, vol. 21, no. 3, pp. 366–376, Mar. 2017, doi: 10.1016/J.JSCS.2016.11.003.
- [5] P. Mandal, “Application of Plasmonics in Solar Cell Efficiency Improvement: a Brief Review on Recent Progress,” *Plasmon. 2022*, vol. 17, no. 3, pp. 1247–1267, Mar. 2022, doi: 10.1007/S11468-022-01616-9.
- [6] B. Gallinet, J. Butet, and O. J. F. Martin, “Numerical methods for nanophotonics: Standard problems and future challenges,” *Laser Photon. Rev.*, vol. 9, no. 6, pp. 577–603, Nov. 2015, doi: 10.1002/LPOR.201500122.
- [7] Y. A. Akimov and W. S. Koh, “Design of Plasmonic Nanoparticles for Efficient Subwavelength Light Trapping in Thin-Film Solar Cells,” *Plasmonics*, vol. 6, no. 1, pp. 155–161, Mar. 2011, doi: 10.1007/S11468-010-9181-4/FIGURES/10.
- [8] A. Said, K.S.R. Atia, and S.S.A. Obayya, “On modeling of plasmonic devices: overview,” *JOSA B*, Vol. 37, Issue 11, pp. A163–A174, vol. 37, no. 11, pp. A163–A174, Nov. 2020, doi: 10.1364/JOSAB.399121.
- [9] D. Sharma, R. K. Sharma, A. Srivastava, P. Kumari, and S. K. Srivastava, “Simulation Study on Broadband Light Harvesting Properties of Aluminium Nanosphere and Silicon Nanopillar Arrays based Tandem Structure,” *Silicon*, vol. 15, no. 3, pp. 1211–1220, Feb. 2023, doi: 10.1007/S12633-022-02100-Z/METRICS.
- [10] P. Banerjee et al., “Light-trapping scheme using silica spheres on ultrathin c-silicon absorber: Transition from antireflection coating to whispering gallery resonator,” *Appl. Phys. A Mater. Sci. Process.*, vol. 128, no. 6, pp. 1–11, Jun. 2022, doi: 10.1007/S00339-022-05591-0/FIGURES/13.
- [11] P. Kou, L. Yang, C. Chang, and S. He, “Improved Flexible Transparent Conductive Electrodes based on Silver Nanowire Networks by a Simple Sunlight Illumination Approach,” *Sci. Reports 2017*, vol. 7, no. 1, pp. 1–11, Feb. 2017, doi: 10.1038/srep42052.
- [12] M. Yao et al., “Performance Improvement of Polymer Solar Cells by Surface-Energy-Induced Dual Plasmon Resonance,” *ACS Appl. Mater. Interfaces*, vol. 8, no. 9, pp. 6183–6189, Mar. 2016, doi: 10.1021/ACSAMI.6B00297.
- [13] W.A. Murray and W.L. Barnes, “Plasmonic Materials,” *Adv. Mater.*, vol. 19, no. 22, pp. 3771–3782, Nov. 2007, doi: 10.1002/ADMA.200700678.
- [14] P.E. Batson, “Plasmonic Modes Revealed,” *Science* (80), pp. 333–334, Jan. 2012, doi: 10.1126/SCIENCE.1215588.
- [15] D. Sharma, R.K. Sharma, A. Srivastava, P. Kumari, and S.K. Srivastava, “Simulation Study on Broadband Light Harvesting Properties of Aluminium Nanosphere and Silicon Nanopillar Arrays based Tandem Structure,” *Silicon*, vol. 15, no. 3, pp. 1211–1220, Feb. 2023, doi: 10.1007/S12633-022-02100-Z/METRICS.
- [16] P. Spinelli et al., “Plasmonic light trapping in thin-film Si solar cells,” *J. Opt.*, vol. 14, no. 2, p. 024002, Jan. 2012, doi: 10.1088/2040-8978/14/2/024002.
- [17] S. Foroutan, G. Rostami, M. Dolatyari, and A. Rostami, “Improvement of the conversion efficiency and power of thin film silicon solar cells by embedding metallic nanostructures in depletion region,” *Optik (Stuttg.)*, vol. 127, no. 20, pp. 8988–8994, Oct. 2016, doi: 10.1016/J.IJLEO.2016.06.100.
- [18] H. A. Atwater and A. Polman, “Plasmonics for improved photovoltaic devices,” *Nat. Mater.* 2010 93, vol. 9, no. 3, pp. 205–213, Feb. 2010, doi: 10.1038/nmat2629.
- [19] P. Spinelli, M. Hebbink, R. De Waele, L. Black, F. Lenzenmann, and A. Polman, “Optical impedance matching using coupled plasmonic nanoparticle arrays,” *Nano Lett.*, vol. 11, no. 4, pp. 1760–1765, Apr. 2011, doi: 10.1021/NL200321U.
- [20] K. Zhou, S. W. Jee, Z. Guo, S. Liu, and J. H. Lee, “Enhanced absorptive characteristics of metal nanoparticle-coated silicon nanowires for solar cell applications,” *Appl. Opt.*, vol. 50, no. 31, Nov. 2011, doi: 10.1364/AO.50.000G63.
- [21] O. Pylypova et al., “Influence of nanostructure geometry on light trapping in solar cells,” *Appl. Nanosci.*, vol. 12, no. 3, pp. 769–774, Mar. 2022, doi: 10.1007/S13204-021-01699-6/METRICS.
- [22] H. Li et al., “Which method is more efficient on enhancing light absorption for silicon nanowires array based solar cells: Plasmonic metal nanoparticles or narrow-bandgap semiconductor quantum dots?,” *Mater. Sci. Semicond. Process.*, vol. 146, p. 106661, Aug. 2022, doi: 10.1016/J.MSSP.2022.106661.
- [23] P.R. Pudasaini and A.A. Ayon, “Modeling the front side plasmonics effect in nanotextured silicon surface for thin film solar cells application,” *Microsyst. Technol.*, vol. 19, no. 6, pp. 871–877, Jun. 2013, doi: 10.1007/S00542-013-1756-5/FIGURES/6.
- [24] X. Huang, C. Lou, H. Zhang, and H. Yang, “Broadband anti-reflection in Si substrate via Ag nanospheres on Si nanopillar arrays,” *Opt. Commun.*, vol. 460, p. 125133, Apr. 2020, doi: 10.1016/J.OPTCOM.2019.125133.
- [25] K. R. Catchpole and A. Polman, “Design principles for particle plasmon enhanced solar cells,” *Appl. Phys. Lett.*, vol. 93, no. 19, p. 191113, Nov. 2008, doi: 10.1063/1.3021072/335818.
- [26] K. S. Yee and J.S. Chen, “The finite-difference time-domain (FDTD) and the finite-volume time-domain

- (FVTD) methods in solving Maxwell's equations," *IEEE Trans. Antennas Propag.*, vol. 45, no. 3, pp. 354–363, 1997, doi: 10.1109/8.558651.
- [27] S.D. Gedney, "Introduction to the Finite-Difference Time-Domain (FDTD) Method for Electromagnetics," *Introd. to Finite-Difference Time-Domain Method Electromagn.*, 2011, doi: 10.1007/978-3-031-01712-4.
- [28] H. Li, Y. Hu, Y. Yang, and Y. Zhu, "Theoretical investigation of broadband absorption enhancement in a-Si thin-film solar cell with nanoparticles," *Sol. Energy Mater. Sol. Cells*, vol. 211, p. 110529, Jul. 2020, doi: 10.1016/J.SOLMAT.2020.110529.
- [29] D. Sharma, P. Kumari, A. Srivastava, and S.K. Srivastava, "Comparative Numerical Analysis of Broadband Light Trapping Structures Based on Plasmonic Metals Nanosphere and Silicon Nanopillar Arrays for Thin Solar Cells," *Plasmonics*, vol. 18, no. 2, pp. 701–710, Apr. 2023, doi: 10.1007/S11468-023-01796-Y/TABLES/2.



Morphological and Optical Analysis of Tungsten Oxide Nanosheets for Gas Sensing Application

Tamanna Jindal¹, Peeyush Phogat², Shreya³, Ranjana Jha⁴ & Sukhvir Singh⁵

ABSTRACT

Tungsten oxide (WO₃) is a widely recognized transition metal oxide known for its stability and non-toxicity in nanoparticle form. Its low cost and simple synthesis procedure make it a promising contender for many applications. In the present work, WO₃ nanoparticles have been synthesized via a one-step hydrothermal route. X-ray diffraction pattern demonstrated the formation of a single phase of high crystallinity tungsten trioxide. Crystallite size and strain were used to explain the structural defects and formation mechanism of WO₃. UV-visible spectroscopy was used to investigate the optical characteristics, and the single phases of WO₃ showed a band gap of 2.5 eV. Field Emission Scanning electron microscope (FESEM) images demonstrated the morphological properties of material. As a result, tungsten trioxide was found to be more environmentally sensitive than pre-transition-metal oxides.

Keywords: Tungsten Oxide, Nanomaterial, Nanosheets, Hydrothermal

INTRODUCTION

The general consensus around nanoparticles and nanotechnology has been evolving over the previous few years, and the position may have changed. The current work focuses on tungsten oxide which is well-known metal for gas sensing applications. It has exceptional optical features, specifically the ability to change colour depending on its oxidation state [1]. This feature has led to its employment in a variety of sectors and gained attention across various research domains due to its versatility in electrochromic devices (such as displays and smart screens), where its transparency can change in response to an applied voltage, as well as in energy storage, catalysis and gas sensing. [2], [3], [4].

Over the past 15 years, the adaptable nature of WO₃ has led to its utilization in a range of applications [5]. Research into photoelectrochemical cells for water

splitting began in 1976, and more recent studies have investigated their potential application in dye-sensitized solar cells, batteries, and sensor technology [6]. Moreover, WO₃ has gathered significant interest for sensing applications due to its role as a prominent n-type gas-sensing material, proving instrumental in detecting various hazardous gases [7].

The structural characteristics and gas-sensing behaviour of nanocrystalline WO₃ powders synthesized through a sol-gel process using tungstic acid [8]. A comparative study of electrochromic tungsten oxide films prepared via spin-coating and dip-coating techniques, evaluating their structural, morphological, optical, and electrochemical properties [9, 10]. Still, there remains a significant research gap concerning the tungsten oxide for gas sensing purposes [11], [12].

¹ Research Lab for Energy System, Department of Physics, Netaji Subhas University of Technology, New Delhi, India.
E-mail: tamannajindal3@gmail.com

² Research Lab for Energy System, Department of Physics, Netaji Subhas University of Technology, New Delhi, India.
E-mail: peeyush.phogat@gmail.com

³ Research Lab for Energy System, Department of Physics, Netaji Subhas University of Technology, New Delhi, India.
E-mail: shreyasharma.aug15@gmail.com

⁴ Research Lab for Energy System, Department of Physics, Netaji Subhas University of Technology, New Delhi, India.
E-mail: drranjanajha@gmail.com

⁵ Research Lab for Energy System, Department of Physics, Netaji Subhas University of Technology, New Delhi, India.
E-mail: sukhvirster@gmail.com

Extensive research has been conducted on tungsten oxide nanoparticles and their flat structures, such as 2D nanosheets or thin films, primarily due to their remarkable surface area-to-volume ratio. Two-dimensional nanosheets, owing to their substantial surface area and relatively small volume, are particularly well-suited for gas sensing applications [13], [14]. Various methods, including sol-gel synthesis, hydrothermal approaches, and chemical vapor deposition, can be employed to produce nanostructured WO_3 materials [15], [16], [17].

Tungsten oxide has been extensively researched for its ability to transition reversibly between a colourless state and a blue colour when subjected to alternating small positive and negative voltages [18], [19]. The stoichiometry of WO_3 can change significantly, causing oxygen vacancies to occur in its crystal structure [20]. These vacancies can have an effect on its electrical and electrochemical characteristics and are useful in some applications like gas sensing, photodetectors, solar cells, etc. Hydrated versions of WO_3 exist, such as H_xWO_3 (where x is a variable) [21]. These hydrates can have unique properties and are useful in applications such as gas detection [22], [23].

Recently, there has been significant interest in tungsten-oxide-based materials due to their capability to absorb near-infrared (NIR) [24], [25], [26] light effectively and their efficient conversion of light into heat. Moreover, these materials possess an intriguing oxygen defect structure and exhibit strong local surface plasma resonance (LSPR) [27], [28], [29] resulting in robust photo absorption across a broad range of NIR wavelengths. Previously, a range of light-absorbing nanomaterials, including noble metals, polymeric materials, and other inorganic nanomaterials, have been investigated for their potential use in photothermal therapy for cancer treatment [30].

Even WO_3 has been utilized as an anode material due to its high theoretical capacity, low cost, and environmentally friendly nature [31]. Its main limitation, however, lies in its low electrical conductivity, a challenge that has been addressed with WO_{3-x} materials. The research focused on the development of high-performance mesoporous WO_{3-x} anodes using a hard template approach to enhance electrical conductivity. The resulting material exhibited an impressive reversible capacity of 748 mAh g^{-1} and a

high volumetric capacity of $1,500 \text{ mAh cm}^{-3}$ compared to bulk WO_{3-x} .

In recent years, the quest for efficient gas sensing materials has intensified due to their crucial role in various industrial [32], environmental [33], and biomedical applications [34]. Among the myriad of materials explored, tungsten oxide (WO_3) has emerged as a promising candidate owing to its unique properties such as high surface area, excellent chemical stability, and sensitivity to various gas species [35], [36].

Nanoscale morphological and optical properties play a significant role in determining the performance of gas sensing materials [37], [38]. Tungsten oxide nanosheets, with their two-dimensional structure, offer a large surface-to-volume ratio and enhanced gas interaction capabilities, making them particularly attractive for gas sensing applications [39], [40].

This paper presents a comprehensive study on the morphological and optical characteristics of tungsten oxide nanosheets and their implications for gas sensing. We investigate the synthesis methods, and examine the structural properties, surface morphology [41], and optical properties of WO_3 nanosheets using various analytical techniques such as XRD, UV-Visible spectroscopy and FESEM [42], [43].

The novelty of this study lies in its exploration of an unaddressed research gap, specifically analysed the morphological and optical properties of the synthesized material [44]. Nanoparticles of WO_3 doped materials were synthesized using the hydrothermal method and subsequently evaluated for their potential application in gas sensors. The orthorhombic structure of WO_3 has been presented in Fig. 1.

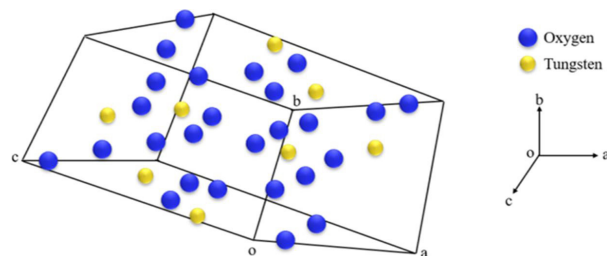


Fig. 1. 3D model of orthorhombic WO_3

EXPERIMENTAL SECTION

Chemical Reagents

During the synthesis process, analytical reagent (AR) grade chemicals and reagents (as detailed in Table

1) were used without further purification. Absolute ethanol and deionized (DI) water were employed for cleaning and washing procedures. Unless otherwise stated, all solutions were prepared using DI water.

Table 1. Chemicals utilized in the synthesis process

Chemical Name	Chemical Formula	Manufacturing Company	Purity
Sodium Tungstate	Na_2WO_4	M/s Thomas Baker	98%
Oxalic Acid	$\text{HO}_2\text{C}=\text{CO}_2\text{H}$	M/s Loba Chemie	99%
Nitric Acid	HNO_3	M/s CDH Ltd	98%

Synthesis

The single-step hydrothermal method was employed to synthesize tungsten oxide nanosheets. To prepare a single phase of WO_3 , a solution of Na_2WO_4 (0.096 M) was initially prepared in 30 ml DI water and stirred for 15 minutes. Afterwards, the mixture was agitated for a few minutes with the addition of 5ml HNO_3 . A 0.249 M solution of oxalic acid was prepared in 20 mL of deionized (DI) water and stirred for 30 minutes. This solution was then added dropwise to the pre-prepared solution under continuous stirring. The resulting mixture was stirred further for one hour at room temperature. Subsequently, the precursor solution was transferred into a Teflon-lined hydrothermal autoclave reactor and heated to 220°C for 24 hours in a hot air oven. It was then left overnight to cool naturally. The solution was later centrifuged and washed with DI water and ethanol several times. Finally, the precipitates were collected and dried in a vacuum oven at 60°C . The sample was then grounded to obtain the nanoparticles of WO_3 . The powder was then calcinated in the presence of oxygen for an hour at 500°C with a heating rate of $1^\circ/\text{min}$.

RESULTS AND DISCUSSION

X-Ray Diffraction

The XRD pattern of the synthesized powder sample was recorded within the 2θ range of 10° to 80° . This technique is used to characterize the structural properties of materials, including tungsten oxide (WO_3) nanosheets, which are essential for understanding their behaviour in gas sensing applications [45], [46].

XRD involves bombarding a sample with X-rays and measuring the intensity and angle of the diffracted X-rays. This data provides information about the crystal

structure, phase composition, lattice parameters, and crystallinity of the material [47].

For our study on the morphological and optical analysis of tungsten oxide nanosheets, XRD serves as a crucial characterization technique. By analysing the diffraction patterns obtained from WO_3 nanosheets, we can identify the crystal phases present, assess their purity, and determine their crystalline structure.

The peaks of the synthesized sample were analysed and indexed using the JCPDS file 01-071-0131, showing a good match with WO_3 . The synthesized WO_3 exhibited an orthorhombic crystal structure corresponding to specific (hkl) planes. given as (002), (020), (200), (120), (112), (220), (122), (222), (004), (040), (140), (420), (432), (440) and (160) as shown in Fig. 2.

The JCPDS file specifies that crystal structure of WO_3 as being in the space group Pmnb which means that WO_3 crystal structure has an orthorhombic symmetry with specific translational and rotational elements [48].

The Pmnb space group specifies the following symmetry elements, where 'P' defines a primitive lattice, 'm' represents the Mirror planes perpendicular to the a-axis, 'n' defines the Mirror planes perpendicular to the b-axis and 'b' illustrates the Glide planes perpendicular to the c-axis. In WO_3 , tungsten atoms are located at the corners and edges of distorted octahedra formed by oxygen atoms. Each tungsten atom is surrounded by six oxygen atoms, and each oxygen atom is shared between two octahedra [49].

This arrangement results in an orthorhombic crystal structure where the lattice parameters are unequal. Typically, in WO_3 , the lattice parameters are $a \neq b \neq c$, and the angles between the lattice vectors are 90° .

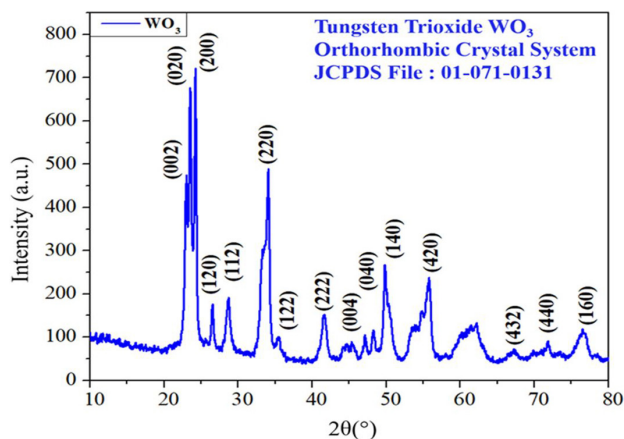


Fig. 2. XRD pattern of WO_3

Lattice Parameters, Crystallite Size and Strain

Lattice parameters are the lengths of the edges and the angles between them that define the unit cell of a crystal lattice. In other words, they describe the geometric arrangement of atoms in a crystal structure.

The crystallite size corresponds to the size of the smallest crystal in, a single crystal in powder form. Debye Scherrer formula provided in equation-1 has often been used to determine the size of crystallites. The Debye Scherrer formula is given as,

$$d = K \frac{\lambda}{\beta \cos \theta} \quad \dots(1)$$

Here, d represents the average diameter of crystallite, value of shape constant (k) is 0.9, λ stands for radiation wavelength (1.54 Å), β refers to full width at half maxima (FWHM), θ is Bragg's angle of respective peaks [50], [51]. The average of analysed peaks was determined and the obtained crystallite size of WO_3 was approx. 23 nm. This signifies the average size of individual crystalline domains. Smaller crystallite sizes can enhance surface area, potentially improving reactivity or electrical properties, particularly in catalysis or semiconductor applications [52], [53]. The lattice parameters for as synthesized sample were calculated using the equation-2.

$$\frac{1}{d^2} = \frac{h^2}{a^2} + \frac{k^2}{b^2} + \frac{l^2}{c^2} \quad \dots(2)$$

The inter planer spacing is denoted by d , with (hkl) representing the Miller indices, while a , b , and c correspond to the lattice sides. Table 2 illustrates the differences between the lattice parameters from the JCPDS file and the calculated values.

Table 2. Lattice parameters of the as-synthesized sample

Parameters	Calculated Value for WO_3	JCPDS Value for WO_3
a (Å)	7.37	7.34
b (Å)	7.57	7.57
c (Å)	7.34	7.75

The deviated value of lattice parameter represents the presence of micro strain. The Williamson Hall (W-H) Plot which is a graphical tool commonly used to calculate the strain and crystallite size, for describing the microstructural characteristics of crystalline materials and which applied the following equation,

$$\beta \cos \theta = (\epsilon \times 4 \sin \theta) + K\lambda / D \quad \dots(3)$$

Here, ϵ indicates the micro strain in the as synthesised material [54], [55]. The W-H plot is in between $(4 \sin \theta)$ and $(\beta \cos \theta)$, for WO_3 the slope and intercept are 0.00325 and 0.00301 respectively observed, as shown in Fig. 3(a). The crystallite size and strain obtained by using the W-H Plot is 46.04 nm and 0.00325 respectively.

The Size Strain (S-S) plot is also used as it offers precise and unbiased measurements of crystallite size and strain [56]. S-S plot accounts for multiple transitions in the material, including direct and indirect transitions, while the W-H plot typically assumes a single type of transition [57], [58].

The S-S plot often yields a more linear relationship between the absorption coefficient squared (α^2) and the photon energy and even requires less data processing. The equation 4 is the formula that was applied [59].

$$(d\beta \cos \theta)^2 = K\lambda/D (d^2\beta \cos \theta) + \epsilon^2/4 \quad \dots(4)$$

The S-S plot was obtained between $(d^2\beta \cos \theta)$ and $(d\beta \cos \theta)^2$ using which the slope is 0.00698 and intercept equals to -1.31905E-7 as observed in Fig. 3(b). The crystallite size and strain calculated by S-S Plot are 19.85 nm and 0.00229 respectively.

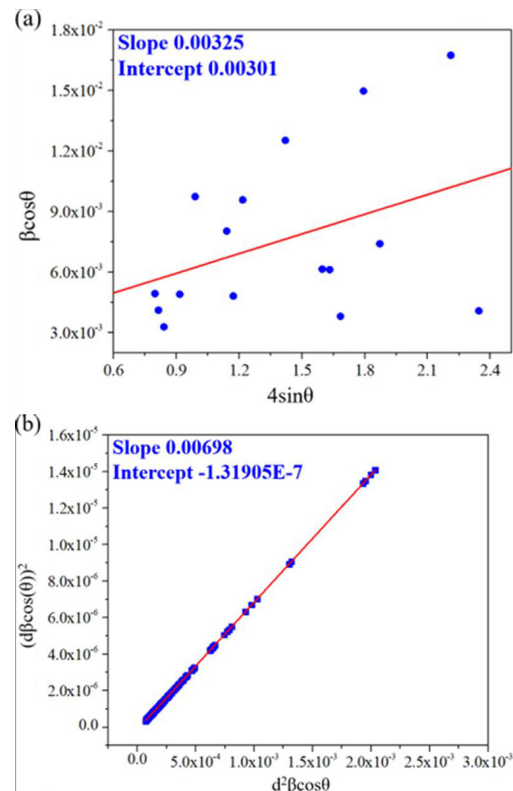


Fig. 3. (a) W-H plot of the synthesized sample, (b) S-S plot of the prepared sample

UV-Visible Spectroscopy

Ultraviolet-visible spectroscopy, is a widely used analytical technique to study the electronic transitions that occur in molecules.

UV-Vis spectroscopy detects the absorption of ultraviolet (UV) or visible light by molecules. When molecules absorb UV or visible light, their electrons transition from lower energy states to higher ones [60]. The difference in energy between these states matches the absorbed light's energy, appearing as absorption bands in the UV-Vis spectrum.

This technique was employed for as synthesized sample with wavelength ranging from 190 to 850 nm. The maximum absorption peaks were seen in the UV region between 190 nm and 450 nm.

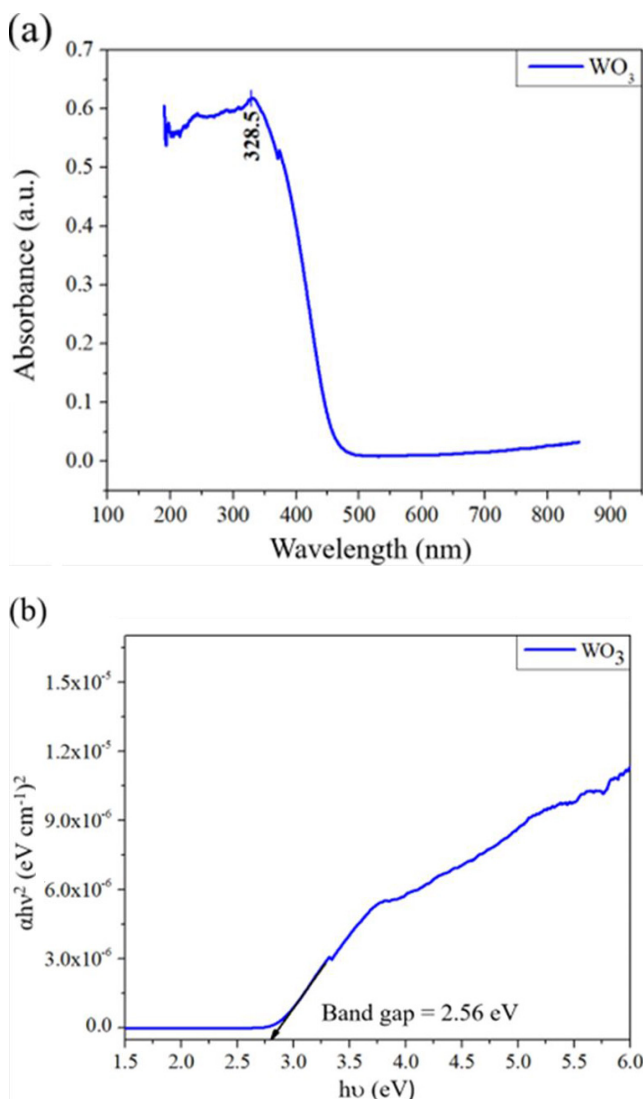


Fig. 4. (a) Absorption spectra of WO₃, (b) Tauc Plot of the synthesized sample

In the UV region, molecules undergo electronic transitions, where electrons are excited from lower energy levels to higher ones. This transition results in absorption of UV light, leading to characteristic absorption spectra [61]. For as synthesized material, 328.5 was the highest absorption peak as shown in Fig. 4(a).

UV analysis represents the optical bandgap, for which we employed the Tauc plot [62], [63]. Tauc plot defines the bandgap energy (E_g) of a material. The Tauc plot is a graphical representation of a semiconductor material's absorption edge, typically plotted against specific parameters, $(\alpha h\nu)^2$ versus the photon energy ($h\nu$). The equation used for this,

$$\alpha h\nu = A[h\nu - E_g]^{1/n} \quad \dots(5)$$

Here, α denotes the absorption coefficient, A is proportionality constant, E_g represents the bandgap and the nature of transition represented by n exponent. Using this formula, the bandgap of WO₃ was determined to be 2.56 eV, as shown in the Fig. 4(b). The bandgap of 2.56 eV was optimum for a number of applications [64], [65].

In the optoelectronic devices like photodetectors and sensors, the bandgap may provide a suitable balance between their sensitivity to visible light and electrical conductivity [66].

The refractive index is a helpful parameter for characterising and identifying compounds. It determines how light propagates through a material. It affects phenomena such as reflection, refraction, and dispersion. Understanding the refractive index is crucial for designing optical components like lenses, prisms, and fibres. Refractive index can serve as a characteristic property for identifying materials. Different substances have distinct refractive indices, allowing for their identification through techniques like refractometry or ellipsometry.

The effective refractive index of a medium can vary when a gas with a different refractive index than the medium in the vicinity interacts with it [67], [68], [69]. The variation of refractive index can detect the presence of specific gas and used for gas sensors. The material's Refractive Index is also calculated using the equation-6.

$$\frac{n^2 - 1}{n^2 + 2} = 1 - \sqrt{E_g / 20} \quad \dots(6)$$

Here, n denotes the refractive index, while E_g represents the corresponding band gap of the sample [70]. As determined earlier the band gap of WO_3 is 2.56 eV, the as synthesized material WO_3 has a refractive index of 2.53.

Morphological Analysis

FESEM (Field-Emission Scanning Electron Microscopy) characterization involves using a high-resolution electron microscope to examine the surface morphology and structure of materials at the nanoscale [71]. It provides detailed images of the sample's surface, revealing features such as size, shape, and distribution of particles or structures [72].

FESEM images can also reveal surface features such as roughness, porosity, and the presence of defects or crystalline facets [73]. These surface characteristics can influence the material's properties and applications.

The image can indicate whether the WO_3 nanoparticles are well-dispersed or aggregated. Aggregation can affect the material's properties, such as its reactivity and optical behaviour [74]. Depending on the imaging conditions and the quality of the sample, FESEM images may provide insights into the crystalline structure of WO_3 . This can be further confirmed by complementary techniques such as X-ray diffraction (XRD).

FESEM technique provides a significant experimental approach used for studying the surface properties and composition of materials at the microscopic level. Depending on the synthesis approach and conditions employed, WO_3 can have a variety of morphologies [75].

The nanoflower like morphology can be seen through hydrothermal route but during this process metal oxides may contain the volatile impurities such as water, which indicated the presence of acidic environment and promotes the nucleation and growth. To remove these volatile elements the calcination process is frequently used [76]. The calcination transforms the morphology of tungsten trioxide into the 2D Nanosheets. These tend to be thin, flat constructions with a high aspect ratio, resembling paper sheets within range of 100 nm as shown in Fig. 5(a).

Energy Dispersive X-ray Spectroscopy (EDX) spectra provide information about the elemental composition

of a sample [77]. When a material is exposed to high-energy electrons or X-rays, it emits characteristic X-rays with energy levels that correspond to the specific elements within the sample. It identifies the elements present in the sample by detecting characteristic X-rays emitted when the electrons of atoms in the sample are

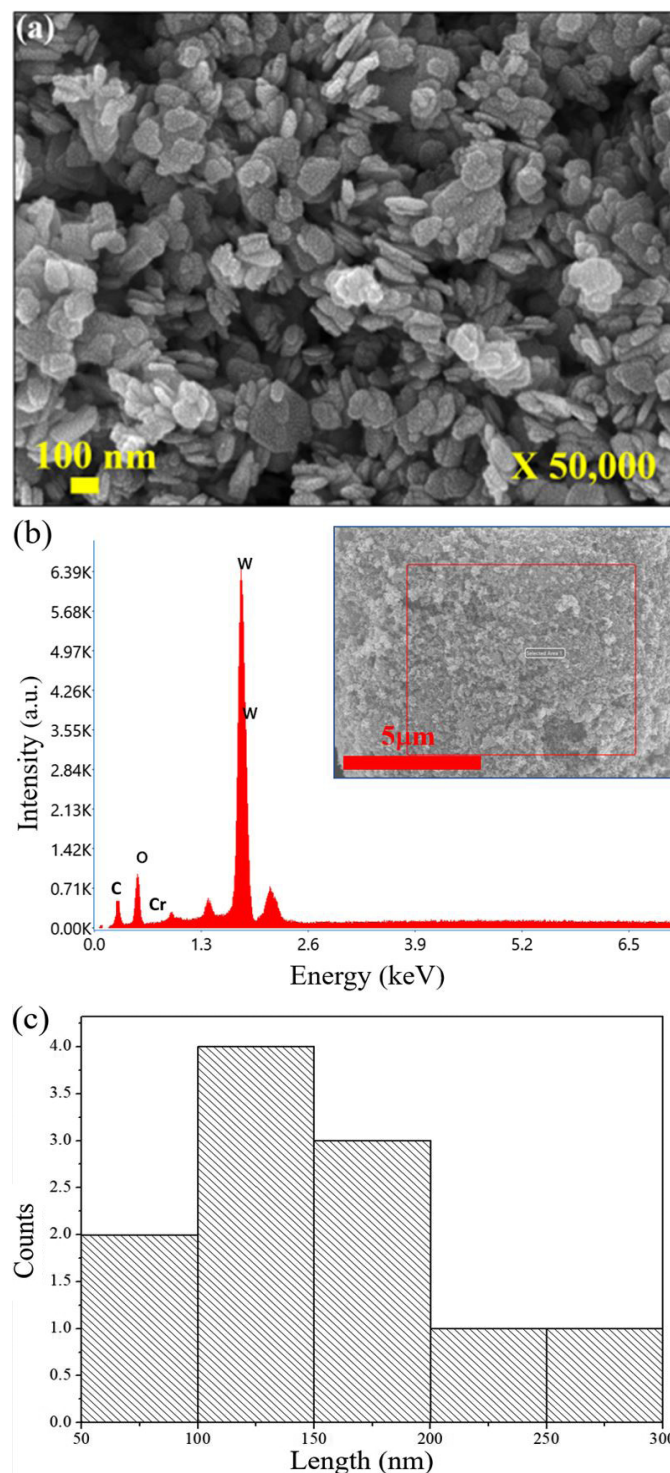


Fig. 5. (a) FESEM Image of the tungsten oxide, (b) EDX Spectra of corresponding area, (c) Particle Size Distribution

excited and transition to lower energy levels [78]. It gives an indication of the relative abundance of each element in the sample by measuring the intensity of the characteristic X-rays emitted.

In conjunction with field emission scanning electron microscopy (FESEM), EDX can provide information on the spatial distribution of elements, showing where specific elements are concentrated in the sample [79].

Fig. 5(b) shows that the tungsten (W) and oxygen (O) are present in the sample. Furthermore, the sample contains a particularly high concentration of tungsten. The signals attributed to carbon and copper in the EDX spectra originated from the carbon coating on the copper grid of electron microscope.

The observed nanosheets exhibited particle sizes ranging from 100 nm to 150 nm, as illustrated in Fig. 5(c). Their high aspect ratio contributed to enhanced material reactivity. They are hexagonal, rectangular 2D shape nanosheets. Even 2D WO_3 nanosheets frequently have outstanding structural and optical characteristics, making them valuable for sensors and photocatalysis.

CONCLUSION

The current work emphasis on the structural and optical study of WO_3 for application in gas sensors. The synthesis process used for WO_3 was the hydrothermal method. XRD analysis of the as-synthesized powder sample revealed that the material's crystal structure has orthorhombic symmetry. The formation of 2D nanosheets demonstrated by the FESEM technique. The band gap obtained from the tauc plot is 2.56 eV, within the region of wide bandgap semiconductors with a refractive index of 2.53. The Debye-Scherrer method yielded a crystallite size of 23.15 nm. The crystallite size and strain values calculated from the W-H Plot were 46.04 nm and 0.00325, respectively. Whereas, the S-S plot showed crystallite size and strain of 19.85 nm and 0.00229, respectively. Because of its varied qualities, WO_3 can be applied to a wide range of situations. WO_3 is widely explored for photocatalytic properties and has been proved useful for environmental cleanup and water splitting for the production of hydrogen. WO_3 has also been explored for gas sensing applications. When exposed to reducing gases, such as hydrogen, its broad bandgap allows the generation of charge carriers in the crystal lattice, or oxygen vacancies in

the crystal lattice when exposed to oxidizing gases like ozone. It can therefore be utilised in gas sensors to identify different gases, such as hydrogen, ozone (O_3) and nitrogen dioxide (NO_2). Thus, the future prospect is to use the as-synthesized WO_3 nanosheets for gas sensing applications due to its high aspect ratio and advantageous band gap.

ACKNOWLEDGMENT

The authors would like to express their gratitude to the Vice Chancellor of NSUT, Prof. Anand Srivastava, for his financial support.

REFERENCES

- [1] H. Pakdel et al., "Synthesis of WO_3 nanopowder using a green surfactant for efficient gas sensing applications," *Ceram Int*, vol. 49, no. 18, pp. 30501–30509, Sep. 2023, doi: 10.1016/J.CERAMINT.2023.06.314.
- [2] A. Hoel, L.F. Reyes, P. Heszler, V. Lantto, and C. G. Granqvist, "Nanomaterials for environmental applications: Novel WO_3 -based gas sensors made by advanced gas deposition," *Current Applied Physics*, vol. 4, no. 5, pp. 547–553, Aug. 2004, doi: 10.1016/J.CAP.2004.01.016.
- [3] H. Su et al., "Nanomaterial-based biosensors for biological detections," *Adv Health Care Technol*, vol. 3, pp. 19–29, Oct. 2017, doi: 10.2147/AHCT.S94025.
- [4] J.S. Meena, S. Bin Choi, S.-B. Jung, and J.-W. Kim, "Advances in Silver Nanowires-Based Composite Electrodes: Materials Processing, Fabrication, and Applications," *Adv Mater Technol*, vol. 8, no. 19, p. 2300602, 2023, doi: <https://doi.org/10.1002/admt.202300602>.
- [5] Y. Zhu, Y. Deng, P. Yi, L. Peng, X. Lai, and Z. Lin, "Flexible Transparent Electrodes Based on Silver Nanowires: Material Synthesis, Fabrication, Performance, and Applications," *Advanced Materials Technologies*, vol. 4, no. 10. Wiley-Blackwell, Oct. 01, 2019. doi: 10.1002/admt.201900413.
- [6] Y. Zhang, P. He, M. Luo, X. Xu, G. Dai, and J. Yang, "Highly stretchable polymer/silver nanowires composite sensor for human health monitoring," *Nano Res*, vol. 13, no. 4, pp. 919–926, 2020, doi: 10.1007/s12274-020-2730-z.
- [7] A. Elzwawy, A.M. Mansour, H.S. Magar, A.B.A. Hammad, R.Y.A. Hassan, and A.M. El Nahrwy, "Exploring the structural and electrochemical sensing of wide bandgap calcium phosphate/ $\text{Cu}_x\text{Fe}_{3-x}\text{O}_4$ core-shell nanoceramics for H_2O_2 detection," *Mater Today Commun*, vol. 33, Dec. 2022, doi: 10.1016/j.mtcomm.2022.104574.

- [8] I. Jiménez, J. Arbiol, A. Cornet, and J.R. Morante, "Structural and gas-sensing properties of WO₃ nanocrystalline powders obtained by a sol-gel method from tungstic acid," *IEEE Sens J*, vol. 2, no. 4, pp. 329–334, 2002, doi: 10.1109/JSEN.2002.803747.
- [9] M. Deepa, T.K. Saxena, D.P. Singh, K.N. Sood, and S.A. Agnihotry, "Spin coated versus dip coated electrochromic tungsten oxide films: Structure, morphology, optical and electrochemical properties," *Electrochim Acta*, vol. 51, no. 10, pp. 1974–1989, Feb. 2006, doi: 10.1016/j.electacta.2005.06.027.
- [10] G. Adilakshmi, A. Sivasankar Reddy, P. Sreedhara Reddy, and C. Seshendra Reddy, "Electron beam evaporated nanostructure WO₃ films for gas sensor application," *Materials Science and Engineering: B*, vol. 273, Nov. 2021, doi: 10.1016/j.mseb.2021.115421.
- [11] Shreya, P. Phogat, R. Jha, and S. Singh, "Microwave-synthesized γ -WO₃ nanorods exhibiting high current density and diffusion characteristics," *Transition Metal Chemistry*, vol. 48, no. 3, pp. 167–183, Jun. 2023, doi: 10.1007/S11243-023-00533-Y.
- [12] P. Van Tong, N.D. Hoa, N. Van Duy, D.T.T. Le, and N. Van Hieu, "Enhancement of gas-sensing characteristics of hydrothermally synthesized WO₃ nanorods by surface decoration with Pd nanoparticles," *Sens Actuators B Chem*, vol. 223, pp. 453–460, Feb. 2016, doi: 10.1016/J.SNB.2015.09.108.
- [13] P. Phogat, Shreya, R. Jha, and S. Singh, "Optical and Microstructural Study of Wide Band Gap ZnO@ZnS Core-Shell Nanorods to be Used as Solar Cell Applications," pp. 419–429, 2023, doi: 10.1007/978-981-99-2349-6_38.
- [14] X. Fang et al., "ZnS nanostructures: From synthesis to applications," *Prog Mater Sci*, vol. 56, no. 2, pp. 175–287, Feb. 2011, doi: 10.1016/J.PMATSCI.2010.10.001.
- [15] B. Deepa and V. Rajendran, "Pure and Cu metal doped WO₃ prepared via co-precipitation method and studies on their structural, morphological, electrochemical and optical properties," *Nano-Structures and Nano-Objects*, vol. 16, pp. 185–192, Oct. 2018, doi: 10.1016/j.nanoso.2018.06.005.
- [16] S. Sharma, P. Phogat, R. Jha, and S. Singh, "Electrochemical and Optical Properties of Microwave Assisted MoS₂ Nanospheres for Solar Cell Application," *International Journal of Smart Grid and Clean Energy*, pp. 66–72, 2023, doi: 10.12720/SGCE.12.3.66-72.
- [17] S. Mohammed Harshulkhan, K. Janaki, G. Velraj, R. Sakthi Ganapthy, and M. Nagarajan, "Effect of Ag doping on structural, optical and photocatalytic activity of tungsten oxide (WO₃) nanoparticles," *Journal of Materials Science: Materials in Electronics*, vol. 27, no. 5, pp. 4744–4751, May 2016, doi: 10.1007/S10854-016-4354-3/FIGURES/9.
- [18] R. Sivakumar, R. Gopalakrishnan, M. Jayachandran, and C. Sanjeeviraja, "Investigation of x-ray photoelectron spectroscopic (XPS), cyclic voltammetric analyses of WO₃ films and their electrochromic response in FTO/WO₃/electrolyte/FTO cells," *Smart Mater Struct*, vol. 15, no. 3, pp. 877–888, Jun. 2006, doi: 10.1088/0964-1726/15/3/025.
- [19] Z. Xie et al., "Fast fabrication of a WO₃·2H₂O thin film with improved electrochromic properties," *J Mater Chem*, vol. 22, no. 37, pp. 19904–19910, Oct. 2012, doi: 10.1039/c2jm33622g.
- [20] J. Dahiya, P. Phogat, A. Hooda, and S. Khasa, "Investigations of Praseodymium doped LiF-ZnO-Bi₂O₃-B₂O₃ glass matrix for photonic applications," Jan. 2024, p. 20065. doi: 10.1063/5.0178197.
- [21] M. Arshad et al., "Synthesis and characterization of Zn doped WO₃ nanoparticles: Photocatalytic, antifungal and antibacterial activities evaluation," *Mater Res Express*, vol. 7, no. 1, 2020, doi: 10.1088/2053-1591/ab6380.
- [22] H. Song et al., "Synthesis of Fe-doped WO₃ nanostructures with high visible-light-driven photocatalytic activities," *Appl Catal B*, vol. 166–167, pp. 112–120, May 2015, doi: 10.1016/j.apcatb.2014.11.020.
- [23] T. Tesfamichael, A. Ponzoni, M. Ahsan, and G. Faglia, "Gas sensing characteristics of Fe-doped tungsten oxide thin films," *Sens Actuators B Chem*, vol. 168, pp. 345–353, Jun. 2012, doi: 10.1016/j.snb.2012.04.032.
- [24] Z. Lv, S. He, Y. Wang, and X. Zhu, "Noble Metal Nanomaterials for NIR-Triggered Photothermal Therapy in Cancer," *Adv Healthc Mater*, vol. 10, no. 6, p. 2001806, 2021, doi: <https://doi.org/10.1002/adhm.202001806>.
- [25] S. Jiang, J. Lin, and P. Huang, "Nanomaterials for NIR-II Photoacoustic Imaging," *Adv Healthc Mater*, vol. 12, no. 16, p. 2202208, 2023, doi: <https://doi.org/10.1002/adhm.202202208>.
- [26] S. Zeng, D. Baillargeat, H.-P. Ho, and K.-T. Yong, "Nanomaterials enhanced surface plasmon resonance for biological and chemical sensing applications," *Chem. Soc. Rev.*, vol. 43, no. 10, pp. 3426–3452, 2014, doi: 10.1039/C3CS60479A.
- [27] A. Bonyár, "Label-Free Nucleic Acid Biosensing Using Nanomaterial-Based Localized Surface Plasmon Resonance Imaging: A Review," *ACS Appl Nano Mater*, vol. 3, no. 9, pp. 8506–8521, Sep. 2020, doi: 10.1021/acsanm.0c01457.
- [28] S. Lee, H. Song, H. Ahn, S. Kim, J. Choi, and K. Kim, "Fiber-Optic Localized Surface Plasmon Resonance Sensors Based on Nanomaterials," *Sensors*, vol. 21, no. 3, 2021, doi: 10.3390/s21030819.
- [29] P. Pei et al., "X-ray-activated persistent luminescence nanomaterials for NIR-II imaging," *Nat Nanotechnol*,

- vol. 16, no. 9, pp. 1011–1018, 2021, doi: 10.1038/s41565-021-00922-3.
- [30] Z. Bao, X. Liu, Y. Liu, H. Liu, and K. Zhao, “Near-infrared light-responsive inorganic nanomaterials for photothermal therapy,” *Asian J Pharm Sci*, vol. 11, no. 3, pp. 349–364, 2016, doi: <https://doi.org/10.1016/j.ajps.2015.11.123>.
- [31] A. Tacca et al., “Photoanodes Based on Nanostructured WO₃ for Water Splitting,” *ChemPhysChem*, vol. 13, no. 12, pp. 3025–3034, 2012, doi: <https://doi.org/10.1002/cphc.201200069>.
- [32] S. Adhikari, K. Sarath Chandra, D.-H. Kim, G. Madras, and D. Sarkar, “Understanding the morphological effects of WO₃ photocatalysts for the degradation of organic pollutants,” *Advanced Powder Technology*, vol. 29, no. 7, pp. 1591–1600, 2018, doi: <https://doi.org/10.1016/j.apt.2018.03.024>.
- [33] N. Naseri, R. Azimirad, O. Akhavan, and A.Z. Moshfegh, “Improved electrochromical properties of sol–gel WO₃ thin films by doping gold nanocrystals,” *Thin Solid Films*, vol. 518, no. 8, pp. 2250–2257, 2010, doi: <https://doi.org/10.1016/j.tsf.2009.08.001>.
- [34] L. Santos et al., “Synthesis of WO₃ nanoparticles for biosensing applications,” *Sens Actuators B Chem*, vol. 223, pp. 186–194, 2016, doi: <https://doi.org/10.1016/j.snb.2015.09.046>.
- [35] X. Mu et al., “High efficiency organic/silicon hybrid solar cells with doping-free selective emitter structure induced by a WO₃ thin interlayer,” *Nano Energy*, vol. 16, pp. 54–61, 2015, doi: <https://doi.org/10.1016/j.nanoen.2015.06.015>.
- [36] S. Ansari, M.S. Ansari, S.P. Satsangee, and R. Jain, “WO₃ decorated graphene nanocomposite based electrochemical sensor: A prospect for the detection of anti-anginal drug,” *Anal Chim Acta*, vol. 1046, pp. 99–109, 2019, doi: <https://doi.org/10.1016/j.aca.2018.09.028>.
- [37] J. Ma et al., “Pt Nanoparticles Sensitized Ordered Mesoporous WO₃ Semiconductor: Gas Sensing Performance and Mechanism Study,” *Adv Funct Mater*, vol. 28, no. 6, p. 1705268, 2018, doi: <https://doi.org/10.1002/adfm.201705268>.
- [38] C. Wang et al., “Hierarchical flower-like WO₃ nanostructures and their gas sensing properties,” *Sens Actuators B Chem*, vol. 204, pp. 224–230, 2014, doi: <https://doi.org/10.1016/j.snb.2014.07.083>.
- [39] B. Behera and S. Chandra, “Synthesis of WO₃ nanorods by thermal oxidation technique for NO₂ gas sensing application,” *Mater Sci Semicond Process*, vol. 86, pp. 79–84, 2018, doi: <https://doi.org/10.1016/j.mssp.2018.06.022>.
- [40] A. Staerz, S. Somacescu, M. Epifani, T. Kida, U. Weimar, and N. Barsan, “WO₃-Based Gas Sensors: Identifying Inherent Qualities and Understanding the Sensing Mechanism,” *ACS Sens*, vol. 5, no. 6, pp. 1624–1633, Jun. 2020, doi: [10.1021/acssensors.0c00113](https://doi.org/10.1021/acssensors.0c00113).
- [41] P.V. Karthik Yadav, B. Ajitha, Y.A.K. Reddy, V.R. Minnam Reddy, M. Reddeppa, and M.-D. Kim, “Effect of sputter pressure on UV photodetector performance of WO₃ thin films,” *Appl Surf Sci*, vol. 536, p. 147947, 2021, doi: <https://doi.org/10.1016/j.apsusc.2020.147947>.
- [42] M. Jamali and F. Shariatmadar Tehrani, “Thermally stable WO₃ nanostructure synthesized by hydrothermal method without using surfactant,” *Materials Science and Engineering: B*, vol. 270, p. 115221, 2021, doi: <https://doi.org/10.1016/j.mseb.2021.115221>.
- [43] A.S. Hammad, H.M. El-Bery, A.H. EL-Shazly, and M. F. Elkady, “Effect of WO₃ Morphological Structure on its Photoelectrochemical Properties,” *Int J Electrochem Sci*, vol. 13, no. 1, pp. 362–372, 2018, doi: <https://doi.org/10.20964/2018.01.32>.
- [44] K. Thiagarajan, M. Muralidharan, and K. Sivakumar, “Defects Induced Magnetism in WO₃ and Reduced Graphene Oxide-WO₃ Nanocomposites,” *J Supercond Nov Magn*, vol. 31, no. 1, pp. 117–125, Jan. 2018, doi: [10.1007/s10948-017-4184-4](https://doi.org/10.1007/s10948-017-4184-4).
- [45] S. Aksay, “Effects of Al dopant on XRD, FT-IR and UV-vis properties of MgO films,” *Physica B Condens Matter*, vol. 570, pp. 280–284, 2019, doi: <https://doi.org/10.1016/j.physb.2019.06.020>.
- [46] M.N. Mirzayev, R.N. Mehdiyeva, R.G. Garibov, N.A. Ismayilova, and S.H. Jabarov, “Influence of gamma irradiation on the surface morphology, XRD and thermophysical properties of silicide hexaboride,” *Modern Physics Letters B*, vol. 32, no. 14, p. 1850151, 2018, doi: [10.1142/S0217984918501518](https://doi.org/10.1142/S0217984918501518).
- [47] S.K. Sen, T.C. Paul, S. Dutta, M.N. Hossain, and M. N.H. Mia, “XRD peak profile and optical properties analysis of Ag-doped h-MoO₃ nanorods synthesized via hydrothermal method,” *Journal of Materials Science: Materials in Electronics*, vol. 31, no. 2, pp. 1768–1786, 2020, doi: [10.1007/s10854-019-02694-y](https://doi.org/10.1007/s10854-019-02694-y).
- [48] J.P. Kollender, A.I. Mardare, and A.W. Hassel, “Effect of Different Cobalt Concentrations on Tungsten Trioxide Photoelectrodes for Use in Solar Water Oxidation,” *J Electrochem Soc*, vol. 162, no. 4, pp. H187–H193, 2015, doi: [10.1149/2.0711503jes](https://doi.org/10.1149/2.0711503jes).
- [49] L. Zhang et al., “Recent progress for silver nanowires conducting film for flexible electronics,” *J Nanostructure Chem*, vol. 11, no. 3, pp. 323–341, 2021, doi: [10.1007/s40097-021-00436-3](https://doi.org/10.1007/s40097-021-00436-3).
- [50] Shreya, P. Phogat, R. Jha, and S. Singh, “Elevated Refractive Index of MoS₂ Amorphous Nanoparticles with a Reduced Band Gap Applicable for Optoelectronics,” pp. 431–439, 2023, doi: [10.1007/978-981-99-2349-6_39](https://doi.org/10.1007/978-981-99-2349-6_39).

- [51] D. Sánchez-Martínez, A. Martínez-De La Cruz, and E. López-Cuellar, "Synthesis of WO_3 nanoparticles by citric acid-assisted precipitation and evaluation of their photocatalytic properties," *Mater Res Bull*, vol. 48, no. 2, pp. 691–697, Feb. 2013, doi: 10.1016/J.MATERRESBULL.2012.11.024.
- [52] D. Meng, T. Yamazaki, Y. Shen, Z. Liu, and T. Kikuta, "Preparation of WO_3 nanoparticles and application to NO_2 sensor," *Appl Surf Sci*, vol. 256, no. 4, pp. 1050–1053, Nov. 2009, doi: 10.1016/J.APSUSC.2009.05.075.
- [53] D. Kumari, S. Sharma, P. Phogat, D. Dipti, S. Singh, and R. Jha, "Enhanced electrochemical behavior of C@CdS Core-Shell heterostructures," *Materials Science and Engineering B*, vol. 301, Mar. 2024, doi: 10.1016/j.mseb.2024.117212.
- [54] T. Kumar, Shreya, P. Phogat, V. Sahgal, and R. Jha, "Surfactant-mediated modulation of morphology and charge transfer dynamics in tungsten oxide nanoparticles," *Phys Scr*, vol. 98, no. 8, Aug. 2023, doi: 10.1088/1402-4896/ACE566.
- [55] Y. Yin, C. Lan, H. Guo, and C. Li, "Reactive Sputter Deposition of $\text{WO}_3/\text{Ag}/\text{WO}_3$ Film for Indium Tin Oxide (ITO)-Free Electrochromic Devices," *ACS Appl Mater Interfaces*, vol. 8, no. 6, pp. 3861–3867, Feb. 2016, doi: 10.1021/acsami.5b10665.
- [56] P. Phogat, Shreya, R. Jha, and S. Singh, "Diffusion Controlled Features of Microwave Assisted ZnS/ZnO Nanocomposite with Reduced Band Gap," *ECS Journal of Solid State Science and Technology*, vol. 12, no. 3, p. 034004, Mar. 2023, doi: 10.1149/2162-8777/ACC426.
- [57] M. Takagi, M. Kawaguchi, and A. Yamakata, "Enhancement of UV-responsive photocatalysts aided by visible-light responsive photocatalysts: Role of WO_3 for H_2 evolution on CuCl ," *Appl Catal B*, vol. 263, p. 118333, 2020, doi: <https://doi.org/10.1016/j.apcatb.2019.118333>.
- [58] O. Gonzalez, T.G. Welearegay, X. Vilanova, and E. Llobet, "Using the Transient Response of WO_3 Nanoneedles under Pulsed UV Light in the Detection of NH_3 and NO_2 ," *Sensors*, vol. 18, no. 5, 2018, doi: 10.3390/s18051346.
- [59] C.C. Mardare and A.W. Hassel, "Review on the Versatility of Tungsten Oxide Coatings," *Physica Status Solidi (A) Applications and Materials Science*, vol. 216, no. 12, Jun. 2019, doi: 10.1002/pssa.201900047.
- [60] P.V.K. Yadav, Y.A.K. Reddy, B. Ajitha, and V.R. Minnam Reddy, "Oxygen partial pressure dependent UV photodetector performance of WO_3 sputtered thin films," *J Alloys Compd*, vol. 816, p. 152565, 2020, doi: <https://doi.org/10.1016/j.jallcom.2019.152565>.
- [61] B. Bouchikhi et al., "Formaldehyde detection with chemical gas sensors based on WO_3 nanowires decorated with metal nanoparticles under dark conditions and UV light irradiation," *Sens Actuators B Chem*, vol. 320, p. 128331, 2020, doi: <https://doi.org/10.1016/j.snb.2020.128331>.
- [62] L. Santos et al., "Synthesis of WO_3 nanoparticles for biosensing applications," *Sens Actuators B Chem*, vol. 223, pp. 186–194, Feb. 2016, doi: 10.1016/j.snb.2015.09.046.
- [63] Dipti, P. Phogat, Shreya, D. Kumari, and S. Singh, "Fabrication of tunable band gap carbon based zinc nanocomposites for enhanced capacitive behaviour," *Phys Scr*, vol. 98, no. 9, Sep. 2023, doi: 10.1088/1402-4896/ACF07B.
- [64] A.C. Anithaa, N. Lavanya, K. Asokan, and C. Sekar, " WO_3 nanoparticles based direct electrochemical dopamine sensor in the presence of ascorbic acid," *Electrochim Acta*, vol. 167, pp. 294–302, Jun. 2015, doi: 10.1016/j.electacta.2015.03.160.
- [65] P. PHOGAT, . S., R. JHA, and S. Singh, "Electrochemical Analysis of Thermally Treated Two Dimensional Zinc Sulphide Hexagonal Nano-Sheets with Reduced Band Gap," *Phys Scr*, Dec. 2023, doi: 10.1088/1402-4896/AD0D93.
- [66] K. Yoon, S. Kim, J.J. Han, S. Han, and M. Preda, "Standard Interfacing Format for Actuators and Sensors," *MPEG-V*, pp. 57–87, 2015, doi: 10.1016/B978-0-12-420140-8.00003-2.
- [67] S. Sharma, P. Phogat, R. Jha, and S. Singh, "Enhanced Electrochemical Performance and Charge-Transfer Dynamics of 2D MoS_2/WO_3 Nanocomposites for Futuristic Energy Applications," *ACS Appl Nano Mater*, Apr. 2024, doi: 10.1021/acsanm.3c06017.
- [68] A. Sharma, S. Sharma, P. Phogat, R. Jha, and S. Singh, "Hydrothermally Synthesized NiS_2 and $\text{NiSO}_4(\text{H}_2\text{O})_6$ Nanocomposites and its Characterizations," *MATEC Web of Conferences*, vol. 393, Mar. 2024, doi: 10.1051/mateconf/202439301016.
- [69] S. Rai, S. Sharma, P. Phogat, R. Jha, and S. Singh, "Hydrothermal synthesis and characterization of selenium-doped MoS_2 for enhanced optoelectronic properties," *MATEC Web of Conferences*, vol. 393, Mar. 2024, doi: 10.1051/mateconf/202439301008.
- [70] S. Sharma, P. Phogat, S. Singh, and R. Jha, "Reduction mechanism of hydrothermally synthesized wide band gap ZnWO_4 nanorods for HER application," *MATEC Web of Conferences*, vol. 393, Apr. 2024, doi: 10.1051/mateconf/202439301004.
- [71] A. K. Thakur et al., "Controlled synthesis of WO_3 nanostructures: optical, structural and electrochemical properties," *Mater Res Express*, vol. 6, no. 2, p. 25006, Nov. 2018, doi: 10.1088/2053-1591/aae991.
- [72] I. Aslam et al., "Synthesis of $\text{WO}_3 \cdot \text{H}_2\text{O}$ spherical particles for efficient photocatalytic properties under visible light source," *Mater Sci Energy Technol*, vol. 2,

- no. 2, pp. 187–193, 2019, doi: <https://doi.org/10.1016/j.mset.2019.02.002>.
- [73] U. T. Nakate, V. K. Singh, Y. T. Yu, and S. Park, “WO₃ nanorods structures for high-performance gas sensing application,” *Mater Lett*, vol. 299, p. 130092, 2021, doi: <https://doi.org/10.1016/j.matlet.2021.130092>.
- [74] C. Kamble, M. Panse, and A. Nimbalkar, “Ag decorated WO₃ sensor for the detection of sub-ppm level NO₂ concentration in air,” *Mater Sci Semicond Process*, vol. 103, p. 104613, 2019, doi: <https://doi.org/10.1016/j.mssp.2019.104613>.
- [75] P. Phogat, S. Sharma, R. Jha, and S. Singh, “Phase Transition of Thermally Treated Polyhedral Nano Nickel Oxide with Reduced Band Gap,” *MATEC Web of Conferences*, vol. 393, Apr. 2024, doi: [10.1051/mateconf/202439301001](https://doi.org/10.1051/mateconf/202439301001).
- [76] A. Rai, P. Phogat, S. Sharma, R. Jha, and S. Singh, “Microwave Assisted Zinc Sulphide Quantum Dots for Energy Device Applications,” *MATEC Web of Conferences*, vol. 393, Mar. 2024, doi: [10.1051/mateconf/202439301011](https://doi.org/10.1051/mateconf/202439301011).
- [77] H. Koohestani, “Characterization of TiO₂/WO₃ composite produced with recycled WO₃ nanoparticles from WNiFe alloy,” *Mater Chem Phys*, vol. 229, pp. 251–256, 2019, doi: <https://doi.org/10.1016/j.matchemphys.2019.03.027>.
- [78] A.-Z. Warsi, F. Aziz, S. Zulfiqar, S. Haider, I. Shakir, and P.O. Agboola, “Synthesis, Characterization, Photocatalysis, and Antibacterial Study of WO₃, MXene and WO₃/MXene Nanocomposite,” *Nanomaterials*, vol. 12, no. 4, 2022, doi: [10.3390/nano12040713](https://doi.org/10.3390/nano12040713).
- [79] M. Rakibuddin and H. Kim, “Synthesis and characterization of facile industrially scalable and cost effective WO₃ micro–nanostructures for electrochromic devices and photocatalyst,” *Ceram Int*, vol. 44, no. 14, pp. 16615–16623, 2018, doi: <https://doi.org/10.1016/j.ceramint.2018.06.088>.



Organic Solar Cell Based with Inorganic Transport Layers: Performance Analysis and Optimisation

Iram Masood¹, Mukesh Pratap Singh² & Mohd Amir³

ABSTRACT

The use of transport layers (with high carrier mobilities) in organic solar cells result in high charge carrier extraction efficiency. In this work, inorganic materials, i.e. ZnO and NiO are utilised as electron and hole transport layers. The thicknesses of each layer in the device structure ITO (anode)/NiO/P3HT:PCBM/ZnO/Al (cathode) of an OSC are optimised. The effect of potential loss mechanisms on the device performance is also studied in this work. Subsequently, the effect of temperature variation on the performance of the device is studied. It is observed as the temperature increases from 250 to 400 K, the short-circuit current density (J_{sc}) increases, while the fill-factor (FF) and open circuit voltage (V_{oc}) of the device shows an inverse dependency on temperature. We have used an open-source computer-based program OghmaNano to perform the calculations in this work.

Keywords: Organic Solar Cells (OSCs), Optimisation, Recombination, Temperature, OghmaNano Software

INTRODUCTION

In present scenario, it is a need of the hour to have a reliable energy harvesting source that is cost effective and sustainable [1]. The most prominent reliable energy source is solar energy, and it may be harvested by the means of solar cells. These cells shows high potential to meet our current and future energy requirement. The silicon (Si) based solar cells dominates the today's market of solar cells mainly due to their excellent stability and high power conversion efficiency (PCE) [2,3]. The manufacturing of these cells include sophisticated machinery leading to increased cost of power per unit. For the past few years, different types of solar cells have been introduced to replace Si based solar cells, continuous research and efforts are being made to bring their PCE as high as possible. Recently, the thin-film solar cell technology has caught the attention of scientific fraternity to contribute towards its development and make use of the same to serve the community [4]. The semiconducting polymer and small molecule based organic solar cell (OSCs) technology is suitable to the required demand as it supports ease of fabrication, i.e.

cost-effective roll to roll processing and flexibility [5]. However, unlike Si based solar cells, the OSCs have limitation of small PCEs and their poor lifetime has triggered the interest to overcome OSCs limitations [2]. Among, all the available varieties of OSCs, the bulk heterojunction (BHJ) OSCs have the advantage of using blend of Donor (D) and Acceptor (A) materials with the selective properties which can possibly be produced by inexpensive fabrication methods [6]. The interconnecting mixture of donor material, i.e. P3HT and acceptor material like PCBM, is used as photon absorbing active material deposited between anode and cathode in BHJ OSCs [6,7]. To forbid the direct contact of active material with the electrodes, and to accelerate the selective charge carrier collection at the reference electrode, the hole and electron transport layers (HTL & ETL) are deposited on anode (below active layer) and cathode (adjacent to active layer), respectively. The thickness optimisation of these ETL and HTL layers promote light absorption within the active layer [7]. A conducting polymer, PEDOT:PSS is the most dominating conducting polymer in the field of OSCs, PEDOT:PSS is recognized for its good conductivity

¹ Department of Applied Sciences & Humanities, Jamia Millia Islamia, New Delhi, India. E-mail: iram188891@st.jmi.ac.in

² Department of Applied Sciences & Humanities, Jamia Millia Islamia, New Delhi, India. E-mail: mpsingh@jmi.ac.in

³ Department of Applied Sciences & Humanities, Jamia Millia Islamia, New Delhi, India. E-mail: mohd169066@st.jmi.ac.in

and transparency (particularly in the visible wavelength range), temperature stability and easy solution-based fabrication-process, but due to the acidic tendency of PEDOT:PSS, the stability of device is affected [8,9].

The metal oxides such as tungsten trioxide (WO_3), zinc oxide (ZnO), nickel oxide (NiO), molybdenum trioxide (MoO_3), and titanium dioxide (TiO_2), show better stability in ambient and may be used as charge carrier transport layers based on their band energies, in OSCs device structure [10-13]. We have selected a positive type hole accepting metal oxide, i.e. NiO as HTL which has broad energy gap, high electron affinity and good conductivity, while ZnO is selected as ETL due to its wide bandgap (3.3 eV), ambient stability, low absorption, transparency in the visible range and good electron mobility [12-16]. In present study the thicknesses of each layer in the stack of an OSC is optimised to enhance the *PCE* of the device. The effect of potential loss mechanisms such as geminate and non-geminate recombination on the performance of the OSC is studied. Furthermore, the device performance is evaluated by varying the temperature and its effect on the OSC parameters such as power conversion efficiency (*PCE*), fill factor (*FF*), short circuit current density (J_{sc}), and open circuit voltage (V_{oc}) is detailed insight.

DEVICE SIMULATION USING OGHMANANO SOFTWARE

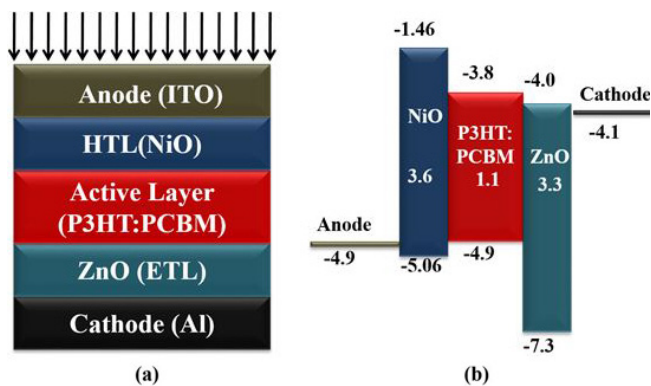


Fig. 1. (a) The schematic of the designed organic solar cell, (b) Energy band diagram of the materials

The schematic of the simulated device and the energy states diagram are presented in the Fig. 1(a) and Fig. 1(b), respectively. We have used an open source, opto-electronic device simulation software OghmaNano supports drift and diffusion transport model for charge carriers, evaluate charge carrier recombination

and trapping [17]. The OghmaNano software offers a material database and is compatible to add new materials with different properties to it. The parameters of the material can be controlled within the program, and maximum of 10 layers can be simulated at once.

The program examine the electrical behaviour of the simulated device by solving equations (1) numerically to obtain the potential distribution (ϕ) with the device [17-18].

$$\epsilon_0 \epsilon_r \nabla \phi = q (n_f - p_f + n_t - p_t) \quad \dots(1)$$

Where q is the electron charge, ϵ_0 is the free space permittivity while the permittivity of the material used as active layer is ϵ_r . The quantities n_f/p_f represents the free carrier concentration of electron/hole, while the trapped concentration is denoted with n_t/p_t for electron/hole [17]. The continuity equations, described by the equations (2) and (3) are solved to obtain the concentrations of free carriers (i.e. electrons and holes)

$$\nabla J_n = q (R_e - G) \quad \dots(2)$$

$$\nabla J_p = q (R_h - G) \quad \dots(3)$$

in terms of net recombination ($R_{e/h}$) and free electrons/holes generation rates (G). Finally, to obtain the total electron current (J_n) and hole current (J_p), drift-diffusion equation, i.e. equations (4) and (5) are solved.

$$J_n = q [n_f \mu_e (\partial E_{LUMO} / \partial x) + (\partial n_f / \partial x) D_n] \quad \dots(4)$$

$$J_p = q [p_f \mu_h (\partial E_{HOMO} / \partial x) + (\partial p_f / \partial x) D_p] \quad \dots(5)$$

Here $D_n(D_p)$ are diffusion coefficients of electrons (holes), μ_e/μ_h is the mobility of electrons/holes. The Shockley-Read-Hall recombination model is followed for charge carrier trapping and recombination [17,18]. The required density of states parameters in the program are listed in Table 1. The Fig. 2 depicts simulated device structure in OghmaNano simulation window.

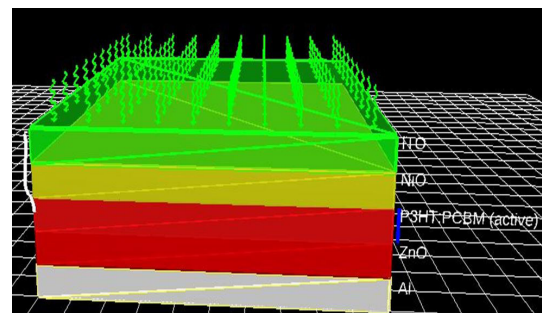


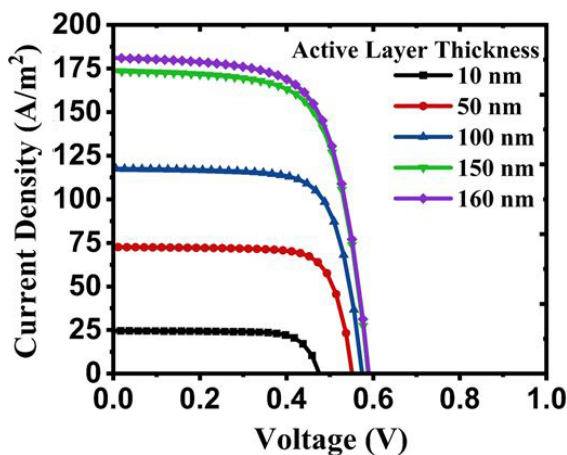
Fig. 2. The simulated device snap-shot of OghmaNano simulation window

Table 1. The density of states parameters

Simulation Parameters for Active layer		
Parameters	Values	Units
Trap density (electron)	3.8×10^{26}	(m^{-3}/eV)
Hole trap density	1.45×10^{25}	(m^{-3}/eV)
Mobility (electron)	2.48×10^{-7}	($\text{m}^2/\text{V/s}$)
Mobility (hole)	2.48×10^{-7}	($\text{m}^2/\text{V/s}$)
Tail slope for electron	0.04	(eV)
Tail slope for hole	0.06	(eV)
Free electron density of states	1.28×10^{27}	($/\text{m}^3$)
Free hole density of states	2.86×10^{25}	($/\text{m}^3$)
Material relative permittivity	3.8	—
Total traps number	20	(bands)
Electron affinity	3.8	(eV)
Energy gap	1.1	(eV)
Trapped electron to free electron	2.5×10^{-20}	($/\text{m}^2$)
Trapped hole to free hole	4.86×10^{-22}	($/\text{m}^3$)
Trapped electron to free hole	1.32×10^{-22}	($/\text{m}^2$)
Trapped hole to free electron	4.67×10^{-26}	($/\text{m}^2$)

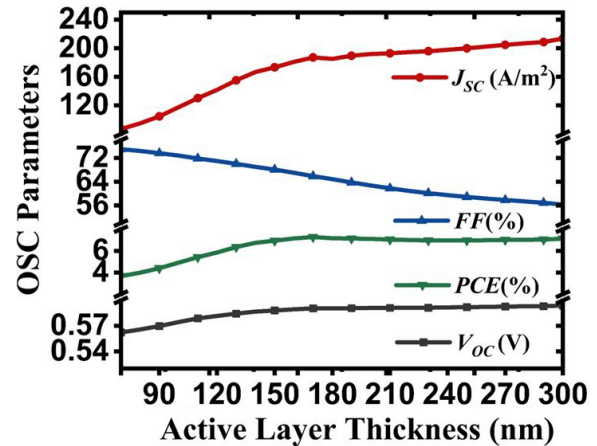
RESULTS AND DISCUSSION

The investigation of active layer (P3HT:PCBM), transport layers and electrodes thicknesses is of immense importance for electron/hole generation, transportation and collection within the OSC device and its effect on parameters of OSC. We made a variation from 60 to 300 nm in the active layer thickness in order to find its optimum value. The obtained current voltage (J - V) characteristics and the corresponding OSC parameters at different values of active layer thicknesses are plotted in Fig. 3 and 4, respectively. The open circuit voltage (V_{oc}) is energy levels (active material) dependent, in Fig. 4. The maximum value of V_{oc} is obtained as

**Fig. 3.** Effect of active layer thickness on J - V characteristics

0.59 V at 170 nm of the active layer thickness. The current density (J_{sc}) is mainly depends on the exciton (loosely bounded electron hole pair) generation upon the absorption of incident light in active layer.

It has observed in the results, a thin active layer leads to less photon absorption resulting in lower J_{sc} . The path length travelled by the free charge carriers increases as the thickness of the active layer increases which results in lower charge carrier collection efficiency and hence the current density of the device reduces. The maximum value of J_{sc} is obtained as 187.10 A/m^2 at the thickness of 170 nm. The increase in the active layer thickness also leads to high series resistance resulting in the degradation of fill factor (FF), shown in Fig. 3. Consequently, thickness of active layer is optimised as 170 nm, resulting in maximum PCE of 7.28%. The value of FF is obtained as 65.86% at the optimised thickness of active layer.

**Fig. 4.** Effect of thickness variation of active layer on OSC parameters

The transport layers (ETL and HTL) thicknesses are varied from 1 to 100 nm. The OSC parameters as a function of thickness variation of hole selective layer or HTL (NiO) is depicted in Fig. 5 and Fig. 6 shows the J - V curves at different values of the HTL thickness. The J_{sc} increases up to 5 nm of HTL thickness due to reduced reflection. The light transmittance is limited by the further increase in HTL thickness and series resistance increase with the increase in HTL thickness which reduces J_{sc} and degrades the FF . So, the optimised thickness of HTL is considered as 5 nm, leading to a PCE of 7.35%. The value of V_{oc} is obtained as 0.59 V while the values of J_{sc} and FF are attained as 188.76 A/m^2 and 65.88%, respectively with the HTL thickness of 5 nm.

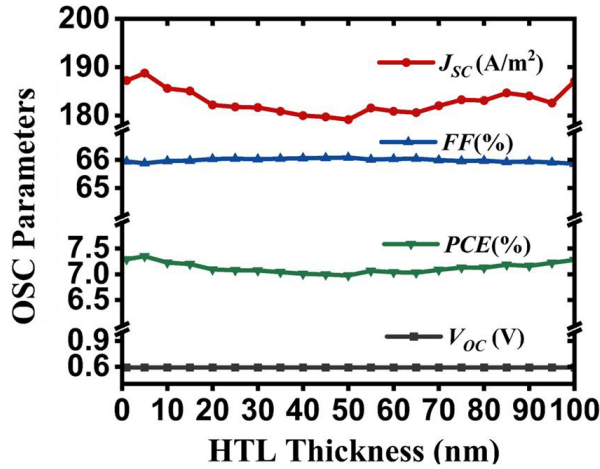


Fig. 5. Effect of thickness variation of HTL on OSC parameters

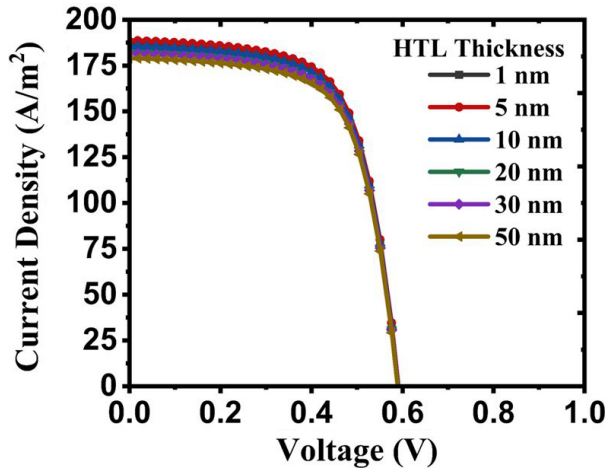


Fig. 6. Effect of HTL thickness on J - V characteristics

The Fig. 7 shows the effect of ETL (ZnO) thickness variation upon the J - V characteristics of the device. The ETL also known as electron selective layer, act as a barrier to stop the direct contact of active layer and cathode. The effect of ETL (ZnO) thickness has also been examined on the parameters of the OSC and plotted in Fig. 8. It is observed as the thickness of ETL increases no significant change occurs in the V_{oc} and FF . However, the J_{sc} increases up to 50 nm of ETL thickness, leading to increase in the PCE as can be observed in the Fig. 8. The advancement in J_{sc} and PCE on an increase in ETL thickness up to 50 nm attributed to the decrease reflection losses of the device. Whereas the reflection increases significantly beyond the 50 nm of ETL lowering the fraction of absorbed light within the active layer, causing a decrease in J_{sc} as well as in PCE . Moreover the increase in ETL thickness beyond 50 nm significantly increases the recombination of free charge carriers adding further decay to J_{sc} . Hence the

thickness of ETL is optimised as 50 nm resulting in a maximum PCE of 7.30%.

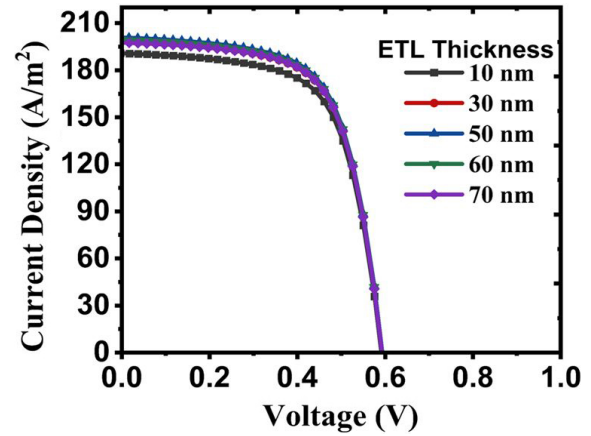


Fig. 7. Effect of ETL thickness on J - V characteristics.

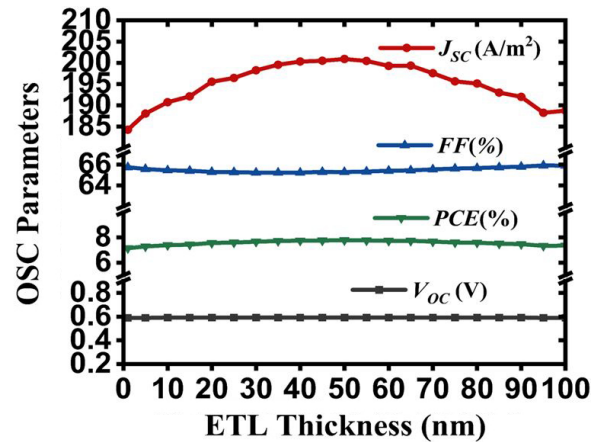


Fig. 8. Effect of ETL thickness on OSC parameters

In order to examine the effect of electrodes (anode and cathode) thicknesses on the device, their thicknesses are changed from 1 nm to 100 nm. The OSC parameters are shown in Fig. 9 for the change in anode thickness, and impact of anode thickness on J - V characteristics is depicted in the Fig. 10.

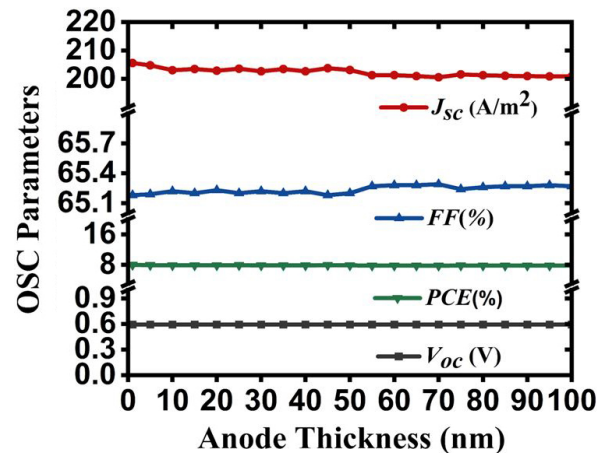


Fig. 9. Effect of anode thickness on OSC parameters

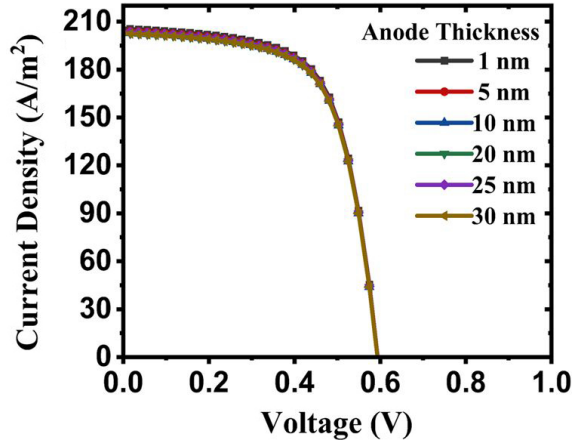


Fig. 10. Effect of anode thickness on J - V characteristics

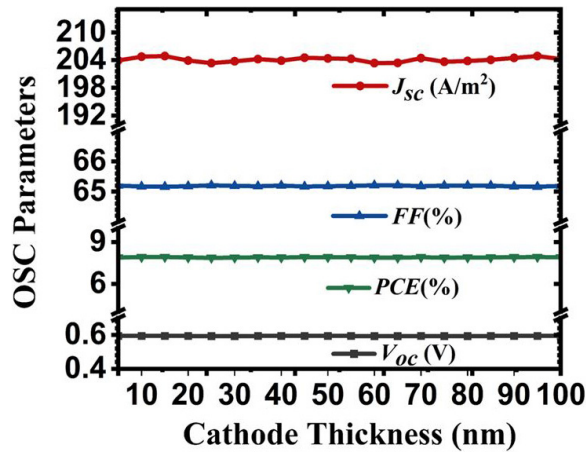


Fig. 11. The effect of cathode thickness on OSC parameters

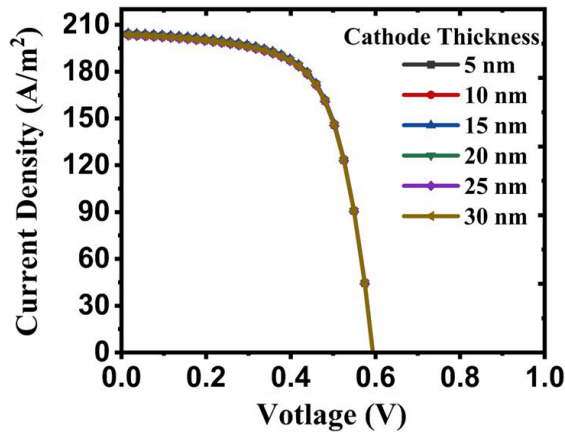


Fig. 12. Effect of cathode thickness on J - V characteristics

The effect of cathode thickness variation on J - V characteristics are represented in Fig. 11 and the corresponding OSC parameters are plotted in Fig. 12.

The anode (ITO) is the top most layer in the device structure hence it must be thin enough to enhance light transmission towards the active layer. After examining OSC parameters as shown in the Fig. 9 the optimised value of its thickness is obtained as 5 nm, resulting

a PCE of 7.91%. The cathode (Al) reflects back the portion of light to the active layer, this slightly enhances J_{sc} initially. The optimal thickness of cathode is found to be 15 nm. After the optimisation cathode thickness the values of V_{oc} , J_{sc} and FF are as 0.59 V, 204.86 A/m² and 65.16% respectively, with 7.93% of PCE .

Now for the device with the optimised layer thicknesses, we investigated the effect of recombination (geminate & non-geminate) on the device performance. The impact of geminate recombination on OSC parameters are shown in Fig. 13 and J - V characteristics are represented in the Fig. 14.

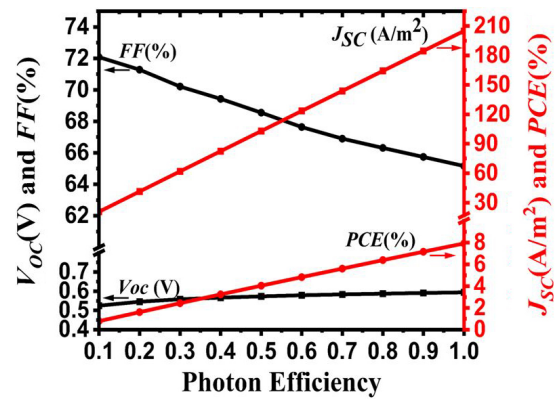


Fig. 13. Effect of geminate recombination on OSC parameters

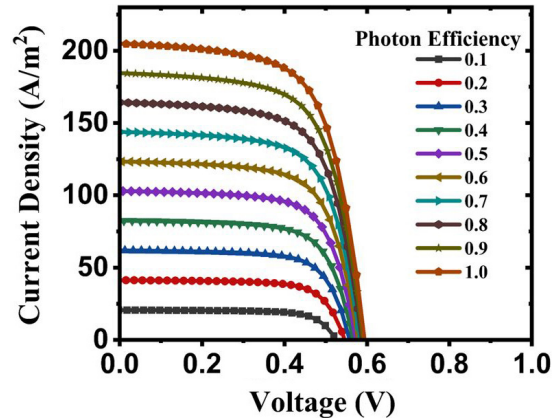


Fig. 14. Effect of geminate recombination on J - V characteristics

The geminate recombination takes place before the charge separation for the same photo generated exciton. If the dissociation of bound electron-hole could not proceed, they will relax into ground state, recombining together. The separation of bounded excitons is measured in terms of photon efficiency, where 100% (or 1) photon efficiency means that each photo generated exciton successfully separate into the free electron hole pairs. The variation in OSC

parameters due to geminate recombination at low and higher photon efficiencies are plotted in Fig. 13. The results show that at 40% photon efficiency, the PCE is attained as 2.42%. which implies that 60% of photon generated excitons are not being separated at charge transfer state (CTS), enabling geminate recombination. Whereas at higher photon efficiencies, J_{sc} and PCE becomes high due to lower geminate recombination, as more excitons dissociate at the CTS. At 90% photon efficiency, PCE is obtained as 7.16%.

Once all the photo generated excitons are separated into free electron hole pairs there is a high chance that these moving (freely) pairs may recombine together which is known as the non-geminate recombination of free carriers. To examine the effect of non-geminate recombination on the performance of the device we have varied the recombination coefficient (R) from 1×10^{-10} to $1 \times 10^{-25} \text{ m}^3/\text{s}$ and the obtained OSC parameters as represented in the Fig. 15 while the correspondingly obtained $J-V$ characteristics are shown in Fig. 16.

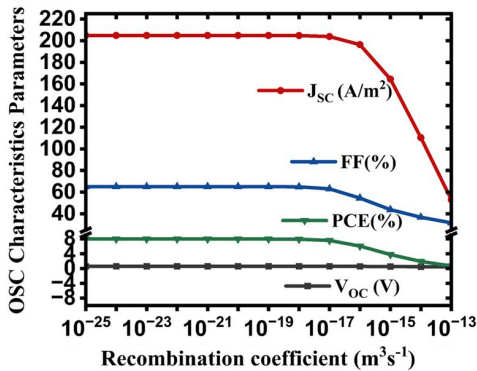


Fig. 15. Effect of non-geminate recombination on OSC parameters

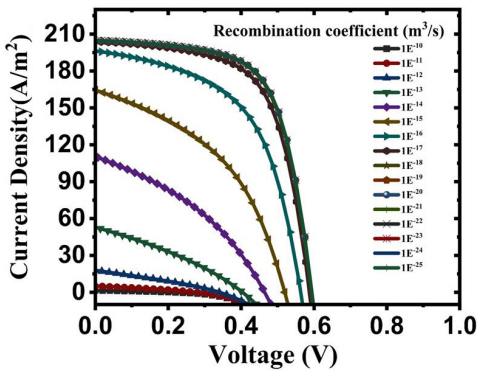


Fig. 16. Effect of non-geminate recombination on $J-V$ characteristics.

It has observed with the increase in R the OSC parameters remains unaffected up to $1 \times 10^{-20} \text{ m}^3/\text{s}$ of R . The further increase in R leads to more enhanced non-

geminate recombination, resulting the degradation in all the OSC parameters. The best value of PCE (7.93%) is achieved with the R values of $1 \times 10^{-20} \text{ m}^3/\text{s}$.

To examine the effect of temperature (T), it is varied from 250K to 400 K and the resulted parameters of the OSC are plotted in the Fig. 17. The results show that the parameters of OSC specially J_{sc} , FF and PCE are severely affected as the temperature increases. It can also be seen in the Fig. 17 the change in temperature from 250K to 400K decreases V_{oc} drastically from 0.59 to 0.44 Volts. The values of fill factor degrades from 62% to 59% and PCE declines and 7.93% to 5.23%. The increment in short circuit current density (J_{sc}), from 204.33 to 206.03 A/m^2 with the increase in temperature from 250K to 400K is mainly attributed to the enhanced thermally generated carrier concentration. Moreover above the 400K, all the OSC parameters severely degrades.

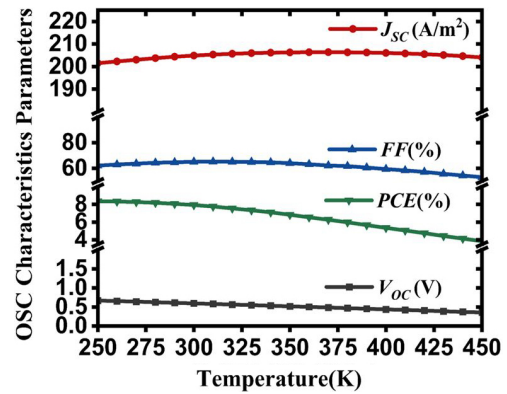


Fig. 17. Effect of temperature on OSC parameters

Since the increment rate of J_{sc} is minor than the degradation rate of V_{oc} and hence the PCE and the fill factor are reduced. The good performance of device is found to be at 300K as higher temperature leads to poor device performance. The optimum values of OSC parameters at the optimised values of the corresponding layer thicknesses are listed in the Table 2 at 300K.

Table 2. The OSC parameters obtained with the optimised layer thicknesses at 300K

Electrical parameter values at optimised thicknesses					
Layer	Thickness (nm)	V_{oc} (V)	J_{sc} (A/m^2)	FF (%)	PCE (%)
Active	170	0.591	187.104	64.85	7.28
HTL	5	0.591	188.76	65.88	7.35
ETL	50	0.593	200.91	65.27	7.78
Anode	5	0.594	118.75	65.19	7.91
Cathode	15	0.594	204.86	65.16	7.93

CONCLUSION

The organic solar cell with the active layer P3HT:PCBM has been analysed by a computer based program, i.e. OghmaNano. After closely monitoring the variation in OSC parameters as a function of each layer thicknesses the thicknesses of all the layers within the structure of the designed device is been optimised. The resulted optimised values of active layer, ETL, HTL, cathode and anode are found to be 170, 50, 5, 15, and 5 nm, respectively. The optimisation has resulted a maximum *PCE* of 7.93%. The device performance is also been analysed for the effect of recombination (i.e., geminate & non-geminate). The best *PCE* of the device is found at $1 \times 10^{-20} \text{ m}^3/\text{s}$ value of *R*. Moreover, the parameters of the OSC are studied at different values of the temperature. It is concluded that the *PCE* degrades with rise in temperature. The *PCE* of 7.93% is obtained at 300 K. The result obtained in our work is compared with the existing work in literature and listed in Table 3.

Table 3. The comparison of our work with results obtained in literature

Structure of Device	V_{oc} (V)	J_{sc} (A/m ²)	FF (%)	PCE (%)	Ref.
ITO/NiO/ P3HT:PCBM/ZnO/Al	0.59	204.8	65.16	7.93	This work
ITO/PEDOT:PSS/ P3HT:PCBM/Ca/Al	0.62	98.0	59.51	3.62	[19]
ITO/PEDOT:PSS/ P3HT:PCBM/TiO ₂ /Al	0.61	129.5	67.91	5.35	[6]
ITO/PEDOT:PSS/ P3HT:PCBM/Al	0.52	74.7	46.0	1.78	[21]
ITO/ZnO/P3HT: PCBM/MoO ₃ /Ag	0.60	131.9	65.0	5.23	[22]

ACKNOWLEDGMENT

The authors are highly thankful to the Prof. Mackenzie for giving us free access to the program (OghmaNano).

REFERENCES

- [1] Medford, A.J., Lilliedal, M.R., Jørgensen, M., Aarø, D., Pakalski, H., Fyenbo, J., & Krebs, F.C. (2010). Grid-connected polymer solar panels: Initial considerations of cost, lifetime, and practicality. *Optics Express*, 18(103), A272-A285.
- [2] Chen, L.X. (2019). Organic solar cells: Recent progress and challenges. *ACS Energy Letters*, 4(10), 2537-2539.
- [3] Chopra, K.L., Paulson, P.D., & Dutta, V. (2004). Thin-film solar cells: An overview. *Progress in Photovoltaics: Research and applications*, 12(2-3), 69-92.
- [4] Krebs, F.C., & Jørgensen, M. (2013). Polymer and organic solar cells viewed as thin film technologies: What it will take for them to become a success outside academia. *Solar energy materials and solar cells*, 119, 73-76.
- [5] Kaltenbrunner, M., White, M.S., Glowacki, E.D., Sekitani, T., Someya, T., Sariciftci, N.S., & Bauer, S. (2012). Ultrathin and lightweight organic solar cells with high flexibility. *Nature communications*, 3(1), 1-7.
- [6] Abdallaoui, M., Sengouga, N., Chala, A., Meftah, A.F., & Meftah, A.M. (2020). Comparative study of conventional and inverted P3HT: PCBM organic solar cell. *Optical Materials*, 105, 109916.
- [7] Berger, P.R., & Kim, M. (2018). Polymer solar cells: P3HT: PCBM and beyond. *Journal of Renewable and Sustainable Energy*, 10(1), 013508.
- [8] Zhang, X., Yang, W., Zhang, H., Xie, M., & Duan, X. (2021). PEDOT:PSS: From conductive polymers to sensors. *Nanotechnology and Precision Engineering*, 4(4), 045004.
- [9] Tseng, Y.T., Lin, Y.C., Shih, C.C., Hsieh, H.C., Lee, W.Y., Chiu, Y.C., & Chen, W.C. (2020). Morphology and properties of PEDOT: PSS/soft polymer blends through hydrogen bonding interaction and their pressure sensor application. *Journal of Materials Chemistry C*, 8(18), 6013-6024.
- [10] Yang, T., Wang, M., Cao, Y., Huang, F., Huang, L., Peng, J., & Cao, Y. (2012). Polymer solar cells with a low-temperature-annealed sol-gel-derived MoO_x film as a hole extraction layer. *Advanced Energy Materials*, 2(5), 523-527.
- [11] Tan, Z. A., Li, L., Cui, C., Ding, Y., Xu, Q., Li, S., ... & Li, Y. (2012). Solution-processed tungsten oxide as an effective anode buffer layer for high-performance polymer solar cells. *The Journal of Physical Chemistry C*, 116(35), 18626-18632.
- [12] Tiwari, D.C., Dwivedi, S.K., Dipak, P., Chandel, T., & Sharma, R. (2017, May). Sol-gel derived ZnO as an electron transport layer (ETL) for inverted organic solar cells. In *AIP Conference Proceedings* (Vol. 1832, No. 1, p. 060024). AIP Publishing LLC.
- [13] Irwin, M. D., Buchholz, D. B., Hains, A. W., Chang, R. P., & Marks, T. J. (2008). p-Type semiconducting nickel oxide as an efficiency-enhancing anode interfacial layer in polymer bulk-heterojunction solar cells. *Proceedings of the National Academy of Sciences*, 105(8), 2783-2787.
- [14] Mahmud, M.A., Elumalai, N.K., Upama, M. B., Wang, D., Chan, K.H., Wright, M., ... & Uddin, A. (2017). Low temperature processed ZnO thin film as electron

- transport layer for efficient perovskite solar cells. *Solar Energy Materials and Solar Cells*, 159, 251-264.
- [15] Sun, N., Fang, G., Qin, P., Zheng, Q., Wang, M., Fan, X., ... & Ye, J. (2010). Efficient flexible organic solar cells with room temperature sputtered and highly conductive NiO as hole-transporting layer. *Journal of Physics D: Applied Physics*, 43(44), 445101.
- [16] Kumar, D., Singh, M.K., & Mehata, M.S. (2022). Exploration of grown cobalt-doped zinc oxide nanoparticles and photodegradation of industrial dye. *Materials Research Bulletin*, 150, 111795.
- [17] MacKenzie, R.C. (2022). GpvdM user manual v7. 88.
- [18] MacKenzie, R.C., Shuttle, C.G., Chabinye, M.L., & Nelson, J. (2012). Extracting microscopic device parameters from transient photocurrent measurements of P3HT: PCBM solar cells. *Advanced Energy Materials*, 2(6), 662-669.
- [19] Brioua, F., Remram, M., Nechache, R., & Bourouina, H. (2017). Electrical and optical modeling of poly (3-hexylthiophene):[6, 6]-phenyl-C61 butyric acid methyl ester P3HT-PCBM bulk heterojunction solar cells. *Applied Physics A*, 123, 1-10.
- [20] Korte, D., Pavlica, E., Klančar, D., Bratina, G., Pawlak, M., Gondek, E., & Derkowska-Zielinska, B. (2023). Influence of P3HT: PCBM Ratio on Thermal and Transport Properties of Bulk Heterojunction Solar Cells. *Materials*, 16(2), 617.
- [21] Husen, M.J., Aga, F.G., & Dibaba, S.T. (2023). Theoretical Performance Analysis of Inverted P3HT: PCBM Based Bulk Hetero-Junction Organic Solar Cells through Simulation. *Advances in Materials Science and Engineering*, 2023.



A Learning based Model for Wheat Disease Detection and Classification

Rakesh Garg¹, Neetu Singla², Charu³, Sachin Lalar⁴ & Shubham Goel⁵

ABSTRACT

Wheat is an important staple crop for large sections of the population for many cultures across the globe. It is vital that one of the major impediments to its cultivation, namely disease, be prevented and controlled appropriately. A possible strategy for controlling yield loss due to disease is early identification to prevent their spread and minimize losses. An automated method must be developed to identify disease and that can be done through the implementation of computer vision. Such a tool can be used in drones on a larger scale or possibly smart phones on a smaller scale to identify diseases in wheat. A computationally efficient model for early detection of wheat crop diseases using a pre-trained convolutional neural network is developed in this research and is compared with models as VGG16, MobileNet, and ResNet50, demonstrating superior performance in terms of computational cost and accuracy, precision, recall, and F1-score.

Keywords: Wheat Disease Detection, Deep Learning, Image Classification, Convolutional Neural Networks

INTRODUCTION

Wheat is one of the most popular cereal grains consumed worldwide. Experts estimate its cultivation began around 10,000 years ago in southeast Turkey. The most popular variety of wheat is bread wheat, sometimes known as common wheat. Compared to other food crops, it is cultivated on the most acreage. (220.4 million hectares, 2014). More wheat is traded globally than all other crops combined. With global productions of 764 million tons of wheat in 2019, and 772 million tons are anticipated to be produced in 2020. It is a good source of carbohydrates, as well as several vitamins and minerals. Particularly whole wheat provides a lot of advantages for our health. Different types of wheat are commonly used in everyday food products. For example, Club wheat (*T. compactum*) is a softer variety used in making cakes, crackers, cookies, pastries, and flours. Durum wheat (*T. durum*) is primarily used for producing pasta varieties such as spaghetti and macaroni, while common wheat (*Triticum aestivum*) is typically used in bread-making. Diseases account about 20% of the annual loss of wheat.

50 of the 200 wheat illnesses generate monetary losses and are widespread. The proposed approach achieved impressive results, with a recognition rate of up to 91%, by utilizing an ANN classifier for classification and a Gabor filter for feature extraction. The ANN classifier combines various features, including textures, colors, and patterns, to effectively categorize and identify different plant diseases. Around the world, fungus-related wheat illnesses result in production losses of roughly 20% and have diverse effects on grain quality. New pathogen races emerge often, well-known illnesses impact new hosts, and newly developing diseases pose a danger to wheat production. A large range of fungal pathogenic diseases pose the greatest danger to wheat because they cause significant crop loss. Rusts, smuts, Fusarium head blight, Septoria leaf blotch, tan spot, and powdery mildew is among the pests that cause the most damage. It is predicted that grain yields must increase by at least 70% by 2050 to fulfil the demands of a worldwide population rising at the current rates, given the pre-existing global hunger issue. It is not feasible to limitlessly expand land under

¹ Computer Science & Engineering Gurugram University, Gurugram. E-mail: drrakeshgarg@gurugramuniversity.ac.in

² Computer Science & Engineering Gurugram University, Gurugram. E-mail: neetusingla@gurugramuniversity.ac.in

³ Computer Science & Engineering Gurugram University, Gurugram. E-mail: drcharu@gurugramuniversity.ac.in

⁴ Computer Science & Engineering Gurugram University, Gurugram. E-mail: sachinlalar@gurugramuniversity.ac.in

⁵ Computer Science & Engineering Gurugram University, Gurugram. E-mail: shubhamgoel@gurugramuniversity.ac.in

architecture because the amount of land that can be used for agriculture is intrinsically limited—whether by fertility, water availability, or owing to the inherent restrictions on land. Therefore, we need to figure out how to increase yields in the current agricultural area. The prevalence of disease in crops is a significant barrier to achieving this goal. According to studies, worldwide grain production losses from diseased crops range between 18% and 21.5%, and in individual wheat hotspots, they range between 10.1% and 28.1%. Given the serious effects of wheat diseases and the importance of wheat as a commodity in the world's food markets, it is crucial that they are identified early and treated.

Disease detection in particular plants presents a problem because it is difficult and expensive to collect large, labelled datasets for them due to a variety of factors, including local weather conditions and challenges in locating experts in the field to identify the diseased plants for which the dataset can be collected. Large datasets for these challenges are therefore difficult to construct or, in certain situations, just not practical. Consequently, in these situations, the datasets are somewhat small (less than 5000 images). When training deep CNN models from scratch, smaller datasets need more time and resources, such as computing hardware (GPUs, CPUs, and RAM), because these models must be trained with a relatively high number of parameters, which increases their computational complexity. Additionally, used smaller datasets mean fewer samples for the model, which can result in overfitting the model. In other words, the model will perform well on training data, but will have limitations with testing and new data because there isn't enough observed variance in the data for the model to be able to generalise the data effectively to use with new data points. Transfer learning, where we leverage models pretrained on a separate, large dataset, can be used to solve deep learning problems with small datasets. Instead of utilising random weights while training the model on the real dataset, the weights learned through pretraining might be employed. By using pretrained weights to reduce the number of parameters to be trained, by “fixing” some of the initial layers, i.e., using their parameters as-is, and only training the final few, the model can apply the knowledge gained from pretraining dataset without

having to start from scratch. As a result of the decreased number of parameters that must be learned the training time and computational needs of the model are both greatly reduced. Furthermore, the model only has to be significantly modified to the specific situation because it already has enough data to make generalisations from the pretraining data. Transfer learning therefore offers a practical, affordable way to train a deep learning model for issues where data is either unavailable or difficult to gather. Disease detection technologies based on mobile applications is a viable use case for disease detection in wheat to improve grain yields. Given that over 90% of people worldwide own a mobile phone, farmers have the opportunity to utilise a smartphone app to identify illnesses in their crops and request assistance as needed. Without specialised assistance, we must rely on visual disease diagnosis in wheat. Since the most common illnesses in wheat tend to be fungal infections that emerge in the leaves, this may be accomplished by categorising photographs of wheat leaves. Convolutional neural networks (CNNs) are one of the most crucial techniques for classifying issues in pictures [1]. In order to solve the problem of disease detection and classification in wheat, a CNN architecture has been proposed in this paper, which draws inspiration from the already existing models and optimises the same in terms of the computational requirements, further leading to the reduction in time taken to evaluate the given input, offering viable real- world application of the model on less powerful machines like more affordable smartphones.

The rest of this paper is organised as follows. Section II reviews the existing literature on illness detection approaches such as convolutional neural networks. Section III describes the architecture of the proposed model, highlighting its different elements. Section IV present the stepwise implementation of proposed model for wheat disease detection, performance evaluation of proposed model followed by comparison with state of art models. Section V provides the major findings of this research followed by the conclusion and future scope in the last section.

LITERATURE REVIEW

There exists a history of literature solving disease classification problems in plants, including maize, potatoes, rice, and wheat among others [2]. Many

authors have proposed solutions to this problem in the form of various architectures. Most of these employ CNNs to perform image classification, with some using self-created CNN architectures and some adapting popular architectures for solving the same [3]. In [4], the authors assessed the performance of support vector machines (SVM), backpropagation neural networks, and generalized regression neural networks, comparing them with traditional multiple regression methods. The study found that an SVM-based regression approach provided a more effective representation of the relationship between environmental factors and disease severity, offering potential benefits for disease management. Further, image processing techniques [5] have been employed for the automated classification of plant diseases through the analysis of leaf images. The study employs the SVM classifier to differentiate between healthy and diseased soybean leaves. To assess the system's performance, a dataset consisting of 120 images, captured from multiple farms using different mobile cameras, was used. The SIFT algorithm enables precise identification of plant species by analyzing leaf shapes. With an average accuracy of 93.79%, the SVM classifier effectively distinguishes between healthy and sick soybean leaves. Researchers in [6] used deep learning technologies to identify diseases in various plants. One of the key processes in their methodology was the in-depth image processing, including histogram equalization, noise filtering, and decolorization, and various image segmentation techniques. By separating the image into different parts and studying each section separately, image segmentation helps to make image identification and analysis simpler. All parts share the same qualities in terms of color, texture, and intensity. The segmentation is a region-based technique to differentiate the unhealthy and healthy parts of the leaves on the bases of color. This approach performed well with multiple plants and crops, highlighting the importance of in-depth image processing techniques. The HOG approach for feature extraction has been applied [7], where, a histogram of gradient orientation representation over the pictures is computed using the HOG, which is utilised to partition the image into distinct portions. By counting the incidence of the gradient orientation, it collects features. HOG is required in many sectors of object identification, including as face recognition and in our study, for plant leaf recognition. Application of Artificial Neural

Network technology and a variety of image processing techniques is done to provide a methodology for early and precise plant disease identification [8]. The suggested method produced superior results with a recognition rate of up to 91% since it is based on an ANN classifier for classification and a Gabor filter for feature extraction. An ANN-based classifier employs a mix of textures, colors, and characteristics to categories various plant diseases and identify them. Authors in [9] used AlexNet architecture to classify wheat disease, with accuracy of 84.54%. They employed the AlexNet architecture to train their model but owing to a smaller dataset chose to pretrain the model on other data to initialize weights. All the photos in the dataset were downsized to ' 227×227 ' in accordance with the requirements of the AlexNet architecture. By using ReLu and MaxPooling, features were retrieved from the convolutional layers of the CNN model. Using powerful machines, the authors trained the deep architectures on a sizable dataset like ImageNet in the pre training phase. It was inferred from the paper that the smaller dataset would lead to overfitting problem. Hence the concept of using a model which has already been trained on a larger dataset was developed so that the model generalizes better. Alternative method is to train only the final classification layer while freezing the weights of the first layer. Further a method for classifying and diagnosing four common diseases affecting apple leaves has been proposed in the study put out by [10], which in comparison to a typical AlexNet model, the architecture achieved an overall accuracy of 97.62% with significantly fewer parameters. It has been observed that advancements in CNN performance are primarily driven by the development of new blocks and structural redesigns [11].

A variation of LeNet architecture [12]. has an additional block of convolutional, activation, and pooling layers. In this architecture, three such blocks are used, followed by completely connected layers and softmax activation. While fully connected layers are used for classification, convolutional and pooling layers were utilised to extract features. The max-pooling layer was used to speed up training and reduce the model's sensitivity to small changes in input by reducing the size of the feature maps. Each of the blocks employed the ReLU activation layer to introduce nonlinearity. In order to prevent overfitting, the train set, the Dropout

regularisation algorithm had also been applied with a probability of 0.4. Dropout regularisation reduces model variance and streamlines the network, which helped minimise overfitting by randomly removing neurons from the network after each iteration of training. LeNet was put forward as an explainable model that could reliably, promptly, and precisely identify and measure leaf tension [13], which further aimed at developing a 95.04% accurate real-time detection system for mobile platforms in order to quickly and broadly observe crips in actual production conditions. A CNN architecture known as the supervised 3D-CNN based model was introduced [14] to learn the spectral and spatial information of hyperspectral images for the categorization of healthy and samples that have been exposed to charcoal rot. The hyperspectral wavelengths that significantly improve classification accuracy were found using a saliency map-based visualization technique. The model's categorization accuracy was 95.73%. Authors in [15] illustrated the extraction and categorization of groundnut leaf disease using color imagery. With the help of a neural network, the color imaginary transform, color co- occurrence matrix, and feature extraction were carried out. With a complicated backdrop, back propagation proved to be effective in groundnut leaf detection, and was successfully able to diagnose the illnesses.

A CNN, that made use of data-augmentation, transfer learning, and MBGD as an optimizer, has been used [16] to obtain an overall testing accuracy of 97.61% with a loss value of 0.35. Loss functions were applied to assess the model's performance. Categorical Cross-Entropy is one such loss function used in this study for multi-class categorization. It contrasts the projections' distribution with the labels' actual distribution. For all other classes, the likelihood is maintained at 0, but the probability of the correct class is maintained at 1. Research presented in [17] employed a 5-layer self-designed convolutional network, along with a regression layer to identify diseased leaves. They explained that the neural network is composed of various layers, including the input layer, convolutional layer, output layer, and fully connected layer. They noted that more layers can be added using the convolutional layer. The first step is to load the input data, followed by creating the convolution layer. It is mentioned that every layer has an activation function.

They discuss the combination of a pooling function with a convolutional neural network. In this particular case, they have constructed five convolutional layers and added matching pooling. They have taken the last fully linked layer and applied a softmax activation function at the end of each layer. In order to receive the result and employ the optimizer, the regression layer is used at the end. A self-designed 6-layer-deep convolutional neural network architecture is used to identify leaf disorders in multiple plants [18], building upon it with addition of other standard algorithms, such as the ADAM optimizer and the softmax classifier. The ReLu activation function, the picture input shape of '256, 256, 3', the filter size of '64', the kernel size of '88', the Padding, and the strides of '11' were all included in the first convolutional layer. The second convolutional layer exhibited the same form as the first layer and added some more features. The image size and the kernel size were reduced in the subsequent layers. They employed the ReLu activation function and max pooling layers with the ADAM optimizer, using an additional softmax layer to classify the healthy and diseased leaves, achieving an accuracy of 96.28% on testing dataset. The use of image expansion techniques like alteration of image shapes and angles have led to higher accuracy when dealing with redundant data. HOREsNet [19], a different ResNet-based architecture that aims for a robust recognition of plant diseases was proposed. With photos captured in actual agricultural situations, the study investigates the issue of low precision in the diagnosis and classification of plant diseases. By experimenting with photographs of various sizes, shooting angles, positions, backgrounds, and lighting, it strengthens the ability to resist influence. The outcomes showed that the method was accurate in detecting diseases between 90.14% and 91.79%. A CNN-based approach of identifying anthracnose lesions by employing data augmentation methods using Cycle-Consistent Adversarial Network (CycleGAN) [20], used a DenseNet to enhance the low-resolution resource layers of the YOLO-V3 model, resulting in accuracy of 95.57%. A novel deep convolutional neural network (DCNN)-based method for the identification of yellow rust crop disease [21], utilises extremely high spatial resolution hyperspectral pictures taken with UAVs. The suggested model included a number of Inception-ResNet layers for feature extraction and was tuned to determine the network's ideal depth and

breadth. The idea uses three-dimensional data and can identify yellow rust in wheat with an accuracy of 85% by using spatial and spectral data. OR-AC-GAN is a technique discussed in [22], that was created for the early identification of the tomato spotted wilt virus utilizing hyperspectral images and an auxiliary external removal classifier using opposed generation networks. Plant segmentation, spectrum classification, and picture classification are all included in the concept. The findings indicated that the accuracy reached 96.25% before the onset of apparent symptoms. The deep study of the available literature points towards some common limitations of the existing methods for wheat disease detection as given below.

- Computational Complexity, the hardware needs required to run these models are significant, limiting total model utilisation and even additional model advancements such as detection of new illnesses or diseases in other crops.
- Training time, or the time required to learn from the database and adjust its internal parameters for making future predictions is high and will continue to rise proportionally with the size of the dataset, making it difficult to update the underlying database on a regular basis to improve the results.
- Inconsistent findings across many performance criteria; aside from accuracy, other performance metrics were inconsistent in all circumstances.

MATERIALS AND METHODS

A deep learning-based framework for wheat disease detection and classification is developed using the convolutional neural network as shown in Fig. 1. The description of all the components of the developed model is provided below.

Convolutional Neural Network

Convolutional Neural Networks have made significant advancements over the past decade in fields pertaining to pattern recognition such as voice recognition and image processing. One of major reasons behind the desirability of Convolutional Neural Networks over Artificial Neural Networks is the reduction in the parameter count [23], thus making it a viable solution for researchers to build bigger models to solve much complex problems that could not be addressed by regular ANNs. One of the most crucial assumption of

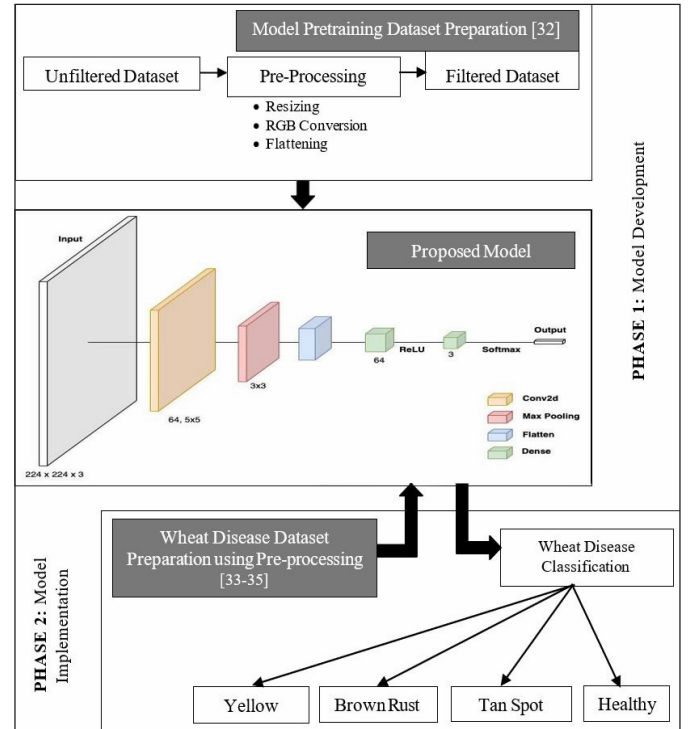


Fig. 1. Architecture diagram of proposed model for wheat disease detection and classification

problems that CNN solves is that they involve spatially independent features, in the case of a leaf detection tool, the primary focus is discovering the leaf in an image regardless of its positioning in that image. Another important aspect of CNN is its ability to extract abstract features while input propagates to deeper levels, in the example of an image detection tool, the first layer could extract the boundary or edges of the image, followed by the second layer extracting simpler forms and finally the higher-level features such as the object such as the leaf being extracted in the subsequent layers [24]. Due to the reduction in the parameter count and the ability to extract features while input propagation, as compared to other algorithms for pattern-based classifications, CNNs require substantially lower pre-processing [25]. CNN have the ability to automatically and adaptively learn filters through the process of back-propagation supported by convolution, pooling and a fully-connected layer in order to extract the relevant features for the classification, taking away from manually preparing these filters in the traditional approaches. This ability enables the network to better understand the complexity of the image, by providing a better fit for the image dataset by reduction in the number of parameters to be examined as well as the ability to reuse the weights.

Layers

- **Pooling:** Pooling is a significant step in any convolution- based networks, it helps in compressing the feature maps extracted in the previous layer. It preserves important information and removes unnecessary information by combining a group of values into a smaller group of values, thus turning the joint feature representation into valuable information. This further enables the model to be trained properly only on the dominating features that are spatially invariant, i.e. not affected by the position or the rotation of the object being classified. Pooling is further divided into two classes: max pooling and average pooling. Max pooling yields the greatest/ largest value from the region covered by the Kernel on the image. Whereas, average pooling yields the average of all the values from the region covered by the Kernel on the image. Our model makes use of the Max Pooling class, it not only derives the highest values from the region but also helps in de-noising as well as completely ignoring the defective activations. Average pooling, on the other hand, only compresses the feature map as a noise suppression technique. Thus, max pooling out performs average pooling and makes it more fit for application with our proposed model.
- **Flatten and Dense (Fully Connected Layer):** Fully connected layer is (usually) an easier and cost-efficient way of learning non-linear combinations of high-level characteristics observed from the result of the convolutional layer, enabling the fully-connected layer to learn a function that may or may not be linear in that area [26]. The initial convolutional layer in a neural network has to know the dimension of the picture that is provided to it as input. The output of the picture will be provided to the dense layer after it has been processed through all convolutional layers and pooling layers. Because the convolutional layer's output is multidimensional and the dense layer's input is single- dimensional, or a 1-D array, we cannot pass the convolutional layer's output directly to the dense layer. As a result, between the convolutional and dense layers, we will utilise the Flatten() technique. A multidimensional matrix is reduced to a single dimension via the flatten() technique. In

neural networks where data is processed in a single direction, the input received is flattened and back propagation is used in each of the training cycle. The model with the help of classification methods such as softmax is able to characterise images across a number of epochs by identifying dominating and specific low-level features. A dense layer is deeply connected with its preceding layers, where each of the neuron in the dense layer receives input from all of the neurons of the previous layer. The results from the convolutional layer serve as a base upon which the dense layer is applied to categorize the images [27].

Activation Function

The neurons calculate a weighted average of their input in each of the layers of the neural network, the output of the same being processed through a non-linear function called the “activation function” serves as the neuron's output. This procedure is applied throughout the neurons present in all the levels of the neural network. The convolution neural network's activation function is a crucial component. A nonlinear activation function is typically used to map the calculated features in the three phases of a convolution neural network, convolution, sub-sampling, and full-connection, in order to overcome the problem of inadequate expressiveness produced by linear operation [27].

- **ReLU:** The Rectified Linear Activation Unit, has become the norm for a variety of neural networks because of its ease to train and the frequent performance enhancements. Depending upon the input, if the input is positive the ReLU returns the input as it is for the output but if the input is negative, the ReLU returns 0 in place of the original input, thus resulting in reduction in the overall computation going forward. The Rectified Linear Activation Function provides a solution for converting a non-linear function to behave like a linear function which is a mandatory requirement for training a deep neural network using stochastic gradient descent with back propagation of mistakes. A ReLU, is a component that performs the REL function or the change in behaviour of a non-linear function to a linear function. Further, rectified networks make use of rectifier function in the hidden layers. Due to the fragility of ReLU

activation neurons, some input during training may fall into the hard saturation area, leading to permanent neuronal death, preventing the updating of the appropriate weight. Additionally, the Relu function generates the output with migration phenomena by setting a portion of the neuron's output to zero. Such obnoxious forced sparse processing may hide numerous beneficial characteristics, having a negative impact on the effectiveness of model learning. Excessive sparsity may cause increased error rates and lower the model's useful capacity. The convergence of the network may be impacted by both the migration phenomena and neuronal death.

- **Softmax:** The Softmax Function, a generalisation of the Logistic Function, guarantees that our forecast adds up to 1. The Softmax function usually serves as the activation function at final layer in a neural network to normalize the output of a network to a probability distribution over predicted output class. The Softmax function and the cross-entropy function are closely related, on application of the Softmax function, the cross-entropy function is acts as the loss function in the network to validate the model's correctness as well as to improve the functioning of the network. The cross entropy helps overcome issues such as the output value being much smaller than the true value at the start of the back propagation, by slowing the gradient descent. The Softmax function reduces the vector of K real values into a vector of K real values that sum up to 1 by converting all of the varying values in the vector to be between 0 and 1, thus enabling it to be interpreted in terms of probability. It translated little or negative values into smaller probability and on the other hand, the larger or positive values into probabilities, but always summing up to '1'.

WHEAT DISEASE DETECTION AND CLASSIFICATION

This section presents the stepwise procedure of wheat disease detection and classification using the developed model described in earlier section-2. The stepwise implementation procedure for the developed model is given in algorithm-1.

Algorithm-1: Developed model for wheat disease Detection and Classification

- To begin, the actual and pretraining datasets are compiled. In order to prepare the images for learning, they are pre-processed by resizing, rescaling, and formatting the color space. The images are then flattened into vectors for processing.
- Next, the compiled pretraining dataset is run through the model. This helps initialize the weights to more relevant values for training, rather than relying on random initialization of weights.
- Then, the actual dataset is split into training and testing sets using random selection.
- Next, the training dataset is run through the pretrained model. This step calibrates the preinitialized weights to the actual dataset for prediction on unseen data, resulting in the final, fully trained prediction model.
- To evaluate the model, the testing dataset is run through the final model and assess it using various selected metrics.

Dataset Description









For the pre-training dataset, the data was compiled from the freely available [28]. A neural network is pre-trained by first applying the model to a single task or dataset. Afterwards, the model is trained on a different task or dataset using the parameters or model from previous training. By doing this, the model gains an advantage over beginning from scratch. This dataset contains approximately 87K RGB images of healthy and diseased leaves and which is divided into 38 classes that include crops of apple, bell pepper, cherry, corn, grapes, orange, peach, blueberry, potato, raspberry, soyabean, strawberry, and tomato, some of which are shown in Table 1 along with their distribution. For the actual training dataset information was gathered from a number of publicly accessible databases [29]. Images of the affected plants were gathered from various databases for the three diseases that account for the majority of the yield loss in wheat: Tan Spot, Leaf Rust, and Stripe Rust.

- *P. striiformis* Westend. F. sp. *tritici* (Pst), a pathogen found in temperate areas with chilly and damp conditions, is the root cause of wheat stripe (yellow) rust [30]. Found mostly on the leaves, but also on the stem and leaf sheaths. Pst affects over 88% of the wheat types in the globe, causing roughly US\$ 1 billion in losses annually.

- Leaf rust, the most common and widespread of the wheat rust diseases, is caused by (*Puccinia triticina* Eriks [31-33]. Although the timing and location of grain losses brought on by leaf rust vary, the disease has a considerable economic impact [34-35]. More than US\$ 350 million in damages are thought to have been incurred by Pt in the US between 2000 and 2004. Leaf rust is a difficult disease to cure due to the pathogen's great diversity, the regular appearance of novel virulence profiles, and the pathogen's strong tolerance to a wide range of temperatures.
- Tan spot, also known as yellow spot or yellow leaf blotch, is a foliar spotted disease caused by *Pyrenophora tritici-repentis* that affects all major wheat-growing regions worldwide [35]. Average yield losses are 50%, although yield losses of up to 50% have been observed in disease-prone regions [36].

To prevent innate biases from showing up in the data, the distribution of the photographs was balanced as shown in Table 1, and they were carefully chosen for their quality and suitability for our intended use.

Table 2. Sample images (each class)

Class Name	Images	Sample Source Image	
Yellow Rust	924		
Brown Rust	902		
Tan Spot	910		
Healthy	1116		

Pre-processing

Real-world datasets are rarely in a usable state as-is, thus some operations need to be performed on the data to optimise it for machine learning. For image data, this can include operations like rescaling, resizing etc. as well as noise reduction, enhancement, normalisation to improve image quality for further processing. CNNs are designed to automatically learn and extract important information from raw image data, which reduces the need for feature engineering, however based on input images, pre-processing may

be required to standardise input, reduce noise and format the images. For pre-processing the compiled dataset, which was assembled from several sources and had various dimensions, we had to resize and rescale images into a standard 224x224x3 format. To make them easier to utilise with the models, these were then compiled into a.csv file in the form of flattened vectors. Further for the purpose of comparison, for each of the existing model, to adapt the images to the models, the pre-processing functions offered by the Keras API was implemented, which include some fundamental pre-processing functionality. For example, in the cases of VGG16 and ResNet50, images were converted from RGB to BGR format, which is the format in which the model was pretrained and thus the pre-trained weights were stored.

Performance Metrics

The following set of classification metrics were used to compare the various aspects of each of our selected models and analyse them based on them because none of the metrics available for assessing the effectiveness of machine learning and deep learning models alone offers a complete picture of the performance of the model.

1. **Accuracy:** A measure of how well the model's predicted values match the actual values. This being a categorization issue, the accuracy is easily determined as:

$$\text{Accuracy} = \frac{\text{\#Data Points Classified Correctly}}{\text{\#Total Data Points}} \quad \dots(1)$$

2. **Precision:** Precision measures the proportion of affirmative identifications that are in fact accurate. In other words, for a specific class:

$$\text{Precision} = \frac{\text{\# No. of True Positives}}{\text{\#True Positives} + \text{\#False Positives}} \quad \dots(2)$$

3. **Recall:** Recall aims to quantify the percentage of true positives for a given class that are properly classified. Mathematically,

$$\text{Recall} = \frac{\text{\# No. of True Positives}}{\text{\#True Positives} + \text{\#False Negatives}} \quad \dots(3)$$

4. **F1-Score:** As stated, precision and recall are counteractive measures to each other. However, they are both important to the model. They are counter to each other, in that attempting to increase precision tends to decrease recall and vice versa. To

solve this problem, the F1-score may be used [37]. The F1-score is the harmonic mean of precision and recall, and a high F1-score is a singular measure that can help us identify a model's performance, as a high F1-score means both precision and recall are significant, while a low F1-score means either or both of them are very low, which is undesirable.

$$\text{F1-Score} = \frac{2 * \text{Precision} * \text{Recall}}{\text{Precision} + \text{Recall}} \quad \dots(4)$$

5. **Number of Parameters:** The number of parameters the model must learn before it may be used to forecast data points that have not yet been observed. The number of parameters directly affects the computational efficiency of the model since the more parameters there are, the longer it will take to train the model and the longer each prediction will take to make when using it on data that has not yet been seen [38].

Training metric graphs are an essential tool for evaluating the performance of a Convolutional Neural Network (CNN) during training. These graphs typically show the improvement of accuracy and reduction of loss over training epochs, respectively. The accuracy metric measures the percentage of correctly classified examples during training. It is a measure of how well the model is able to classify input data correctly. The loss metric, on the other hand, measures the difference between the predicted output of the model and the actual output. It is a measure of how well the model is able to fit the training data. Overall, the training metric graphs are a valuable tool for evaluating the performance of a model during training and can provide insights into both the learning capability and optimization process of the model. The training metric graphs for the proposed model are presented in Fig. 2, which illustrate the evolution of accuracy and loss over the training epochs. The graphs indicate that the model achieves a high accuracy score and low loss within a few epochs of training, demonstrating that the model quickly learns to classify the input data with high accuracy and minimal error. This observation suggests that the proposed model has a strong capability to learn and generalize from the training data, which is a desirable property for any machine learning model. However, it is important to note that the performance of the model on the training data may not always reflect its performance on unseen data, and further

evaluation on a separate test set is necessary to confirm the generalization ability of the model, which are discussed earlier.

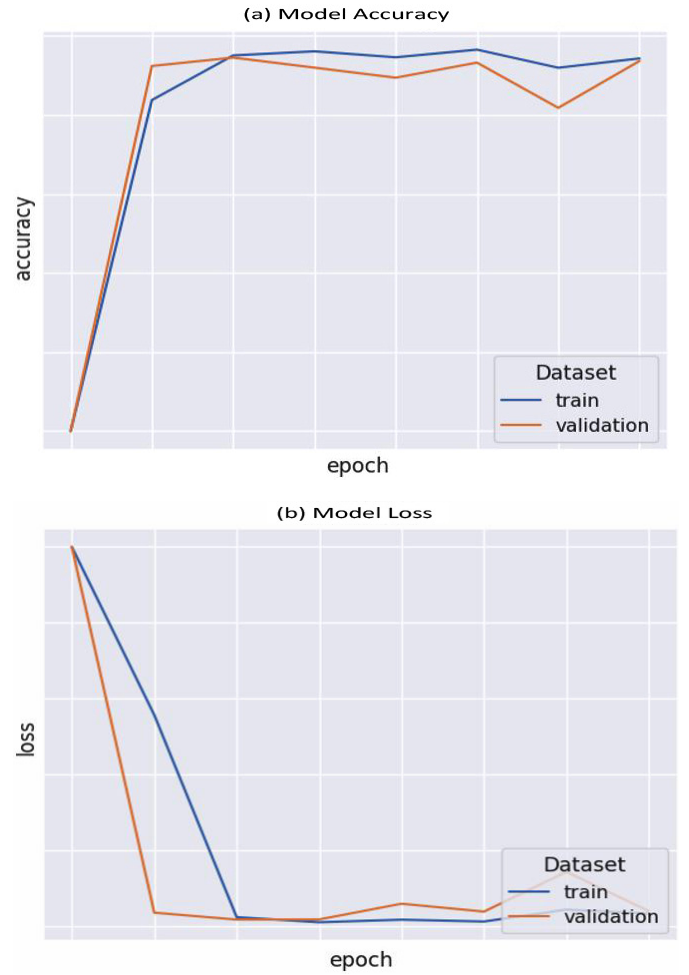


Fig. 2. (a) Model Accuracy, and (b) Model Loss

Performance Evaluation of Proposed Model

In this research, the dataset described earlier in this section, was split in the ratio of (70:30), where 70%

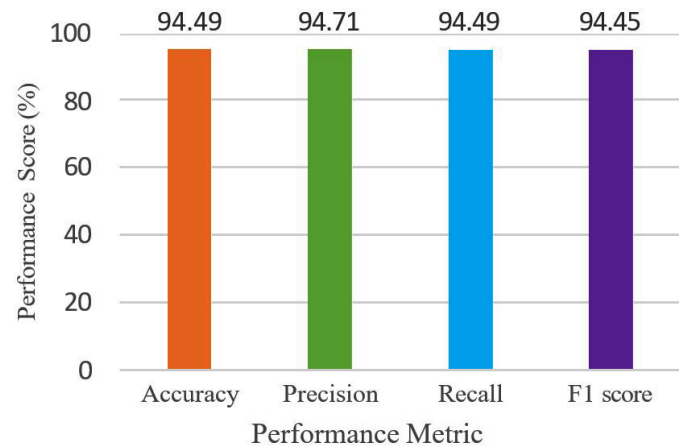


Fig. 3. Performance Statistics of Developed Model

data was used to train the developed model and 30% was used for model testing. The performance of the developed model for wheat disease detection and classification is measured on four performance metrics as shown in Fig. 3.

Comparison with State-of-Art Models

The developed model for wheat disease detection and classification is also compared with three pre-trained models as VGG16, MobileNet and ResNet50 in order to gauge its effectiveness and performance. The description about these three existing models is briefed below.

1. **VGG16:** The VGG16 model [39], along with the VGG19, was created for the 2014 ImageNet Challenge, where they won numerous problems. It is a popular deep learning architecture for image classification datasets. It includes 16 layers, including a fully connected layer for classification and a convolutional layer stack of 13 levels for feature extraction. It has 1000 output classes and a $224 \times 224 \times 3$ picture input layer. The same input structure is used for our purposes, the fully connected layers were modified to output four classes—one for the healthy class label and three for each of the diseases in the dataset.
2. **MobileNet:** A lightweight, mobile CNN architecture called MobileNet was created with the goal of balancing latency and accuracy while outperforming existing state-of-the-art architectures with fewer training parameters. It offers two hyperparameters that enable a user to change the trade-off between latency and accuracy based on the limitations of the situation [40]. It includes 1000 output classes and a $224 \times 224 \times 3$ picture input layer, similar to VGG16. As a result,

the MobileNet architecture was altered to suit our needs.

3. **ResNet50:** By reformatting layers as residual learning functions that act with relation to the input layers rather than unreferenced functions, ResNets, also known as Residual Networks, attempt to simplify the difficulty of training deeper neural networks [40] compared to less complicated non-residual designs, residual networks can reach depths that are many times greater. The architects triumphed in the ILSVRC and COCO classification competitions, among others. ResNet50 is a residual network with 50 layers, according to its specifications. Even among the deeper Residual Networks, while being one of the least deep, it performs on par with cutting-edge designs. To assess its performance, a customized the ResNet50 architecture, a 50-layer deep residual network design, was used for the problem at hand.

The last fully connected layer of each model had a SoftMax implementation with 1000 classes since it was pretrained on the ImageNet dataset, which has 1000 classes; we reduced this to 4 classes by altering the fully connected layers suitably. Furthermore, we freeze all levels of the model except from the completely linked layers in order to incorporate the idea of transfer learning as previously mentioned (see section 1 and Fig. 1). This resulted in a large decrease in trainable parameters and, consequently, computational complexity since only the parameters in the fully connected layer were trained and the convolutional layer's parameters were utilized as-it-is for training. Using approved techniques that guarantee data balance, the dataset was randomly divided into training and testing sets for the purpose of proper training and testing. 70% and 30%, respectively, of the

Table 3. Performance comparative statistics with state-of-art models

	<i>VGG16</i>	<i>MobileNet</i>	<i>ResNet50</i>	<i>Developed Model</i>
Layers	16	28	50	6
Parameters	1,51,17,667	64,40,387	3,00,10,499	5,04,71,939
Accuracy	0.9381	0.9434	0.8749	0.9449
Precision	0.9418	0.9456	0.9022	0.9471
Recall	0.9381	0.9487	0.8749	0.9449
F1-Score	0.9372	0.9472	0.8748	0.9445
Average training time	100	30	60	5
Average time taken per image	560	50	206	38

entire dataset were made up of the training and testing datasets, which offered enough pictures for training as well as a sizeable quantity of testing data to produce insightful testing findings. Using the training data and batches of 32 photos at a time, the training was carried out across 10 epochs for each model. With the Adaptive Moment Estimator (ADAM) optimizer and Sparse Categorical Cross-Entropy as the loss function, the pretrained models used were made accessible via the Keras API. The model was then evaluated over the testing dataset to verify its correctness while using fresh data. The comparative performance statistics so obtained are given in Table 3.

MAJOR FINDINGS AND DISCUSSIONS

The major findings of the present research are discussed in this section.

- To categorise the photos as either healthy or having one of the illnesses mentioned as having occurred, each of the models was applied to the compiled dataset. On the basis of the previously mentioned metrics—accuracy, precision, recall, and F1 score—the models were assessed on the test dataset to see how well they performed while trying to classify fresh data. Fig. 3 depicts the performance metric results that have been achieved by the proposed model, having accuracy: ‘94.49%’, precision: ‘94.71%’, Recall: ‘94.49’ and F1-Score: ‘94.45%’, maintaining consistent results across the various performance criteria which were one of the limitations observed in the related works.
- Table 3 shows the comparison between the proposed model and three other models, namely: VGG16, MobileNet and ResNet50. Even though the performance metrics achieved by the proposed model: Accuracy: ‘94.49%’, Precision: ‘94.71%’, Recall: ‘94.49’ and F1-Score: ‘94.45%’, do not significantly differ from those observed in the case of MobileNet : Accuracy: ‘94.34%’, Precision: ‘94.56%’, Recall: ‘94.87’ and F1-Score: ‘94.72%’, under the same circumstances (number of epochs and dataset preparation), the main difference between the two can be observed in the case of average training time – Proposed model: ‘5 minutes’ and MobileNet: ‘30 minutes’, as well as the average time taken per image – Proposed model: ‘38 milliseconds’ and MobileNet: ‘50

milliseconds’, these considerable deviations has been achieved by the overall reduction in the complexity of the proposed model as compared to MobileNet.

- As is evident in Table 3. the proposed model only consists of a minimal ‘6’ layers (nearest being VGG16 with 16 layers) which is considerably lower than any of the other models whilst still maintaining on par or better performance than the other models taken under consideration. This has been attained by tweaking the hyper-parameters, leading to significant reduction in the computational requirements to run the model along with the strides in time for training of the model and classification of the images, thus providing the proposed model with an advantage in the real-time application of the models for day-to-day analysis.

CONCLUSION AND FUTURE SCOPE

This paper proposes a novel model for the early detection of diseases in wheat crops using image analysis. Our model is based on a convolutional neural network that was pre-trained on a plant disease dataset. Notably, our model was shallower than the other models compared, making it more computationally efficient. Through comparative analysis with popular models such as VGG16, MobileNet, and ResNet50, we demonstrated that our proposed model outperformed these models in terms of computational cost, while still achieving comparable or even better results in terms of accuracy, precision, recall, and F1- score, all within the same training time. This suggests that our model is a more efficient and effective solution for this task, especially for devices with limited computational power. Given the impressive performance of our model in terms of computation and time, it has the potential to revolutionize disease diagnosis and treatment in the agricultural industry. By integrating the model with a knowledge base, it can be used to provide real-time remedies for various diseases in their early stages, thereby increasing the annual production of crops such as wheat. Moreover, the computational efficiency of our model makes it suitable for deployment on affordable mobile devices with a camera module, enabling farmers to diagnose crop diseases using their smartphones. This is particularly valuable for farmers in remote areas who may not have access to specialized

equipment or experts. While our model has already demonstrated excellent performance, there is still room for improvement. By continuously training the model on an extended dataset, we can further enhance its accuracy and precision. Additionally, we plan to test the model for more diseases and more crops, expanding its potential uses and impact. Overall, our proposed model represents an exciting advancement in the field of disease detection in crops and has the potential to significantly improve crop yields and food security.

REFERENCES

- [1] C. Affonso, A.L. Rossi, F.H. Vieira, and A.C. de Carvalho, "Deep Learning for Biological Image Classification," *Expert Systems with Applications*, vol. 85, pp. 114–122, 2017. Doi: 10.1016/j.eswa.2017.05.039
- [2] W. Shafik, A. Tufail, A. Namoun, L.C. De Silva and R.A.A.H.M. Apong, "A Systematic Literature Review on Plant Disease Detection: Motivations, Classification Techniques, Datasets, Challenges, and Future Trends," *IEEE Access*, vol. 11, pp. 59174–59203, 2023, doi: 10.1109/ACCESS.2023.3284760
- [3] Ramadan, S.T.Y., Sakib, T., Farid, F.A., Islam, M.S., Abdullah, J., Bhuiyan, M.R., Mansor, S., & Karim, H.A. (2024). Improving Wheat Leaf Disease Classification: Evaluating Augmentation Strategies and CNN-Based Models with Limited Dataset. *IEEE Access*, 1. <https://doi.org/10.1109/access.2024.3397570>
- [4] R. Kaundal, A.S. Kapoor, and G.P.S. Raghava, "Machine learning techniques in disease forecasting: A case study on Rice Blast Prediction," *BMC Bioinformatics*, vol. 7, no. 1, 2006, doi: 10.1186/1471-2105-7-485
- [5] D. Kim, T.F. Burks, J. Qin, D.M. Bulanon, "Classification of grapefruit peel diseases using color texture feature analysis". *International Journal on Agriculture and Biological Engineering*, vol. 2, no. 3, September 2009, doi: 10.3965/j.issn.1934-6344.2009.03.041-050
- [6] B. Kowshik, V. Savitha, M. Nimosh madhav, G. Karpagam, Sangeetha K. "Plant Disease Detection Using Deep Learning", *International Research Journal on Advanced Science Hub*, 3, Special Issue ICARD-2021 3S, 2021, 30-33. doi: 10.47392/irjash.2021.057
- [7] G. Geetha, S. Samundeswari, G. Saranya, K. Meenakshi, and M. Nithya, "Plant Leaf Disease Classification and Detection System using machine learning," *Journal of Physics: Conference Series*, vol. 1712, no. 1, p. 012012, 2020, doi: 10.1088/1742-6596/1712/1/012012
- [8] A.H. Kulkarni and A. Patil (2012), "Applying image processing technique to detect plant diseases", vol 2. 3661-3664.
- [9] A. Hussain, M. Ahmad, I.A. Mughal, and H. Ali, "Automatic Disease Detection in Wheat Crop using Convolution Neural Network," *The 4th International Conference on Next Generation Computing 2018*, Dec. 2018, doi: 10.13140/RG.2.2.14191.46244
- [10] B. Liu, Y. Zhang, D.J. He, and Y. Li, "Identification of Apple leaf diseases based on deep convolutional neural networks," *Symmetry*, vol. 10, no. 1, p. 11, 2017, doi: 10.3390/sym10010011
- [11] A. Khan, A. Sohail, U. Zahoor, and A.S. Qureshi, "A survey of the recent architectures of deep convolutional Neural Networks," *Artificial Intelligence Review*, vol. 53, no. 8, pp. 5455–5516, 2020, doi: 10.1007/s10462-020-09825-6
- [12] A. Patel and M.B. Joshi, "A survey on the plant leaf disease detection techniques", *IJARCCCE*, pp. 229–231, 2017, doi: 10.17148/ijarccce.2017.6143
- [13] S. Ghosal, D. Blystone, A.K. Singh, B. Ganapathy-subramanian, A. Singh, and S. Sarkar, "An explainable deep machine vision framework for Plant Stress Phenotyping," *Proceedings of the National Academy of Sciences*, vol. 115, no. 18, pp. 4613–4618, 2018, doi: 10.1073/pnas.1716999115
- [14] K. Nagasubramanian, S. Jones, A.K. Singh, S. Sarkar, A. Singh, and B. Ganapathysubramanian, "Plant disease identification using explainable 3D deep learning on hyperspectral images," *Plant Methods*, vol. 15, no. 1, 2019, doi: 10.1186/s13007-019-0479-8
- [15] J. Kaur, R. Chadha, S. Thakur, R. Kaur, "A Review Paper on Plant Disease Detection using Image Processing and Neural Network Approach". *International Journal of Engineering Sciences & Research Technology*. April 2016. ISSN: 2277-9655.
- [16] M. Kumar, P. Gupta, P. Madhav and Sachin, "Disease Detection in Coffee Plants Using Convolutional Neural Network", *2020 5th International Conference on Communication and Electronics Systems (ICCES)*, Coimbatore, India, 2020, pp. 755-760, doi: 10.1109/ICCES48766.2020.9138000.
- [17] A.M. Reshmi, P. Prasidhan, "Leaf Disease Detection Using CNN", *International Journal of Creative Research Thoughts (IJCRT)*, Volume 10, Issue 3, pp. 235-f241, March 2022, ISSN:2320-2882
- [18] Md. Tariqul Islam, "Plant Disease Detection using CNN Model and Image Processing", *International Journal of Engineering Research & Technology (IJERT)*, Volume 09, Issue 10, October 2020, doi: 10.17577/IJERTV9IS100123
- [19] W. Zeng, M. Li, J. Zhang, L. Chen, S. Fang, and J. Wang, "High-order residual convolutional neural network for robust crop disease recognition," *Proceedings of the 2nd International Conference on*

- Computer Science and Application Engineering, 2018, doi: 10.1145/3207677.3277952
- [20] Y. Tian, G. Yang, Z. Wang, E. Li, and Z. Liang, "Detection of apple lesions in orchards based on deep learning methods of cyclegan and yolov3-dense," *Journal of Sensors*, vol. 2019, pp. 1–13, 2019, doi: 10.1155/2019/7630926
- [21] X. Zhang, L. Han, Y. Dong, Y. Shi, W. Huang, L. Han, P. González-Moreno, H. Ma, H. Ye, and T. Sobeih, "A deep learning-based approach for automated yellow rust disease detection from high-resolution hyperspectral UAV images," *Remote Sensing*, vol. 11, no. 13, p. 1554, 2019, doi: 10.3390/rs11131554
- [22] D. Wang, R. Vinson, M. Holmes, G. Seibel, A. Bechar, S. Nof, and Y. Tao, "Early detection of tomato spotted wilt virus by hyperspectral imaging and outlier removal auxiliary classifier generative adversarial nets (orac-gan)," *Scientific Reports*, vol. 9, no. 1, 2019, doi: 10.1038/s41598-019-40066-y
- [23] Sahu, Madhusmita & Dash, Rasmita (2021). A Survey on Deep Learning: Convolution Neural Network (CNN). 10.1007/978-981-15-6202-0_32.
- [24] S. Albawi, T.A. Mohammed and S. Al-Zawi, "Understanding of a convolutional neural network", 2017, *International Conference on Engineering and Technology (ICET)*, Antalya, Turkey, 2017, pp. 1-6, doi: 10.1109/ICEngTechnol.2017.8308186.
- [25] Yamashita, R., Nishio, M., Do, R.K.G. et al. Convolutional neural networks: An overview and application in radiology. *Insights Imaging* 9, 611– 629 (2018). <https://doi.org/10.1007/s13244-018-0639-9>
- [26] H. Gholamalinezhad and H. Khosravi, "Pooling Methods in Deep Neural Networks: A Review," arXiv.org, 16-Sep-2020. [Online] Available: <https://doi.org/10.48550/arXiv.2009.07485>
- [27] G. Lin and W. Shen, "Research on convolutional neural network based on improved ReLU piecewise activation function," *Procedia Computer Science*, vol. 131, pp. 977–984, 2018, doi: 10.1016/j.procs.2018.04.239CNN and Softmax [Online] Available: <https://www.andreaperlato.com/aipost/cnn-and-softmax/>
- [28] L. Goyal, C. Sharma, A. Singh, and P. Singh, "Leaf and spike wheat disease detection & classification using an improved deep convolutional architecture," *Informatics in Medicine Unlocked*, vol. 25, p. 100642, 2021, doi: 10.1016/j.imu.2021.100642
- [29] W. Chen, C. Wellings, X. Chen, Z. Kang, and T. Liu, "Wheat stripe (yellow) rust caused by puccinia striiformis sp. tritici," *Molecular Plant Pathology*, vol. 15, no. 5, pp. 433–446, 2014, doi: 10.1111/mpp.12116.
- [30] Y. Anikster, J. Manisterski, D.L. Long, and K.J. Leonard, "Leaf Rust and stem rust resistance in triticum dicoccoides populations in Israel," *Plant Disease*, vol. 89, no. 1, pp. 55–62, 2005, doi: 10.1094/pd-89-0055
- [31] M. Bolton, J. Kolmer, and D. Garvin, "Wheat leaf rust caused by puccinia tritricina," *Molecular Plant Pathology*, vol. 9, no. 5, pp. 563–575, 2008, doi: 10.1111/j.1364-3703.2008.00487.x
- [32] J. Huerta-Espino, R.P. Singh, S. Germán, B.D. McCallum, R.F. Park, W.Q. Chen, S.C. Bhardwaj, and H. Goyeau, "Global status of wheat leaf rust caused by puccinia tritricina," *Euphytica*, vol. 179, no. 1, pp. 143–160, 2011, doi: 10.1007/s10681-011-0361-x
- [33] W. Spielmeyer, R.A. McIntosh, J. Kolmer, and E.S. Lagudah, "Powdery mildew resistance and LR34/YR18 genes for durable resistance to leaf and stripe rust cosegregate at a locus on the short arm of chromosome 7d of wheat," *Theoretical and Applied Genetics*, vol. 111, no. 4, pp. 731–735, 2005, doi: 10.1007/s00122-005-2058-9.
- [34] S. E. Strelkov and L. Lamari, "Host–parasite interactions in tan spot [pyrenophora tritici-repentis] of wheat," *Canadian Journal of Plant Pathology*, vol. 25, no. 4, pp. 339–349, 2003, doi: 10.1080/07060660309507089.
- [35] A. Shabeer, "Tan spot effects on yield and yield components relative to growth stage in winter wheat," *Plant Disease*, vol. 72, no. 7, p. 599, 1988, doi: 10.1094/pd-72-0599
- [36] C. Goutte and E. Gaussier, "A probabilistic interpretation of precision, recall and F-score, with implication for evaluation," *Lecture Notes in Computer Science*, pp. 345–359, 2005, doi: 10.1007/978-3-540-31865-1_25.
- [37] S. Sun, Z. Cao, H. Zhu and J. Zhao, "A Survey of Optimization Methods from a Machine Learning Perspective" in *IEEE Transactions on Cybernetics*, vol. 50, no. 8, pp. 3668-3681, Aug. 2020, doi: 10.1109/TCYB.2019.2950779.
- [38] K. Simonyan and A. Zisserman, "Very deep convolutional networks for large-scale image recognition," arXiv.org, 10-Apr-2015. [Online]. Available: <https://arxiv.org/abs/1409.1556>.
- [39] A.G. Howard, M. Zhu, B. Chen, D. Kalenichenko, W. Wang, T. Weyand, M. Andreetto, and H. Adam, "MobileNets: Efficient convolutional neural networks for Mobile Vision Applications," arXiv.org, 17-Apr-2017. Available: <https://arxiv.org/abs/1704.04861>
- [40] K. He, X. Zhang, S. Ren, and J. Sun, "Deep residual learning for image recognition," *2016 IEEE Conference on Computer Vision and Pattern Recognition (CVPR)*, 2016, doi: 10.1109/cvpr.2016.90.



Energy Consumption Trends in India and Its Impact on Indian Economy

Meraj Alam¹, Rajesh Kumar Saluja², Priyanka Vashisht³, Nishi Gupta⁴ & Rashmi Jha⁵

ABSTRACT

In the current scenario, various energy studies and surveys have projected India as one of the fastest growing Economy (with last 5-year GDP average equal to 7.178%) and that the energy demand will continue growing in India. In the previous decade, the energy demand has consistently soared steadily for all sectors including agriculture, industry, commercial and residential, and is expected further increase at a fast pace. This paper represents the present and the future Indian trends up to 2050 for energy consumption and production from various resources such as coal, petroleum, nuclear energy and renewable energy including hydro energy, biofuels and wind and solar energy. This paper also compares the Indian energy consumption and production trends with those of the developed countries like China and USA; the largest energy consumers at present. This paper points towards the various challenges that lie ahead for India to reduce energy demand and supply gap. This work focuses on the fact that proper planning, development and management of the energy resources is required to make the road of India's development smooth and to lower the burden of various energy imports.

Keywords: Energy Scenario, India Energy Trends, Energy Resources, Energy Planning

INTRODUCTION

The three “Es”; Energy, Economy and Environment, are closely associated with each other. Population and Economy are the driving factors of the Energy demand of any country and energy consumption is the indicator of country's development. A developed country has the more consumption of energy due to advancement in the industry, agriculture and transportation sector. India is still among the developing countries. The population has increased by 30% in the last 2 decades and is projected to be over 1500 million by the year 2036 [1]. At present, the population of India is 1339 million as compared to 1443 million of China and 332 million of United States of America [2]. China is the world's largest consumer of energy with annual consumption of 3284 million tonnes of oil equivalent (MTOE) in 2019[3]. Both USA and China have 40% share of world's energy consumption.

United states, though having very less population as compared to India and China has the higher per capita energy consumption in the world at 6.87 tonnes of oil equivalent (TOE) per capita, which is approximately 12 times that of India having per capita energy consumption of 0.6 TOE [3]. Table 1 reflects the present energy scenario of the world and other countries as compared to India. It can be clearly concluded from the table 1 that India is far behind in energy supply and production than USA or China. India is steadily progressing on its development journey. However, the nation's energy resources are limited in comparison to its population size. While having nearly one-sixth of the global population, India possesses only about 0.8% of the world's total geological reserves. It holds 5.7% of the total confirmed coal reserves and a mere 0.4% of proven hydrocarbon reserves [3]. The efforts are always being made by the government to make

¹ Amity Institute of Aerospace Engineering, Amity University, Noida, Uttar Pradesh. E-mail: alammeraj152003@gmail.com

² Amity Institute of Aerospace Engineering, Amity University, Noida, Uttar Pradesh. E-mail: rksaluja@amity.edu

³ Department of Computer Science and Engineering, Amity University, Manesar, Haryana. E-mail: priyankavashisht@ncuindia.edu

⁴ Department of Computer Science and Engineering, Gurugram University, Gurugram, Haryana.
E-mail: nishigupta@gurugramuniversity.ac.in

⁵ Department of Computer Science and Engineering, Gurugram University, Gurugram, Haryana.
E-mail: rashmijha@gurugramuniversity.ac.in

Table 1. Various energy indicators (World Energy Scenario 2018-19) [3-5]

Country/ Region	Population (Million)	GDP (Trillion USD)	TPE Consumption (MTOE)	Per Capita Energy Consumption (MTOE)	TPE Production (MTOE)	Co ₂ Emissions (Gt)
World	7577.1	98.63	13371	1.912	14421.15	33.51
Africa	1373.4	2.6	733	0.55	1168.72	1.24
Middle East	456.1	3.63	681	3.19	2039	1.773
USA	332.9	20.81	2298.7	7.3	2172.52	4.77
China	1444.2	14.86	2972.1	2.19	2562.24	9.57
India	1393.4	2.59	637.8	0.506	573.558	2.3

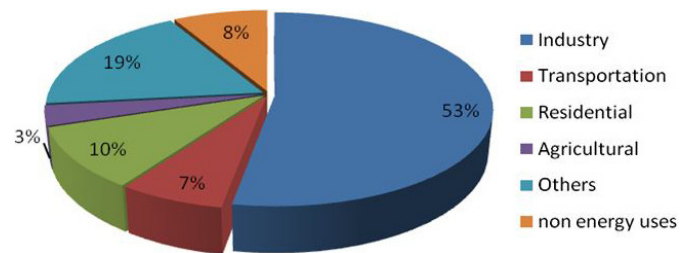
India stand among the developed countries. There are many developments in technology in Industrial and the agricultural sectors. Also, the electrification of the remote areas, where electricity has yet not reached, is being done. The number of vehicles, both passenger as well as goods, are increasing. In short, the demand of energy is increasing at a high rate. It is projected in various world energy surveys [1-7] that India will be the top consumers of energy in the world along with China in the future. Therefore, India needs to be self reliant for its energy needs and reduce the gap between the demand and supply to keep on moving smoothly on the path of development. Energy consumption also has the effect on the environment. The high energy demand can push to the exploitation of the conventional energy resources on one hand and also affect the environment with various types of pollution. Global warming, air pollution, water pollution, food pollution and overuse of non biodegradable materials are the results of the high energy use which have forced the researchers and the lawmakers to look for clean and green alternatives to the conventional energy resources. An attempt has been made in this paper to analyze the present and the future Indian trends up to 2030 of energy consumption and production from various resources and the challenges that India faces in becoming self reliant for its energy needs.

INDIA ENERGY SCENARIO

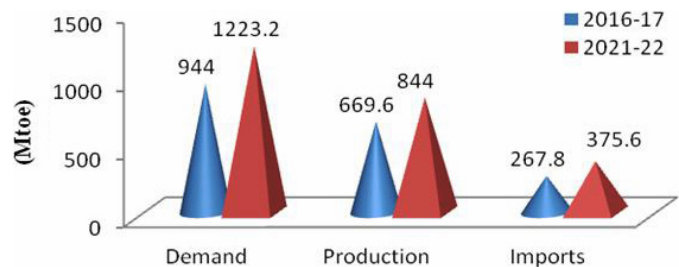
Present Energy Balance

According to India energy statistics 2018, the total primary energy supply in the year 2017-18 was 837.4 MTOE and the final energy consumption for the same year was 553.904 MTOE. The energy Import was 419.11 MTOE. Figure 1 shows the sector wise energy consumption for the year 2017-18. It is clear from figure 1 that Industrial sector is the largest consumer

of energy with 307.49 MTOE (55.51% share). The non energy uses include energy transformation, industry and chemical industry, etc.

**Fig. 1.** Final energy consumption sectorwise (2013-14) [8]

In the current scenario, various energy studies and surveys have projected India as a fastest growing Economy (with last 5-year GDP rate equal to 6.5%) and also that the energy demand will continue growing in India at the rate of 6.3% [1,6]. The Twelfth Plan document from the Planning Commission projected that domestic energy production is expected to reach 669.6 million tons of oil equivalent (MTOE) by 2016-17 and increase to 844 MTOE by 2021-22. (figure 2) [7]. This production level is expected to cover approximately 69% energy demand in 2021-22, with the remaining energy requirements being fulfilled through imports.

**Fig. 2.** Trends of demand and production of energy as projected in 12th planning commission report

The last 10-year trends from 2004 onwards show the average growth of energy demand of 6.26% [2]. As a result of continuous economic growth backed by the strong government policies, it can be expected to 8% average. Figure 3 shows the shows the energy

requirement by 2030 in these scenarios (i.e. at average rate 6%, 7% and 8%).

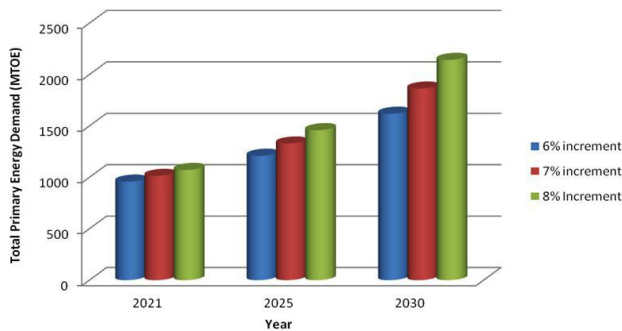


Fig. 3. Future trends of demand and production of energy as projected in 12th planning commission report

Considering the 6% average rise in demand annually, about 1525 MTOE would be required by 2030. The present resources will not be enough to cope up with the surging demand. India is presently an energy deficient country and has to export crude oil and various other energy sources. There is also a great challenge before government in managing the present energy resources and developing the new ones so that the demand of the required energy can be filled indigenously. Presently the burden lies on conventional energy resources like coal and crude petroleum which are limited in numbers in India. The share of non conventional energy resources is 12.1% of the total supply. These resources need to be developed so that the burden on conventional resources as well as the export burden may be reduced.

Future Energy Trends Sector-wise

The demand for energy is projected to increase due to the population growth, economic policies, and growth in Industry. Various Energy surveys and research works [9-11] have analysed and predicted the growth rate of energy in each sector, viz., Industry, domestic, transport and agriculture. The trends of energy consumption for these sectors according to these predictions are shown in Figs. 4–7.

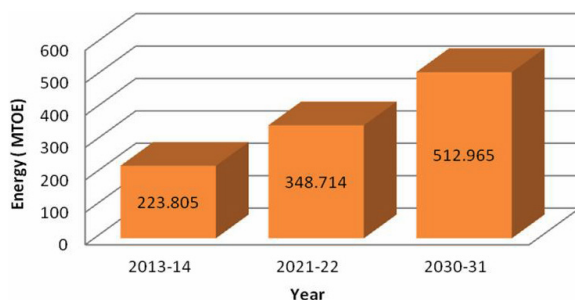


Fig. 4. Trends in energy demand for industries [9]

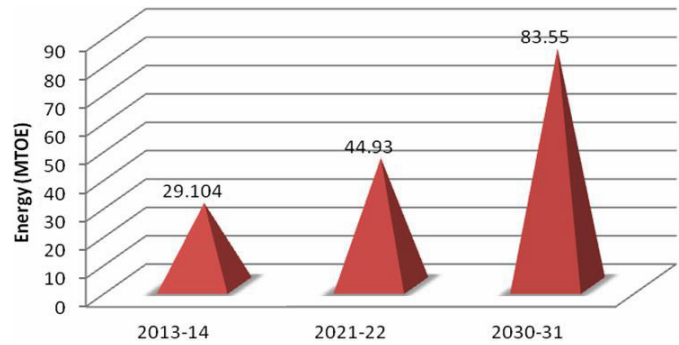


Fig. 5. Trends in energy demand for transport [10]

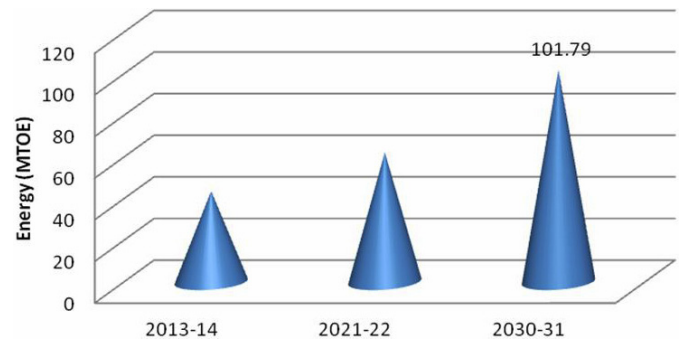


Fig. 6. Trends in energy demand for domestic sector [10]

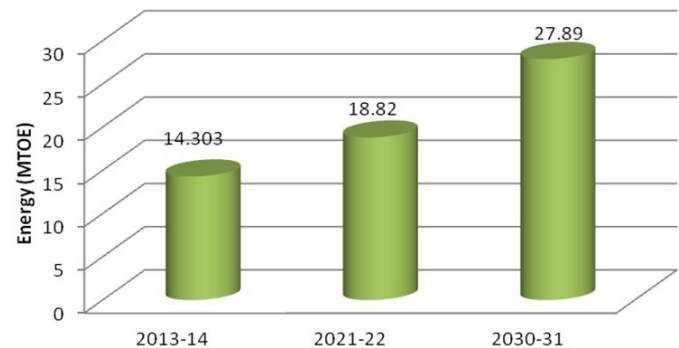


Fig. 7. Trends in energy demand for agriculture sector [11]

- Industrial sector:** Projected energy consumption of Indian industry as per International energy agency, France is 600-634 MTOE by year 2050 [9] which reflects average 3% annual growth in Industrial energy consumption. The last 7-8 years have seen the Industrial energy consumption growth at the average annual rate of 5.8%. [7-8, 12, 13]. Backed up by strong policies of Indian government for Indian industry boost further, we can assume the same progress up to next 15 years and the energy demand has been predicted as shown in Fig. 4.
- Transportation sector:** The total number of vehicles in India have increased at the average rate of approximately 10.5% per annum [12]. India has the largest consumer of two wheelers in the world. The two wheelers have around 72% of the

share in the number of vehicles present in India at present (Fig. 8). Trends further indicate that India's energy consumption in the transportation sector is expected to grow at the highest rate globally, averaging 5.5% annually, significantly outpacing the global average of 1.4% per year. Additionally, overall energy demand in India is projected to rise at an average rate of 6.4% per year. [10].

- **Domestic sector:** India is the third largest producer of electricity in the world with production of 1208400 GWh in year 2014 [2]. India is presently the fourth-largest electricity consuming country and accounts for about 5% of the world's total annual electricity consumption. India's demand for electricity is rising at a remarkable pace. Over the past decade, the country's annual electricity generation and consumption have grown by approximately 64%. Looking ahead, India's electricity consumption is expected to grow at one of the fastest rates globally, with overall energy consumption projected to increase by an average of 5.2% annually [10]. Figure 6 shows the trend in demand up to 2030.
- **Agriculture sector:** The trends of energy consumption in agriculture sector are represented

in Fig. 7. The use of technology and fertilizers enhance the energy consumption. It has been estimated in various energy reviews that the energy consumption will increase at an average rate of 4% per annum. Therefore, India would be requiring approximately 28 MTOE of energy during this year for agriculture sector.

From the trends of energy demand discussed above, It can be concluded that:

- The demand for energy continues to increase in all the sectors with industry sector having the largest share.
- The energy resources need to be developed in India to make up for the increased energy demand.
- The strategies need to be developed and analysed so that the import of various energy resources can be reduced.
- The consumption in energy also leads to increased CO₂ and other emissions which is of prime concern to the World and India today.

THE ENERGY RESOURCES OF INDIA

Currently, fossil fuels such as petroleum, coal, and natural gas serve as the primary sources of energy. Although these fuels continue to form under the earth's heat and pressure, their consumption far exceeds the rate at which they are replenished. This imbalance classifies fossil fuels as non-renewable resources, as they cannot be replaced quickly enough to match their usage. In India, the major burden for the supply of energy is on coal as there is increase in the electric energy demand as well as materials in which coal is a key component of production such as steel and cement. The crude oil is another major energy resource. India, not having much of the reserves, has to import around 80% of its crude oil demand. The renewable has lesser shares in energy supply at present though the share of hydro energy is significant among the renewables

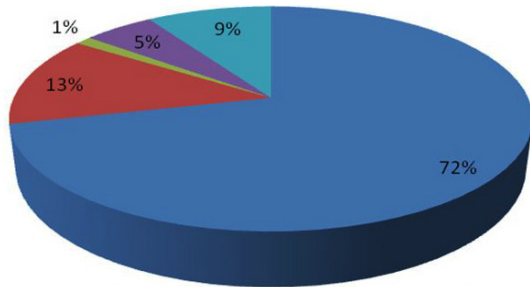


Fig. 8. The vehicle population shares in India

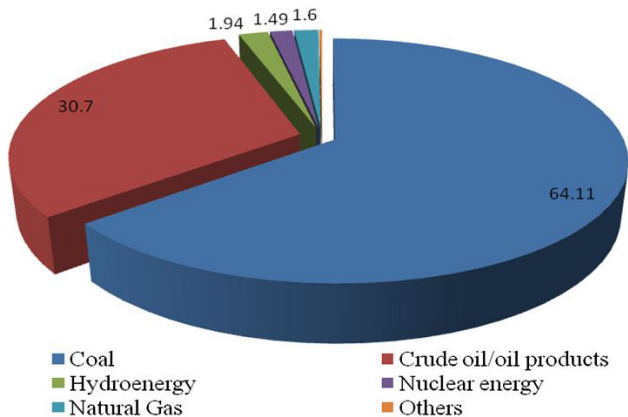


Fig. 9. Percentage share of each resource in TPES [8]

Table 2. Primary energy supply from various resource

Resource	Share (MTOE)	Percentage Share
Coal	382.355	64.11
Crude oil/oil products	183.120	30.7
Hydro energy	11.587	1.94
Natural Gas	9.896	1.6
Nuclear energy	8.913	1.49
Others	0.954	0.08

(around 1.9%). Nuclear energy is another significant resources and is currently being developed to large extent.

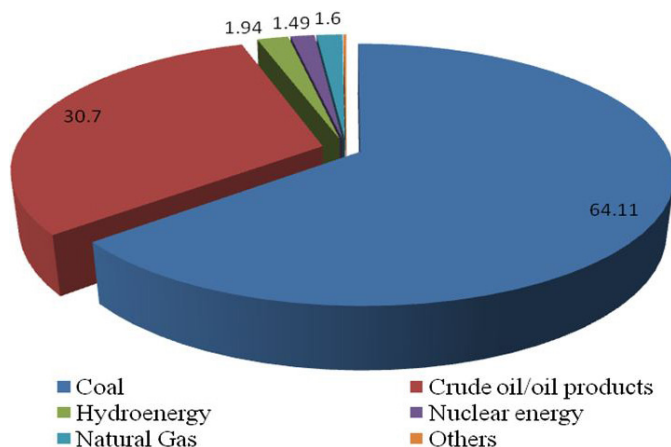


Fig. 10. Share of each resource in total primary energy supply

Coal

Coal is the most abundant fossil fuel on earth, with confirmed reserves of approximately 1,000 billion tonnes. [14] and its consumption is next only to oil. Coal contributes to about 26% of the world's primary energy consumption and approximately 40% of the global energy used for electricity generation. [15]. Bituminous coal is the most abundant type of coal, serving as the primary source of coke for smelting, coal tar, and various chemically modified fuels. At existing production rates, current coal reserves are expected to meet demand for nearly 150 years. The remaining recoverable resources are even greater, making a shortage of coal unlikely to limit production. Additionally, coal is the most widely distributed fossil fuel, with 43% of proven reserves located in OECD countries, compared to 10% for natural gas and 16% for oil. [15]

The rise in global coal consumption is mainly due to the growing demand for electricity in China, India, and other non-OECD countries, where total power generation has more than doubled since 2000. More than half of this increased electricity generation has been fuelled by coal.

Coal accounts for approximate 26% of the world's primary energy consumption and around 40% of the energy consumed worldwide for electricity generation. At present coal production levels, the world reserves would meet demand for almost 110 years. India has

proven coal reserves of 344.05 billion tons which is 6.8% of the world reserves. India was 3rd largest in the world producer of coal after China and USA with production equal to 565.77 million tons in 2014 (MTs).

- Reserve/Production (R/P) Ratio = No. of years the reserve can last = 223 years
- Net coal imports = 166 million tons
- Import burden approximately 22 lakh USD/year

Crude Oil

India is the fourth largest consumer of crude oil in the world. The present proven reserves of oil in India are 800 million tons against the 240,000 million tons with R/P 52.5. The Demand for diesel in India is about 8 times that of petrol. India imports about 80% of its crude oil demand at present.

Table 3. Imports of crude oil (value) in 2005-06 and 2013-14

Year	Imports (MMT)	Value (Thousand Crore Rs)
2005-06	100	249546
2013-14	190	864875

Natural Gas

The Natural Gas reserves in the world are 187 trillion cubic meters R/P is 54. India's present share in world production of Natural Gas is a less than 1%. The proven reserves in India are 1.4 trillion cubic meters R/P 45.

Nuclear Energy

There are 7 nuclear plants across India with 21 Nuclear reactors at present. Further 8 sites have been proposed to be set up. The present Capacity is 5780 MW. But the potential of nuclear power generation is 43644 MW.

Renewable Energy

The total potential for renewable power potential generation in the country estimated at 531414 GWh [17]. That means we are utilizing just 1/3 of the Renewable resources Share of Renewable energy can be 46 MTOE, i.e. around 11%.

Table 4. Use of renewable energy country-wise

Country	Hydropower	Wind Power	Biomass and Waste	Solar Power	Geothermal	Total
China	1,070,000	160,000	4,2000	2,8200	-	1300,000
USA	260,000	180,000	64,000	18,300	16,600	540,000
Brazil	510,00	7,000	42,300	—	—	559,300
Canada	395,700	12,000	9,400	800	—	417900
Russia	176400	-	3,400	—	—	179800
India	135000	30,000	5,000	3,000	—	178000

Units: GWh Data for 2013-14; Source: [2, 8, 15, 16, 18, 19]

Table 5. Per capita energy consumption for various countries/regions

Country/Region	CO ₂ Emissions/Capita (Gt) [2,4]
World	31.734
OECD countries	12.341
Africa	0.968
Middle East	1.607
USA	5.2
China	8.7
India	1.8

ENERGY ISSUES

There are many issues pertaining to the energy consumption that arise concerns. The foremost issue due to which the whole world is concerned is global warming. With development and the energy consumption, CO₂ consumption is increasingly rejected into the environment. Table 5 shows the CO₂ emissions per capita for various countries and regions of the world.

The other energy challenges that are bothering the leaders of the world are:

- Energy Poverty – in 2009–2010, an estimated 29.8% of India's population—350 million people—lived below the poverty line [20]
- Energy efficiency
- Energy Intensity
- Energy Subsidies
- Pollution
- Import Burden

ENERGY BALANCE 2030

As per the trends of energy demand from all the sectors, the energy 1500 MTOE considering 6% AGR. Then the trends of energy production from various resources are indicated in Table 6. The Total Primary energy

supply From conventional resources is predicted to be 1018 MTOE and from the Non conventional Energy resources is 216 MTOE which is assumed on the basis that it will have 20% share in the total energy production. Therefore there will be still an energy deficit of 280 MTOE by 2030.

Table 6. Trends of energy production from various resources

Resource	CAGR (Last 8 years)
Coal and Lignite	3.85%
Crude petroleum	1.79%
Natural Gas	1.06%
Nuclear	7.2%
Hydro	3.8%

CONCLUSION

- China and India are projected to dominate in global energy demand.
- The present energy scenario in India is not satisfactory.
- Energy demand is expected to increase at an annual rate of 6-7% with final energy demand of 1700 MTOE by 2030
- Maximum demand for Energy by will be form the Industry sector.
- Coal will continue to have the largest share in Total Primary energy supply.
- There is tremendous scope in the potential of Nuclear energy consumption and Renewable energy.

REFERENCES

- [1] India Population census website, 2021. https://censusindia.gov.in/Census_Data_2001/Projected_Population/Projected_Population.pdf
- [2] http://www.worldpopulationbalance.org/population_energy

- [3] India's Ministry of Petroleum and Natural Gas, Indian Petroleum and Natural Gas Statistics 2014-15, page 35; Indian Petroleum and Natural Gas Statistics 2017-18, page 44.
- [4] Global Energy Statistical Yearbook, 2020, <https://yearbook.enerdata.net/>
- [5] IEA (2021), India Energy Outlook 2021, IEA, Paris <https://www.iea.org/reports/india-energy-outlook-2021>
- [6] BP statistical review of world energy, 2015, 64th ed., url: www.bp.com/statisticalreview.
- [7] European business and technology centre, Report on transportation and energy in India, 2019.
- [8] Key world energy statistics, International Energy agency, 2019, url: www.worldenergyoutlook.org
- [9] Energy and Climate change: World outlook special report, International Energy Agency, 2019.
- [10] 2019 world Energy Issues Monitor, World Energy Council, 2019. www.worldenergy.org.
- [11] Energy statistics (2019), Ministry of statistics and programme implementation, Twentieth issue, Govt. of India.
- [12] Energy statistics (2020), Ministry of statistics and programme implementation, Twentieth issue, Govt. of India.
- [13] International Energy Agency. Energy transition for Industry: India and the Global context. France, 2011.
- [14] Stephane de la Rue du Can, Virginie Letscher, Michael McNeil, Nan Zhou, and Jayant Sathay. Residential and transport energy use in India. *Berkeley National Laboratory*, USA. 2009.
- [15] Girish Kumar Jha (2012), Suresh Pal and Alka Singh. Energy Requirement for Indian Agriculture, Division of Agricultural Economics, Indian Agricultural Research Institute, New Delhi.
- [16] <https://data.gov.in/visualize3/?inst=556520bb219fe4ee7ad43af7cd98089b#>
- [17] Narasimha Rao (2009), Girish Sant, & Sudhir Chella Rajan. An overview of Indian Energy Trends: Low Carbon Growth and Development Challenges. *Prayas*, Energy Group, Pune.
- [18] BGR (2009), Energy Resources, Reserves, Resources, Availability (Crude Oil, Natural Gas, Coal, Nuclear Fuels, Geothermal Energy).
- [19] World Energy Council (2013), World Energy Resources: Coal.
- [20] Energy statistics (2014), Ministry of statistics and programme implementation, Twenty first issue, Govt. of India.



Trajectory Tracking Control of a Two-Link Manipulator Including Actuator Dynamics Based on Sliding Mode Controller

Manju Rani¹ & Naveen Kumar²

ABSTRACT

This paper presents a robust trajectory tracking control strategy for a two-link manipulator, considering the actuator dynamics, using a Sliding Mode Controller (SMC). The proposed method effectively addresses the inherent challenges of nonlinearity, uncertainties, and disturbances in manipulator dynamics, which are common in real-world robotic systems. By incorporating actuator dynamics into the control framework, the SMC ensures that the manipulator can maintain high precision in its trajectory tracking, even in the presence of external disturbances and parameter uncertainties. The SMC's inherent robustness makes it particularly suitable for applications where system parameters are not perfectly known or subject to change. The stability and convergence of tracking errors are thoroughly analyzed using Lyapunov-based methods, providing a solid theoretical foundation for the controller's effectiveness. The Lyapunov analysis guarantees that the tracking errors converge to zero asymptotically, ensuring the manipulator follows the desired trajectory with minimal deviation over time. Moreover, the control strategy accounts for the actuator dynamics, minimizing the impact of voltage and current fluctuations, thereby improving the efficiency and longevity of the actuators. Simulation results confirm the robustness and effectiveness of the proposed controller, demonstrating fast error convergence, stability, and precise trajectory tracking even in the presence of model uncertainties and external disturbances. These results validate the applicability of the Sliding Mode Controller in real-world scenarios, highlighting its potential for high-precision robotic tasks.

Keywords: Sliding Mode Control, Two-Link Manipulator, Actuator Dynamics, Trajectory Tracking, Robust Control

INTRODUCTION

Robotic manipulators have become an essential component in various industries, including precision assembly, welding, and medical robotics, where accurate and fast motion control is of paramount importance. These manipulators are designed to perform complex tasks that require high precision, such as assembling microelectronics, performing delicate surgeries, or welding intricate parts. In these applications, the ability to precisely control the manipulator's movement is critical for ensuring product quality, safety, and operational efficiency. However, achieving accurate and reliable motion control in robotic manipulators is not a straightforward task, as the system dynamics are inherently nonlinear, and are often influenced by external disturbances and

uncertainties, such as variable loads or environmental changes.

The control systems of robotic manipulators are complicated by several factors, including nonlinearities in the manipulator's dynamics, actuator uncertainties, and external disturbances.

These challenges are further exacerbated in electrically driven robotic manipulators (EDRMs), where the performance of the actuator depends heavily on factors such as motor electrical circuits, friction, and back electromotive force (EMF). Traditional control approaches, including classical PID and modelbased controllers, often assume ideal conditions, neglecting the influence of actuator dynamics. This oversight can significantly degrade the performance of the control

¹ Department of Mathematics, Gurugram University, Gurugram, Haryana, India. E-mail: manjumathematics@gurugramuniversity.ac.in

² Department of Applied Mathematics, Mahatma Jyotiba Phule Rohilkhand University Bareilly, Bareilly, Uttar Pradesh, India.
E-mail: navinfma@mjprou.ac.in

system, particularly under high-speed and high-torque operations, where the effects of actuator dynamics become more pronounced. As a result, traditional control techniques may struggle to achieve the desired performance in real-world conditions, where actuator characteristics, such as voltage and current variations, can significantly influence the torque generation and the overall performance of the manipulator[1-29].

For electrically driven robotic manipulators, actuator dynamics, including the motor's electrical circuits, friction, and back EMF, play a crucial role in determining the torque generated by the actuator. These dynamics can lead to inaccuracies in the control system if they are not properly accounted for. Ignoring these effects can lead to significant deviations from the desired trajectory, reducing the precision of the manipulator's motion. In fact, actuator dynamics are particularly important when considering high-speed or high torque operations, where variations in voltage, current, and the electromagnetic forces within the motor can have a substantial impact on the performance of the manipulator. While several methods have been proposed to model and account for these actuator dynamics, many of these techniques fail to provide robust performance under varying operating conditions. They often neglect uncertainties and disturbances that can arise due to environmental changes, system wear, or modeling inaccuracies.

Moreover, the interaction between the mechanical dynamics of the manipulator and the actuator dynamics introduces additional complexity. Traditional model-based control methods, which rely on detailed knowledge of the system dynamics, often struggle to address this complexity efficiently. These methods assume that the system parameters are known precisely and remain constant throughout the operation. However, in practice, uncertainties in model parameters and environmental disturbances can significantly affect the performance of these controllers. The nonlinear coupling between the manipulator's mechanical dynamics and actuator dynamics further complicates the control design, as the system's behavior can change rapidly depending on the operating conditions.

To address these challenges, Sliding Mode Control (SMC) has emerged as a promising solution. SMC is a nonlinear robust control technique known for its ability

to handle uncertainties, nonlinearities, and external disturbances effectively. The key feature of SMC is its ability to force the system trajectories to "slide" along a predefined surface, called the sliding surface, which is designed to guarantee robustness and stability. This sliding motion ensures that the system remains insensitive to uncertainties and disturbances, as long as the system stays on the sliding surface. This makes SMC particularly suitable for systems like robotic manipulators, where uncertainties, disturbances, and nonlinearities are prevalent. The robustness of SMC arises from its ability to provide consistent performance, even in the presence of significant uncertainties or model inaccuracies. Previous works have applied SMC to robotic manipulators, demonstrating its ability to achieve stable and accurate trajectory tracking. However, most of these works have focused on the manipulator's mechanical dynamics and have not fully integrated the actuator dynamics into the control framework.

In this paper, we propose an advanced Sliding Mode Control strategy that explicitly incorporates actuator dynamics for trajectory tracking of a two-link manipulator. The key idea is to model the actuator dynamics, including the motor's electrical circuits, friction, and back EMF, and integrate them into the control framework. This allows the controller to compensate for the influence of actuator dynamics, ensuring that the manipulator can track the desired trajectory accurately, even under realistic operating conditions. The proposed method improves the performance of the manipulator by addressing both the mechanical and actuator dynamics, which are often overlooked in traditional control strategies. By doing so, the SMC guarantees robust trajectory tracking performance, even in the presence of model uncertainties and external disturbances.

The main contributions of this paper are as follows:

- The integration of actuator dynamics, including the motor's electrical dynamics, into the manipulator's control framework, improving accuracy and robustness.
- The design of a Sliding Mode Controller (SMC) that ensures robust trajectory tracking performance by compensating for nonlinearities, uncertainties, and disturbances.

- The application of Lyapunov's direct method for stability analysis, providing theoretical guarantees for the convergence of tracking errors and ensuring the robustness of the control system.

Through the proposed method, the manipulator is able to achieve accurate trajectory tracking in the presence of uncertainties and external disturbances, providing an enhanced level of performance compared to traditional control strategies. Simulation results validate the effectiveness of the proposed controller, demonstrating its ability to handle the complexities of both the mechanical and actuator dynamics. This approach represents a significant step forward in the design of robust controllers for robotic manipulators, ensuring their reliable performance in real-world applications.

DYNAMICS OF A TWO-LINK MANIPULATOR

The dynamics are described as:

$$M(q)\ddot{q} + C(q, \dot{q})\dot{q} + G(q) + \tau_f = \tau$$

where:

- q is a joint position vector.
- $M(q)$ is an inertia matrix.
- $C(q, \dot{q})$ is Coriolis and centrifugal forces.
- $G(q)$ gravitational force vector.
- τ_f : Frictional torque.
- τ : Actuator torque.

Actuator dynamics are modeled as:

$$L\dot{I} + RI + K_e\dot{q} = u$$

where

- I is the armature current, are the inductance, resistance, and back EMF constants, respectively.
- u is the input voltage vector applied to the actuator.

The actuator dynamics are tightly coupled with the manipulator's mechanical system. The actuator's torque output depends on the voltage input, which is in turn influenced by the motor's electrical dynamics. This coupling makes it essential to design a control system that accounts for both the mechanical and electrical aspects of the system.

INTEGRATION OF ACTUATOR AND MANIPULATOR DYNAMICS

Actuator dynamics, including the electric motor dynamics, are modeled as second-order systems

influencing the joint torque generation. The motor's response to the input voltage and its feedback loop with the manipulator are essential for precise trajectory control. These dynamics introduce time delays and nonlinearities, which must be mitigated in the control design.

To model the complete system, the manipulator's dynamics and actuator dynamics are integrated into a unified system. The overall system's state-space representation is constructed by combining the equations of motion for both the manipulator and the actuator. This comprehensive model forms the basis for the Sliding Mode Controller (SMC) design, which is robust to variations in load, speed, and external disturbances.

SLIDING MODE CONTROLLER DESIGN

Sliding Surface

The tracking error is defined as:

$$e_q = q_d - q; \dot{e}_q = \dot{q}_d - \dot{q}$$

Where q and \dot{q} are the desired position and velocity trajectories. The sliding surface is defined as:

Sliding surface:

$$s = \dot{e}_q + \lambda e_q$$

where $\lambda > 0$ is a design parameter that ensures exponential convergence of the error.

Control Law

The control law is designed to minimize the tracking error by forcing the system to slide along the sliding surface. The control input is given by

$$u = -K_s - \phi \text{sign}(s) + K_e \dot{q} + Ri$$

where:

- K is a gain matrix that determines the rate of convergence of the system.
- $\phi \text{sign}(s)$ compensates for uncertainties and disturbances.
- The term $K_e \dot{q} + Ri$ accounts for actuator dynamics, compensating for the electrical and mechanical coupling.

Chattering Mitigation

To mitigate the chattering effect typical in sliding mode control, we use a smooth approximation of the sign function:

$$\text{sign}(s) \approx \frac{s}{\varepsilon + |s|}$$

where ε is a small constant that smoothens the control input.

STABILITY ANALYSIS

Lyapunov Function for Stability

The stability of the control system is analyzed using Lyapunov's direct method. We define the Lyapunov candidate function:

$$V = 1/2 S^T S$$

Taking the time derivative of V , we get:

$$\dot{V} \leq -K \|s\|^2$$

where $k > 0$ is a positive constant. This condition ensures that the sliding surface decreases over time, leading to the convergence of the tracking error.

Barbalat's Lemma

According to Barbalat's Lemma, if is semi-negative and bounded, the system will converge to the equilibrium state. In our case, this guarantees that the tracking error will converge to zero as $t \rightarrow \infty$.

SIMULATION RESULTS

System Parameters

- $m_1 = 1.0$ kg: Mass of link 1
- $m_2 = 1.0$ kg: Mass of link 2
- $l_1 = 1.0$ m: Length of link 1
- $l_2 = 1.0$ m: Length of link 2
- $r_1 = l_1/2 = 0.5$ m: Distance to center of mass of link 1
- $r_2 = l_2/2 = 0.5$ m: Distance to center of mass of link 2
- $I_1 = 0.333$ kg.m² Inertia of link 1
- $I_2 = 0.333$ kg.m² Inertia of link 2
- $g = 9.81$ m/s²: Gravitational acceleration.

Actuator Parameters

The actuator parameters are given by:

- $L = 0.5$ H: Inductance
- $R = 1.0$ Ω : Resistance
- $k_e = 0.01$ V. s/rad: Back EMF constant.

Desired Trajectory

The desired trajectory for the manipulator is sinusoidal with adjustable frequency and amplitude. The desired joint angles, velocities, and accelerations are defined as:

- Desired joint angles: $q_d(t) = \begin{bmatrix} \frac{\text{amp} \cdot \sin(2\pi \cdot \text{freq} \cdot t)}{\text{amp} \cdot \cos(2\pi \cdot \text{freq} \cdot t)} \end{bmatrix}$
- Desired velocities: $\dot{q}_d(t) = \begin{bmatrix} \frac{2\pi \cdot \text{amp} \cdot \cos(2\pi \cdot \text{freq} \cdot t)}{-2\pi \cdot \text{amp} \cdot \sin(2\pi \cdot \text{freq} \cdot t)} \end{bmatrix}$
- Desired accelerations: $\ddot{q}_d(t) = \begin{bmatrix} \frac{-2\pi \cdot 2\pi \cdot \text{amp} \cdot \sin(2\pi \cdot \text{freq} \cdot t)}{-2\pi \cdot 2\pi \cdot \text{amp} \cdot \cos(2\pi \cdot \text{freq} \cdot t)} \end{bmatrix}$

The figures provided illustrate the successful implementation of the Sliding Mode Controller (SMC) in a robotic manipulator, demonstrating its effectiveness in trajectory tracking under realistic operational conditions, including actuator dynamics, external disturbances, and model uncertainties. The system's behavior is analyzed through the actuator voltages, currents, and joint angle trajectories, which reflect the performance of the proposed controller.

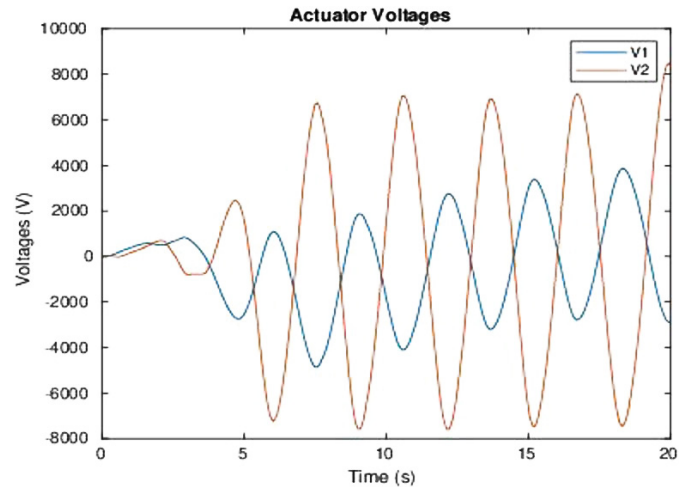


Fig. 1. Joint 1 and joint 2 actuator voltages

Figure 1, which shows the actuator voltages for Joint 1 and Joint 2, highlights the control signals necessary to drive the actuators and maintain desired joint movements. The voltage profiles reveal the dynamic adjustments made by the controller to correct any discrepancies between the actual and desired positions. The Sliding Mode Controller effectively stabilizes the system by ensuring that the applied voltages remain within an optimal range, despite external disturbances and potential actuator dynamics. Notably, the controller's ability to regulate the voltages ensures the manipulator's accuracy and stability during the entire

trajectory, demonstrating the robustness of the SMC in maintaining consistent performance under challenging conditions.

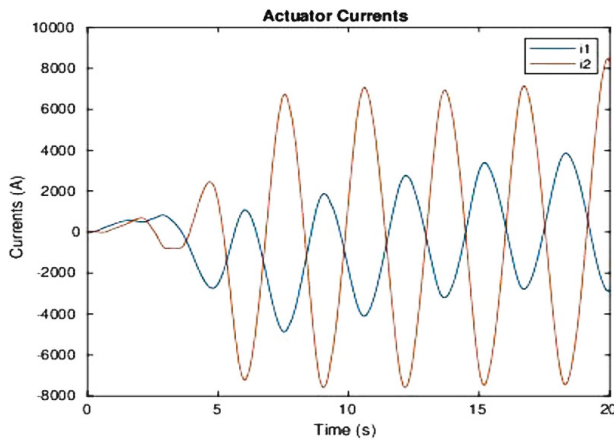


Fig. 2: Joint 1 and joint 2 actuator currents

Figure 2, presents the actuator currents for Joint 1 and Joint 2, which are crucial for understanding the power requirements Voltages (V) Currents (A) Joint Angles (rad) for the actuators to achieve the desired trajectory. The actuator currents provide a direct measurement of the torque exerted by the motors at each joint, which in turn influences the joint movements. From the data, it is evident that the sliding mode controller compensates for both model uncertainties and disturbances, providing current profiles that are smooth and efficient. The current responses remain stable and exhibit minimal fluctuations, ensuring that the actuators generate the required torques without significant overshoot or excessive oscillations. This behavior highlights the controller's efficiency in managing power demands, preventing unnecessary energy consumption, and avoiding actuator saturation.

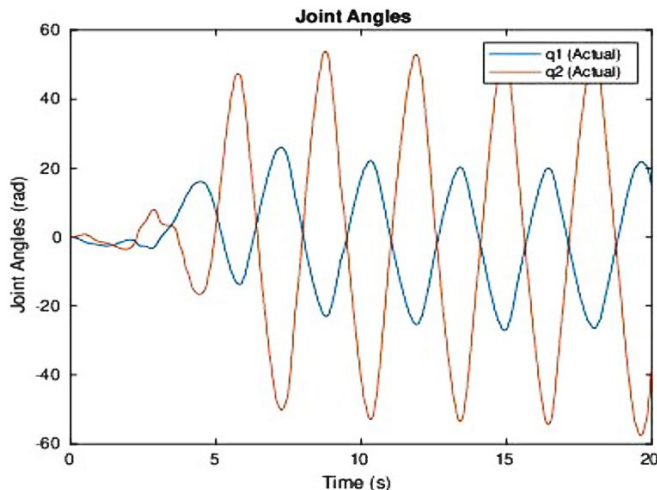


Fig. 3: Joint 1 and joint 2 joint angles trajectories

Figure 3 illustrates the joint angle trajectories for both Joint 1 and Joint 2 over time. The trajectories show that the manipulator's joints follow the desired path with minimal error, which is a key indicator of the controller's accuracy. The system demonstrates fast convergence to the reference angles, with the tracking error rapidly reducing and stabilizing. Despite the presence of external disturbances and actuator dynamics, the joints are able to accurately follow the desired trajectory, confirming the effectiveness of the sliding mode controller in achieving robust trajectory tracking. The minimal tracking error also emphasizes the controller's ability to compensate for uncertainties in the system's model and ensure precise control in real-time. Overall, these figures collectively demonstrate the superior performance of the Sliding Mode Controller in handling actuator dynamics, compensating for disturbances, and ensuring accurate joint trajectory tracking. The fast error convergence and the smooth actuator voltage and current profiles underscore the controller's effectiveness in stabilizing the system and maintaining performance over time. The robust nature of the SMC is evident from the smooth control signals and the precise trajectory tracking, which not only satisfy the desired control objectives but also optimize system efficiency. The results suggest that the proposed Sliding Mode Controller is highly effective in dealing with uncertainties in both the actuators and the manipulator's model, making it a suitable approach for real-world applications in robotics and automation.

In summary, the Sliding Mode Controller provides a reliable solution for trajectory tracking in robotic manipulators, demonstrating both robustness and precision. The successful implementation of this controller underlines its potential for broader applications in systems requiring high precision, disturbance rejection, and fault tolerance. Future work can explore further optimizations and extensions of this approach, such as adapting the sliding mode controller to dynamic environments or integrating it with machine learning techniques for even greater adaptability and performance in complex scenarios.

CONCLUSION

This paper presents a robust trajectory tracking control strategy for a two-link manipulator, incorporating actuator dynamics to achieve high precision in motion

control. The proposed Sliding Mode Controller (SMC) ensures exceptional robustness when handling uncertainties, nonlinearities, and external disturbances, which are common in real-world robotic systems. The stability analysis, conducted using Lyapunov's method, guarantees the convergence of tracking errors, ensuring that the manipulator's end-effector follows the desired trajectory accurately over time. This approach effectively compensates for dynamic discrepancies and external forces, which are often unpredictable, demonstrating the controller's capability to maintain robust performance even in less-than ideal conditions. Simulation results presented in this paper validate the effectiveness of the Sliding Mode Controller in both ideal and real-world scenarios. The controller succeeds in minimizing trajectory tracking errors, exhibiting fast error convergence and stability, even under disturbances such as varying load conditions and modeling inaccuracies. Furthermore, the controller handles actuator dynamics smoothly, ensuring minimal voltage and current fluctuations while maintaining the desired performance. The absence of significant overshoot or oscillations in the system further underscores the potential of this control strategy for use in high-precision robotic applications, where consistency and reliability are critical.

The results highlight the proposed Sliding Mode Controller as a strong candidate for industrial applications that demand high accuracy, such as robotic arms used in manufacturing, medical surgery, and automation tasks. The controller's ability to maintain stability and accuracy even in dynamic and uncertain environments makes it highly adaptable for real-time applications. Additionally, the smooth voltage and current profiles produced by the controller enhance system efficiency, reducing the wear on actuators and promoting longterm reliability of the robotic system.

Looking ahead, future work will focus on extending the proposed control strategy to multi-degree-of-freedom manipulators, which present additional complexities in terms of system dynamics, control structure, and error convergence. The increased degrees of freedom will require more sophisticated control strategies that can handle the added complexity while maintaining performance. Experimental validation of the Sliding Mode Controller will also be a critical next step to confirm the theoretical results obtained through

simulation. Real-world experiments will provide further insights into the controller's robustness, including its ability to cope with environmental uncertainties and real-time system dynamics.

Moreover, future developments will explore the integration of the Sliding Mode Controller with adaptive control techniques and machine learning-based approaches. These hybrid strategies have the potential to further enhance the controller's performance, especially in highly dynamic environments where real-time adaptations are essential. By combining the inherent robustness of SMC with adaptive learning mechanisms, it may be possible to achieve even greater performance, particularly in environments with unpredictable disturbances or where system parameters change over time.

Furthermore, the integration of sensor feedback and realtime data processing could help to fine-tune the controller's performance, leading to further improvements in precision and system response.

In conclusion, the work presented in this paper offers a solid foundation for the design and implementation of robust trajectory tracking controllers in robotic manipulators. The proposed Sliding Mode Controller is an effective solution for handling actuator dynamics, uncertainties, and disturbances, providing a reliable control strategy for a wide range of robotic applications. With continued research, the approach can be further extended to more complex systems, paving the way for more autonomous, precise, and reliable robotic technologies in the future.

REFERENCES

- [1] J. Peng, S. Ding, Z. Yang, and J. Xin, "Adaptive neural impedance control for electrically driven robotic systems based on a neuro-adaptive observer," *Nonlinear Dynamics*, vol. 100, pp. 1359-1378, 2020.
- [2] J. Peng, S. Ding, and R. Dubay, "Adaptive Impedance Control Based on Neural Network for Electrically-Driven Robotic Systems," in *2020 IEEE International Systems Conference (SysCon)*, 2020, pp. 1-6.
- [3] W. Si, L. Zhao, J. Wei, and Z. Guan, "Task-space regulation of rigidlink electrically-driven robots with uncertain kinematics using neural networks," *Measurement and Control*, vol. 54, no. 1-2, pp. 102-115, 2021.
- [4] M. Rani and N. Kumar, "An Intelligent Tracking Control Scheme for Electrically-Driven Redundant

- Robots,” *Pertanika Journal of Science & Technology*, vol. 27, no. 3, 2019.
- [5] M. Rani and N. Kumar, “Intelligent tracking control of redundant robot manipulators including actuator dynamics,” *Procedia Computer Science*, vol. 125, pp. 50-58, 2018.
- [6] K. Rani and N. Kumar, “Intelligent controller for hybrid force and position control of robot manipulators using RBF neural network,” *International Journal of Dynamics and Control*, vol. 7, pp. 767-775, 2019.
- [7] Y. C. Chang, “Robust adaptive neural tracking control for a class of electrically driven robots with time delays,” *International Journal of Systems Science*, vol. 45, no. 11, pp. 2418-2434, 2014.
- [8] J. Yun, Y. Sun, C. Li, D. Jiang, B. Tao, G. Li, et al., “Self-adjusting force/bit blending control based on quantitative factor-scale factor fuzzy PID bit control,” *Alexandria Engineering Journal*, vol. 61, no. 6, pp. 4389-4397, 2022.
- [9] Y.C. Chang, “Adaptive tracking control for electrically-driven robots without overparametrization,” *International Journal of Adaptive Control and Signal Processing*, vol. 16, no. 2, pp. 123-150, 2002.
- [10] J. Park and I. W. Sandberg, “Universal approximation using radial-basisfunction networks,” *Neural Computation*, vol. 3, no. 2, pp. 246-257, 1991.
- [11] H. Gao, L. Wang, and Y. Liu, “Entirely coupled recurrent neural network-based backstepping control for global stability of power system networks,” *IEEE Transactions on Neural Networks and Learning Systems*, vol. 31, no. 5, pp. 1572-1584, 2020, doi: 10.1109/TNNLS.2019.2942240.
- [12] X. Yang and Q. Zhu, “Adaptive backstepping control for a class of robotic systems with unknown dynamics and disturbances,” *IEEE Transactions on Systems, Man, and Cybernetics: Systems*, vol. 48, no. 10, pp. 1671-1680, 2018, doi:10.1109/TSMC.2017.2759452.
- [13] D.T. Tran, D.X. Ba, and K.K. Ahn, “Adaptive backstepping sliding mode control for equilibrium position tracking of an hydroelectrically elastic manipulator,” *IEEE Transactions on Industrial Electronics*, vol. 67, pp. 3860-3869, 2020.
- [14] J.J. Slotine and W. Li, *Applied Nonlinear Control*, Prentice Hall, 1991.
- [15] V.I. Utkin, “Variable structure systems with sliding modes,” *IEEE Transactions on Automatic Control*, vol. 22, no. 2, pp. 212-222, 1977.
- [16] D. Xu, Y. Huang, X. Zhou, and H. Xu, “Path following control for large inland ships in a restricted waterway using the nonlinear terminal sliding mode method,” *Ocean Eng.*, vol. 284, 2023, Art. no. 115159.
- [17] H.P. Singh, “Simulation of neural network based adaptive compensator control scheme for multiple mobile manipulators with uncertainties,” *Int. J. Nonlinear Sci. Numer. Simul.*, vol. 15, no. 3-4, pp. 181-188, 2011.
- [18] H.P. Singh and N. Sukavanam, “Intelligent robust adaptive trajectory and force tracking controller for holonomic constrained nonholonomic mobile manipulator,” *Adv. Sci. Lett.*, vol. 16, pp. 313-321, 2012.
- [19] S. Zhang, M. Lei, and Y. Dong, “Adaptive neural network control of coordinated robotic manipulators with output constraint,” *IET Control Theory Appl.*, vol. 10, no. 17, pp. 2271-2278, 2014.
- [20] Y. Wang, T. Mai, and J. Mao, “Adaptive motion/force control strategy for nonholonomic mobile manipulator robot using fuzzy wavelet neural networks,” *Adv. Robotics*, vol. 34, pp. 137-153, 2014.
- [21] Z. P. Wang, T. Zhou, and Y. Mao, “Adaptive recurrent neural network control of uncertain constrained nonholonomic mobile manipulators,” *Int. J. Syst. Sci.*, vol. 45, no. 2, pp. 133-144, 2014.
- [22] Z. Li, S.S. Ge, and M. Adams, “Adaptive robust output feedback motion/force control of electrically driven nonholonomic mobile manipulators,” *IEEE Trans. Control Syst. Technol.*, vol. 16, no. 6, pp. 1308-1315, 2008.
- [23] A. Karry and M. Feki, “Adaptive tracking control of a mobile manipulator actuated by DC motors,” *Int. J. Modelling, Identification and Control*, vol. 21, no. 2, pp. 193-201, 2014.
- [24] B.S. Park, J.B. Park, and Y.H. Choi, “Robust formation control of electrically driven nonholonomic mobile robots via sliding mode technique,” *Int. J. Control, Autom. Syst.*, vol. 9, no. 5, pp. 888-894, 2011.
- [25] H. Guangxin and Z. Yanhui, “Trajectory tracking control of nonholonomic wheeled mobile robots with actuator dynamics being considered,” *Adv. Mater. Res.*, vol. 433-440, pp. 2596-2601, 2012.
- [26] Y. Zhu and L. Fan, “On robust hybrid force/motion control strategies based on actuator dynamics for nonholonomic mobile manipulators,” *J. Appl. Math.*, pp. 1-19, 2012.
- [27] S. J. Yoo, J. B. Park, and Y. H. Choi, “Adaptive formation tracking control of electrically driven multiple mobile robots,” *IET Control Theory Appl.*, vol. 4, no. 8, pp. 1489-1500, 2009.
- [28] M. Boukens, A. Boukabou, and M. Chadli, “Robust adaptive neural network based trajectory tracking control approach for nonholonomic electrically driven mobile robots,” *Robotics and Autonomous Systems*, vol. 92, pp. 30-40, 2017.
- [29] Y.C. Chang, “Robust adaptive neural tracking control for a class of electrically driven robots with time delays,” *Int. J. Syst. Sci.*, vol. 45, no. 11, pp. -2434, 2014.



Study of Wave Propagation in Piezo-visco-thermo-elastic Material

Vipin Gupta¹ & Daksh Sen²

ABSTRACT

This study examines plane wave propagation in orthotropic piezo-visco-thermo-elastic half-space using memory-dependent derivative analysis within the three-phase lag heat model. Coupled governing equations incorporating kernel function and delay time are solved via the normal mode technique. This research is vital for enhancing the performance of advanced materials in sensors, actuators, and energy harvesters, where wave propagation and thermoelectric interactions are key factors. The results could significantly impact aerospace and mechanical engineering, particularly in developing materials that can withstand complex thermal and mechanical stresses.

Keywords: Kernel Function, Memory-dependent Derivative, Three-phase Lag, Piezo-visco-thermo-elastic

INTRODUCTION

The field of thermoelasticity has evolved significantly since its inception. Biot's [1] classical thermoelasticity theory (CTT) introduced a parabolic type differential equation, but it failed to accurately describe thermal signal velocity. This limitation led to several important advancements in the field. Lord and Shulman [2] enhanced the CTT by modifying Fourier's law with the addition of a relaxation time parameter. Subsequently, Green and Naghdi [3], [4], [5] introduced three distinct thermoelastic models (GN-I, GN-II, and GN-III) to address various heat flow problems. Tzou's [6] contribution came in the form of the dual-phase-lag (2PL) model, which incorporated phase lags into Fourier's law to account for thermal inertia and microstructural interactions. Finally, Roy Choudhuri [8] expanded the 2PL heat model into the three-phase lag (3PL) by using an additional delay time to represent the thermal displacement gradient. These progressive developments have significantly enhanced our understanding and modeling capabilities in thermoelasticity.

The field of piezoelectricity has seen significant advancements since its discovery in 1880 by the Curie brothers [9]. This phenomenon, which involves the generation of electrical charge in response to applied mechanical stress, has found applications in various

domains including actuation, dynamic sensing, and intelligent structures. Abo-Dahab and colleagues [12]–[16] conducted extensive studies on reflection problems involving fractional derivatives, providing new insights into the behavior of these systems. Numerous researchers [17]–[25] have explored various aspects of plane wave behavior in piezoelectric materials, furthering our understanding of wave propagation in these systems. These studies have collectively advanced our knowledge of piezoelectric materials and their applications, paving the way for innovative developments in fields such as civil engineering and energy harvesting systems.

Wang and Li's innovative concept of memory-dependent derivatives (MDD) [26] emerged from fractional derivative analysis. Their work illuminates how sliding intervals transform a Caputo-type [27] fractional derivative into an integral derivative form, characterized by a distinctive kernel function. For a function f defined on a sliding interval $[(t - \tau), t]$, the first-order MDD is expressed as an integral, incorporating a kernel function $K(t - \xi)$ and a delay time factor $\tau > 0$. This formulation can be represented mathematically as:

$$D_{\tau} f(t) = \frac{1}{\tau} \int_{t-\tau}^t K_{(\Omega_1, \Omega_2)}(t - \xi) f'(\xi) d\xi \quad \dots(1)$$

¹ Department of Mathematics, Gurugram University, Gurugram, India. E-mail: vipin@gurugramuniversity.ac.in

² Department of Mathematics, Gurugram University, Gurugram, India. E-mail: dakshsen2@gmail.com

The D_τ operates as a nonlocal operator. When the order of differentiation approaches unity, the MDD can be interpreted as a standard derivative in its most rigorous sense. The selection of an appropriate kernel function can be tailored to suit the intricacy of the problem under consideration.

$$K_{(\Omega_1, \Omega_2)}(t - \xi) = 1 - \frac{2\Omega_2}{\tau}(t - \xi) + \frac{\Omega_1^2}{\tau^2}(t - \xi)^2$$

$$= \begin{cases} 1 & \text{if } \Omega_1 = \Omega_2 = 0 \\ 1 - (t - \xi)/\tau & \text{if } \Omega_1 = 0, \Omega_2 = 1/2 \\ (1 - (t - \xi)/\tau)^2 & \text{if } \Omega_1 = \Omega_2 = 1 \end{cases} \quad \dots(2)$$

Viscous materials, encompassing amorphous substances, polymers, and semi-crystalline materials are crucial in diverse engineering disciplines. The Voigt model [30] stands out as a prominent macroscopic mechanical model for describing viscoelastic material behavior. It effectively demonstrates how elastic materials respond to stress, emphasizing that while deformation is time-dependent, it remains recoverable. Extensive research has been conducted on various facets of viscoelasticity and thermo-viscoelasticity, exploring issues such as [31]–[36].

The present study the propagation of plane waves in piezo-visco-thermo-elastic materials, utilizing the 3PL MDD model to account for the complex interplay between thermal, mechanical, and electrical fields. The 3PL model, known for its ability to describe non-Fourier heat conduction, is particularly well-suited to capture the intricate time-dependent phenomena inherent in piezo-visco-thermo-elastic behavior.

BASIC EQUATIONS

Following Roy Choudhuri [8], Voigt [30], Guha and Singh [37], the fundamental dynamical governing equations for anisotropic piezo-visco-thermo-elastic crystals incorporating the MDD three-phase lag model under the assumption of no heat sources, body forces, or electric forces are given as:

- Generalized Hooke's law

$$\sigma_{ij} = c_{ijrl} e_{rl} - \eta_{ijr} E_r - \beta_{ij} T \quad \dots(3)$$

- Equation of motion

$$\sigma_{ji,j} = \ddot{\rho} u_i \quad \dots(4)$$

- Electric constitutive equation

$$D_i = \epsilon_{ij} E_j + \eta_{ijr} e_{jr} + \tau_i T \quad \dots(5)$$

with

$$E_i = -\varphi_i \quad \dots(6)$$

- Equation of electrostatics

$$D_{i,i} = 0 \quad (7)$$

The 3PL heat law incorporating MDD can be expressed as

$$(1 + \tau_V D_T) K_{ij}^* T_{ij} + (1 + \tau_T D_\tau) K_{ij}^* T_{ij}$$

$$= \left(e + \tau_q D_\tau + \frac{\tau_q^2}{2} D_\tau^2 \right) \left(\rho \ddot{C}_E T + T_0 (\ddot{\beta}_{ij} u_{i,j} - \ddot{\tau}_i \varphi_j) \right) \quad (8)$$

where

$$c_{ijrl} = \bar{c}_{ijrl} + c_{ijrl}^V \frac{\partial}{\partial t} \quad \dots(9)$$

$$\beta_{ij} = c_{ijrl} a_{ro}^* \cdot (i, j, r, l = 1, 2, 3) \quad \dots(10)$$

Nomenclature

τ_q	= phase lag of heat flux
T	= thermal temperature
ρ	= density
β_{ij}	= thermal moduli tensors
φ	= electrical potential
$\eta_{ijr}, \epsilon_{ij}$	= piezothermal moduli tensors
τ_T	= phase lag of the temperature gradient
\bar{C}_{ijrl}	= elastic stiffness tensor
E_i	= electric field density
a	= fractional order parameter
K_{ij}^*	= heat conduction tensor
τ_i	= pyroelectric constants
T_0	= reference temperature
C_E	= specific heat at constant strain
K_{ij}	= components of the thermal conductivity
D_i	= electric displacement
σ_{ij}	= components of the stress
τ_V	= phase lag of thermal disp. Gradient
e_{ij}	= component of strain
C_{ijrl}^V	= viscoelastic constants

An over-dot signifies a time derivative, while the subscript followed by a comma denotes the partial derivative.

FORMULATION OF THE PROBLEM

This study focuses on a homogeneous, orthotropic piezo-visco-thermo-elastic medium situated in the x_1x_3 -plane and influenced by MDD. The constitutive relations specific to the x_1x_3 -plane are represented component-wise as:

$$\sigma_{11} = \eta_{31} \varphi_3 + c_{11} u_{1,1} + c_{13} u_{3,3} - \beta_1 T \quad \dots(11)$$

$$\sigma_{13} = \eta_{15} \varphi_1 + c_{55} (u_{1,3} + u_{3,1}) \quad \dots(12)$$

$$\sigma_{33} = \eta_{33} \varphi_3 + c_{13} u_{1,1} + c_{33} u_{3,3} - \beta_3 T \quad \dots(13)$$

$$D_1 = \eta_{15} (u_{1,3} + u_{3,1}) - \varepsilon_{11} \varphi_1 \quad \dots(14)$$

$$D_3 = \eta_{31} u_{1,1} + \eta_{33} u_{3,3} - \varepsilon_{33} \varphi_3 + \tau_3 T \quad \dots(15)$$

By applying equations (11) to (13) to equation (4), the resulting equations of motion are derived as follows:

$$c_{11} u_{1,11} + c_{55} u_{1,33} + (c_{55} + c_{13}) u_{3,13} + (\eta_{31} + \eta_{15}) \varphi_{13} - \beta_1 T_{,1} = \rho \ddot{u}_1 \quad \dots(16)$$

$$(c_{55} + c_{13}) u_{1,13} + c_{33} u_{3,33} + c_{55} u_{3,11} + \eta_{15} \varphi_{11} + \eta_{33} \varphi_{33} - \beta_3 T_{,3} = \rho \ddot{u}_3 \quad \dots(17)$$

Utilizing equation (16), the 3PL heat equation with MDD is derived in the x_1x_3 -plane

$$(1 + \tau_v D_\tau) (K_1^* T_{,11} + K_3^* T_{,33}) + (1 + \tau_\tau D_\tau) (K_1 \dot{T}_{,11} + K_3 \dot{T}_{,33}) = \left(1 + \tau_q D_\tau + \frac{\tau_q^2}{2} D_\tau^2 \right) (\rho C_E \ddot{T} + T_0 (\beta_1 \ddot{u}_{1,1} + \beta_3 \ddot{u}_{3,3} - \tau_3 \ddot{\varphi}_3)) \quad \dots(18)$$

Equations (14) and (15) are substituted into equation (15) to obtain the electrostatics equation as follows:

$$(\eta_{15} + \eta_{31}) u_{1,13} + \eta_{15} u_{3,11} + \eta_{33} u_{3,33} - \varepsilon_{11} \varphi_{11} - \varepsilon_{33} \varphi_{33} + \tau_3 T_{,3} = 0 \quad \dots(19)$$

where, $\beta_{ij} = \beta_{ij} \delta_{ij}$, $K_{ij}^* = K_i^* \delta_{ij}$, $K_{ij} = K_i \delta_{ij}$, and i is not summed.

The following non-dimensional formulas are considered:

$$(x_1', x_3') = \frac{\omega_1}{c_1} (x_1, x_3), \quad \varphi' = \frac{\omega_1 \eta_{31}}{c_1 \beta_1 T_0} \varphi,$$

$$(t', \tau_\tau', \tau_q', \tau_v') = \omega_1 (t, \tau_\tau, \tau_q, \tau_v), \quad T' = \frac{\beta_1 T}{\rho c_1^2},$$

$$(u_1', u_3') = \frac{\omega_1}{c_1} (u_1, u_3), \quad (D_1', D_3') = \frac{c_1}{\eta_{33} \beta_1 T_0} (D_1, D_3),$$

$$\sigma'_{ij} = \frac{\sigma_{ij}}{\beta_1 T_0}, \text{ where } \omega_1 = \frac{\rho C_E c_1^2}{K_1}, \quad c_1 = \sqrt{\frac{c_{11}}{\rho}} \quad \dots(20)$$

After applying dimensionless transformations to equations (16)-(19) and subsequently omitting the prime notation, we obtain the following set of equations in their non-dimensional form

$$\left(\frac{\partial^2}{\partial x_1^2} + b_{11} \frac{\partial^2}{\partial x_3^2} - b_{12} \frac{\partial^2}{\partial t^2} \right) u_1 + b_{13} \frac{\partial^2 u_3}{\partial x_1 \partial x_3} + b_{14} \frac{\partial^2 \varphi}{\partial x_1 \partial x_3} - b_{12} \frac{\partial T}{\partial x_1} = 0 \quad \dots(21)$$

$$\frac{\partial^2 u_1}{\partial x_1 \partial x_3} + \left(b_{21} \frac{\partial^2}{\partial x_1^2} + b_{22} \frac{\partial^2}{\partial x_3^2} - b_{23} \frac{\partial^2}{\partial t^2} \right) u_3 + \left(b_{24} \frac{\partial^2}{\partial x_1^2} + b_{25} \frac{\partial^2}{\partial x_3^2} \right) \varphi - b_{26} \frac{\partial T}{\partial x_3} = 0 \quad \dots(22)$$

$$(1 + \tau_v D_\tau) \left(b_{31} \frac{\partial^2}{\partial x_1^2} + b_{32} \frac{\partial^2}{\partial x_3^2} \right) T + (1 + \tau_\tau D_\tau) \left(b_{33} \frac{\partial^2}{\partial x_1^2} + b_{34} \frac{\partial^2}{\partial x_3^2} \right) T = \left(1 + \tau_q D_\tau + \frac{\tau_q^2}{2} D_\tau^2 \right) \left(\frac{\partial u_1}{\partial x_1} + b_{35} \frac{\partial u_3}{\partial x_3} - b_{36} \frac{\partial \varphi}{\partial x_3} + b_{37} T \right) \quad \dots(23)$$

$$\frac{\partial^2 u_1}{\partial x_1 \partial x_3} + \left(b_{41} \frac{\partial^2}{\partial x_1^2} + b_{42} \frac{\partial^2}{\partial x_3^2} \right) u_3 - \left(b_{43} \frac{\partial^2}{\partial x_1^2} + b_{44} \frac{\partial^2}{\partial x_3^2} \right) \varphi + b_{45} \frac{\partial T}{\partial x_3} = 0 \quad \dots(24)$$

where,

$$b_{11} = \frac{c_{44}}{c_{11}}, \quad b_{12} = \frac{c_{11}}{c_{11}}, \quad b_{13} = \frac{c_{13} + c_{44}}{c_{11}},$$

$$b_{14} = \frac{(\eta_{31} + \eta_{15}) \beta_1 T_0}{c_{11} \eta_{31}}, \quad b_{21} = \frac{c_{44}}{c_{44} + c_{13}},$$

$$b_{22} = \frac{c_{33}}{c_{44} + c_{13}}, \quad b_{23} = \frac{c_{11}}{c_{44} + c_{13}},$$

$$b_{24} = \frac{\eta_{15} \beta_1 T_0}{\eta_{31} (c_{44} + c_{13})}, \quad b_{25} = \frac{\eta_{33} \beta_1 T_0}{\eta_{31} (c_{44} + c_{13})},$$

$$b_{26} = \frac{c_{11} \beta_3}{(c_{44} + c_{13}) \beta_1}, \quad b_{31} = \frac{K_1^* \rho}{T_0 \beta_1^2}, \quad b_{32} = \frac{K_3^* \rho}{T_0 \beta_1^2},$$

$$\begin{aligned}
b_{33} &= \frac{K_1 \omega_1 \rho}{T_0 \beta_1^2}, \quad b_{34} = \frac{K_3 \omega_1 \rho}{T_0 \beta_1^2}, \quad b_{35} = \frac{\beta_3}{\beta_1}, \\
b_{36} &= \frac{\tau_3 T_0}{\eta_{31}}, \quad b_{37} = \frac{c_{11} \rho C_E}{T_0 \beta_1^2}, \quad b_{41} = \frac{\eta_{15}}{(\eta_{15} + \eta_{31})}, \\
b_{42} &= \frac{\eta_{33}}{(\eta_{15} + \eta_{31})}, \quad b_{43} = \frac{\varepsilon_{11} \beta_1 T_0}{\eta_{31}(\eta_{15} + \eta_{31})}, \\
b_{44} &= \frac{\varepsilon_{33} \beta_1 T_0}{\eta_{31}(\eta_{15} + \eta_{31})}, \quad b_{45} = \frac{c_{11} \tau_3}{\beta_1(\eta_{15} + \eta_{31})}.
\end{aligned}$$

SOLUTION OF THE PROBLEM

The solution can be decomposed into normal modes as follows [38]:

$$\begin{aligned}
&[\varphi, u_1, u_3, T](x_1, x_3, t) = \\
&[\varphi^*, u_1^*, u_3^*, T^*](x_3) \exp[ia(x_1 - ct)]
\end{aligned} \quad \dots(25)$$

where, φ^* , u_1^* , u_3^* , and T^* are the amplitudes of the functions φ , u_1 , u_3 , and T , respectively.

Using equation (25) into equations (21)–(24) and using $D = d/dz$, we obtain

$$(A_1 + b_{11} D^2)u_1^* + A_2 Du_3^* + A_3 D\varphi^* - A_4 T^* = 0 \quad \dots(26)$$

$$\begin{aligned}
&A_4^* Du_1^* + (b_{22} D^2 + A_5)u_3^* + (A_6 + b_{25} D^2)\varphi^* \\
&- b_{26} DT^* = 0
\end{aligned} \quad \dots(27)$$

$$\begin{aligned}
&A_7 u_1^* + A_8 Du_3^* - A_9 D\varphi^* + \\
&\left(A_{10} + H_1 A_{11} + H_1 b_{32} D^2 + \right. \\
&\left. H_2 A_{12} + H_2 A_{13} D^2 \right) T^* = 0
\end{aligned} \quad \dots(28)$$

$$\begin{aligned}
&A_4^* Du_1^* + (A_{14} + b_{42} D^2)u_3^* - (A_{15} + b_{44} D^2)\varphi^* \\
&+ b_{45} DT^* = 0
\end{aligned} \quad \dots(29)$$

where,

$$\begin{aligned}
A_1 &= a^2(b_{12}c^2 - 1), \quad A_2 = iab_{13}, \quad A_3 = iab_{14}, \\
A_4 &= iab_{12}, \quad A_4^* = ia, \quad A_5 = -b_{21}a^2 + b_{23}a^2c^2, \\
A_6 &= -b_{24}a^2, \quad A_7 = ia^3c^2, \quad A_8 = b_{35}a^2c^2, \\
A_9 &= b_{36}a^2c^2, \quad A_{10} = b_{37}a^2c^2, \quad A_{11} = -b_{31}a^2, \\
A_{12} &= ib_{33}a^3c, \quad A_{13} = -b_{34}iac, \quad A_{14} = -a^2b_{41},
\end{aligned}$$

$$A_{15} = -a^2b_{43}, \quad H_1 = \frac{1 + \tau_v \Lambda(\tau, b)}{1 + \tau_q \Lambda(\tau, b) + \tau_q^2 b \Lambda(\tau, b)/2},$$

$$H_2 = \frac{1 + \tau_T \Lambda(\tau, b)}{1 + \tau_q \Lambda(\tau, b) + \tau_q^2 b \Lambda(\tau, b)/2}, \quad b^* = -iac,$$

$$\Lambda(\tau, b^*) = \frac{\left(\begin{aligned} &-b^2 \tau^2 (\Omega_1^2 - 2\Omega_2 + 1) + \\ &2b^* \tau (\Omega_1^2 - \Omega_2) + 2\Omega_1^2 \\ &+ b^{*2} \tau^2 - 2b^* \Omega_2 \tau + 2a\Omega_1^2 \end{aligned} \right) \exp(-b^* \tau)}{b^{*2} \tau^3} \quad \dots(30)$$

A non-trivial solution for equations (4.2) to (4.5) exists only if the determinant of the coefficient matrix of the preceding linear system is zero. Then

$$\begin{aligned}
&(D^8 - AD^6 + BD^4 - CD^2 + E) \\
&\{\varphi^*(x_3), u_1^*(x_3), u_3^*(x_3), T^*(x_3)\} = 0
\end{aligned} \quad \dots(31)$$

where, the coefficient expressions are written in the Appendix.

Equation (31) can be expressed as:

$$\begin{aligned}
&(D^2 - k_1^2)(D^2 - k_2^2)(D^2 - k_3^2)(D^2 - k_4^2) \\
&\{\varphi^*(x_3), u_1^*(x_3), u_3^*(x_3), T^*(x_3)\} = 0
\end{aligned} \quad \dots(32)$$

The solutions of equation (32) can be written as, which are bounded as $x_3 \rightarrow \infty$.

$$(u_1^*, u_3^*, \varphi^*, T^*) = \sum_{n=1}^4 (1, L_{1n}, L_{2n}, L_{3n}) M_n \exp(-k_n x_3) \quad \dots(33)$$

where, k_n^2 , ($n = 1 - 4$) are the roots of equation (33).

Substituting equation (33) into equations (11)–(15) and performing a dimensionless analysis within the normal mode approach yields

$$\begin{pmatrix} \sigma_{11}^*, \sigma_{33}^*, \sigma_{13}^* \\ D_1^*, D_3^* \end{pmatrix} = \sum_{n=1}^4 \begin{pmatrix} L_{4n}, L_{5n}, L_{6n} \\ L_{7n}, L_{8n} \end{pmatrix} \exp(-k_n x_3) \quad \dots(34)$$

where L_{jn} , $n = 1 - 4$, $j = 1 - 8$ are provided in the Appendix.

BOUNDARY CONDITIONS

The following boundary conditions enable the solution of the governing equations in a half-space ($x_1, x_2, x_3 \geq 0$)

$$\begin{aligned}
\sigma_{33}(x_1, 0, t) &= f_1(x_1, t) = -f_1^* \exp[ia(x_1 - ct)], \\
\sigma_{13}(x_1, 0, t) &= 0
\end{aligned} \quad \dots(35)$$

$$T(x_1, 0, t) = f_2(x_1, t) = f_2^* \exp[i a(x_1 - ct)] \quad \dots(35)$$

$$\varphi_3(x_1, 0, t) = 0 \quad \dots(37)$$

where, f_1 and f_2 are functions of (x_1, t) , f_1^* , f_2^* are constant, $\omega = ac$ is the wave frequency, and a be the wave number in the x_1 -direction.

By inserting the proposed solutions into the boundary conditions specified in equations (35)–(37) to solve for the coefficients M_n ($n = 1 - 4$), we obtain

$$\sum_{n=1}^4 L_{5n} M_n = -f_1^* \quad \dots(38)$$

$$\sum_{n=1}^4 L_{6n} M_n = 0 \quad \dots(39)$$

$$\sum_{n=1}^4 L_{3n} M_n = f_2^* \quad (40)$$

$$\sum_{n=1}^4 k_n L_{2n} M_n = 0 \quad \dots(41)$$

After solving equations (38)–(41), we get

$$\begin{bmatrix} M_1 \\ M_2 \\ M_3 \\ M_4 \end{bmatrix} = \begin{bmatrix} L_{51} & L_{52} & L_{53} & L_{54} \\ L_{61} & L_{62} & L_{63} & L_{64} \\ L_{31} & L_{32} & L_{33} & L_{34} \\ k_1 L_{21} & k_2 L_{22} & k_3 L_{23} & k_4 L_{24} \end{bmatrix}^{-1} \begin{bmatrix} -f_1^* \\ 0 \\ f_2^* \\ 0 \end{bmatrix} \quad \dots(42)$$

where, the elements of matrix $L_{5i}, L_{6i}, L_{3i}, L_{2i}, i = 1 - 4$ are provided in Appendix.

Consequently, we are able to derive exact mathematical expressions for the components of the displacement vector, the temperature distribution, the electric potential field, the stress tensor elements, and the electric displacement vector.

CONCLUSIONS

This study has examined the propagation of plane waves in an orthotropic piezo-visco-thermoelastic half-space using memory-dependent derivative analysis within the three-phase lag heat model. The research has yielded several significant findings:

1. The incorporation of the memory-dependent derivative and three-phase lag model has allowed for a more comprehensive description of the complex behavior of piezo-visco-thermoelastic materials under wave propagation.

2. The governing equations, which include crucial factors such as relaxation time, time delay, and kernel functions, have been successfully formulated and solved using the normal mode analysis technique.
3. The study has provided analytical expressions for various physical quantities, including displacement components, temperature distribution, electric potential, stress tensor elements, and electric displacement vector.
4. The analytical solutions derived in this study offer a foundation for understanding the intricate interplay between thermal, mechanical, and electrical fields in piezo-visco-thermoelastic materials.

These results contribute to the broader understanding of wave propagation in advanced materials and have potential applications in the development and optimization of sensors, actuators, and energy harvesters.

APPENDIX

$$P_1 = b_{11} b_{26}, P_2 = b_{26} A_1 - A_4 A_4^*, P_3 = b_{26} A_2 - b_{24} A_4,$$

$$P_4 = -A_4 A_5, P_5 = b_{26} A_3 - b_{25} A_4, P_6 = -A_4 A_6,$$

$$P_7 = b_{11} A_{17}, P_8 = b_{11} A_{16} + A_1 A_{17}, P_9 = A_1 A_{16} + A_4 A_7,$$

$$P_{10} = A_2 A_{17}, P_{11} = A_2 A_{16} + A_4 A_8, P_{12} = A_3 A_{17},$$

$$P_{13} = A_3 A_{16} - A_4 A_9, P_{14} = b_{11} b_{45}, P_{15} = b_{45} A_1 - A_4 A_4^*,$$

$$P_{16} = b_{45} A_2 + b_{42} A_4, P_{17} = A_4 A_{14},$$

$$P_{18} = b_{45} A_3 - A_4 b_{44}, P_{19} = -A_4 A_{15}$$

$$\Delta_0 = P_5 P_7 P_{16} - P_3 P_7 P_{18} + P_1 P_{10} P_{18} - P_1 P_{12} P_{16} + \\ + P_3 P_{12} P_{24} - P_5 P_{10} P_{24}$$

$$\Delta_1 = P_5 P_7 P_{17} + P_5 P_8 P_{16} - P_6 P_7 P_{16} + P_1 P_{10} P_{19} \\ - P_3 P_8 P_{18} - P_4 P_7 P_{18} - P_3 P_7 P_{19} + P_1 P_{11} P_{18} \\ - P_1 P_{12} P_{17} - P_1 P_{13} P_{16} + P_2 P_{10} P_{18} - P_2 P_{12} P_{16} \\ - P_3 P_{12} P_{15} + P_3 P_{13} P_{14} + P_4 P_{12} P_{14} - P_5 P_{10} P_{15} \\ - P_5 P_{11} P_{14} - P_6 P_{10} P_{14}$$

$$\Delta_2 = P_5 P_8 P_{17} - P_3 P_9 P_{18} - P_4 P_7 P_{19} - P_4 P_8 P_{18} \\ - P_3 P_8 P_{19} + P_5 P_9 P_{16} + P_6 P_7 P_{17} + P_6 P_8 P_{16} \\ + P_1 P_{11} P_{19} - P_1 P_{13} P_{17} + P_2 P_{10} P_{19} + P_2 P_{11} P_{18} \\ - P_2 P_{12} P_{17} - P_2 P_{13} P_{16} + P_3 P_{13} P_{15} + P_4 P_{12} P_{15} \\ + P_4 P_{13} P_{14} - P_5 P_{11} P_{15} - P_6 P_{10} P_{15} - P_6 P_{11} P_{14}$$

$$\Delta_3 = P_5 P_9 P_{17} - P_4 P_8 P_{19} - P_4 P_9 P_{18} - P_3 P_9 P_{19} \\ + P_6 P_8 P_{17} + P_6 P_9 P_{16} + P_2 P_{11} P_{19} - P_2 P_{13} P_{17} \\ + P_4 P_{13} P_{15} - P_6 P_{11} P_{15}$$

$$\Delta_4 = P_6 P_9 P_{17} - P_4 P_9 P_{19}$$

$$q_{1n} = -P_1 k_n^3 - P_2 k_n, \quad q_{2n} = P_3 k_n^2 + P_4,$$

$$q_{3n} = P_5 k_n^2 + P_6, \quad q_{4n} = P_7 k_n^4 + P_8 q_n^2 + P_9,$$

$$q_{5n} = -P_{10} k_n^3 - P_{11} k_n, \quad q_{6n} = -P_{12} k_n^3 - P_{13} k_n$$

$$A = -\frac{\Delta_1}{\Delta_0}, \quad B = \frac{\Delta_2}{\Delta_0}, \quad C = -\frac{\Delta_3}{\Delta_0}, \quad E = \frac{\Delta_4}{\Delta_0}$$

$$L_{1n} = \frac{q_{3n} q_{4n} - q_{1n} q_{6n}}{q_{2n} q_{6n} - q_{3n} q_{5n}}, \quad L_{2n} = \frac{-q_{1n} - q_{2n} L_{1n}}{q_{3n}},$$

$$L_{3n} = \frac{A_1 + d_{11} k_n^2 - A_2 k_n L_{1n} - A_3 k_n L_{2n}}{A_4}$$

$$L_{4n} = \frac{c_{13} \iota a}{\beta_1 T_0} - \frac{c_{33} k_n L_{1n}}{\beta_1 T_0} - \frac{\eta_{33} k_n L_{2n}}{\eta_{31}} - \frac{c_{11} \beta_3 L_{3n}}{\beta_1^2 T_0},$$

$$L_{5n} = \frac{c_{55} (\iota a L_{1n} - k_n)}{\beta_1 T_0} + \frac{\eta_{15} \iota a L_{2n}}{\eta_{31}},$$

$$L_{6n} = \frac{\iota a c_{11}}{\beta_1 T_0} - \frac{c_{13} k_n L_{1n}}{\beta_1 T_0} - k_n L_{2n} - \frac{L_{3n} c_{11}}{\beta_1 T_0},$$

$$L_{7n} = \frac{c_{11} \eta_{15} (\iota a L_{1n} - k_n)}{\beta_1 T_0 \eta_{33}} - \frac{c_{11} \epsilon_{11} \iota a L_{2n}}{\eta_{33} \eta_{31}},$$

$$L_{8n} = \frac{c_{11}}{\beta_1 T_0} \left(\frac{\iota a \eta_{31}}{\eta_{33}} - k_n L_{1n} + \frac{\epsilon_{33} \beta_1 T_0 k_n L_{2n}}{\eta_{31} \eta_{33}} + \frac{\tau_3 c_{11} L_{3n}}{\beta_1 \eta_{33}} \right),$$

$$n = 1 - 4$$

REFERENCES

- [1] M.A. Biot, 'Thermoelasticity and irreversible thermodynamics', *J. Appl. Phys.*, vol. 27, no. 3, pp. 240–253, 1956, doi: 10.1063/1.1722351.
- [2] H.W. Lord and Y. Shulman, 'A generalized dynamical theory of thermoelasticity', *J. Mech. Phys. Solids*, vol. 15, no. 5, pp. 299–309, 1967, doi: 10.1016/0022-5096(67)90024-5.
- [3] A.E. Green and P.M. Naghdi, 'A re-examination of the basic postulates of thermomechanics', *Proc. R. Soc. London. Ser. A Math. Phys. Sci.*, vol. 432, no. 1885, pp. 171–194, 1991, doi: 10.1098/rspa.1991.0012.
- [4] A. E. Green and P. M. Naghdi, 'On undamped heat waves in an elastic solid', *J. Therm. Stress.*, vol. 15, no. 2, pp. 253–264, 1992.
- [5] A.E. Green and P.M. Naghdi, 'Thermoelasticity without energy dissipation', *J. Elast.*, vol. 31, no. 3, pp. 189–208, 1993, doi: 10.1007/BF00044969.
- [6] D.Y. Tzou, 'A Unified Field Approach for Heat Conduction From Macro- to Micro-Scales', *J. Heat Transfer*, vol. 117, no. 1, pp. 8–16, Feb. 1995, doi: 10.1115/1.2822329.
- [7] M.A. Ezzat, A.S. El-Karamany, and A.A. El-Bary, 'On dual-phase-lag thermoelasticity theory with memory-dependent derivative', *Mech. Adv. Mater. Struct.*, vol. 24, no. 11, pp. 908–916, Aug. 2017, doi: 10.1080/15376494.2016.1196793.
- [8] S.K.R. Choudhuri, 'On a thermoelastic three-phase-lag model', *J. Therm. Stress.*, vol. 30, no. 3, pp. 231–238, Jan. 2007, doi: 10.1080/01495730601130919.
- [9] J. Curie and P. Curie, 'Development by compression of polar electricity in hemihedral crystals with slanted faces', *Bull. Mineral. Soc. Fr.*, vol. 3, no. 4, pp. 90–93, 1880, doi: 10.3406/bulmi.1880.1564.
- [10] R.D. Mindlin, 'Equations of high frequency vibrations of thermopiezoelectric crystal plates', *Int. J. Solids Struct.*, vol. 10, no. 6, pp. 625–637, 1974, doi: 10.1016/0020-7683(74)90047-X.
- [11] W. Nowacki, 'Some general theorems of thermopiezoelectricity', *J. Therm. Stress.*, vol. 1, no. 2, pp. 171–182, Oct. 1978, doi: 10.1080/01495737808926940.
- [12] S. M. Abo-Dahab and K. Lotfy, 'Generalized magneto-thermoelasticity with fractional derivative heat transfer for a rotation of a fibre-reinforced thermoelastic', *J. Comput. Theor. Nanosci.*, vol. 12, no. 8, pp. 1869–1881, 2015, doi: 10.1166/jctn.2015.3972.
- [13] S.M. Abo-Dahab, A.A. Kilany, E.A.B. Abdel-Salam, and A. Hatem, 'Fractional derivative order analysis and temperature-dependent properties on P- and SV-waves reflection under initial stress and three-phase-lag model', *Results Phys.*, vol. 18, June, p. 103270, 2020, doi: 10.1016/j.rinp.2020.103270.
- [14] S.M. Abo-Dahab, A.E. Abouelregal, and H. Ahmad, 'Fractional heat conduction model with phase lags for a half-space with thermal conductivity and temperature dependent', *Math. Methods Appl. Sci.*, May, pp. 1–16, 2020, doi: 10.1002/mma.6614.
- [15] F.S. Bayones, S.M. Abo-Dahab, A.E. Abouelregal, A. Al-Mullise, S. Abdel-Khalek, and E.M. Khalil, 'Model of fractional heat conduction in a thermoelastic thin slim strip under thermal shock and temperature-dependent thermal conductivity', *Comput. Mater. Contin.*, vol. 67, no. 3, pp. 2899–2913, 2021, doi: 10.32604/cmc.2021.012583.

- [16] M. Ragab, S.M. Abo-Dahab, A.E. Abouelregal, and A.A. Kilany, 'A Thermoelastic Piezoelectric Fixed Rod Exposed to an Axial Moving Heat Source via a Dual-Phase-Lag Model', *Complexity*, vol. 2021, pp. 1–11, Jul. 2021, doi: 10.1155/2021/5547566.
- [17] M.S. Barak, R. Kumar, R. Kumar, and V. Gupta, 'Energy analysis at the boundary interface of elastic and piezothermoelastic half-spaces', *Indian J. Phys.*, vol. 97, no. 8, pp. 2369–2383, Jul. 2023, doi: 10.1007/s12648-022-02568-w.
- [18] M.S. Barak et al., 'Behavior of higher-order MDD on energy ratios at the interface of thermoelastic and piezothermoelastic mediums', *Sci. Rep.*, vol. 13, no. 1, p. 17170, Oct. 2023, doi: 10.1038/s41598-023-44339-5.
- [19] V. Gupta and M. S. Barak, 'Fractional and MDD analysis of piezo-photo-thermo-elastic waves in semiconductor medium', *Mech. Adv. Mater. Struct.*, pp. 1–16, Jul. 2023, doi: 10.1080/15376494.2023.2238201.
- [20] V. Gupta, R. Kumar, M. Kumar, V. Pathania, and M.S. Barak, 'Reflection/transmission of plane waves at the interface of an ideal fluid and nonlocal piezo-thermoelastic medium', *Int. J. Numer. Methods Heat Fluid Flow*, vol. 33, no. 2, pp. 912–937, Jan. 2023, doi: 10.1108/HFF-04-2022-0259.
- [21] V. Gupta, M.S. Barak, and S. Das, 'Impact of memory-dependent heat transfer on Rayleigh waves propagation in nonlocal piezo-thermo-elastic medium with voids', *Int. J. Numer. Methods Heat Fluid Flow*, Mar. 2024, doi: 10.1108/HFF-10-2023-0615.
- [22] V. Gupta, M.S. Barak, and H. Ahmad, 'Reflection of quasi plasma wave in photo-piezo semiconductor medium with distinct higher order fractional derivative two temperature models', *Phys. Scr.*, vol. 99, no. 2, p. 025515, Feb. 2024, doi: 10.1088/1402-4896/ad1972.
- [23] V. Gupta, M.S. Barak, and S. Das, 'Vibrational analysis of size-dependent thermo-piezo-photo-electric semiconductor medium under memory-dependent Moore–Gibson–Thompson photo-thermoelasticity theory', *Mech. Adv. Mater. Struct.*, vol. 0, no. 0, pp. 1–17, Dec. 2023, doi: 10.1080/15376494.2023.2291804.
- [24] V. Gupta and M. S. Barak, 'Quasi-P wave through orthotropic piezo-thermoelastic materials subject to higher order fractional and memory-dependent derivatives', *Mech. Adv. Mater. Struct.*, pp. 1–15, Jun. 2023, doi: 10.1080/15376494.2023.2217420.
- [25] V. Gupta, M.S. Barak, H. Ahmad, S. Das, and B. Almohsen, 'Response of Moisture and Temperature Diffusivity on an Orthotropic Hygro-thermo-piezo-elastic Medium', *J. Nonlinear Math. Phys.*, vol. 31, no. 1, 2024, doi: 10.1007/s44198-024-00187-z.
- [26] J.-L. Wang and H.-F. Li, 'Surpassing the fractional derivative: Concept of the memory-dependent derivative', *Comput. Math. with Appl.*, vol. 62, no. 3, pp. 1562–1567, Aug. 2011, doi: 10.1016/j.camwa.2011.04.028.
- [27] M. Caputo and F. Mainardi, 'A new dissipation model based on memory mechanism', *Pure Appl. Geophys.*, vol. 91, no. 1, pp. 134–147, 1971.
- [28] J.L. Wang and H.F. Li, 'Memory-dependent derivative versus fractional derivative (I): Difference in temporal modeling', *J. Comput. Appl. Math.*, vol. 384, p. 112923, 2021, doi: 10.1016/j.cam.2020.112923.
- [29] J.L. Wang and H.F. Li, 'Memory-dependent derivative versus fractional derivative (II): Remodelling diffusion process', *Appl. Math. Comput.*, vol. 391, no. March, 2021, doi: 10.1016/j.amc.2020.125627.
- [30] W. Voigt, Theoretical studies on the elasticity of crystals. Royal Society of Sciences in Göttingen, 1887.
- [31] E. Gurtin, Morton E. and Sternberg, 'On the linear theory of viscoelasticity', *Brown Univ Provid. Ri Div Appl. Math.*, 1962.
- [32] K. Sharma and P. Kumar, 'Propagation of Plane Waves and Fundamental Solution in Thermoviscoelastic Medium with Voids', *J. Therm. Stress.*, vol. 36, no. 2, pp. 94–111, Feb. 2013, doi: 10.1080/01495739.2012.720545.
- [33] K. Sharma, S. Sharma, and R.R. Bhargava, 'Propagation of waves in micropolar thermoelastic solid with two temperatures bordered with layers or half spaces of inviscid liquid', *Meccanica*, vol. 16, no. 1, pp. 66–81, Nov. 2013, [Online]. Available: <http://link.springer.com/10.1007/s11012-013-9732-9>.
- [34] D.R. Bland, The theory of linear viscoelasticity. Courier Dover Publications, 2016.
- [35] A.E. Abouelregal, H. Ahmad, S.-W. Yao, and H. Abu-Zinadah, 'Thermo-viscoelastic orthotropic constraint cylindrical cavity with variable thermal properties heated by laser pulse via the MGT thermoelasticity model', *Open Phys.*, vol. 19, no. 1, pp. 504–518, Sep. 2021, doi: 10.1515/phys-2021-0034.
- [36] A.E. Abouelregal, H. Ahmad, S.K. Badr, B. Almutairi, and B. Almohsen, 'Viscoelastic stressed microbeam analysis based on Moore–Gibson–Thompson heat equation and laser excitation resting on Winkler foundation', *J. Low Freq. Noise Vib. Act. Control*, vol. 41, no. 1, pp. 118–139, 2022, doi: 10.1177/14613484211040318.
- [37] S. Guha and A.K. Singh, 'Effects of initial stresses on reflection phenomenon of plane waves at the free surface of a rotating piezothermoelastic fiber-reinforced composite half-space', *Int. J. Mech. Sci.*, vol. 181, no. February, p. 105766, 2020, doi: 10.1016/j.ijmecsci.2020.105766.
- [38] E.A.A. Ahmed, M.S. Abou-Dina, and A.F. Ghaleb, 'Plane wave propagation in a piezo-thermoelastic rotating medium within the dual-phase-lag model', *Microsyst. Technol.*, vol. 26, no. 3, pp. 969–979, 2020, doi: 10.1007/s00542-019-04567-0.

- [39] S. Mondal and M.I.A. Othman, 'Memory dependent derivative effect on generalized piezo-thermoelastic medium under three theories', *Waves Random Complex Media*, vol. 31, no. 6, pp. 2150–2167, 2021, doi: 10.1080/17455030.2020.1730480.
- [40] S. Biswas, 'Surface waves in piezothermoelastic transversely isotropic layer lying over piezothermoelastic transversely isotropic half-space', *Acta Mech.*, vol. 232, no. 2, pp. 373–387, 2021, doi: 10.1007/s00707-020-02848-8.
- [41] R. Quintanilla and R. Racke, 'A note on stability in three-phase-lag heat conduction', *Int. J. Heat Mass Transf.*, vol. 51, no. 1–2, pp. 24–29, Jan. 2008, doi: 10.1016/j.ijheatmasstransfer.2007.04.045.



Fixed Point for Chatterjea Contraction and Its Application to Cauchy Problem

Anshuka Kadyan¹, Savita Rathee² & Anil Kumar³

ABSTRACT

As an extension of the main result of Rathee et al. (2022), we establish a fixed point theorem in the framework of convex -metric spaces for Chatterjea contraction. Also, the fixed point is approximated by Kransnoselkij iterative procedure. We finally employ these findings to solve Cauchy problem.

Keywords: Metric Spaces, Convex Metric Spaces, Approximation, Chatterjea Contraction

INTRODUCTION AND PRELIMINARIES

The most useful and widely applied fixed point theorem in the field of fixed point theory ensuring the existence of fixed point for any contraction defined on complete metric spaces was proved by Stefan Banach[5] in 1922. In the literature, this result is also known with the name of Banach contraction principle. By introducing the notion of Chatterjea contraction in 1972, a generalization was set out of this principle by Chatterjea [6]. In 1989, the notion of b -metric spaces was introduced by Bakhtin[4] in lieu to extend this contraction principle. For more detail about this space one can refer to [8],[3], [1], [10], [2]. Chen et al. [7] introduced the concept of convex b -metric spaces in the recent years by using the concept of convex structure defined by Takahashi[13] in 1970.

Definition 1: “Let $\mathcal{U} \neq \phi$ and $s \geq 1$ (a real number). A mapping $\underline{\varrho}_b: \mathcal{U} \times \mathcal{U} \rightarrow [0, \infty)$ is said to be a b -metric if the following holds for every $\underline{q}, \underline{\varsigma}, \underline{\eta} \in \mathcal{U}$

$$1. \quad \underline{\varrho}_b(\underline{q}, \underline{\varsigma}) = 0 \text{ iff } \underline{q} = \underline{\varsigma}$$

$$2. \quad \underline{\varrho}_b(\underline{q}, \underline{\varsigma}) = \underline{\varrho}_b(\underline{\varsigma}, \underline{q})$$

$$3. \quad \underline{\varrho}_b(\underline{q}, \underline{\varsigma}) \leq s[\underline{\varrho}_b(\underline{q}, \underline{\eta}) + \underline{\varrho}_b(\underline{\eta}, \underline{\varsigma})]$$

Further, a function $\underline{\Omega}: \mathcal{U} \times \mathcal{U} \times I \rightarrow \mathcal{U}$ (where $I = [0, 1]$) is said to have convex structure on \mathcal{U} if $\underline{\varrho}_b(\underline{\eta}, \underline{\Omega}(\underline{q}, \underline{\varsigma}; \vartheta)) \leq \vartheta \underline{\varrho}_b(\underline{\eta}, \underline{q}) + (1 - \vartheta) \underline{\varrho}_b(\underline{\eta}, \underline{\varsigma})$ for each $\underline{\eta}, \underline{q}, \underline{\varsigma} \in \mathcal{U}$.

The triplet $(\mathcal{U}, \underline{\varrho}_b, \underline{\Omega})$ is called a convex b -metric space.

Additionally, by using the Mann’s iterative algorithm, the authors established the Banach contraction principle in the framework of this lately introduced space, viz. convex b -metric space. In 2022, Rathee et al. [11] established a fixed point theorem for Chatterjea contraction and extended this result:

Theorem 1: “Suppose $\underline{I}: (\mathcal{U}, \underline{\varrho}_b, \underline{\Omega}) \rightarrow (\mathcal{U}, \underline{\varrho}_b, \underline{\Omega})$ is a quasi-contraction, that is, \underline{I} satisfies

$$\underline{\varrho}_b(\underline{I}\underline{q}, \underline{I}\underline{\varsigma}) \leq \kappa[\underline{\varrho}_b(\underline{q}, \underline{I}\underline{\varsigma}) + \underline{\varrho}_b(\underline{\varsigma}, \underline{I}\underline{q})] \quad \dots(1)$$

for all $\underline{q}, \underline{\varsigma} \in \mathcal{U}$ and some $\kappa \in [0, \frac{1}{2})$, where $(\mathcal{U}, \underline{\varrho}_b, \underline{\Omega})$ is a complete convex b -metric space with $s > 1$. Let

¹ Department of Mathematics, Gurugram University, Gurugram, Haryana, India. E-mail: anshuka.math@gurugramuniversity.ac.in

² Department of Mathematics, Maharshi Dayanand University, Rohtak, Haryana, India

³ Department of Mathematics, Sir Chhotu Ram Government College for Women, Sampla, Rohtak, Haryana, India

$\underline{q}_n = \underline{\Omega}(\underline{q}_{n-1}, \underline{I}\underline{q}_{n-1}; \vartheta_{n-1})$ be a sequence defined by choosing an initial point $\underline{q}_0 \in \mathcal{U}$ with the property $\wp_b(\underline{q}_0, \underline{I}\underline{q}_0) < \infty$, where $0 \leq \vartheta_{n-1} < 1$ for each $n \in \mathbb{N}$. If $\underline{\kappa} \leq \frac{1}{s^2(s^2+1)}$ and $\vartheta_{n-1} < \frac{\frac{1}{s^4} - \frac{\underline{\kappa}}{s^2} - \underline{\kappa}}{\frac{1+\underline{\kappa}}{s} - \underline{\kappa}}$ for each $n \in \mathbb{N}$, then \underline{I} has a fixed point in \mathcal{U} that is unique.

In the present work, we improve this theorem by enlarging the range of $\underline{\kappa} \in [0, \frac{1}{2})$. Furthermore, the fixed point is computed by means of Kransnoselkij iteration. Moreover, some examples are presented to prove the universality of the proven results over Theorem 1 as well as over the similar results existing in the literature. As an application, we arrive at the solution for the Cauchy problem.

MAIN RESULT

We start this section with the following lemma that is required in the sequel to assure the existence and approximation of fixed point.

Lemma 1: Let $\underline{I}: \mathcal{U} \rightarrow \mathcal{U}$ be a self mapping defined on (\mathcal{U}, \wp_b) , a complete b -metric space, such that for all $\underline{q}, \underline{\zeta} \in \mathcal{U}$ and $\underline{\kappa} \in [0, \frac{1}{2})$, it satisfies

$$\wp_b(\underline{I}\underline{q}, \underline{I}\underline{\zeta}) \leq \underline{\kappa}[\wp_b(\underline{q}, \underline{I}\underline{\zeta}) + \wp_b(\underline{\zeta}, \underline{I}\underline{q})] \quad \dots(2)$$

If $\underline{\kappa} < \frac{1}{s^2}$, then \underline{I} has a unique fixed point if and only if \underline{I} has approximate fixed point property, i.e. $\inf\{\wp_b(\underline{q}, \underline{I}\underline{q}); \underline{q} \in \mathcal{U}\} = 0$.

Proof. Firstly, assume that a unique fixed point of \underline{I} , say \underline{q} , exists, i.e., $\underline{I}\underline{q} = \underline{q}$. Then,

$$\wp_b(\underline{q}, \underline{I}\underline{q}) = 0,$$

$$\inf\{\wp_b(\underline{q}, \underline{I}\underline{q}); \underline{q} \in \mathcal{U}\} = 0.$$

Thus, \underline{I} exhibits approximate fixed point property.

Conversely, assume that \underline{I} exhibits approximate fixed point property, i.e. $\inf\{\wp_b(\underline{q}, \underline{I}\underline{q}); \underline{q} \in \mathcal{U}\} = 0$. This indicates the existence of $\langle \underline{q}_n \rangle_{n \in \mathbb{N}}$, a sequence in \mathcal{U} satisfying $\lim_{n \rightarrow \infty} \wp_b(\underline{q}_n, \underline{I}\underline{q}_n) = 0$ and by using (2)

and triangle inequality for all $m, n \in \mathbb{N}$,

$$\begin{aligned} \wp_b(\underline{I}\underline{q}_n, \underline{I}\underline{q}_m) &\leq \underline{\kappa}[\wp_b(\underline{q}_n, \underline{I}\underline{q}_m) + \wp_b(\underline{q}_m, \underline{I}\underline{q}_n)] \\ &\leq \underline{\kappa}[s\wp_b(\underline{q}_n, \underline{I}\underline{q}_n) + 2s\wp_b(\underline{I}\underline{q}_n, \underline{I}\underline{q}_m) \\ &\quad + s\wp_b(\underline{q}_m, \underline{I}\underline{q}_m)](1 - 2\underline{\kappa}s)\wp_b(\underline{I}\underline{q}_n, \underline{I}\underline{q}_m) \leq \\ &\quad \underline{\kappa}s[\wp_b(\underline{q}_n, \underline{I}\underline{q}_n) + \wp_b(\underline{I}\underline{q}_m, \underline{q}_m)] \end{aligned}$$

Now, since $\lim_{n \rightarrow \infty} \wp_b(\underline{q}_n, \underline{I}\underline{q}_n) = 0$ and $\underline{\kappa} < \frac{1}{s^2}$, we obtain a Cauchy sequence $\langle \underline{I}\underline{q}_n \rangle_{n \in \mathbb{N}}$ as $n \rightarrow \infty$. Also, there exists an element $\underline{q} \in \mathcal{U}$ satisfying $\lim_{n \rightarrow \infty} \underline{I}\underline{q}_n = \underline{q}$ as the space (\mathcal{U}, \wp_b) is complete. Again using triangle inequality

$$\wp_b(\underline{q}_n, \underline{q}) \leq s[\wp_b(\underline{q}_n, \underline{I}\underline{q}_n) + \wp_b(\underline{I}\underline{q}_n, \underline{q})].$$

Taking limit as $n \rightarrow \infty$, we get

$$\lim_{n \rightarrow \infty} \wp_b(\underline{q}_n, \underline{q}) = 0 \Rightarrow \underline{q}_n \rightarrow \underline{q}.$$

Also, consider

$$\wp_b(\underline{I}\underline{q}_n, \underline{I}\underline{q}) \leq \underline{\kappa}[\wp_b(\underline{q}_n, \underline{I}\underline{q}) + \wp_b(\underline{q}, \underline{I}\underline{q}_n)].$$

Now taking limit as $n \rightarrow \infty$,

$$\frac{1}{s}\wp_b(\underline{q}, \underline{I}\underline{q}) \leq \underline{\kappa}[s\wp_b(\underline{q}, \underline{I}\underline{q}) + 0]$$

$$= \underline{\kappa}s\wp_b(\underline{q}, \underline{I}\underline{q})$$

$$\wp_b(\underline{q}, \underline{I}\underline{q}) \leq \underline{\kappa}s^2\wp_b(\underline{q}, \underline{I}\underline{q})$$

$$(1 - \underline{\kappa}s^2)\wp_b(\underline{q}, \underline{I}\underline{q}) \leq 0$$

Since $\underline{\kappa} < \frac{1}{s^2}$, i.e., $1 - \underline{\kappa}s^2 < 1$, we get

$$\wp_b(\underline{q}, \underline{I}\underline{q}) = 0 \Rightarrow \underline{I}\underline{q} = \underline{q}$$

and $\underline{q} \in \mathcal{U}$. Thus \underline{I} has a fixed point in \mathcal{U} .

If possible, now consider two fixed points of \underline{I} , say \underline{q} and $\underline{\zeta}$, exist and thus $\wp_b(\underline{q}, \underline{\zeta}) \neq 0$. By using inequality (2), we get

$$\begin{aligned} \wp_b(\underline{q}, \underline{\zeta}) &= \wp_b(\underline{I}\underline{q}, \underline{I}\underline{\zeta}) \\ &\leq \underline{\kappa}[\wp_b(\underline{q}, \underline{I}\underline{\zeta}) + \wp_b(\underline{\zeta}, \underline{I}\underline{q})] \\ &\leq 2\underline{\kappa}\wp_b(\underline{q}, \underline{\zeta}) \end{aligned}$$

that is a contradiction as $\kappa \in [0, \frac{1}{2})$.

$\varphi_b(\underline{q}, \underline{\varsigma}) = 0$ and thus $\underline{q} = \underline{\varsigma}$, i.e. the fixed point is unique.

Theorem 2: Let $I: \mathcal{U} \rightarrow \mathcal{U}$ be a self mapping defined on $(\mathcal{U}, \varphi_b, \underline{\Omega})$, a complete convex b -metric space with parameter $s \geq 2$ such that for all $\underline{q}, \underline{\varsigma} \in \mathcal{U}$ and $\kappa \in [0, \frac{1}{2})$, it satisfies

$$\varphi_b(I\underline{q}, I\underline{\varsigma}) \leq \kappa [\varphi_b(\underline{q}, I\underline{\varsigma}) + \varphi_b(\underline{\varsigma}, I\underline{q})] \quad \dots(3)$$

Then, I has approximate fixed point property.

Proof. For every $\underline{q} \in \mathcal{U}$, we have

$$\begin{aligned} \varphi_b(I^{n+1}\underline{q}, I^n\underline{q}) &\leq \kappa [\varphi_b(I^n\underline{q}, I^n\underline{q}) \\ &+ \varphi_b(I^{n-1}\underline{q}, I^{n+1}\underline{q})] \\ &\leq \kappa s [\varphi_b(I^{n-1}\underline{q}, I^n\underline{q}) + \varphi_b(I^n\underline{q}, I^{n+1}\underline{q})] \\ (1 - \kappa s) \varphi_b(I^{n+1}\underline{q}, I^n\underline{q}) &\leq \kappa s \varphi_b(I^{n-1}\underline{q}, I^n\underline{q}) \\ \varphi_b(I^{n+1}\underline{q}, I^n\underline{q}) &\leq \frac{\kappa s}{1 - \kappa s} \varphi_b(I^{n-1}\underline{q}, I^n\underline{q}) \\ &< \varphi_b(I^{n-1}\underline{q}, I^n\underline{q}) \end{aligned}$$

since $\kappa < \frac{1}{s^2}$. Thus the sequence $\langle \varphi_b(I^{n+1}\underline{q}, I^n\underline{q}) \rangle_{n \in \mathbb{N}}$ is non-increasing and for $\lambda \in \mathbb{N}$,

$$\begin{aligned} \varphi_b(I^{\lambda+1}\underline{q}, I^\lambda\underline{q}) &< \varphi_b(I^\lambda\underline{q}, I^{\lambda-1}\underline{q}) \\ &< \dots < \varphi_b(I^2\underline{q}, I\underline{q}) < \varphi_b(I\underline{q}, \underline{q}). \end{aligned}$$

Now, consider

$$\begin{aligned} \varphi_b(I^\lambda\underline{q}, I^{\lambda+2}\underline{q}) &\leq \kappa [\varphi_b(I^{\lambda-1}\underline{q}, I^{\lambda+2}\underline{q}) + \\ &\varphi_b(I^{\lambda+1}\underline{q}, I^\lambda\underline{q})] \\ &< \kappa [\varphi_b(\underline{q}, I\underline{q}) + \varphi_b(I^{\lambda-1}\underline{q}, I^{\lambda+2}\underline{q})] \\ &\leq \kappa [\varphi_b(\underline{q}, I\underline{q}) + s \{ \varphi_b(I^{\lambda-1}\underline{q}, I^\lambda\underline{q}) \\ &+ \varphi_b(I^\lambda\underline{q}, I^{\lambda+2}\underline{q}) \}] \\ &< \kappa(s+1) \varphi_b(\underline{q}, I\underline{q}) + \kappa s \varphi_b(I^\lambda\underline{q}, I^{\lambda+2}\underline{q}) \end{aligned}$$

$$\begin{aligned} (1 - \kappa s) \varphi_b(I^\lambda\underline{q}, I^{\lambda+2}\underline{q}) &\leq \kappa(s+1) \varphi_b(\underline{q}, I\underline{q}) \\ \varphi_b(I^\lambda\underline{q}, I^{\lambda+2}\underline{q}) &\leq \frac{\kappa(s+1)}{1 - \kappa s} \varphi_b(\underline{q}, I\underline{q}) \\ &= \varsigma \varphi_b(\underline{q}, I\underline{q}) \end{aligned} \quad \dots(4)$$

where $\varsigma = \frac{\kappa(s+1)}{1 - \kappa s}$.

We let $\inf \{ \varphi_b(\underline{q}, I\underline{q}); \underline{q} \in \mathcal{U} \} = \underline{\Delta}$. We need to prove that this $\underline{\Delta} = 0$. For this, let $\langle \underline{q}_n \rangle$ be a sequence such that $\lim_{n \rightarrow \infty} \varphi_b(\underline{q}_n, I\underline{q}_n) = \underline{\Delta}$, i.e., by (4), we have, for every $n \in \mathbb{N}$ and some $\lambda(n) \in \mathbb{N}$,

$$\varphi_b(I^{\lambda(n)}\underline{q}_n, I^{\lambda(n)+2}\underline{q}_n) \leq \varsigma \varphi_b(\underline{q}_n, I\underline{q}_n). \quad \dots(5)$$

Now, $(\mathcal{U}, \varphi_b, \underline{\Omega})$ being a complete convex b -metric space, defining $\underline{\eta}_n = \underline{\Omega}(I^{\lambda(n)+1}\underline{q}_n, I^{\lambda(n)+2}\underline{q}_n, \vartheta)$ leads to a well defined $\underline{\eta}_n$ belonging to \mathcal{U} , where we can choose $\vartheta \in (0, 1)$ such that $\vartheta < \frac{1-s\kappa}{\kappa}$ and then we have,

$$\begin{aligned} \varphi_b(\underline{\eta}_n, I\underline{\eta}_n) &\leq \vartheta \varphi_b(I^{\lambda(n)+1}\underline{q}_n, I\underline{\eta}_n) \\ &+ (1 - \vartheta) \varphi_b(I^{\lambda(n)+2}\underline{q}_n, I\underline{\eta}_n) \\ &\leq \kappa \vartheta [\varphi_b(I^{\lambda(n)}\underline{q}_n, I\underline{\eta}_n) \\ &+ \kappa(1 - \vartheta) [\varphi_b(I^{\lambda(n)+1}\underline{q}_n, I\underline{\eta}_n) \\ &+ \varphi_b(\underline{\eta}_n, I^{\lambda(n)+1}\underline{q}_n) \\ &+ \varphi_b(\underline{\eta}_n, I^{\lambda(n)+2}\underline{q}_n)] \\ &\leq \kappa \vartheta [s \varphi_b(I^{\lambda(n)}\underline{q}_n, \underline{\eta}_n) + s \varphi_b(\underline{\eta}_n, I\underline{\eta}_n) + \\ &+ \varphi_b(\underline{\eta}_n, I^{\lambda(n)+1}\underline{q}_n)] \\ &+ \kappa(1 - \vartheta) [s \varphi_b(I^{\lambda(n)+1}\underline{q}_n, \underline{\eta}_n) \\ &+ s \varphi_b(\underline{\eta}_n, I\underline{\eta}_n) + \varphi_b(\underline{\eta}_n, I^{\lambda(n)+2}\underline{q}_n)] \\ &\leq \kappa \vartheta [s \vartheta \varphi_b(I^{\lambda(n)}\underline{q}_n, I^{\lambda(n)+1}\underline{q}_n) + s \varphi_b(\underline{\eta}_n, I\underline{\eta}_n) \\ &+ s(1 - \vartheta) \varphi_b(I^{\lambda(n)}\underline{q}_n, I^{\lambda(n)+2}\underline{q}_n) \\ &+ (1 - \vartheta) \varphi_b(I^{\lambda(n)+2}\underline{q}_n, I^{\lambda(n)+1}\underline{q}_n)] \\ &+ \kappa(1 - \vartheta) [s(1 - \vartheta) \varphi_b(I^{\lambda(n)+1}\underline{q}_n, I^{\lambda(n)+2}\underline{q}_n) \end{aligned}$$

$$\begin{aligned}
& +s\underline{\varrho}_b(\underline{\eta}_n, \underline{I}\underline{\eta}_n) + \vartheta \underline{\varrho}_b(\underline{I}^{\lambda(n)+1}\underline{q}_n, \underline{I}^{\lambda(n)+2}\underline{q}_n)] \\
& \leq \underline{\kappa}\vartheta[s\vartheta \underline{\varrho}_b(\underline{q}_n, \underline{I}\underline{q}_n) + s(1-\vartheta)\underline{\varrho}_b(\underline{q}_n, \underline{I}\underline{q}_n) \\
& \quad +s\underline{\varrho}_b(\underline{\eta}_n, \underline{I}\underline{\eta}_n) + (1-\vartheta)\underline{\varrho}_b(\underline{q}_n, \underline{I}\underline{q}_n)] \\
& +\underline{\kappa}(1-\vartheta)[s(1-\vartheta)\underline{\varrho}_b(\underline{q}_n, \underline{I}\underline{q}_n) \\
& +s\underline{\varrho}_b(\underline{\eta}_n, \underline{I}\underline{\eta}_n) + \vartheta \underline{\varrho}_b(\underline{q}_n, \underline{I}\underline{q}_n)]. \quad \dots(6)
\end{aligned}$$

Suppose $\lim_{n \rightarrow \infty} \underline{\varrho}_b(\underline{\eta}_n, \underline{I}\underline{\eta}_n) = \underline{\delta}$.

We notice that $\underline{\delta}$ is finite, and also, $\underline{\lambda} \leq \underline{\delta}$ is true. Next, we claim that $\underline{\delta} = 0$ which shall prove that $\underline{\lambda} = 0$.

Taking \limsup as $n \rightarrow \infty$ on both sides of inequality (6) and using $\underline{\lambda} \leq \underline{\delta}$

$$\begin{aligned}
\underline{\delta} & \leq \underline{\kappa}\vartheta[s\vartheta \underline{\delta} + s(1-\vartheta)\underline{\rho}\underline{\delta} + s\underline{\delta} + (1-\vartheta)\underline{\delta}] \\
& \quad +\underline{\kappa}(1-\vartheta)[s(1-\vartheta)\underline{\delta} + s\underline{\delta} + \vartheta\underline{\delta}] \\
& = \underline{\kappa}[2s\vartheta^2 + s\vartheta(1-\vartheta)\underline{\rho} + 2\vartheta(1-\vartheta) \\
& \quad +2s(1-s)]\underline{\delta} \\
& = \underline{\kappa}s[(\underline{\rho}-2)\vartheta(1-\vartheta) + 2]\underline{\delta} + \underline{\kappa}\vartheta(1-\vartheta)\underline{\delta} \\
& \leq \underline{\kappa}[2s + 2\vartheta(1-\vartheta)]\underline{\delta}.
\end{aligned}$$

If possible, suppose that $\underline{\delta} > 0$. Then, by inequality (6), we get

$$\begin{aligned}
1 & \leq \underline{\kappa}[2s + 2\vartheta(1-\vartheta)] \\
& \leq 2s\underline{\kappa} + 2\underline{\kappa}\vartheta \\
\vartheta & \geq \frac{1 - s\underline{\kappa}}{\underline{\kappa}},
\end{aligned}$$

which is a contradiction since $\vartheta < \frac{1-s\underline{\kappa}}{\underline{\kappa}}$.

Thus, \underline{I} has approximate fixed point property.

Lemma 2: Let $(\mathcal{U}, \underline{\varrho}_b, \underline{\Omega})$ be a convex b -metric space. Define self-mappings $\underline{I}: \mathcal{U} \rightarrow \mathcal{U}$ and $\underline{I}_\vartheta: \mathcal{U} \rightarrow \mathcal{U}$ by

$$\underline{I}_\vartheta \underline{q} = \underline{\Omega}(\underline{q}, \underline{I}\underline{q}; \vartheta), \underline{q} \in \mathcal{U}.$$

Then, for any $\vartheta \in [0, 1)$,

$$\text{Fix}(\underline{I}) = \text{Fix}(\underline{I}_\vartheta).$$

Proof. By definition,

$$\underline{I}_\vartheta = \vartheta \underline{q} + (1-\vartheta)\underline{I}\underline{q}.$$

If $\vartheta = 0$, then

$$\underline{I}_\vartheta \underline{q} = \underline{I}\underline{q} \quad \forall \underline{q} \in \mathcal{U}$$

$$\text{i.e., } \underline{I}_\vartheta = \underline{I}$$

$$\text{Fix}(\underline{I}) = \text{Fix}(\underline{I}_\vartheta).$$

Now assume that $\vartheta \in (0, 1)$ and let a fixed point of \underline{I} , say \underline{q}^* , exists, i.e., $\underline{q}^* = \underline{I}\underline{q}^*$ and therefore,

$$\begin{aligned}
\underline{\varrho}_b(\underline{q}^*, \underline{I}_\vartheta \underline{q}^*) & = \underline{\varrho}_b(\underline{q}^*, \underline{\Omega}(\underline{q}^*, \underline{I}\underline{q}^*; \vartheta)) \\
& \leq \vartheta \underline{\varrho}_b(\underline{q}^*, \underline{q}^*) + (1-\vartheta)\underline{\varrho}_b(\underline{q}^*, \underline{I}\underline{q}^*) = 0 \\
\underline{q}^* & = \underline{I}_\vartheta \underline{q}^*
\end{aligned}$$

i.e., \underline{q}^* is a fixed point of \underline{I}_ϑ .

Conversely, presume that \underline{q}^* is a fixed point of \underline{I}_ϑ , i.e.,

$$\begin{aligned}
\underline{\varrho}_b(\underline{q}^*, \underline{I}_\vartheta \underline{q}^*) & = 0, \text{ then} \\
\underline{\varrho}_b(\underline{q}^*, \underline{\Omega}(\underline{q}^*, \underline{I}\underline{q}^*; \vartheta)) & = 0 \\
\vartheta \underline{\varrho}_b(\underline{q}^*, \underline{q}^*) + (1-\vartheta)\underline{\varrho}_b(\underline{q}^*, \underline{I}\underline{q}^*) & = 0 \quad (6) \\
(1-\vartheta)\underline{\varrho}_b(\underline{q}^*, \underline{I}\underline{q}^*) & = 0.
\end{aligned}$$

Since $\vartheta \neq 1$, \underline{q}^* is a fixed point of \underline{I} .

Hence, the proof.

The following result is an extension of Chatterjea fixed point theorem in the case of Convex b -metric spaces by Rathee et al. [11]

Theorem 3: Let $\underline{I}: \mathcal{U} \rightarrow \mathcal{U}$ be a self mapping defined on $(\mathcal{U}, \underline{\varrho}_b, \underline{\Omega})$, a complete convex b -metric space with parameter $s \geq 2$ such that for all $\underline{q}, \underline{\zeta} \in \mathcal{U}$ and $\underline{\kappa} \in [0, \frac{1}{2})$, it satisfies

$$\underline{\varrho}_b(\underline{I}\underline{q}, \underline{I}\underline{\zeta}) \leq \underline{\kappa}[\underline{\varrho}_b(\underline{q}, \underline{I}\underline{q}) + \underline{\varrho}_b(\underline{\zeta}, \underline{I}\underline{\zeta})] \quad \dots(7)$$

If $\underline{\kappa} < \frac{1}{s^2}$, then

1. A fixed point of \underline{I} , say \underline{q} , exists that is unique.

2. The sequence $\langle \underline{q}_n \rangle_{n \in \mathbb{N}}$ converges to \underline{q} for any $\underline{q}_0 \in \mathcal{U}$ that is obtained from the iterative procedure

$$\underline{q}_{n+1} = \underline{\Omega}(\underline{q}_n, \underline{I}\underline{q}_n; \vartheta); n \geq 0.$$

3. The error estimate

$$\frac{1}{s} \underline{\wp}_b(\underline{q}_{n+i-1}, \underline{q}) \leq \frac{\underline{\xi}^i}{1 - \underline{\xi}} \underline{\wp}_b(\underline{q}_n, \underline{q}_{n-1})$$

holds for $n = 1, 2, \dots; i = 1, 2, \dots$.

Proof.

1. Lemma 1 and Theorem 2 concludes the proof.

2. We observe that $\underline{q}_{n+1} = \underline{\Omega}(\underline{q}_n, \underline{I}\underline{q}_n; \vartheta)$, i.e.

$$\underline{q}_{n+1} = \underline{I}\vartheta \underline{q}_n; n \geq 0.$$

Taking $\underline{q} = \underline{q}_n$ and $\underline{\varsigma} = \underline{q}_{n-1}$, in (7)

$$\begin{aligned} \underline{\wp}_b(\underline{q}_{n+1}, \underline{q}_n) &\leq \underline{\kappa}[\underline{\wp}_b(\underline{q}_n, \underline{q}_n) + \underline{\wp}_b(\underline{q}_{n-1}, \underline{q}_{n+1})] \\ &\leq \underline{\kappa}[\underline{\wp}_b(\underline{q}_{n-1}, \underline{q}_n) + \underline{\wp}_b(\underline{q}_n, \underline{q}_{n+1})] \end{aligned}$$

implying

$$\begin{aligned} \underline{\wp}_b(\underline{q}_{n+1}, \underline{q}_n) &\leq \frac{\underline{\kappa} \underline{s}}{1 - \underline{\kappa} \underline{s}} \underline{\wp}_b(\underline{q}_n, \underline{q}_{n-1}) \\ &\leq \underline{\kappa} \underline{s}^2 \underline{\wp}_b(\underline{q}_n, \underline{q}_{n-1}) \\ &= \underline{\xi} \underline{\wp}_b(\underline{q}_n, \underline{q}_{n-1}), \text{ say, } \underline{\kappa} \underline{s}^2 = \underline{\xi} \\ &\vdots \\ &\leq \underline{\xi}^n \underline{\wp}_b(\underline{q}_1, \underline{q}_0) \end{aligned} \quad \dots(8)$$

As $\underline{\xi} \in [0, 1)$, we have

$$\lim_{n \rightarrow \infty} \underline{\wp}_b(\underline{q}_{n+1}, \underline{q}_n) = 0. \quad (9)$$

Now consider the points \underline{q} and $\underline{\varsigma}$ as \underline{q}_{n+k} and \underline{q}_n , respectively, in inequality (7).

$$\begin{aligned} \underline{\wp}_b(\underline{q}_{n+k+1}, \underline{q}_{n+1}) &\leq \underline{\kappa}[\underline{\wp}_b(\underline{q}_{n+k}, \underline{q}_{n+1}) \\ &\quad + \underline{\wp}_b(\underline{q}_n, \underline{q}_{n+k+1})] \\ &\leq \underline{\kappa} \underline{s}[\underline{\wp}_b(\underline{q}_{n+k}, \underline{q}_{n+k+1}) \\ &\quad + 2 \underline{\wp}_b(\underline{q}_{n+k+1}, \underline{q}_{n+1}) \underline{\wp}_b(\underline{q}_n, \underline{q}_{n+1})] \end{aligned}$$

This implies

$$\begin{aligned} (1 - 2 \underline{\kappa} \underline{s}) \underline{\wp}_b(\underline{q}_{n+k+1}, \underline{q}_{n+1}) &\leq \underline{\kappa} \underline{s} \underline{\wp}_b(\underline{q}_{n+k}, \underline{q}_{n+k+1}) \\ &\quad + \underline{\kappa} \underline{s} \underline{\wp}_b(\underline{q}_{n+1}, \underline{q}_n) \\ (1 - \underline{\kappa} \underline{s}^2) \underline{\wp}_b(\underline{q}_{n+k+1}, \underline{q}_{n+1}) &< \underline{\kappa} \underline{s}^2 \underline{\wp}_b(\underline{q}_{n+k}, \underline{q}_{n+k+1}) \\ &\quad + \underline{\kappa} \underline{s}^2 \underline{\wp}_b(\underline{q}_{n+1}, \underline{q}_n) \\ (1 - \underline{\xi}) \underline{\wp}_b(\underline{q}_{n+k+1}, \underline{q}_{n+1}) &\leq \underline{\xi} [\underline{\wp}_b(\underline{q}_{n+k}, \underline{q}_{n+k+1}) \\ &\quad + \underline{\wp}_b(\underline{q}_{n+1}, \underline{q}_n)] \\ \text{and } \underline{\wp}_b(\underline{q}_{n+k+1}, \underline{q}_{n+1}) &\leq \frac{\underline{\xi}}{1 - \underline{\xi}} [\underline{\wp}_b(\underline{q}_{n+k}, \underline{q}_{n+k+1}) \\ &\quad + \underline{\wp}_b(\underline{q}_{n+1}, \underline{q}_n)] \quad (10) \end{aligned}$$

In inequality (7), taking limit as $n \rightarrow \infty$ and using condition (9), we get,

$$\lim_{n \rightarrow \infty} \underline{\wp}_b(\underline{q}_{n+k+1}, \underline{q}_{n+k}) = 0.$$

This shows that $\langle \underline{q}_n \rangle_{n \in \mathbb{N}}$ is Cauchy and owing to completeness of the space $(\mathcal{U}, \underline{\wp}_b, \underline{\Omega})$, converges to some point, say $\underline{\varsigma}$. Now, consider the inequality (8),

$$\begin{aligned} \underline{\wp}_b(\underline{q}_{n+1}, \underline{q}_n) &\leq \underline{\xi}^n \underline{\wp}_b(\underline{q}_1, \underline{q}_0) \\ \underline{\wp}_b(\underline{I}\vartheta \underline{q}_n, \underline{q}_n) &\leq \underline{\xi}^n \underline{\wp}_b(\underline{q}_1, \underline{q}_0) \end{aligned}$$

Now taking limit as $n \rightarrow \infty$, we get,

$$\frac{1}{s} \underline{\wp}_b(\underline{I}\vartheta \underline{\varsigma}, \underline{\varsigma}) = 0$$

$$\underline{\wp}_b(\underline{I}\vartheta \underline{\varsigma}, \underline{\varsigma}) = 0.$$

Thus, $\underline{I}\vartheta \underline{\varsigma} = \underline{\varsigma}$, and therefore $\underline{\varsigma}$ is a fixed point of $\underline{I}\vartheta$. But by using Lemma 2, we must have

$$\text{Fix}(\underline{I}) = \text{Fix}(\underline{I}\vartheta),$$

and $\text{Fix}(\underline{I}) = \{\underline{q}\}$, i.e. Fixed point of \underline{I} is \underline{q} , which is unique.

So, $\underline{\varsigma} = \underline{q}$ and thus $\langle \underline{q}_n \rangle_{n \in \mathbb{N}}$ obtained from the above iteration converges to \underline{q} .

3. Using inequalities (10) and (8), we have

$$\begin{aligned} \underline{\rho}_b(\underline{q}_{n+m}, \underline{q}_n) &\leq \frac{\underline{\xi}}{1-\underline{\xi}} [\underline{\rho}_b(\underline{q}_{n+m-1}, \underline{q}_{n+m}) \\ &+ \underline{\rho}_b(\underline{q}_n, \underline{q}_{n-1})] \\ &\leq \frac{\underline{\xi}}{1-\underline{\xi}} [\underline{\xi}^{n+m-1} \underline{\rho}_b(\underline{q}_1, \underline{q}_0) \\ &+ \underline{\xi}^{n-1} \underline{\rho}_b(\underline{q}_1, \underline{q}_0)] \\ &= \frac{\underline{\xi}^n (\underline{\xi}^m + 1)}{1-\underline{\xi}} \underline{\rho}_b(\underline{q}_1, \underline{q}_0) \end{aligned}$$

Now letting $m \rightarrow \infty$, we get,

$$\frac{1}{s} \underline{\rho}_b(\underline{q}, \underline{q}_n) \leq \frac{\underline{\xi}^n}{1-\underline{\xi}} \underline{\rho}_b(\underline{q}_1, \underline{q}_0) \quad \dots(11)$$

$$\begin{aligned} \text{and } \underline{\rho}_b(\underline{q}_{n+m}, \underline{q}_n) &\leq \frac{\underline{\xi}}{1-\underline{\xi}} [\underline{\rho}_b(\underline{q}_{n+m-1}, \underline{q}_{n+m}) \\ &+ \underline{\rho}_b(\underline{q}_n, \underline{q}_{n-1})] \\ &\leq \frac{\underline{\xi}}{1-\underline{\xi}} [\underline{\xi}^{m-1} \underline{\rho}_b(\underline{q}_{n-1}, \underline{q}_n) \\ &+ \underline{\rho}_b(\underline{q}_n, \underline{q}_{n-1})] \\ &= \frac{\underline{\xi} (\underline{\xi}^{m-1} + 1)}{1-\underline{\xi}} \underline{\rho}_b(\underline{q}_{n-1}, \underline{q}_n) \end{aligned}$$

Now letting $m \rightarrow \infty$, we get,

$$\frac{1}{s} \underline{\rho}_b(\underline{q}, \underline{q}_n) \leq \frac{\underline{\xi}}{1-\underline{\xi}} \underline{\rho}_b(\underline{q}_{n-1}, \underline{q}_n). \quad \dots(12)$$

After combining (11) and (12), the following error estimate holds

$$\frac{1}{s} \underline{\rho}_b(\underline{q}_{n+i-1}, \underline{q}) \leq \frac{\underline{\xi}^i}{1-\underline{\xi}} \underline{\rho}_b(\underline{q}_n, \underline{q}_{n-1}).$$

Hence, the result.

The following example illustrates importance of the above theorem.

Example 1: Let the set of non-negative real numbers be $\mathbb{U} = \mathbb{R}_0^+$ and $\underline{\rho}_b(\underline{q}, \underline{\varsigma}) = |\underline{q} - \underline{\varsigma}|^3 + |\underline{q} - \underline{\varsigma}|$ for all $\underline{q}, \underline{\varsigma} \in \mathbb{U}$. Here, we perceive that

1. $\underline{\rho}_b(\underline{q}, \underline{\varsigma}) \geq 0$ for all $\underline{q}, \underline{\varsigma} \in \mathbb{U}$;
2. $\underline{\rho}_b(\underline{q}, \underline{\varsigma}) = 0 \iff \underline{q} = \underline{\varsigma}$;
3. $\underline{\rho}_b(\underline{q}, \underline{\varsigma}) = \underline{\rho}_b(\underline{\varsigma}, \underline{q})$;
4. $\underline{\rho}_b(\underline{q}, \underline{\varsigma}) \leq 4 [\underline{\rho}_b(\underline{q}, \underline{\eta}) + \underline{\rho}_b(\underline{\eta}, \underline{\varsigma})]$, $\underline{\eta} \in \mathbb{U}$
as $\underline{\rho}_b(\underline{q}, \underline{\varsigma})$
 $= |\underline{q} - \underline{\varsigma}|^3 + |\underline{q} - \underline{\varsigma}|$
 $= |(\underline{q} - \underline{\eta}) + (\underline{\eta} - \underline{\varsigma})|^3 + |(\underline{q} - \underline{\eta}) + (\underline{\eta} - \underline{\varsigma})|$
 $\leq 4[|\underline{q} - \underline{\eta}|^3 + |\underline{\eta} - \underline{\varsigma}|^3] + |\underline{q} - \underline{\eta}| + |\underline{\eta} - \underline{\varsigma}|$
 $\leq 4[|\underline{q} - \underline{\eta}|^3 + |\underline{q} - \underline{\eta}|] + 4[|\underline{\eta} - \underline{\varsigma}|^3 + |\underline{\eta} - \underline{\varsigma}|]$
 $= 4[\underline{\rho}_b(\underline{q}, \underline{\eta}) + \underline{\rho}_b(\underline{\eta}, \underline{\varsigma})].$

We define the convex structure $\underline{\Omega}: \mathbb{U} \times \mathbb{U} \times \left\{\frac{1}{2}\right\} \rightarrow \mathbb{U}$ as $\underline{\Omega}(\underline{q}, \underline{\varsigma}; \vartheta) = \frac{\underline{q} + \underline{\varsigma}}{2}$, for any $\underline{q}, \underline{\varsigma} \in \mathbb{U}$ and $\vartheta \in [0, 1]$. As a consequence,

$$\begin{aligned} \underline{\rho}_b(\underline{\eta}, \underline{\Omega}(\underline{q}, \underline{\varsigma}; \vartheta)) &= \left| \underline{\eta} - \frac{\underline{q} + \underline{\varsigma}}{2} \right|^3 + \left| \underline{\eta} - \frac{\underline{q} + \underline{\varsigma}}{2} \right| \\ &\leq \left(\frac{1}{2} |\underline{\eta} - \underline{q}| + \frac{1}{2} |\underline{\eta} - \underline{\varsigma}| \right)^3 \\ &\quad + \left(\frac{1}{2} |\underline{\eta} - \underline{q}| + \frac{1}{2} |\underline{\eta} - \underline{\varsigma}| \right) \\ &\leq 4 \left[\frac{1}{8} |\underline{\eta} - \underline{q}|^3 + \frac{1}{8} |\underline{\eta} - \underline{\varsigma}|^3 \right] \\ &\quad + \left(\frac{1}{2} |\underline{\eta} - \underline{q}| + \frac{1}{2} |\underline{\eta} - \underline{\varsigma}| \right) \\ &= \frac{1}{2} [|\underline{\eta} - \underline{q}|^3 + |\underline{\eta} - \underline{q}|] + \frac{1}{2} [|\underline{\eta} - \underline{\varsigma}|^3 + |\underline{\eta} - \underline{\varsigma}|] \\ &= \vartheta [|\underline{\eta} - \underline{q}|^3 + |\underline{\eta} - \underline{q}|] + (1 - \vartheta) [|\underline{\eta} - \underline{\varsigma}|^3 \\ &\quad + |\underline{\eta} - \underline{\varsigma}|] \\ &= \vartheta \underline{\rho}_b(\underline{\eta}, \underline{q}) + (1 - \vartheta) \underline{\rho}_b(\underline{\eta}, \underline{\varsigma}). \end{aligned}$$

Thus, for $s \geq 4$, $(\mathbb{U}, \underline{\rho}_b, \underline{\Omega})$ is a convex b -metric space.

Let the mapping $\underline{I}: \mathbb{U} \rightarrow \mathbb{U}$ be defined as

$$I(\underline{q}) = \left\{ \frac{\underline{q}}{17}, \underline{q} \in \Lambda = [0, 1) \right\} \frac{1}{20\underline{q}}, \underline{q} \in \Sigma = [1, \infty). \quad = -\frac{1}{17} \underline{\wp}_b(\underline{\zeta}, \underline{I}\underline{q}) \leq 0.$$

The following cases exist:

1. If both $\underline{q}, \underline{\zeta} \in \Lambda$, then the inequality (7) holds.
2. If $\underline{q} \in \Lambda$ and $\underline{\zeta} \in \Sigma$, then

$$\begin{aligned} & \underline{\wp}_b(\underline{I}\underline{q}, \underline{I}\underline{\zeta}) - \frac{1}{17} [\underline{\wp}_b(\underline{q}, \underline{I}\underline{\zeta}) + \underline{\wp}_b(\underline{\zeta}, \underline{I}\underline{q})] \\ &= \left[|\underline{I}\underline{q} - \underline{I}\underline{\zeta}|^3 + |\underline{I}\underline{q} - \underline{I}\underline{\zeta}| \right] - \frac{1}{17} [\underline{\wp}_b(\underline{q}, \underline{I}\underline{\zeta}) \\ &+ \underline{\wp}_b(\underline{\zeta}, \underline{I}\underline{q})] \\ &= \left[\left| \frac{\underline{q}}{17} - \frac{1}{20\underline{\zeta}} \right|^3 + \left| \frac{\underline{q}}{17} - \frac{1}{20\underline{\zeta}} \right| \right] - \frac{1}{17} [\underline{\wp}_b(\underline{q}, \underline{I}\underline{\zeta}) \\ &+ \underline{\wp}_b(\underline{\zeta}, \underline{I}\underline{q})] \\ &= \frac{1}{17} \left[\frac{1}{17^2} \left| \underline{q} - \frac{17}{20\underline{\zeta}} \right|^3 + \left| \underline{q} - \frac{17}{20\underline{\zeta}} \right| \right] \\ &- \frac{1}{17} [\underline{\wp}_b(\underline{q}, \underline{I}\underline{\zeta}) + \underline{\wp}_b(\underline{\zeta}, \underline{I}\underline{q})]. \end{aligned}$$

If $\underline{q} > \frac{17}{20\underline{\zeta}}$, then

$$\begin{aligned} & \underline{\wp}_b(\underline{I}\underline{q}, \underline{I}\underline{\zeta}) - \frac{1}{17} [\underline{\wp}_b(\underline{q}, \underline{I}\underline{\zeta}) + \underline{\wp}_b(\underline{\zeta}, \underline{I}\underline{q})] \\ &= \frac{1}{17} \left[\frac{1}{17^2} \left(\underline{q} - \frac{17}{20\underline{\zeta}} \right)^3 + \left(\underline{q} - \frac{17}{20\underline{\zeta}} \right) \right] \\ &- \frac{1}{17} [\underline{\wp}_b(\underline{q}, \underline{I}\underline{\zeta}) + \underline{\wp}_b(\underline{\zeta}, \underline{I}\underline{q})] \\ &< \frac{1}{17} \left[\left(\underline{q} - \frac{17}{20\underline{\zeta}} \right)^3 + \left(\underline{q} - \frac{17}{20\underline{\zeta}} \right) \right] \\ &- \frac{1}{17} [\underline{\wp}_b(\underline{q}, \underline{I}\underline{\zeta}) + \underline{\wp}_b(\underline{\zeta}, \underline{I}\underline{q})] \\ &< \frac{1}{17} \left[\left(\underline{q} - \frac{1}{20\underline{\zeta}} \right)^3 + \left(\underline{q} - \frac{1}{20\underline{\zeta}} \right) \right] \\ &- \frac{1}{17} [\underline{\wp}_b(\underline{q}, \underline{I}\underline{\zeta}) + \underline{\wp}_b(\underline{\zeta}, \underline{I}\underline{q})] \\ &= \frac{1}{17} \underline{\wp}_b(\underline{q}, \underline{I}\underline{\zeta}) - \frac{1}{17} [\underline{\wp}_b(\underline{q}, \underline{I}\underline{\zeta}) + \underline{\wp}_b(\underline{\zeta}, \underline{I}\underline{q})] \end{aligned}$$

If $\underline{q} < \frac{17}{20\underline{\zeta}}$, then

$$\begin{aligned} & \underline{\wp}_b(\underline{I}\underline{q}, \underline{I}\underline{\zeta}) - \frac{1}{17} [\underline{\wp}_b(\underline{q}, \underline{I}\underline{\zeta}) + \underline{\wp}_b(\underline{\zeta}, \underline{I}\underline{q})] \\ &= \frac{1}{17} \left[\frac{1}{17^2} \left(\frac{17}{20\underline{\zeta}} - \underline{q} \right)^3 + \left(\frac{17}{20\underline{\zeta}} - \underline{q} \right) \right] \\ &- \frac{1}{17} [\underline{\wp}_b(\underline{q}, \underline{I}\underline{\zeta}) + \underline{\wp}_b(\underline{\zeta}, \underline{I}\underline{q})] \\ &= \frac{1}{17} \left[\frac{1}{17^2} \left(\frac{1}{\underline{\zeta}} - \underline{q} \right)^3 + \left(\frac{1}{\underline{\zeta}} - \underline{q} \right) \right] \\ &- \frac{1}{17} [\underline{\wp}_b(\underline{q}, \underline{I}\underline{\zeta}) + \underline{\wp}_b(\underline{\zeta}, \underline{I}\underline{q})] \\ &< \frac{1}{17} \left[\frac{1}{17^2} (\underline{\zeta} - \underline{q})^3 + (\underline{\zeta} - \underline{q}) \right] \\ &- \frac{1}{17} [\underline{\wp}_b(\underline{q}, \underline{I}\underline{\zeta}) + \underline{\wp}_b(\underline{\zeta}, \underline{I}\underline{q})] \\ &< \frac{1}{17} \left[\left(\underline{\zeta} - \frac{\underline{q}}{17} \right)^3 + \left(\underline{\zeta} - \frac{\underline{q}}{17} \right) \right] \\ &- \frac{1}{17} [\underline{\wp}_b(\underline{q}, \underline{I}\underline{\zeta}) + \underline{\wp}_b(\underline{\zeta}, \underline{I}\underline{q})] \\ &= \frac{1}{17} \underline{\wp}_b(\underline{\zeta}, \underline{I}\underline{q}) - \frac{1}{17} [\underline{\wp}_b(\underline{q}, \underline{I}\underline{\zeta}) + \underline{\wp}_b(\underline{\zeta}, \underline{I}\underline{q})] \\ &= -\frac{1}{17} \underline{\wp}_b(\underline{q}, \underline{I}\underline{\zeta}) \leq 0. \end{aligned}$$

Thus, we have

$$\underline{\wp}_b(\underline{I}\underline{q}, \underline{I}\underline{\zeta}) \leq \frac{1}{17} [\underline{\wp}_b(\underline{q}, \underline{I}\underline{\zeta}) + \underline{\wp}_b(\underline{\zeta}, \underline{I}\underline{q})] \quad \dots(13)$$

3. If $\underline{q} \in \Sigma$ and $\underline{\zeta} \in \Lambda$,

$$\underline{\wp}_b(\underline{I}\underline{q}, \underline{I}\underline{\zeta}) \leq \frac{1}{17} [\underline{\wp}_b(\underline{q}, \underline{I}\underline{\zeta}) + \underline{\wp}_b(\underline{\zeta}, \underline{I}\underline{q})] \quad \dots(14)$$

4. If both $\underline{q}, \underline{\zeta} \in \Sigma = [1, \infty)$

$$\begin{aligned} & \underline{\wp}_b(\underline{I}\underline{q}, \underline{I}\underline{\zeta}) - \frac{1}{17} [\underline{\wp}_b(\underline{q}, \underline{I}\underline{\zeta}) + \underline{\wp}_b(\underline{\zeta}, \underline{I}\underline{q})] \\ &= \left[\left| \frac{1}{20\underline{q}} - \frac{1}{20\underline{\zeta}} \right|^3 + \left| \frac{1}{20\underline{q}} - \frac{1}{20\underline{\zeta}} \right| \right] \end{aligned}$$

$$\begin{aligned}
& -\frac{1}{17} [\varphi_b(\underline{q}, \underline{I}\underline{\varsigma}) + \varphi_b(\underline{\varsigma}, \underline{I}\underline{q})] \\
& = \frac{1}{20} \left[\frac{1}{20^2} \left| \frac{1}{\underline{q}} - \frac{1}{\underline{\varsigma}} \right|^3 + \left| \frac{1}{\underline{q}} - \frac{1}{\underline{\varsigma}} \right| \right] - \frac{1}{17} [\varphi_b(\underline{q}, \underline{I}\underline{\varsigma}) \\
& \quad + \varphi_b(\underline{\varsigma}, \underline{I}\underline{q})].
\end{aligned}$$

If $\underline{\varsigma} > \underline{q}$, then

$$\begin{aligned}
& \varphi_b(\underline{I}\underline{q}, \underline{I}\underline{\varsigma}) - \frac{1}{17} [\varphi_b(\underline{q}, \underline{I}\underline{\varsigma}) + \varphi_b(\underline{\varsigma}, \underline{I}\underline{q})] \\
& \leq \frac{1}{20} \left[\frac{1}{20^2} \left(\underline{q} - \frac{1}{\underline{\varsigma}} \right)^3 + \left(\underline{q} - \frac{1}{\underline{\varsigma}} \right) \right] - \frac{1}{17} [\varphi_b(\underline{q}, \underline{I}\underline{\varsigma}) \\
& \quad + \varphi_b(\underline{\varsigma}, \underline{I}\underline{q})] \\
& < \frac{1}{20} \left[\frac{1}{20^2} \left(\underline{q} - \frac{1}{20\underline{\varsigma}} \right)^3 + \left(\underline{q} - \frac{1}{20\underline{\varsigma}} \right) \right] \\
& \quad - \frac{1}{17} [\varphi_b(\underline{q}, \underline{I}\underline{\varsigma}) + \varphi_b(\underline{\varsigma}, \underline{I}\underline{q})] \\
& < \frac{1}{20} \left[\left(\underline{q} - \frac{1}{20\underline{\varsigma}} \right)^3 + \left(\underline{q} - \frac{1}{20\underline{\varsigma}} \right) \right] - \frac{1}{17} [\varphi_b(\underline{q}, \underline{I}\underline{\varsigma}) \\
& \quad + \varphi_b(\underline{\varsigma}, \underline{I}\underline{q})] \\
& \leq \frac{1}{20} \varphi_b(\underline{q}, \underline{I}\underline{\varsigma}) - \frac{1}{17} [\varphi_b(\underline{q}, \underline{I}\underline{\varsigma}) + \varphi_b(\underline{\varsigma}, \underline{I}\underline{q})] \\
& < \frac{1}{17} \varphi_b(\underline{q}, \underline{I}\underline{\varsigma}) - \frac{1}{17} [\varphi_b(\underline{q}, \underline{I}\underline{\varsigma}) + \varphi_b(\underline{\varsigma}, \underline{I}\underline{q})] \\
& = -\frac{1}{17} \varphi_b(\underline{\varsigma}, \underline{I}\underline{q}) \leq 0.
\end{aligned}$$

If $\underline{q} > \underline{\varsigma}$, then

$$\begin{aligned}
& \varphi_b(\underline{I}\underline{q}, \underline{I}\underline{\varsigma}) - \frac{1}{17} [\varphi_b(\underline{q}, \underline{I}\underline{\varsigma}) + \varphi_b(\underline{\varsigma}, \underline{I}\underline{q})] \\
& \leq \frac{1}{20} \left[\frac{1}{20^2} \left(\underline{\varsigma} - \frac{1}{\underline{q}} \right)^3 + \left(\underline{\varsigma} - \frac{1}{\underline{q}} \right) \right] - \frac{1}{17} [\varphi_b(\underline{q}, \underline{I}\underline{\varsigma}) \\
& \quad + \varphi_b(\underline{\varsigma}, \underline{I}\underline{q})] \\
& < \frac{1}{20} \left[\frac{1}{20^2} \left(\underline{\varsigma} - \frac{1}{20\underline{q}} \right)^3 + \left(\underline{\varsigma} - \frac{1}{20\underline{q}} \right) \right] \\
& \quad - \frac{1}{17} [\varphi_b(\underline{q}, \underline{I}\underline{\varsigma}) + \varphi_b(\underline{\varsigma}, \underline{I}\underline{q})]
\end{aligned}$$

$$\begin{aligned}
& < \frac{1}{20} \left[\left(\underline{\varsigma} - \frac{1}{20\underline{q}} \right)^3 + \left(\underline{\varsigma} - \frac{1}{20\underline{q}} \right) \right] - \frac{1}{17} [\varphi_b(\underline{q}, \underline{I}\underline{\varsigma}) \\
& \quad + \varphi_b(\underline{\varsigma}, \underline{I}\underline{q})] \\
& \leq \frac{1}{20} \varphi_b(\underline{\varsigma}, \underline{I}\underline{q}) - \frac{1}{17} [\varphi_b(\underline{q}, \underline{I}\underline{\varsigma}) + \varphi_b(\underline{\varsigma}, \underline{I}\underline{q})] \\
& < \frac{1}{17} \varphi_b(\underline{\varsigma}, \underline{I}\underline{q}) - \frac{1}{17} [\varphi_b(\underline{q}, \underline{I}\underline{\varsigma}) + \varphi_b(\underline{\varsigma}, \underline{I}\underline{q})] \\
& = -\frac{1}{17} \varphi_b(\underline{q}, \underline{I}\underline{\varsigma}) \leq 0,
\end{aligned}$$

which infers that for all $\underline{q}, \underline{\varsigma} \in \mathbb{U}$

$$\varphi_b(\underline{I}\underline{q}, \underline{I}\underline{\varsigma}) \leq \frac{1}{17} [\varphi_b(\underline{q}, \underline{I}\underline{\varsigma}) + \varphi_b(\underline{\varsigma}, \underline{I}\underline{q})].$$

Therefore, for $k = \frac{1}{17} < \frac{1}{s^2}$, \underline{I} satisfies the inequality.

Generate the sequence iteration

$$\underline{q}_n = \underline{\Omega}(\underline{q}_{n-1}, \underline{I}\underline{q}_{n-1}; \vartheta) \text{ with } 0 < \vartheta = \frac{1}{2} < 1.$$

There are two possibilities for \underline{q}_0 :

1. If $\underline{q}_0 \in \Lambda$, then

$$\underline{I}\underline{q}_0 = \frac{\underline{q}_0}{17}$$

$$\underline{q}_1 = \frac{1}{2}\underline{q}_0 + \frac{1}{2}T\underline{q}_0 = \left(\frac{9}{17}\right)\underline{q}_0$$

$$\underline{q}_2 = \frac{1}{2}\underline{q}_1 + \frac{1}{2}T\underline{q}_1 = \left(\frac{9}{17}\right)^2 \underline{q}_0$$

⋮

$$\underline{q}_n = \frac{1}{2}\underline{q}_{n-1} + \frac{1}{2}T\underline{q}_{n-1} = \left(\frac{9}{17}\right)^n \underline{q}_0.$$

Certainly, $\underline{q}_n \rightarrow 0$ as $n \rightarrow \infty$.

2. If $\underline{q}_0 \in \Sigma$, then

$$\underline{I}\underline{q}_0 = \frac{1}{20\underline{q}_0}$$

$$\underline{q}_1 = \frac{1}{2}\underline{q}_0 + \frac{1}{2}\underline{I}\underline{q}_0 = \frac{1}{2}\underline{q}_0 + \frac{1}{2} \cdot \frac{1}{20\underline{q}_0}$$

$$\frac{\underline{q}_1}{\underline{q}_0} = \frac{1}{2} + \frac{1}{40} \cdot \frac{1}{\underline{q}_0^2} \leq \frac{21}{40}.$$

If $\underline{q}_1 \in \Lambda$, as $n \rightarrow \infty, \underline{q}_n \rightarrow 0$ as in the previous case. If $\underline{q}_1 \in \Sigma$, then $\frac{\underline{q}_2}{\underline{q}_1} = \frac{1}{2} + \frac{1}{2} \cdot \frac{1}{\underline{q}_1^2} = \frac{21}{40}$. Continuing in comparable manner, we presume that $\underline{q}_{n-1} \in \Sigma$ yielding

$$\frac{\underline{q}_n}{\underline{q}_{n-1}} = \frac{1}{2} + \frac{1}{2} \cdot \frac{1}{\underline{q}_{n-1}^2} = \frac{21}{40}$$

and

$$\frac{\underline{q}_n}{\underline{q}_0} = \frac{\underline{q}_1}{\underline{q}_0} \cdot \frac{\underline{q}_2}{\underline{q}_1} \dots \frac{\underline{q}_n}{\underline{q}_{n-1}} = \left(\frac{21}{40}\right)^n,$$

and hence $\lim_{n \rightarrow \infty} \underline{q}_n = 0$.

Now, if $\underline{q}_0 \in \Lambda$, consider

$$\begin{aligned} \wp_b(\underline{q}_n, \underline{Iq}_n) &= |\underline{q}_n - \underline{Iq}_n|^3 + |\underline{q}_n - \underline{Iq}_n| \\ &= \left| \left(\frac{9}{17}\right)^n \underline{q}_0 - \left(\frac{9}{17}\right)^{n+1} \underline{q}_0 \right|^3 \\ &\quad + \left| \left(\frac{9}{17}\right)^n \underline{q}_0 - \left(\frac{9}{17}\right)^{n+1} \underline{q}_0 \right| \\ &= \left(\frac{9}{17}\right)^{3n} \left(\frac{8}{17}\right)^3 \underline{q}_0^3 + \left(\frac{9}{17}\right)^n \left(\frac{8}{17}\right) \underline{q}_0. \end{aligned}$$

Clearly,

$$\lim_{n \rightarrow \infty} \wp_b(\underline{q}_n, \underline{Iq}_n) = 0. \quad (15)$$

Also, if $\underline{q}_0 \in \Sigma$, then

$$\begin{aligned} &\wp_b(\underline{q}_n, \underline{Iq}_n) \\ &= |\underline{q}_n - \underline{Iq}_n|^3 + |\underline{q}_n - \underline{Iq}_n| \leq |\underline{q}_n|^3 + |\underline{q}_n| \\ &= \left| \left(\frac{21}{40}\right)^n \underline{q}_0 \right|^3 + \left| \left(\frac{21}{40}\right)^n \underline{q}_0 \right| \\ &= \left(\frac{21}{40}\right)^{3n} \underline{q}_0^3 + \left(\frac{21}{40}\right)^n \underline{q}_0. \end{aligned}$$

Clearly,

$$\lim_{n \rightarrow \infty} \wp_b(\underline{q}_n, \underline{Iq}_n) = 0. \quad \dots(16)$$

Thus, from equations 15 and 16, we get

$$\inf\{\wp_b(\underline{q}, \underline{Iq}); \underline{q} \in \mathcal{U}\} = 0.$$

Remark 1: If $\underline{q} = 0$ and $\underline{\varsigma} = \frac{1}{2}$, then $\underline{Iq} = 0$ and $\underline{I\varsigma} = \frac{1}{20}$ resulting in

$$\wp_b(\underline{Iq}, \underline{I\varsigma}) = \kappa[\wp_b(\underline{q}, \underline{I\varsigma}) + \wp_b(\underline{\varsigma}, \underline{Iq})]$$

$$\left(\frac{1}{20}\right)^3 + \left(\frac{1}{20}\right) \leq \kappa \left[\left(\frac{1}{20}\right)^3 + \left(\frac{1}{20}\right) + 1^3 + 1 \right] \dots(17)$$

which is true for all $\kappa \geq \frac{1}{41} < \frac{1}{s(s+1)}$ and $\kappa \geq \frac{1}{41} > \frac{1}{s^2(s^2+1)}$ and therefore Theorem 3 is an extension of Chatterjea fixed point theorem proved by Rathee et al.[11]

APPLICATION TO CAUCHY PROBLEM

Consider space $\mathcal{U} = \mathcal{C}[\underline{\delta}, \underline{\xi}] = \{\underline{q}(\varpi); \underline{q}: [\underline{\delta}, \underline{\xi}] \rightarrow R\}$ and the Cauchy problem

$$\frac{d\underline{\varsigma}(\varpi)}{d\varpi} = \phi(\varpi, \underline{\varsigma}(\varpi)), \text{ with } \underline{\varsigma}(\varpi_0) = \underline{\varsigma}_0, \} \dots(18)$$

where $\phi(\varpi, \underline{\varsigma}(\varpi)): [\underline{\delta}, \underline{\xi}] \times R \rightarrow R$, $\underline{\varsigma}(\varpi)$ are continuous functions in $[\underline{\delta}, \underline{\xi}]$ and $\underline{\varsigma}(\varpi)$ is differentiable in $[\underline{\delta}, \underline{\xi}]$. Here, ϖ_0 is a point in the interior of the interval $[\underline{\delta}, \underline{\xi}]$.

This Cauchy Problem 18 is identical to the following integral equation:

$$\underline{\varsigma}(\varpi) = \underline{\varsigma}_0 + \int_{\varpi_0}^{\varpi} \phi(\underline{\Lambda}, \underline{\varsigma}(\underline{\Lambda})) d\underline{\Lambda}. \quad \dots(19)$$

Define $\wp_b: \mathcal{U} \times \mathcal{U} \rightarrow [0, \infty)$ by

$$\wp_b(\underline{q}, \underline{\varsigma}) = \sup_{\varpi \in [\underline{\delta}, \underline{\xi}]} (\underline{q}(\varpi) - \underline{\varsigma}(\varpi))^2 \quad \forall \underline{q}, \underline{\varsigma} \in \mathcal{U}$$

Define $\underline{\Omega}: \mathcal{U} \times \mathcal{U} \times [0, 1] \rightarrow \mathcal{U}$ as

$$\underline{\Omega}(\underline{q}, \underline{\varsigma}; \vartheta) = \vartheta \underline{q} + (1 - \vartheta) \underline{\varsigma}.$$

Additionally, consider a self-mapping $\underline{I}: \mathcal{U} \rightarrow \mathcal{U}$ defined as

$$\underline{I\varsigma}(\varpi) = \underline{\varsigma}_0 + \int_{\varpi_0}^{\varpi} \Psi(\underline{\Lambda}, \underline{\varsigma}(\underline{\Lambda})) d\underline{\Lambda} \quad \forall \varpi, \underline{\Lambda} \in [\underline{\delta}, \underline{\xi}].$$

Then, existence of unique fixed point of mapping \underline{I} implies the existence and uniqueness of solution of the integral equation 19 and hence, the Cauchy Problem 18.

Lemma 3: Let $\mathcal{U} = C[\underline{\delta}, \underline{\xi}] = \{\underline{q}(\omega); \underline{q}: [\underline{\delta}, \underline{\xi}] \rightarrow R\}$ and define $\underline{\wp}_b: \mathcal{U} \times \mathcal{U} \rightarrow [0, \infty)$ by

$$\underline{\wp}_b(\underline{q}, \underline{\varsigma}) = \sup_{\omega \in [\underline{\delta}, \underline{\xi}]} (\underline{q}(\omega) - \underline{\varsigma}(\omega))^2 \quad \forall \underline{q}, \underline{\varsigma} \in \mathcal{U}$$

Define the convex structure $\underline{\Omega}: \mathcal{U} \times \mathcal{U} \times [0, 1] \rightarrow \mathcal{U}$ as

$$\underline{\Omega}(\underline{q}, \underline{\varsigma}; \vartheta) = \vartheta \underline{q} + (1 - \vartheta) \underline{\varsigma} \quad \forall \underline{q}, \underline{\varsigma} \in \mathcal{U}.$$

Then, $(\mathcal{U}, \underline{\wp}_b, \underline{\Omega})$ is a convex b -metric space.

Proof. We observe that

1. $\underline{\wp}_b(\underline{q}, \underline{\varsigma}) \geq 0 \quad \forall \underline{q}, \underline{\varsigma} \in \mathcal{U}.$
2. $\underline{\wp}_b(\underline{q}, \underline{\varsigma}) = 0 \iff \underline{q} = \underline{\varsigma}.$
3. $\underline{\wp}_b(\underline{q}, \underline{\varsigma}) = \underline{\wp}_b(\underline{\varsigma}, \underline{q}).$
4. $\underline{\wp}_b(\underline{q}, \underline{\varsigma}) \leq 2[\underline{\wp}_b(\underline{q}, \underline{\eta}) + \underline{\wp}_b(\underline{\eta}, \underline{\varsigma})]$ as

$$\begin{aligned} \underline{\wp}_b(\underline{q}, \underline{\varsigma}) &= \sup_{\omega \in [\underline{\delta}, \underline{\xi}]} (\underline{q}(\omega) - \underline{\varsigma}(\omega))^2 \\ &= \sup_{\omega \in [\underline{\delta}, \underline{\xi}]} (\underline{q}(\omega) - \underline{\eta}(\omega) + \underline{\eta}(\omega) - \underline{\varsigma}(\omega))^2 \\ &\leq 2\{\sup_{\omega \in [\underline{\delta}, \underline{\xi}]} (\underline{q}(\omega) - \underline{\eta}(\omega))^2 \\ &\quad + \sup_{\omega \in [\underline{\delta}, \underline{\xi}]} (\underline{\eta}(\omega) - \underline{\varsigma}(\omega))^2\} \\ &= 2[\underline{\wp}_b(\underline{q}, \underline{\eta}) + \underline{\wp}_b(\underline{\eta}, \underline{\varsigma})]. \end{aligned}$$

Also, for $\underline{\Omega}(\underline{q}, \underline{\varsigma}; \vartheta) = \vartheta \underline{q} + (1 - \vartheta) \underline{\varsigma} \quad \forall \underline{q}, \underline{\varsigma} \in \mathcal{U}$, we have

$$\begin{aligned} &\underline{\wp}_b(\underline{\eta}, \underline{\Omega}(\underline{q}, \underline{\varsigma}; \vartheta)) \\ &= \sup_{\omega \in [\underline{\delta}, \underline{\xi}]} (\underline{\eta}(\omega) - \underline{\Omega}(\underline{q}(\omega), \underline{\varsigma}(\omega); \vartheta))^2 \\ &= \sup_{\omega \in [\underline{\delta}, \underline{\xi}]} (\underline{\eta}(\omega) - \{\vartheta \underline{q}(\omega) + (1 - \vartheta) \underline{\varsigma}(\omega)\})^2 \\ &\leq \sup_{\omega \in [\underline{\delta}, \underline{\xi}]} (\vartheta |\underline{\eta}(\omega) - \underline{q}(\omega)| + (1 - \vartheta) |\underline{\eta}(\omega) - \underline{\varsigma}(\omega)|)^2 \\ &= \sup_{\omega \in [\underline{\delta}, \underline{\xi}]} [\vartheta^2 (\underline{\eta}(\omega) - \underline{q}(\omega))^2 \\ &\quad + (1 - \vartheta)^2 (\underline{\eta}(\omega) - \underline{\varsigma}(\omega))^2 + 2\vartheta(1 - \vartheta) |\underline{\eta}(\omega) - \underline{q}(\omega)| |\underline{\eta}(\omega) - \underline{\varsigma}(\omega)|] \\ &\leq \sup_{\omega \in [\underline{\delta}, \underline{\xi}]} [\vartheta^2 (\underline{\eta}(\omega) - \underline{q}(\omega))^2 \end{aligned}$$

$$\begin{aligned} &+ (1 - \vartheta)^2 (\underline{\eta}(\omega) - \underline{\varsigma}(\omega))^2 + \vartheta(1 - \vartheta) \{(\underline{\eta}(\omega) - \underline{q}(\omega))^2 + (\underline{\eta}(\omega) - \underline{\varsigma}(\omega))^2\}] \\ &\leq \vartheta \sup_{\omega \in [\underline{\delta}, \underline{\xi}]} (\underline{\eta}(\omega) - \underline{q}(\omega))^2 \\ &\quad + (1 - \vartheta) \sup_{\omega \in [\underline{\delta}, \underline{\xi}]} (\underline{\eta}(\omega) - \underline{\varsigma}(\omega))^2 \\ &= \vartheta \underline{\wp}_b(\underline{\eta}, \underline{q}) + (1 - \vartheta) \underline{\wp}_b(\underline{\eta}, \underline{\varsigma}) \end{aligned}$$

Thus, for $s \geq 2$, $(\mathcal{U}, \underline{\wp}_b, \underline{\Omega})$ is convex b -metric space.

Theorem 4: Consider

$$|\phi(\underline{\Lambda}, \underline{q}(\underline{\Lambda})) - \phi(\underline{\Lambda}, \underline{\varsigma}(\underline{\Lambda}))| \leq [\kappa M(\underline{q}, \underline{\varsigma})]^{\frac{1}{2}}$$

for all $\omega, \underline{\Lambda} \in [\underline{\delta}, \underline{\xi}]; \underline{q}, \underline{\varsigma} \in \mathcal{U}$ and some $\kappa < \frac{1}{(\underline{\xi} - \underline{\delta})^2} \leq \frac{1}{s^2}$

where

$$M(\underline{q}, \underline{\varsigma}) = \underline{\wp}_b(\underline{q}, \underline{I}\underline{\varsigma}) + \underline{\wp}_b(\underline{\varsigma}, \underline{I}\underline{q}).$$

Then, a unique solution exists for Integral Equation 19.

Proof. Consider

$$\begin{aligned} &(\underline{I}\underline{q}(\omega) - \underline{I}\underline{\varsigma}(\omega))^2 \\ &\leq \left(\int_{\omega_0}^{\omega} |\phi(\underline{\Lambda}, \underline{q}(\underline{\Lambda})) - \phi(\underline{\Lambda}, \underline{\varsigma}(\underline{\Lambda}))| d\underline{\Lambda} \right)^2 \\ &\leq \left(\int_{\omega_0}^{\omega} [\kappa M(\underline{q}, \underline{\varsigma})]^{\frac{1}{2}} d\underline{\Lambda} \right)^2 \\ &\leq \kappa M(\underline{q}, \underline{\varsigma}) \left(\int_{\omega_0}^{\omega} d\underline{\Lambda} \right)^2 \\ &= \kappa M(\underline{q}, \underline{\varsigma}) (\omega - \omega_0)^2 \\ &\leq \kappa M(\underline{q}, \underline{\varsigma}) (\underline{\xi} - \underline{\delta})^2 \end{aligned}$$

implying Integral Equation 19 and hence, the Cauchy Problem 18, has a unique solution that is unique as all the hypothesis of Theorem 3 are satisfied.

CONCLUSION

As an extension of the elementary result of Rathee et al.[11], we put forward a fixed point theorem that ensures the existence of a fixed point for Chatterjea contraction in the setting of convex b -metric spaces.

The Kransnoselkij iterative process is used for approximating the fixed point and the conclusions drawn here and use these conclusions to solve Cauchy problem.

OPEN PROBLEM

Rathee et al.[11] ensured the existence of fixed point for Chatterjea contraction for the constant $\underline{\kappa} \in [0, \frac{1}{s^2(s^2+1)})$. In addition, we extended the same for $\underline{\kappa} \in [\frac{1}{s^2(s^2+1)}, \frac{1}{s(s+1)})$. Is it viable to further relax the condition for $\underline{\kappa} \in [\frac{1}{s(s+1)}, \frac{1}{2})$?

REFERENCES

- [1] Afshari, H., Aydi, H., Karapinar, E. (2020). On generalized ϑ - ψ -Geraghty contractions on b-metric spaces, *Georgian Math. J.* 27, (2020), 9-21.
- [2] Aleksić, S., Huang, H., Mitrović, Z., Radenović, S. (2018). Remarks on some fixed point results in b-metric space, *J. Fixed Point Theory Appl.* 20(147), 1-17.
- [3] Aydi, H., Bota, M.F., Karapinar, E., Moradi, S., *A common fixed point for weak contractions on b-metric spaces*, Fixed Point Theory, **13**, (2012), 337-346.
- [4] Bakhtin, I.A. (1989). The contraction mapping principle in quasi-metric spaces, *Funct. Anal., Unianowsk Gos. Ped. Inst.* 30, 26-37.
- [5] Banach, S. (1922). Sur les operations dans les ensembles abstraits et leur applications aux equations integrales, *Fund. Math.* 3, 133-181. .
- [6] Chatterjea, S.K. (1972). Fixed-point theorems, *Comptes Rendus de l'Académie Bulgare des Sciences*, vol. 25, pp. 727–730.
- [7] Chen, L., Li, C., Kaczmarek, R., Zhao, Y. (2020). Several fixed point theorems in convex b-metric spaces and applications, *Mathematics*, 8(2), 1-16.
- [8] Czerwik, S., (1993). Contraction mappings in b-metric spaces, *Acta Mathematica et Informatica Universitatis Ostraviensis* 1, 5-11.
- [9] Djafari-Rouhani, B., Moradi, S. (2014), On the existence and approximation of fixed points for Ćirić type contractive mappings. *Quaestiones Mathematicae*, 37(2), 179-189.
- [10] Kirk, W., Shahzad, N. (2024). Fixed Point Theory in Distance Spaces, Springer: Berlin, Germany
- [11] Rathee, S., Kadyan, A., Kumar, A., Tas, K. (2022). Fixed point results for Ćirić and almost contractions in convex b-metric spaces, *Mathematics*, 10(3), 1-21.
- [12] Reich, S. (1971). Chatterjea 's fixed point theorem. *Boll. UMI*, 4, 1-11.
- [13] Takahashi, W. (1970). A convexity in metric space and nonexpansive mappings, *I. Kodai Math. Semin. Rep.* 22, 142-149.



Techniques of Improving Electric Characteristics of Si Strip Sensors Equipped using Various Isolation Methods

Ranjeet Dalal¹

ABSTRACT

Si sensors in future generations of accelerators will face a harsh radiation environment. Additionally, the double-sided silicon sensors are having an electron accumulation layer between the n+ strips in the p+-n--n+ configuration. Various techniques, like p-spray and p-stop, which provide interstrip isolation, have an additional impact on other properties of sensors including capacitance and breakdown voltage. The p-spray has good interstrip trends, but isolation ensuring p-spray dose leads to very poor VBD. P-stop doping ($\sim 10^{18} \text{ cm}^{-3}$) ensures strip isolation but leads to high inter-strip capacitance and low VBD, particularly for high surface damage. Thus, to find out the optimized electric characteristics of the p+-n--n+ sensors, a simulation-based comprehensive analysis is performed for a combination of these two techniques.

Keywords: Si Sensors, Strip Isolation, Simulation, P-stop, P-spray

INTRODUCTION

Si strip sensors are widely used in present-day nuclear and particle physics experiments [1]. Double-sided Si Strip Detectors (DSSDs) can be useful for particle tracking purposes due to their durability and low mass tracker design required. However, a positive oxide charge density Q_F ($\sim 10^{11} \text{ cm}^{-2}$) is produced around the Si-SiO₂ interface of the sensor. Further, during the detector operation, high energy radiation introduces bulk damage [2] in sensor volume and at the Si-SiO₂ interface, causing surface damage [3], leading to an increase in Q_F up to a high value of around $3 \times 10^{12} \text{ cm}^{-2}$ shorting the adjacent n+-strips, leading to loss of position resolution. Surface damage can affect the operational characteristics of silicon sensors. The presence of Q_F near the Si-SiO₂ interface results in the formation of an electron accumulation layer just below the Si-SiO₂ interface. The increment in the value of Q_F after exposure to ionizing radiation results in a denser electron accumulation layer. The dense electron accumulation layer results in various degrading effects for silicon sensors. For p-on-n sensors (with p+ pixel or strip implants), a dense electron accumulation layer creates high electric field regions near p+ doping. These high electric field regions may decrease the breakdown voltage for the irradiated p-on-n strip/pixel sensors.

Further, the presence of a dense accumulation layer creates non-depleted regions between the strips/pixels, which may result in a reduction of signal for particles hitting between the strips/pixels. Further, surface damage results in an increase in interstrip capacitance (C_{int}), and affects the breakdown voltage (V_{BD}) of Si sensors.

For the n+ side of double-sided strip sensors, the strip isolation problem can be resolved by introducing p-stop [4] and p-spray [5] under SiO₂. However, using these strategies adversely affects the V_{BD} and C_{int} of the sensors. It has been shown that [6] individual p-stop or p-spray techniques do not provide an adequate solution. In this work, a comprehensive simulation study of the combination of these two isolation techniques, along with various numbers of p-stops and p-stops with metal overhang for the ohmic side of p+-n--n+ sensors, is carried out for different designs. For this work, we have used Q_F values from $1 \times 10^{11} \text{ cm}^{-2}$ (non-irradiated sensor) to $3 \times 10^{12} \text{ cm}^{-2}$ (highly irradiated sensor). Present work may be useful for surface damage; however, bulk damage effects should also be considered for the proper simulation of sensors. The proposed design guideline is a tradeoff between interstrip conductance G_{int} , C_{int} and V_{BD} .

¹ Department of Physics, Gurugram University, Gurugram, India. E-mail: ranjeet@gurugramuniversity.ac.in

The silicon sensor device simulations using the TCAD (Technology Computer Aided Design) software have become an indispensable tool in the development of radiation-hard silicon sensor designs. The Silvaco and Synopsys TCAD tools [7, 8] are the common software used by the silicon sensor community. These TCAD software are widely used in the semiconductor industry, and their simulation capabilities have been well tested for different silicon device designs over many years. These TCAD tools have a significantly large user base and can be used with ease. The proliferation of TCAD tools in silicon sensor development is due to some of the reasons outlined below:

- (a) The TCAD simulations help in predicting the various properties of silicon sensors under operating conditions without actual device fabrication. Using these simulations, it is possible to visualize the effect of variation of particular sensor parameters (say bulk doping) on different sensor properties (electrical, thermal and optical properties). So, these simulations allow the optimization of sensor fabrication process and geometrical design parameters, which would be a very difficult task using experimental investigation only.
- (b) These TCAD tools can be used to simulate the radiation damage using the appropriate bulk and surface damage models. Using these TCAD software, it is possible to mimic the bulk damage by implementing the different trap levels inside the band gap of silicon. Moreover, surface damage can be implemented using the appropriate oxide charge density and interface traps along the Si-SiO₂ interface. The TCAD simulations can be used to understand the radiation damage mechanism on silicon sensors by comparing various macroscopic quantities like electric fields, electron/hole currents, space charge density etc. inside the sensor volume under different operating conditions and irradiation fluence.

Present simulations are performed with the help of a semiconductor device simulator, ATLAS [7].

DESIGN STRUCTURE AND SIMULATION TECHNIQUE

Simulations are performed on a n-type substrate having bulk doping of $7 \times 10^{11} \text{ cm}^{-3}$, thickness of $300 \mu\text{m}$ with n^+ strips of $18 \mu\text{m}$ and strip pitch of $80 \mu\text{m}$. The n^+ and

p^+ depths are kept at $1 \mu\text{m}$ (where concentration is equal to bulk n^-) with the Gaussian profile.

The schematic of the structures simulated in this work is shown in Figure 1. Set A defines the basic reference structures with p-stop and p-spray isolation techniques. A1 defines a p-spray structure with a peak doping concentration of $2.8 \times 10^{17} \text{ cm}^{-3}$ and a doping depth of $0.5 \mu\text{m}$. In contrast, A2 defines a structure with a $40 \mu\text{m}$ wide single p-stop with a doping concentration of $1 \times 10^{18} \text{ cm}^{-3}$ and a p-stop doping depth of $1 \mu\text{m}$. Set B contains symmetrically placed double p-stop structures (B1) separated by $d_1 = 12 \mu\text{m}$ along with triple p-stop structures (B2) separated by $d_2 = 11 \mu\text{m}$. As distances between the outer edges of outer p-stops are always equal to $40 \mu\text{m}$, all the configurations can be considered equivalent to $40 \mu\text{m}$ single p-stop and hence are compared in this work.

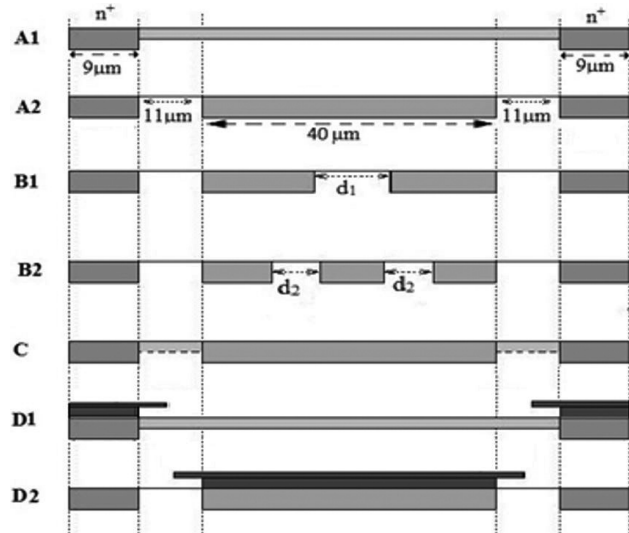


Fig. 1. Schematics of the simulated strip sensors with different isolation structures

Set C defines p-stop – p-spray combined isolation in which a $40 \mu\text{m}$ wide p-stop with a doping depth of $1 \mu\text{m}$ on a p-spray layer of doping depth of $0.5 \mu\text{m}$ is considered. The effect of metal overhang over p-spray and p-stop is quantified using structures D1 and D2, respectively. All these structures have good strip isolation properties, so only C_{int} and V_{BD} comparisons are shown in the results section.

SIMULATION RESULTS

Multiple P-stop isolation

C_{int} vs. Q_F plot for multiple P-stops is shown in figure 2(I). For all the configurations, an increase in Q_F

results in an increase in the electron accumulation concentration, which leads to a narrower depletion width between n-substrate and p-stop and hence causes a higher value of C_{int} . A structure having single p-stop (A2) has the highest C_{int} as compared to double (B1) and triple (B2) p-stops since, in latter cases, additional capacitors in series lead to lower C_{int} . It can be observed from figure 2(II) that a single p-stop set (A2) has the lowest V_{BD} , followed by double and triple p-stops. Thus, triple p-stop provides better C_{int} and V_{BD} performance than single p-stop while ensuring isolation.

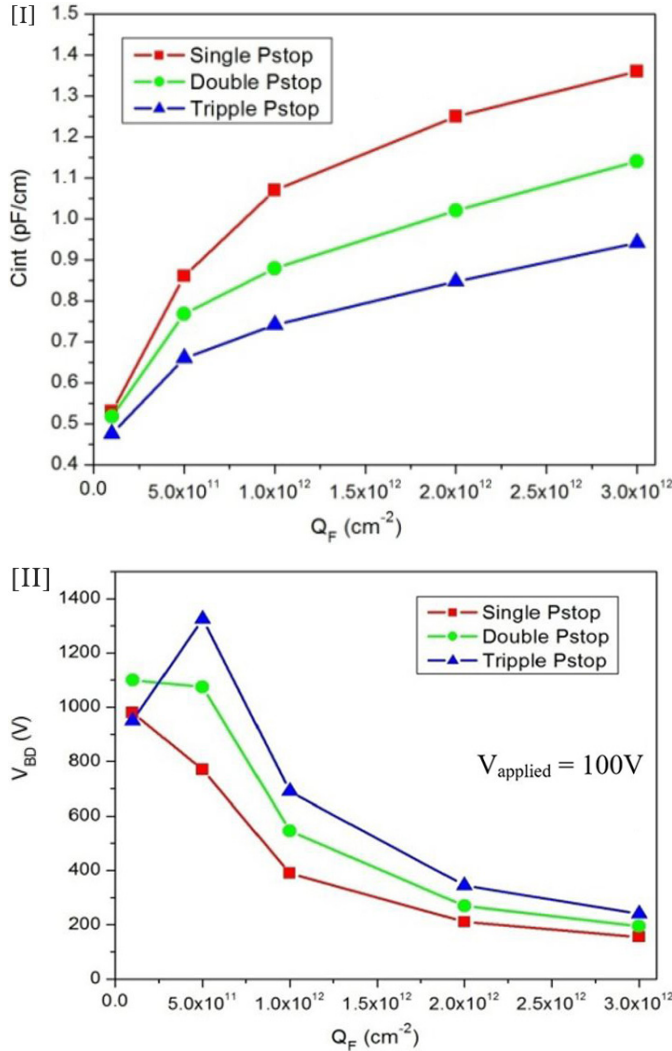


Fig. 2. (I) Plot of C_{int} vs Q_F , and (II) Plot of V_{BD} vs. Q_F , for the different multiplicity of p-stops

P-stop – P-spray Combined Isolation

Simulations have found that for $N_{pspray} = 4 \times 10^{16}$ cm⁻³ and $N_{pstop} = 1 \times 10^{17}$ cm⁻³, the most optimized results of C_{int} and V_{BD} are achieved which are shown as set C in

figure 3. For comparison, plots of A1 (p-spray) and A2 (p-stop) are also shown.

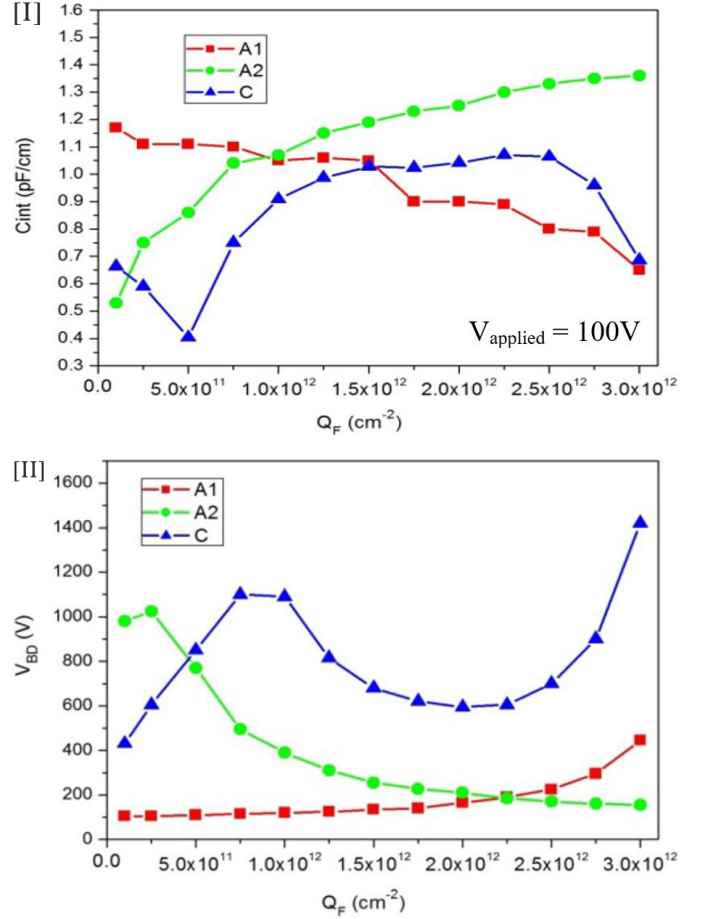


Fig. 3. (I) Plot of G_{int} vs. Q_F , and (II) Plot of V_{BD} vs Q_F , for p-stop – p-spray combinations

P-spray/P-stop with Metal Overhang (MO)

Since the metal overhang is directly coupled to the electron accumulation layer below it, forming a parallel

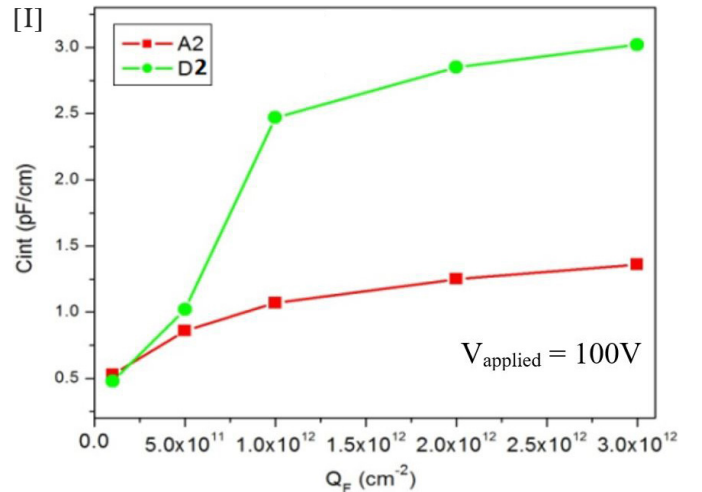


Fig. 4. (I) Plot of C_{int} vs. Q_F at $V_{applied} = 100V$

capacitor, its introduction results in a significant increase in C_{int} (Figure 4(I)) both for D1 and D2 configurations. The metal overhang structure is useful in increasing the V_{BD} for D1 and D2 for intermediate values of Q_F . As the metal overhang structure is tied with p-stop in D2, it has a negative potential compared to the electron accumulation layer. This results in the smoothening of potential contours, thus increasing the V_{BD} (Figure 4(II)).

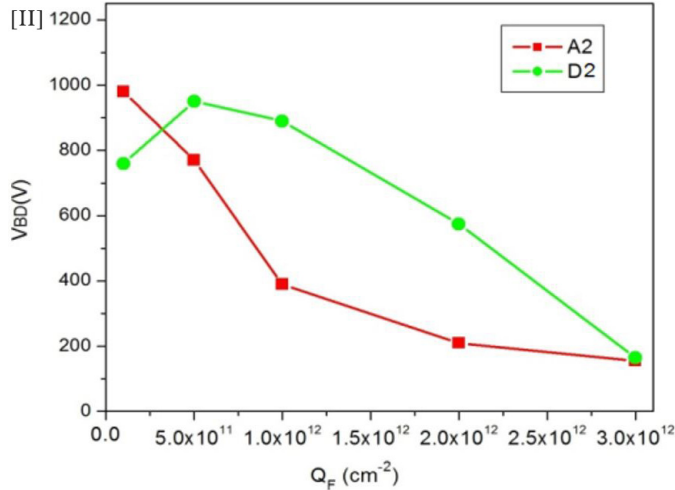


Fig. 4. (II) Plot of V_{BD} vs Q_F , for A2 and D2 structures

SUMMARY AND CONCLUSION

The P-stop and p-spray are commonly used techniques for strip isolation on the n^+ side of the $p^+-n^- - n^+$ Si strip sensors. Here, we have investigated the effect of other alternative designs, which include one or more p-stop, p-spray – p-stop combinations and metal overhangs. It

is found that using multiple p-stops improves the C_{int} and V_{BD} without degrading G_{int} . Similarly, optimized p-spray – p-stop combined isolation has good C_{int} and V_{BD} without losing strip isolation. The use of metal overhang over p-stop to improve V_{BD} is not an attractive option as it results in significant deterioration of C_{int} .

ACKNOWLEDGEMENTS

The author would like to thank Prof. Ashutosh and Kirti Ranjan from the CDRST lab at the University of Delhi for their insightful guidance in this work.

REFERENCES

- [1] H. G. Moser, Si detector systems in high energy physics, *Prog. in Particle and Nucl. Phys.* 63 (2009) 186
- [2] R.D 50 Status Reports <http://rd50.web.cern.ch/rd50/>
- [3] R. Wonstorf, Radiation Hardness of Silicon Detectors: Current Status, *IEEE Trans. Nucl. Sc.* NS 44(1997)806
- [4] Y. Unno et al., Novel p-stop structure in n-side of silicon microstrip detector, *Nucl. Inst. Methods A* 541 (2005) 40
- [5] C. Fleta et al., P-spray implant optimization for the fabrication of n-in-p microstrip detectors, *Nucl. Inst. Methods A* 573 8.
- [6] P. Saxena et al., Simulation studies of the n^+n^- Si sensors having p-spray/p-stop implant for the SiD experiment, *Nucl. Instrum. Methods A* 658 (2011) 66
- [7] ATLAS Silvaco version 5.15.32.R Nov 2009, User's manual, <http://www.silvaco.com>
- [8] Synopsys TCAD tool, California, U.S.A. <http://www.synopsys.com>



Visual Narratives: Enhancing Image Captioning with CNN-RNN-LSTM Fusion

Kapil Kumar Choudhary¹, Naveen Kumar² & Dishant Kumar³

ABSTRACT

This paper introduces an effective image captioning system that has been developed using the most advanced deep learning techniques. The current study uses a diverse Flickr dataset with the pre-trained VGG16 model for feature extraction and LSTM networks for caption generation. The system is very effective in creating meaningful captions for all types of images, which increases accessibility for visually impaired individuals. More importantly, the text-to-speech functionality is inappropriately integrated, and thus the generated captions are accessible through verbalized words. The paper deals with system architecture, data preprocessing subtleties, and evaluation measures, thus giving an appropriate overview of the results and implications in the real world.

Keywords: VGG16, LSTM, BLEU, Caption Generation

INTRODUCTION

In recent years, the integration of computer vision and natural language processing has experienced significant advancements, particularly in the domain of AI-driven image captioning. This field specializes in the development of algorithms and models capable of automatically generating descriptive and contextually relevant captions for images. The growing prevalence of social media, ecommerce platforms, and autonomous vehicles has amplified the demand for systems that can interpret and decode visual data in a human-like manner [9, 20].

Early approaches to image captioning primarily relied on encoding visual information into a single feature vector representing the entire image [13, 23]. However, such methods often neglected critical details about objects and their spatial and semantic relationships within a scene, limiting descriptive accuracy and contextual understanding [29]. To address these challenges, recent research has focused on incorporating spatial and semantic relationships and leveraging attention mechanisms to enhance the generation of coherent and detailed captions [2, 12, 27].

This paper provides a comprehensive survey of recent advancements in AI image captioning, emphasizing innovative techniques that utilize spatial relationships, attention mechanisms, and transformer architectures to improve caption accuracy and contextual relevance [5, 20, 24]. We begin with a discussion of foundational principles and the technical challenges of implementation. Subsequently, we explore key developments in the field, including advancements in object detection [11], geometric and semantic excitation methods [25], and hybrid transformer-based architectures [5, 29].

RELATED WORK

- **Early Deep Learning Models:** This includes models that use Convolutional Neural Networks (CNNs) for the extraction of image feature and Recurrent Neural Networks (RNNs) or alternatives like Long Short-Term Memory (LSTM) networks for generating captions.
- **CNN-RNN Based Models:** Focus on more recent developments that combine both CNNs and RNNs/LSTMs for image captioning. It discusses how

¹ Department of Mathematics, IIIT, Kota, Rajasthan, India. E-mail: kapil.maths@iiitkota.ac.in

² Department of Mathematics Gurugram University, Gurugram, Haryana. E-mail: naveen@gurugramuniversity.ac.in

³ Department of Mathematics IIIT, Kota, Rajasthan, India. E-mail: 2021kucp1068@iiitkota.ac.in

CNNs are used for encoding image features while RNNs/LSTMs are used for generating captions.

- **Evaluation Metrics:** Briefly touch on the evaluation metrics commonly used in assessing the performance of image captioning models, such as BLEU, METEOR, CIDEr and ROUGE. In this research paper, we are using BLEU as our evaluation Metrics Discuss their strengths and limitations in capturing the quality of generated captions.
- **Challenges and Limitations:** Highlight challenges and limitations faced by existing image captioning models, such as handling different domains of image content, generating descriptive and coherent captions, and scalability to large datasets.

METHODOLOGY

- **Data Collection:** We carefully Curate a diverse dataset of images and corresponding captions from reliable sources, ensuring representation across various domains and scenarios

Dataset: We trained our model with flickr8k Dataset, which comprises of approximately 8000 images, and for each image there are up to five captions per image. The images we choose are from six different Flickr groups, and these images do not contain any well-known people or locations, but were manually selected to depict a variety of scenes and situations.

- **Data Preprocessing:** Employ robust data preprocessing techniques such as resizing, normalizing to enhance the quality and diversity of the data set for optimal model training.

We converted the text into lowercases and resized all the images. we also removed the additional spaces, special characters, and digits from the texts. We added startseq in the starting of each

caption and endseq in the end of each caption that is generated by our model.

- **Data Partitioning:** Divide the dataset into appropriate training, validation and testing subsets to ensure a reliable evaluation of the model's performance and generalization capabilities.

Description	Count
Total Images	8091
Training Data	7282
Testing Data	1009
Flickr8k Token (text)	40455
Flickr8k Lemmatized Token (text)	40455

- **Model Selection:** Choose an appropriate deep learning model architecture, such as Convolutional Neural Network (CNN) for the purpose of image feature extraction and a recurrent neural network (RNN).

Base CNN Architecture

- Pre-trained CNNs:** It leverages the power of pre-trained convolutional neural networks like VGG16. These models have been trained on large image datasets and they can extract rich and quality visual features from images.
- VGG16:** This is the pre-trained CNN model having 16 layers, which was trained in that model. The CNN-based VGG16 was trained with a dataset of ImageNet. Developed by the Visual Geometry Group of Oxford University. The 16 layers of VGG16 have 13 convolutional layers and 3 fully connected layers. It basically is used as the first stage in any image recognition processes. The fully connected layers in the network do predictions based on the characteristics learned from the convolutional layers. The layers use the retrieved characteristics as inputs for classifying input images to a predefined set of classes.

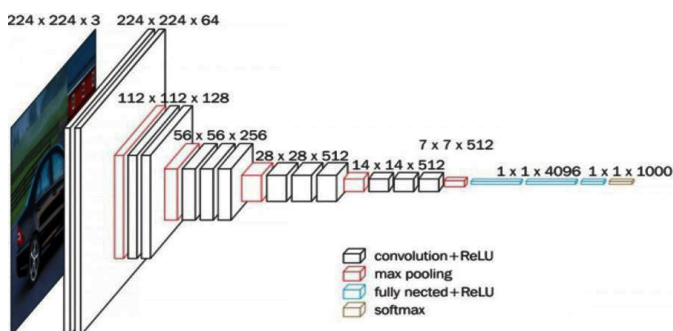
```
# before preprocess of text
mapping['1000260201_693b08cb0e']

'A child in a pink dress is climbing up a set of stairs in an entry way .',
'A girl going into a wooden building .',
'A little girl climbing into a wooden playhouse .',
'A little girl climbing the stairs to her playhouse .',
'A little girl in a pink dress going into a wooden cabin .'

# preprocess the text
clean(mapping)

# after preprocess of text
mapping['1000260201_693b08cb0e']

'startseq child in pink dress is climbing up set of stairs in an entry way endseq',
'startseq girl going into wooden building endseq',
'startseq little girl climbing into wooden playhouse endseq',
'startseq little girl climbing the stairs to her playhouse endseq',
'startseq little girl in pink dress going into wooden cabin endseq'
```



CNN is a general term used in image processing related algorithms. CNN evolves from a very simple ANN. CNN gets a better outcome over images and this simple dense network tends to work perfectly whenever there are specific features used while classifying the image with classification work. The CNN does very well with some more feature inside an image and hence used for processing it in local features too. Since images are made of repeated patterns of a particular thing any image. It takes the images as input and then it understands that input for the assigned task. Among all, CNN has basically two functions convolution and pooling. In that, Convolution is used in CNN to determine an edge of an image and reduction of an image size uses pooling. It is a technique where we will take a small size matrix called kernel or filter, and after that we will move it to over our image and convert it according to the filter values. The formula for the feature map is Thus, symbols f and h denote the input image and filter respectively, while m , n denote the row and column indices of the matrix that results from:

$$G[M, N] = ([F * H])(M, N)$$

$$S = \sum_J \sum_K H[J, K] F[M - J, N - K]$$

Two main computational procedures realize the convolution layer calculation, performed below. The step is applied to calculate the intermediate value Z , and its addition by distortion. Next in line is a non-linear activation g applied to the intermediate value.

$$Z^i = W^i * A^{i-1} + b^i$$

$$A^i = g^i * Z^i$$

Recurrent Neural Network (RNN)

Generally, CNNs do not perform well on sequential data when input data is connected. In the case of CNNs, there is no interaction between previous inputs and subsequent data. Hence, all the outputs depend solely on the input at that moment. Depending on the trained model, CNN takes the input and gives an output.

For performing tasks requiring sequence-based relationships, RNNs are used. RNNs have memory, allowing them to remember what has passed or happened earlier in the data. “Earlier” refers to the previous inputs that has passed. RNN performs best on textual data because textual data is interrelated or we can say that text data is sequential data. Basic formula for RNN is written as follow:

$$h(t) = f(h^{t-1}, x(t); \theta)$$

Here:

- f represents the hidden state function.
- $h(t-1)$ is the previous hidden state.
- $x(t)$ is the current input.
- θ denotes the parameters of the function.

LSTM Network Design

LSTM is the variant of RNN. It performs much better than simple RNN because it offers the solution for the problems faced by simple RNN. Two major problems encountered with Simple RNN are:

- exploding gradient and vanishing gradient.
- long term dependency.

LSTM uses the gates for memory; however, gates are the core of LSTM. There are the following in the list of LSTM gates are:

- input gate
- forget gate
- output gate

All of them have sigmoid activation function. Sigmoid: Output is between 0 and 1, mainly 0 or 1. If output is 0, then it blocks. If output is 1, then pass everything.

Number of LSTM Layers

The number of layers of LSTM impacts the capturing of long-term dependencies in the image and more complex captions being generated. Experiment with different configurations of layers to find a good depth for your application.

Size of the Hidden State

The size of the hidden state within an LSTM cell determines at any point in time what information the model can hold and process. A greater size in the hidden state increases reasoning but requires more computation.

C. Additional Consideration

Beam Search Decoding: Beam search can actually be applied to explore multiple candidate captions and choose the best one for a scoring function, although it would increase diversity and general quality of the generated captions.

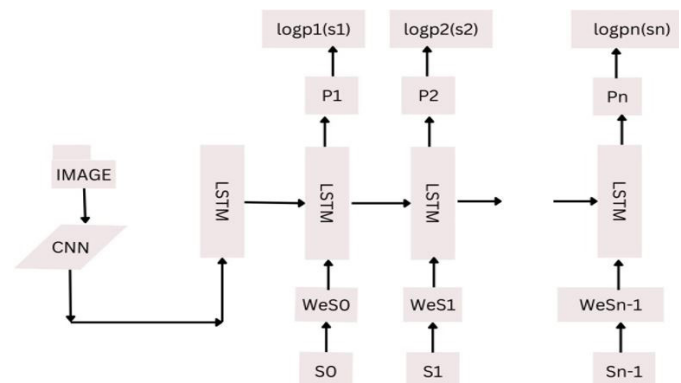
MODEL TRAINING

After designing the model and preparing and before that, preprocess the data followed by fitting the data with Repeat the model and apply it in turn to the training data. The training procedure is very computer resource intensive, because of it this requires cycling through the entire training set that is available or we are using numerous times, and then we will estimate the loss function. Passing the training data set into the model numerous times is called epochs. Therefore, instead of loading the whole data set in one go, we come up with a new method or way that passes that data gradually by means of a generator, that is called Progressive Loading. We can see that the size of any data set is proportional. In terms of memory requirements. However, we are trying to design one of the efficient methods of this, and hence we will create a generator function that is called a data generator. This generator will generate a function that will accept an image array as input: embeddings and encoded word sequences, it will produce one shot encoded words one after another. These one-shot encoded words in addition to their embeddings, will feed the image progressively in two sets of neural networks and we will sequentially train the data to produce the good weights. After loading of data, we will come to the training of the model. Here we will apply 20 epochs and each of the epochs will contain 6000 images for training. It is to take a note to mention that the number of epochs that we have taken is on intuitive basis i.e. based on instinct and natural understanding. Quite fortunately, these numbers of epochs have proved to drastically reduce the model loss, and these epoch also prevent under-fitting and over-fitting of the model. Moreover, as we traditionally train our model it takes some amount of time-span, so it is worth of using model checkpoints which periodically saves the progress of model after the completion of each epoch. In this way, even if a process suddenly stops due to a reason, it resumes so that no significant progress gets lost. It works efficiently with its memory without causing a system crash even when working on large data sets, and one is able to get a full view during training and validation of loss curves, fine-tune hyper-parameters, and judge performance of a model. This would, besides monitoring validation metrics and applying the early stopping, give over-fitting another level of protection and would build a tougher model, potentially saving compute in later epochs.

MODEL IMPLEMENTATION

We are using CNN combined with LSTM, for developing an efficient model that is require to generate captions of the images. The model will take input as an image and produce text as an output. We will use Keras functional API model to stack the model. There will a total of three sections to the structure:

- A. **Feature Extractor:** This one is being used to reduce the dimension from 4096 down to 256. Dropout Layer will be used here. One of them will add the CNN and LSTM. Its characteristic is that this model will predict what we are feeding into it, with having the photographs already been pre-processed, we will use the Xception model without the final classification layer.
- B. **Sequence Processor:** It processes input text through the Embedding layer and LSTM layer.
- C. **Decoder:** We will combine all the outputs of the last two layers by using a dense layer to come up with our final predictions. The feature extractor and the sequence processor produce an output vector of fixed length. A dense layer processes them after combining. In the final layer, the number of nodes will be equal to our vocabulary size. Considering the words already formed and the visual context preserved in characteristics of the image, the LSTM learns to form words word-by-word. The model has attention features that enable it to focus on relevant picture areas while generating captions. The model updates its parameters by training on the paired image-caption data to give captions that accurately represent the content of the input pictures. CNN + LSTM enables the creation of relevant and coherent captions for pictures through the combination of visual feature extraction with sequential caption creation.



D. Evaluation Metrics

BLEU Score: BLEU is, in fact, a statistical measure used to determine the quality of automatically generated captions through comparison with human-made reference captions. BLEU that is known as Bilingual Evaluation Understudy. This evaluation mechanics or matrix is widely used in textual generation. This is a comparison of the machine-generated text with one or more texts to those are manually written by human. Basically, it says how close a generated text is to an expected text. It is majorly used in automated machine translation, though it can be used with image Captioning, text summarization, speech recognition, etc. Especially in image captioning, BLEU score is the correctness that how close a generated caption is to a manual human generated caption of that particular image. The score scale lies between 0.0 and 1.0. Here 1.0 represents a best score and 0.0 is the worst score. We know all of them use BLEU score as an evaluation matrix and they evaluated BLEU-1 to 4 where:

BLEU-1 = Precision of uni-gram matches (single words).

BLEU-2 = Precision of 2-grams (pairs of consecutive words).

BLEU-3 = Precision of 3-gram matches.

BLEU-4 = Precision of 4-gram matches.

Epoch	5	15	20
Loss	3.2707	2.1933	2.7436
Bleu1	0.453804	0.553867	0.51345
Bleu2	0.236148	0.335146	0.304321

MODEL ARCHITECTURE

In the above data preparation segment, we had already preprocessed two distinct units of data. one of them is

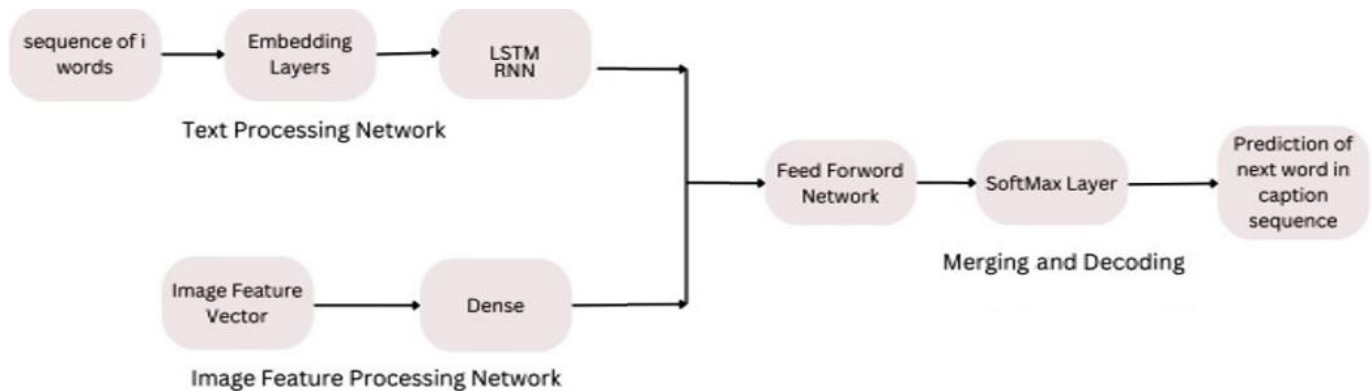
image data and the other one is caption data and now both of them will create encoded image feature vectors and encoded text embeddings, respectively. Both of the sets represent the preprocessed data, and both should be able to suitable for fitting into the neural network. Regardless image feature vectors and text embedding both cannot be combined in the same input layer of a singular neural network. As a result of this it is essential to have distinct input layers for the two types of data inputs. Following this model, the idea of the 'merge model' becomes relevant.

Merge Model

In the merge model, we will integrate two distinct types of encoded input data neural networks which is then subsequently or sequentially processed by a simpler decoder network to produce the next or upcoming word in the caption sequence. The preprocessed text is then taken as input into an embedding layer, followed by a recurrent neural network known as LSTM (Long Short-Term Memory). While that process continues in the same time the image features are processed through a densely connected neural network layer, followed by a feed-forward network, culminating in a softmax layer. The outputs encoded by the LSTM in the first neural network are combined with the encoded image embeddings from the second neural network in the second dense layer, allowing for the decoding process to predict the next word in the caption sequence.

Long Short-Term Memory (LSTM)

In the first network, we're working with text data, so we're using Natural Language Processing (NLP). For NLP, the best type of neural network is usually a recurrent neural network (RNN). Among RNNs, the long short-term memory (LSTM) network is preferred because it helps in the vanishing and exploding



gradient problems. LSTMs can back-propagate errors over many time steps and have three main gates: input, forget, and output gates.

Model Designing

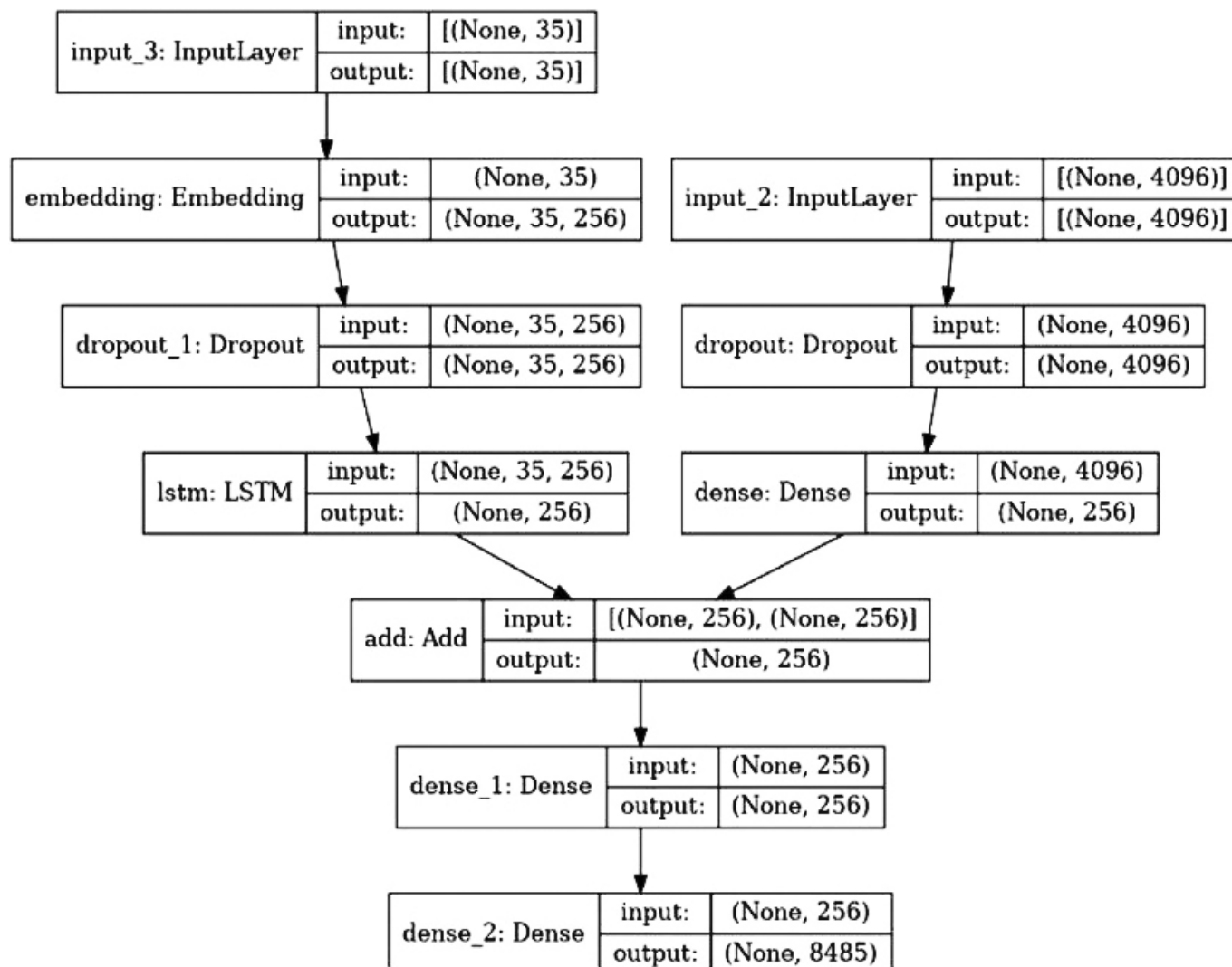
After combining all the parts in the merge model and after that we will focus on making of architecture of neural network structure. The image feature processing network takes a 1D image embedding (4096 dimensions) as input. Next, it uses a regularization layer with 50% dropout to stop the model from learning too fast and overfitting during training. Then, a dense layer shrinks the 1D vector from 4096 to 256 dimensions before it reaches the addition layer. The text processing network handles a 1D text input vector (34 dimensions). It sends this through an embedding layer to turn words into word embeddings. Again, it uses 50% dropout to prevent overfitting while training. After that, it goes

through an LSTM network of the same size to create rich detailed sentences for a given image. Once we have the results from both networks, we build the merging and decoding part of the neural network. This section has an addition layer to join the two outputs. Then, it has a dense 1D layer (256 dimensions) with a 'Rectified Linear Unit' activation followed by another dense layer of the same size with 'softmax' activation.

RESULT

BLEU Performance

After training the model, we try to determine the accuracy and efficiency of the model in generating the respective captions of the respective images. As discussed earlier in the above section BLEU metric is widely used to determine the accuracy and efficiency of word generation. We would work out the procedure



for generating text with the help of 1 and 2-gram BLEU scores. Each gram represents a different weight. Below are some observations on BLEU evaluation metrics on different BLEU gram scores.

BLEU-1	1.0,1.0,1.0,1.0	.553867
BLEU-2	0.5,0.5,0,0	.335146

Table. Comparison between original and predicted description of images

Image	Original Description	Predicted Description
101669240_b2d3e7f17b.jpg	Man skis past another man displaying painting in the snow	Two people are hiking up snowy
1002674143_1b742ab4b8.jpg	Small grid in the grass plays with finger paints in front of white canvas with rainbow on it	Little girl in pink dress is lying on the side of the grass

CONCLUSION

The results have shown the successfulness of the deep architecture used in this research. Together, the CNN and the LSTM model were able to capture and synchronize their functions in recognizing relationships between objects in an image. Therefore, this synchronization between the two architectures signifies the ability of deep learning to extract complex features for processing. Our experiments reveal that this method significantly works well towards generating an image caption, and this could be significantly improved further with the growth of dataset size and during training when there are even more varied images. A huge benefit the integration of this text-to-speech ability gives towards a visually-impaired individual to perceive surroundings much more clearly through clear and meaningful captions of an image.

The present model has been trained on the relatively compact and homogeneous Flickr8K dataset. It could be very interesting work in the future to train the model in larger and more diverse datasets, such as the Flickr30K and MSCOCO, which is highly expected to improve the robustness and accuracy of the system.

REFERENCES

- [1] Jafar A Alzubi, Rachna Jain, Preeti Nagrath, Suresh Satapathy, Soham Taneja, and Paras Gupta. 2021. Deep image captioning using an ensemble of CNN and LSTM based deep neural networks. *Journal of Intelligent & Fuzzy Systems* 40, 4 (2021), 5761–5769.
- [2] Peter Anderson, Xiaodong He, Chris Buehler, Damien Teney, Mark Johnson, Stephen Gould, and Lei Zhang. 2017. Bottom-up and top-down attention for image captioning and vqa. arXiv preprint arXiv:1707.07998 2, 4 (2017), 8.
- [3] Peter Anderson, Xiaodong He, Chris Buehler, Damien Teney, Mark Johnson, Stephen Gould, and Lei Zhang. 2018. Bottom-up and top-down attention for image captioning and visual question answering. In *Proceedings of the IEEE conference on computer vision and pattern recognition*. 6077–6086.
- [4] K AnithaKumari, C Mouneeshwari, RB Udhaya, and R Jasmitha. 2020. Automated image captioning for flickr8k dataset. In *Proceedings of International Conference on Artificial Intelligence, Smart Grid and Smart City Applications: AISGSC 2019*. Springer, 679–687.
- [5] Marcella Cornia, Lorenzo Baraldi, and Rita Cucchiara. 2022. Explaining transformer-based image captioning models: An empirical analysis. *AI Communications* 35, 2 (2022), 111–129.
- [6] Yang Feng, Lin Ma, Wei Liu, and JieboLuo. 2019. Unsupervised image captioning. In *Proceedings of the IEEE/CVF Conference on Computer Vision and Pattern Recognition*. 4125–4134.
- [7] Seung-Ho Han, Min-Su Kwon, and Ho-Jin Choi. 2020. EXplainable AI (XAI) approach to imagecaptioning. *The Journal of Engineering* 2020, 13 (2020), 589– 594.
- [8] Sen He, Hamed R Tavakoli, Ali Borji, and Nicolas Pugeault. 2019. Human attention in image captioning: Dataset and analysis. In *Proceedings of the IEEE/CVF International Conference on Computer Vision*. 8529–8538.
- [9] MD ZakirHossain, FerdousSohel, Mohd Fairuz Shiratuddin, and Hamid Laga. 2019. A comprehensive survey of deep learning for image captioning. *ACM Computing Surveys (CSUR)* 51, 6 (2019), 1–36.
- [10] Feicheng Huang, Zhixin Li, Shengjia Chen, Canlong Zhang, and Huifang Ma. 2020. Image captioning with internal and external knowledge. In *Proceedings of the 29th ACM international conference on information & knowledge management*. 535–544.
- [11] Gao Huang, Zhuang Liu, Laurens Van Der Maaten, and Kilian Q Weinberger. 2017. Densely connected convolutional networks. In *Proceedings of the IEEE conference on computer vision and pattern recognition*. 4700–4708.
- [12] Lun Huang, Wenmin Wang, Jie Chen, and Xiao-Yong Wei. 2019. Attention on attention for image captioning. In *Proceedings of the IEEE/CVF international conference on computer vision*. 4634–4643.

- [13] Andrej Karpathy and Li Fei-Fei. 2015. Deep visual-semantic alignments for generating image descriptions. In *Proceedings of the IEEE conference on computer vision and pattern recognition*. 3128–3137.
- [14] Burak Makav and Volkan Kılıç. 2019. A new image captioning approach for visually impaired people. In *2019 11th International Conference on Electrical and Electronics Engineering (ELECO)*. IEEE, 945–949.
- [15] Borneel Bikash Phukan and Amiya Ranjan Panda. 2021. An efficient technique for image captioning using deep neural network. In *Cognitive Informatics and Soft Computing: Proceeding of CISC 2020*. Springer, 481–491.
- [16] Steven J Rennie, Etienne Marcheret, Youssef Mroueh, Jerret Ross, and Vaibhava Goel. 2017. Self-critical sequence training for image captioning. In *Proceedings of the IEEE conference on computer vision and pattern recognition*. 7008–7024.
- [17] Himanshu Sharma, Manmohan Agrahari, Sujeet Kumar Singh, Mohd Firoj, and Ravi Kumar Mishra. 2020. Image captioning: a comprehensive survey. In *2020 International Conference on Power Electronics & IoT Applications in Renewable Energy and its Control (PARC)*. IEEE, 325–328.
- [18] Karen Simonyan and Andrew Zisserman. 2014. Very deep convolutional networks for large-scale image recognition. arXiv preprint arXiv:1409.1556 (2014).
- [19] Yajush Pratap Singh, Sayed Abu Lais Ezaz Ahmed, Prabhishek Singh, Neeraj Kumar, and Manoj Diwakar. 2021. Image captioning using artificial intelligence. In *Journal of Physics: Conference Series*, Vol. 1854. IOP Publishing, 012048.
- [20] Matteo Stefanini, Marcella Cornia, Lorenzo Baraldi, Silvia Cascianelli, Giuseppe Fiameni, and Rita Cucchiara. 2022. From show to tell: A survey on deep learning based image captioning. *IEEE transactions on pattern analysis and machine intelligence* 45, 1 (2022), 539–559.
- [21] Ishaan Taneja and Sunil Maggu. 2023. Generating Captions for Images Using Neural Networks. (2023).
- [22] Oriol Vinyals, Alexander Toshev, Samy Bengio, and Dumitru Erhan. 2015. Show and tell: A neural image caption generator. In *Proceedings of the IEEE conference on computer vision and pattern recognition*. 3156–3164.
- [23] Oriol Vinyals, Alexander Toshev, Samy Bengio, and Dumitru Erhan. 2016. Show and tell: Lessons learned from the 2015 mscoco image captioning challenge. *IEEE transactions on pattern analysis and machine intelligence* 39, 4 (2016), 652–663.
- [24] Yiyu Wang, Jungang Xu, and Yingfei Sun. 2022. End-to-end transformer based model for image captioning. In *Proceedings of the AAAI Conference on Artificial Intelligence*, Vol. 36. 2585–2594.
- [25] Haiyang Wei, Zhixin Li, Feicheng Huang, Canlong Zhang, Huifang Ma, and Zhongzhi Shi. 2021. Integrating scene semantic knowledge into image captioning. *ACM Transactions on Multimedia Computing, Communications, and Applications (TOMM)* 17, 2 (2021), 1–22.
- [26] Jiahong Wu, He Zheng, Bo Zhao, Yixin Li, Baoming Yan, Rui Liang, Wenjia Wang, Shippei Zhou, Guosen Lin, Yanwei Fu et al., 2017. AI challenger: A large-scale dataset for going deeper in image understanding. arXiv preprint arXiv:1711.06475 (2017).
- [27] Kelvin Xu, Jimmy Ba, Ryan Kiros, Kyunghyun Cho, Aaron Courville, Ruslan Salakhudinov, Rich Zemel, and Yoshua Bengio. 2015. Show, attend and tell: Neural image caption generation with visual attention. In *International conference on machine learning*. PMLR, 2048–2057.
- [28] Jufeng Yang, Yan Sun, Jie Liang, Bo Ren, and Shang-Hong Lai. 2019. Image captioning by incorporating affective concepts learned from both visual and textual components. *Neurocomputing* 328 (2019), 56–68.
- [29] Ting Yao, Yingwei Pan, Yehao Li, and Tao Mei. 2018. Exploring visual relationship for image captioning. In *Proceedings of the European conference on computer vision (ECCV)*. 684–699.
- [30] Quanzeng You, Hailin Jin, Zhaowen Wang, Chen Fang, and Jiebo Luo. 2016. Image captioning with semantic attention. In *Proceedings of the IEEE conference on computer vision and pattern recognition*. 4651–4659.



Book Review

Rashmi Jha¹

TITLE : Fundamentals of Machine Learning using Python
AUTHOR(S) : Manaranjan Pradhan & U. Dinesh Kumar
PUBLISHER : Wiley
PRICE : INR 689
PUBLICATION DATE : 1st January 2019
ISBN : 978-81-26579-90-7

eBook also available for institutional users

Fundamentals of Machine Learning using Python by Manaranjan Pradhan and U. Dinesh Kumar is an overall Manual with a strong foundation in Machine learning using Python libraries with practical implementation of theories and real-life case studies. The book broadly covers topics like “Foundations of Machine Learning”, “Introduction to Python”, “Descriptive Analytics and Predictive Analytics” and its advanced concepts such as “Decision Tree Learning”, “Random Forest”, “Boosting”, “Recommender Systems” and “Text Analytics”. Each topic includes real-world examples and offers a step-by-step guide to exploring, building, evaluating and optimizing machine learning models. The authors have successfully combined theoretical foundations with hands-on coding exercises and have been able to present complex topics in an accessible way.

STRUCTURE AND CONTENT

The book is divided into 13 chapters, each crafted to flow carefully from the previous one. Chapter 1 introduces the basic flow of ML and goes ahead to give a description of the fundamental applications of ML within industries such as finance, health, and marketing. This provides a very good background to

the readers entering this domain for the first time and provides a broader context on how significant ML is in solving real-world problems.

In further chapters, the basics of Python programming are explained in depth; it describes the core libraries, such as NumPy, Pandas, Matplotlib, and scikit-learn, required for basic data manipulation, visualization, and implementation of ML algorithms. The clarity in explanation and progressive step-by-step description allow readers, regardless of whether they have knowledge in programming or not, to easily work through what is presented.

The book proceeds with the explanation of linear regression, logistic regression, and decision trees as some of the most important supervised learning techniques. Each concept is first explained theoretically and then followed by a detailed Python implementation on real datasets. This dual approach cements understanding by showing how theoretical principles translate into practical applications.

The class that advanced topics including ensemble methods on support vector machines and neural networks is covered with. The authors discuss very elaborately critical issues of the process, specifically

¹ Department of Engineering & Technology – CSE, Gurugram University, Gurugram, Delhi-NCR, India.
E-mail: rashmijha@gurugramuniversity.ac.in

features selection and feature engineering, mentioning that these process steps may definitely bring a seriously sharp impetus to improvements of model performance. It covers other key techniques common within the general ML paradigm in unsupervised learning, covering such topics as clustering and the reduction of dimensionalities. These latter elements indeed contribute to presenting quite a reasonably even curricula of education in ML methodology.

PRACTICAL ORIENTATION

There can be no doubt that one of the most outstanding no-brainers in this respect is the feature of practical applicability: each chapter illustrates hands-on practice that encourages a reader to work out what has just been read. There are case studies dealing with real examples, such as Customer Retention Analysis and Stock price forecasting, including ML models into which they might be gainfully deployed. This will no doubt mean that through this practical direction, the learner will definitely experience immediate use after learning in practice.

It also covers model evaluation metrics such as precision, recall, F1-score, and ROC curves that let the readers critically look into the performance of their models, something very important in developing reliable ML systems.

SCIENTIFIC RIGOR AND DEPTH

From a scientific point of view, the book excels in introducing ML concepts in a rigorous and crystal-clear manner. The authors refrain from oversimplification and offer detailed explanations of algorithms and their mathematical background. For example, when discussing the SVMs, the book goes into an explanation of the idea of hyperplanes and how the kernel trick works for the case of non-linear separable data. The presence of such detailed discussions will help readers to get a better view of the internal structure of ML algorithms, thus fostering a deeper understanding.

While the treatment of neural networks is introductory, it lays a good foundation for further exploration. The coverage of activation functions, backpropagation, and gradient descent is well done and very fundamental to understand more complex deep learning architectures. Those who would like an in-depth explanation of deep

learning will find this book a bit lacking and will have to look elsewhere in greater detail.

STRENGTHS

The strengths in this book are as follows, which make it a useful reference:

- **Accessibility:** The writing style is clear and approachable; intractable topics are made understandable. The use of diagrams and tables further facilitates comprehension.
- **Full Coverage:** The book varies from basic to advanced ML techniques and hence may be suitable for learners in different stages.
- **Practical Focus:** The reasons why Python would be used for the implementation of methodologies discussed throughout the book bring readers, along with all theoretical aspects, to a very practical stance.
- **Self-Contained Resource:** With the basics included, Python can be learned by people who have never programmed before, hence extending the scope of the book's audience.

LIMITATIONS

Despite its many strengths, the book does have some limitations:

- **Advanced Topic Depth:** While the book does introduce advanced topics such as neural networks, it does not go into great detail about them. Anyone interested in deep learning will find it necessary to look elsewhere for more information.
- **Library Focus:** The high usage of scikit-learn, though practical, does not give enough exposure to other ML libraries and frameworks such as TensorFlow or PyTorch, which are quite necessary in deep learning applications. Ethical Issues: There is no discussion of the ethical issues that may arise in the development of ML models; for example, bias and fairness. These, if included, would turn this book into a very important one with relevance to present-day ML practice, since the topics have been burgeoning interests of late.

CONCLUSION

Machine Learning Using Python by Manaranjan Pradhan and U. Dinesh Kumar is a perfectly balanced

introduction in the field of ML, combining theoretical knowledge with practical applications. It is very suitable for both beginners and practitioners. The style of the book is easy to understand, with comprehensive coverage which is practical in nature, thus enabling readers to build a very strong foundation in ML and Python programming. While it may have gone a little deeper regarding both more advanced topics and ethical considerations, it is not touching on the latter elements

lessens neither the merit nor the potential utility that scholars will have with it. Educators will find it to be quite a reasonable textbook at an introductory level and for practitioners, this will be an excellent way of reviewing ML basics. In particular, this book is recommended for those at the beginning of their journey in ML both as a means of learning and as a reference.

International Journal of Science & Technology (PRAGYANAM)

Call for Papers

Department of Engineering & Technology, Gurugram University invites researchers, academicians and industry professionals to submit their original research papers, articles, case studies, book review, synopsis and summary of Ph.D. thesis recently completed on various emerging trends in Computer Science, IT and all interdisciplinary streams of Engineering, Technology & Applied Sciences, for International Journal of Science & Technology (PRAGYANAM) forthcoming issues. It provides a platform for publishing results and research with a strong empirical component that aims to bridge the significant gap between education and practice by promoting the publication of original, novel, industry-relevant research.

The Authors/Contributors are requested to kindly follow the given guidelines strictly:

- The contribution must be original. Submitted papers must NOT have been previously published or accepted for publication anywhere else.
- To facilitate the blind peer review process, remove ALL authors identifying information, including acknowledgements, from the text. Please provide a separate sheet including the details about the authors.
- The entire paper (title page, abstract, main text, figures, tables, references, etc.) must be in ONE word document format.
- The maximum length of the paper is 12 pages (including ALL tables, appendices and references). The paper format should follow the IEEE Style Paper Guidelines as available on journal website.
- Number all of the pages of the paper.
- Check that the paper prints correctly (i.e. all imported figures and tables are there) and ensure that the file is virus-free.
- Plagiarism should be less than 10 per cent (including references).

Note: All the submissions will be double blind peer reviewed. The Editors reserves the right to reject any submission that is clearly out of scope or well below the expected quality of this journal without further review. All material and editorial correspondence should be addressed to:

Prof. Rashmi Jha

Editor, International Journal of Science & Technology (PRAGYANAM)

GURUGRAM UNIVERSITY

Nirvana Road, Mayfield Garden, Sector 51
Samaspur, Gurugram, Haryana – 122003, Delhi-NCR, India

E-mail: ijst.pragyanam@gurugramuniversity.ac.in

Phone: 9810948766 (M)

Certificate of Originality

International Journal of Science & Technology (PRAGYANAM)

Department of Engineering & Technology, Gurugram University

Nirvana Road, Mayfield Garden, Sector 51, Samaspur, Gurugram, Haryana – 122003, Delhi-NCR, India

Title of Manuscript: _____

Author(s) Details:

1. _____
2. _____
3. _____
4. _____
5. _____

Corresponding Author's Name: _____

Contact Information: E-mail ID: _____ Phone: _____

Declaration:

1. I/We declare that the manuscript submitted is an original work and has not been published elsewhere or submitted for publication in any other journal or medium.
2. I/We confirm that all sources used in the preparation of this manuscript have been properly acknowledged, and proper citations have been provided for any material derived from other sources.
3. I/We confirm that the manuscript does not contain any unlawful statements, and it does not violate any copyright, trademark, intellectual property, or privacy rights of any third party.
4. I/We confirm that all authors have significantly contributed to the research, writing, and preparation of the manuscript and that there are no undisclosed conflicts of interest.
5. I/We understand that any breach of this declaration may lead to the rejection of the manuscript, retraction of the publication, and/or legal consequences.

Author(s) Signatures and Date:

- | | | |
|-------------|-------------|-------------|
| 1. _____ | 2. _____ | 3. _____ |
| Date: _____ | Date: _____ | Date: _____ |
| 4. _____ | 5. _____ | |
| Date: _____ | Date: _____ | |

For Official Use Only:

Verified by : _____
Designation : _____
Date : _____

(Signature of the Editor)



Editorial Board Member's Profiles



Prof. S. S. TYAGI, Dean (Faculty of Science & Technology) of Gurugram University, Gurugram is having an experience of more than 30 years of academics, teaching, and research. He has been holding various academic and administrative positions during his career. He completed his Ph.D. in Computer Science and Engineering after completing his B.Tech. and ME in Computer Engineering from reputed institutions. He has represented on various Committees at NAAC, NBA, UGC and AICTE.

Ten (10) PhDs have already been awarded under his guidance and he is guiding 04 Ph.D. Scholars in the field of Ad hoc networks, Software Defined Networking, Cloud Computing, Wireless Security etc. There are more than 110 research publications to his credit published in reputed International Journals, National Journals and in the proceedings of International and National Conferences. He is contributing to the research for the benefit of mankind and society at large. His knowledge covers all major areas of Computer Science and Engineering but not only limited to this. Currently his areas of research interest are Software Defined Networking, Image Processing, Wireless Communication, Mobile Ad hoc Networks, Cloud Computing, and Internet of Things (IOT). He has given many talks across the country as keynote speaker or Invited expert at National and International level.

Dr. S. S. Tyagi is a senior member of various prestigious professional bodies of the world like IEEE, ACM, CSI, QCI, ASQ, etc. He is serving as Chair, IEEE Computer Society (SAC), India and as Chair, IEEE SMC Society, Delhi Section. Earlier he has served as Chair of IEEE Computer Society and IEEE TEMS society, Delhi Section. He has been associated with some International Journals in the capacity of Editor, Advisor and Member of Editorial board. He is on Academic Councils, Board of Faculty and Board of Studies of various institutions.



Prof. RASHMI JHA is highly accomplished academician and researcher with nearly three decades of distinguished experience in Computer Science education, research and programming. Currently serving as an Adjunct Professor in the CSE – E&T Department at Gurugram University since July 2024. She has taught B.Tech., MCA students across reputed institutions like GGSIPU, Delhi University for over two decades, blending academic instruction with program/project coordination and administrative leadership as HOD of various departments.

Her expertise spans curriculum innovation, cutting-edge technology-enabled teaching and educational design in collaboration with various universities. A prolific researcher and editor, she has contributed around 51 research papers in reputed international and national journals and conferences. Her research interests include Natural Language Processing & AI, E-Commerce Security, Software Engineering, ERP, Lean Six Sigma and SME sustainability.

A Lean Six Sigma Green Belt Certified Computer Professional with Ph.D., M.Phil. and MCA degrees, she has actively organized and participated in over 70 conferences, seminars, workshops and FDPs. A life member of IEEE, CSI, ISTE and KINDUZ Consulting, she has delivered technical talks and chaired sessions globally. She has contributed to national committees such as NIRF, NAAC, NBA, UGC, and AICTE and was honoured with the “IEOM Woman in Industry & Academia Award” at Lawrence Technological University, USA in 2016.



Dr. CHARU GANDHI is working as an Associate Professor in the Department of Engineering and Technology at Gurugram University, Gurugram, a state university approved by Haryana Government. She has worked as Professor and Departmental Coordinator of Computer Science and Engineering at Jaypee Institute of Information Technology, Noida for 14 years. She holds a doctorate degree in Computer Science from Kurukshetra University, and Master of Technology from Banasthali Vidyapith Rajasthan. She has an academic and research experience of above 20 years in the areas of Computer Networks, Mobile Computing, Information Security and Internet of Things. She is a member of CSI, senior member IEEE, ACM and ISTE. She has been actively involved in organizing various conferences, summer schools and development programs for students as well as faculty. Currently she also holds a position of Director Employability at Gurugram University.



Dr. RAKESH GARG is an Associate Professor in the Department of Computer Science and Engineering at Gurugram University, Gurugram, Haryana, India. He received his Bachelor of Engineering, Master of Technology and Doctor of Philosophy degrees in Computer Science and Engineering in 2003, 2006 and 2016 respectively. He has a rich teaching experience of more than 19 years. His research interests include component-based software engineering, software reliability, machine learning and multi-criteria decision-making optimisation. He has published a number of research papers in reputed international journals as IEEE Transactions on Reliability, IEEE Transactions on Education, IEEE Transactions on Engineering Management, IEEE Transactions on Cloud Computing etc. and guided a number of Master's and Doctoral degree dissertations.



Dr. ARCHANA DIXIT is currently serving as an Associate Professor and Chairperson in the Department of Mathematics at Gurugram University, Gurugram. She completed her B.Sc. and M.Sc. degrees from Dr. B.R. Ambedkar University and earned her Ph.D. in the field of Bio-Mathematics from the Institute of Basic Science, Khandari, Agra. Additionally, she has significant research experience in the field of Cosmology.

Dr. Dixit has an extensive research background, having received the prestigious Best Researcher Award in 2022 and 2023 at GLA University. She has published more than 100 research papers in reputed SCI and Scopus-indexed journals. Furthermore, she is a Visiting Associate at The Inter-University Centre for Astronomy and Astrophysics (IUCAA) Pune, India. IUCAA is a UGC Autonomous Centre.

Currently Dr. Dixit was appointed as a Research Fellow for three years at the University of Zululand, South Africa. Over her career, she has successfully supervised numerous students, contributing to the advancement of knowledge in her fields of expertise.



Dr. RANJEET has been working as an Associate Prof. in the Department of Physics at Gurugram University, Gurugram, India. He has published more than 70 research papers in prestigious journals. He has worked on radiation damage of Si sensors for particle and nuclear physics experiments and contributed to developing radiation-hard Si sensors for CMS trackers in the Large Hadron Collider (LHC). He is working on 2N & 3N short-ranged NN correlations inside nuclei. Also, he is pursuing an investigation of nuclear radiation in the natural environment and an SRC-based photonuclear model. He is a member of the Electron-Ion Collider (EIC) collaboration and the Photo-Absorption of Nuclei and Decay Observation for Reactions in Astrophysics (PANDORA) project. He has 20 years of experience in teaching and research.



PROF. HARI M. UPADHYAYA is a distinguished Professor of Clean Energy Technologies at London South Bank University's School of Engineering, UK. He joined LSBU in 2018 as Head of the Advanced Materials Centre and is the founding Director of the London Centre for Energy Engineering (LCEE), a multidisciplinary hub driving innovative energy research. With over three decades of experience, Prof. Upadhyaya is an expert in thin-film photovoltaics, including dye-sensitised, perovskite, CdTe, and CIGS solar cells, as well as energy storage systems like sodium batteries and supercapacitors. His prior roles include professorships at Brunel University and Heriot-Watt University, and a pivotal contribution to establishing the PV lab at Loughborough University. He has led major UK–India research initiatives—including the EPSRC-DST APEX projects (£8m) and the SUNRISE network (~£7m)—earning the prestigious Newton Prize for excellence. Prof. Upadhyaya's prolific contributions feature 3739 citations (h-index 28), underscoring his impact in renewable energy engineering. He teaches Renewable Energy Systems and Advanced Power Electronics, shaping the next generation of energy innovators.



PROF. PRAVEEN KUMAR is a distinguished academician currently serving as Director and Professor, Department of Computer Engineering at Astana IT University, Kazakhstan. He holds a Ph.D. and M.Tech in Computer Science and Engineering. Previously, he was Professor and Head, Department of IT & Engineering, Amity University, Tashkent. With over 19 years of experience in teaching and research, he has published 130+ research papers including 6 SCI and 15 UGC-listed journal articles. He holds 9 patents and 4 copyrights, and has chaired sessions at 60+ conferences globally. He has delivered keynote speeches at prestigious institutions such as Jamia Millia Islamia and international venues in France, UK, Vietnam, and Japan. Dr. Kumar is an active Senior Member of IEEE, ACM, IETE, and IET (UK). He guides Ph.D. scholars in AI, Big Data Analytics, and Data Mining, and serves as a technical advisor to tech firms in India. He is known for his excellence in AI/ML education and innovation.



DR. KUSUM YADAV is an Associate Professor at the College of Computer Science and Software Engineering, University of Ha'il, Saudi Arabia. She received her Ph.D. in Computer Science from JJTU, India, in 2012. With over a decade of academic experience, she has held key academic positions at reputed Saudi universities, including King Abdulaziz University and Prince Sattam bin Abdulaziz University. Her primary research interests include Security, Internet of Things (IoT), Blockchain, Artificial Intelligence, and Health Informatics. She has authored over 80 peer-reviewed publications and has actively contributed to KSA Ministry of Education-funded projects. Dr. Yadav is also known for her contributions as a reviewer for more than 100 journals and as a coordinator for the Software Engineering program. She has earned over 1,300 citations, underscoring her impact on the field. Her dedication to research, teaching, and academic leadership makes her a respected name in global computer science education and innovation.

<https://www.gurugramuniversity.ac.in>



GURUGRAM UNIVERSITY

Nirvana Road, Mayfield Garden, Sector 51, Samaspur,
Gurugram, Haryana – 122003, Delhi-NCR, India

